Development of Micro to Milli-Scale Multiphase Reactors With and Without Solids For Integration Into Mini-Monoplants

Brendon Doyle

Thesis submitted to the University of Ottawa
in partial fulfillment of the requirements for the degree of
Doctor of Philosophy

Department of Chemical and Biological Engineering
Faculty of Engineering
University of Ottawa

Abstract

Typical modes of chemical processing differ between the bulk and pharmaceutical industries. Bulk chemicals are produced in large-scale, dedicated, continuous processes that are known to be more economical when flexibility in the equipment, reactions, and capacity is not required. In the pharmaceutical industry, flexibility is typically required in order to accommodate the constantly changing product market, where production campaigns may be shorter and have product amounts in the order of a few kilograms to 100 tonnes per year. Accordingly, pharmaceutical and fine chemical production is typically performed in flexible batch reactors, where larger scale vessels inherit both reduced heat transfer through a loss in surface-to-volume ratio, and decreased mass transfer through solvent dilution. As a result, pharmaceutical production processes are often run at suboptimal efficiency with large amounts of waste relative to the amount of generated product.

In this work, an alternative method of intensified and dedicated pharmaceutical process design is proposed. 'Mini-monoplant' development is outlined through three stages; including lab-based development of best-in-class processes, factory-based development for an accelerated time to market, and mini-monoplant production at commercial scale. Within the scope of such a method of process design, several intensified reactor technologies are developed and characterized for implementation into mini-monoplants.

Plate-type LL microreactors are characterized through two experimental programs. In the first, the impact of fluids (CO_2(g), water) flow rates, channel geometry, and presence of surfactant (ethanol) on the resulting gas-liquid flow regime (bubble, bubble/slug, annular), pressure drop and interphase mass transfer coefficient ($k_l a$) are investigated. Here, the interphase mass transfer coefficients ranged from ~0.05 to 1 s^{-1} and were found to correlate well with an energy dissipation

rate model in the bubble flow regime. In the second, scale-up calculations are performed for LL microreactors within the context of running a viscous nitration reaction, leading to scale-up rules derived with the goal of maintaining mean micromixing performance. In this study, mean energy dissipation rates and relative contributions of chaotic flow were used as measures for the overall micromixing performance, with both being conserved or increased upon reactor scale-up when either water or 96 wt% $H_2SO_{4\,(aq)}$ were used as the fluid.

Then, the solid suspension handling of a baffleless oscillatory flow coil reactor is characterized through two solid forming reactions, with the first being a model precipitation reaction and the second being a more mixing intensive phase transfer catalysis reaction having difficulties associated to gas and salt formation. In the first reaction, an oscillatory energy dissipation rate of 13 W/kg was effective in continuously keeping solids suspended at concentrations of 7.9 wt% and 5.8 wt% for 2 hours and 5 hours, respectively, whereas gas generation in the phase transfer catalysis reaction resulted in a 10-fold decrease of the oscillatory energy dissipation rate leading to subsequent clogging. Finally, and as a result of its success in continuous solid handling, a larger scale baffleless oscillatory flow coil reactor is then implemented for the continuous production of an active pharmaceutical ingredient (API) suspension at elevated temperature and pressure. Development of both the reaction apparatus itself as well as the operating conditions are outlined, leading to final operating conditions that produced 40 g/hr of the API at lab scale. A mixing-based design methodology is then proposed for maintaining geometric similarity and energy dissipation rates in a production scale reactor with an API production rate of 11.9 kg/hr. This work thus expands on the toolbox approach developed by Plouffe et al [1] for reactor selection, with the objective of implementation into continuous and dedicated pharmaceutical processes at commercial scale.

Sommaire

Les modes typiques de synthèses chimiques diffèrent entre les industries en vrac et pharmaceutique. Les produits chimiques en vrac sont produits dans le cadre de procédés continus dédiés à grande échelle qui sont connus pour être plus économiques lorsque la flexibilité de l'équipement, des réactions et de la capacité n'est pas requise. Dans l'industrie pharmaceutique, la flexibilité est généralement requise pour s'adapter au marché des produits en constante évolution, où les campagnes de production peuvent être plus courtes et avoir des quantités de produits de l'ordre de quelques kilogrammes à 100 tonnes par an. En conséquence, la production de produits pharmaceutiques et de produits chimiques fins est généralement réalisée dans des réacteurs discontinus flexibles, où des récipients à plus grande échelle héritent à la fois d'un transfert de chaleur réduit par une perte de rapport surface-volume et d'un transfert de masse réduit par dilution du solvant. En conséquence, les procédés de production pharmaceutique sont souvent exécutés à une efficacité sous-optimale avec de grandes quantités de déchets.

Dans ce travail, une méthode alternative de conception de procédés pharmaceutiques intensifiés et dédiés est proposée. Le développement de ‘mini-monoplant’ se déroule en trois étapes; y compris le développement en laboratoire des meilleurs procédés de sa catégorie, le développement en usine pour une mise sur le marché accélérée, et la production de mini-monoplant à l'échelle commerciale. Dans le cadre d'une telle méthode de conception de procédés, plusieurs technologies de réacteurs intensifiés sont développées et caractérisées pour être mises en œuvre dans des mini-monoplants.

Les microréacteurs LL de type plaque sont caractérisés par deux programmes expérimentaux. Dans le premier, l'impact des débits de fluides ($CO2_{(g)}$, eau), la géométrie du canal et la présence de surfactant (éthanol) sur le régime d'écoulement gaz-liquide résultant (bulle,

bulle/bouchon, annulaire), la perte de charge et les coefficients de transfert de masse interphase ($k_l a$) sont étudiés. Ici, les coefficients de transfert de masse interphase variaient de ~ 0,05 à 1 s^{-1} et se sont révélés bien corrélés avec un modèle de taux de dissipation d'énergie dans le régime d'écoulement à bulle. Dans le second, des calculs de mise à l'échelle sont effectués pour les microréacteurs LL dans le contexte de l'exécution d'une réaction de nitration visqueuse, conduisant à des règles de mise à l'échelle dérivées dans le but de maintenir les performances moyennes de micromélange. Dans cette étude, les taux moyens de dissipation d'énergie et les contributions relatives du flux chaotique ont été utilisés comme mesures de la performance globale du micromélange, les deux étant conservés ou augmentés lors de la mise à l'échelle du réacteur lorsque de l'eau ou 96% en poids de $H_2SO_{4\,(aq)}$ a été utilisé comme fluide.

Ensuite, la manipulation de la suspension solide d'un réacteur à serpentin à écoulement oscillatoire sans déflecteur est caractérisée par deux réactions de formation de solides, la première étant une réaction de précipitation modèle et la seconde étant une réaction de catalyse de transfert de phase plus intensive en mélange ayant des difficultés associées à la formation de gaz et de sel. Dans la première réaction, un taux de dissipation d'énergie oscillatoire de 13 W/kg était efficace pour maintenir en continu les solides en suspension à des concentrations de 7,9% massique et 5,8% massique pendant 2 heures et 5 heures, respectivement, alors que la génération de gaz dans la réaction de catalyse par transfert de phase a entraîné une diminution de 10 fois du taux de dissipation d'énergie oscillatoire conduisant au colmatage ultérieur. Enfin, et en raison de son succès dans la manipulation continue des solides, un réacteur à serpentin à écoulement oscillatoire sans déflecteur à plus grande échelle est ensuite mis en œuvre pour la production continue d'une suspension d'ingrédient pharmaceutique actif (API) à température et pression élevées. Le développement de l'appareil de réaction lui-même ainsi que les conditions de fonctionnement sont

décrits, conduisant aux conditions de fonctionnement finales qui ont produit 40 g/h de l'API à l'échelle du laboratoire. Une méthodologie de conception basée sur le taux mélange est ensuite proposée pour maintenir la similitude géométrique et les taux de dissipation d'énergie dans un réacteur à l'échelle de production avec un taux de production API de 11,9 kg / h. Ce travail étend donc l'approche de la boîte à outils développée par Plouffe et al [1] pour la sélection des réacteurs, avec l'objectif de mise en œuvre dans des procédés pharmaceutiques continus et dédiés à l'échelle commerciale.

Statement of Contribution of Collaborators

I hereby declare that I am the sole author this thesis. Dr. Arturo Macchi and Dr. Dominique Roberge provided guidance and editorial comments and corrections throughout this work.

Sections 2.3.1 - 2.3.3 contain data from processes that were developed prior to my studies, specifically those processes shown in figures 2.5 and 2.6, 2.10, and 2.12, by Dr. Roberge and colleagues, who are listed as co-authors of this paper. Manuscript preparation was performed by myself and Dr. Roberge.

Experimental work and manuscript preparation for the gas-liquid work in Chapter 3 was assisted by Fred Morin, as well as editorial input by Dr. Jan Haelssig. Both are listed as co-authors of this paper.

The collection of pressure drop data for the micromixing studies in Chapter 4 was assisted by Sarah Filliger at Lonza, Visp. Data analysis and manuscript preparation were performed by myself.

Commissioning of the reaction apparatus in Chapter 5 was assisted by Michel Bittel and Thierry Hubler at Lonza, Visp. Bernhard Gutmann provided insight related to the chemistry of the phase transfer catalysis reaction. All are listed as co-authors of this paper. Experiments, data analysis, and manuscript preparation were performed by myself.

Commissioning of the reaction apparatus in Chapter 6 was assisted by Sarah Filliger and Annabelle Gantenbein at Lonza, Visp. Experimental planning was assisted by Christof Aellig at Lonza, Visp, as well as external collaborators. Experiments, data analysis, and manuscript preparation were performed by myself.

Acknowledgements

I would first and foremost like to express my deep gratitude to my supervisors Dr. Arturo Macchi and Dr. Dominique Roberge for providing me with the opportunity to perform this work. Their continued support and mentorship throughout have been invaluable to my professional development, and I owe much of my success to their guidance.

I would like to acknowledge the financial support of Lonza AG, the Natural Sciences and Engineering Research Council of Canada, and the University of Ottawa in funding this work.

I would like to thank my colleagues and friends at Lonza, Visp, for making my internships enjoyable, productive, and memorable. At the University of Ottawa, I would like to express my gratitude to Fred Morin for his scientific contributions to the Gas-Liquid work.

Finally, I would like to thank my friends, family, and partner, for their continued love and support, no matter where I was in the world.

Table of Contents

Abstract ii

Statement of Contribution of Collaborators vii

Acknowledgements viii

Table of Contents ix

List of Figures xiii

List of Tables xxii

1. Introduction 1

1.1 Thesis Outline 3

2. Mini-Monoplant Technology for Pharmaceutical Manufacturing 5

2.1 Introduction 6

2.2 Process Intensification 8

2.2.1 Pharmaceutical Process Intensification 9

2.2.2 Keeping pharmaceutical processing flexible through modularity 13

2.3 Mini-monoplant concept 14

2.3.1 Lab-based development of best-in-class pharmaceutical production processes 18

2.3.2 Factory-based development for accelerated development and time to market 20

2.3.3 Mini-monoplant production technology at commercial scale 27

2.4 Conclusions 33

Abbreviations 34

3. Gas-Liquid Flow and Interphase Mass Transfer in LL Microreactors 36

3.1 Introduction 38

3.2 Materials and Methods 40

3.3 Results and Discussion 43

3.3.1 Flow Regimes 43

3.3.1.1 Effect of gas and liquid flow rates 45

3.3.1.2 Effect of Surfactant 47

3.3.2 Pressure Drop 48

3.3.2.1 Impact of Operating Conditions 48

3.3.2.2 Model 49

3.3.3 Volumetric liquid-side mass transfer coefficient (kla) 53

3.3.3.1 Impact of Operating Conditions 54

3.3.3.2 Model 56

3.4 Conclusions 58

List of Nomenclature and Indices 59

4. Micromixing Study for the Scale-up of a Continuous Flow Viscous Nitration 61

4.1 Introduction 62

4.2 Materials and Methods 63

4.3 Scale-up methodology 67

4.4 Scale-up validation with water 71

4.5 Scale-up validation with 96 wt% $H_2SO_{4\,(aq)}$ 75

4.6 Conclusions 84

Nomenclature 86

Greek Symbols 86

5. Handling of Solids and Flow Characterization in a Baffle-Less Oscillatory Flow Coil Reactor 87

5.1 Introduction 89

5.2 Materials and Methods 91

5.2.1 Reaction Apparatus 91

5.2.2 Solid Handling Characterization 94

5.2.3 Mixing Dependent Phast Transfer Catalytic Reaction 95

5.2.4 Flow Characterization 98

5.2.5 Particle Size Distribution and Morphology 99

5.3 Results and Discussion 100

5.3.1 EDDC Reaction Characterization 100

5.3.2 Effect of Pulsation on Solid Handling 103

5.3.3 Effect of Gas Formation on Pulsation 107

5.3.4 Flow Characterization 110

5.3.5 Particle Size Distribution and Morphology 115

5.4 Conclusions 117

Abbreviations 119

Nomenclature 119

Greek Symbols 120

6. Continuous and Intensified Production of an API Suspension Under Oscillatory Flow 122

6.1 Introduction 123

6.2 Materials and Methods 125

6.2.1 ZS-9 Crystallization Reaction 125

6.2.2 Lab-Based Development of the Continuous Reaction System [100] 126

6.2.3 Product Collection and Analysis 129

6.3 Development of the Continuous Reaction System 131

6.4 Parametric Analysis of Reaction Conditions 136

6.5 Scale-Up to Production Scale 144

6.6 Conclusions 152

Nomenclature 154

Greek Symbols 155

7. Conclusions and Future Research 156

7.1 Conclusions 156

7.2 Recommendations for future research 165

8. References 167

List of Figures

Figure 2.1. Examples of fundamental continuous reaction technologies. a = FlowPlate rack with ultrasound unit for deplugging. b = Coiled tubed reactor. c = CSTR. d = Tubular reactor with static mixer inserts. e = FlowPlate rack with ultrasound used in series with a tubular reactor with static mixer inserts. 11

Figure 2.2. Schematic view of supply security comparison between a multi-purpose plant and a monoplant. CusX = Customer X. 16

Figure 2.3. Defining factors in the design of a mini-monoplant. 17

Figure 2.4. Three key advantages realized through the intensification of monoplants into mini-monoplants for pharmaceutical production. 18

Figure 2.5. Lab-based development of a continuous mini-monoplant contained within three fume hoods. 19

Figure 2.6. Simplified process flow diagram for the lab-based mini-monoplant development shown in Figure 2.5. 20

Figure 2.7. Factory-based process development. Use of an available cabin within the existing production infrastructure allows for a reduction in development time and time to market. 21

Figure 2.8. Reactor platform module. Reprinted with permission from reference [88]. Copyright 2015 Microinnova. 22

Figure 2.9. Comparison of required reactor sizes for various flow continuous-flow rates and for batch. The use of dedicated continuous technology drastically reduces the required footprint when compared to the batch and campaign approaches. Product flow rates assume a 10 wt% concentration of the bulk flow rate. AX = Size A5 or larger. SSP = Small Scale Plant, LP = Launch Plant, FCC = Fine Chemicals Complex. 24

Figure 2.10. Production of 2-nitroethanol where unit operations are intensified via continuous operation. 26

Figure 2.11. Potential routes for batch work-up downstream in a mini-monoplant. 29

Figure 2.12. Intensified reaction with automated batch work-up. Here applied to the production of tetraalkyl phosphonium salt. 31

Figure 3.1. Set-up for flow visualization, pressure drop and interphase mass transfer experiments 42

Figure 3.2. Geometry of FlowPlate™ and mixing elements: a) LL (liquid-liquid)-Reactor (triangle) size A7 plate arrangement [111] (licensed under https://creativecommons.org/licenses/by/4.0/); b) Three-dimensional visualization and characteristic dimensions of the (rhombus) mixing element; and c) Repeating mixing elements in the LL-Rhombus and LL-Triangle [111] (licensed under https://creativecommons.org/licenses/by/4.0/). 42

Figure 3.3. Flow regimes identified in this work: a) bubble flow, b) slug flow, and c) annular flow. 44

Figure 3.4. Flow regime maps of a) LL-Rhombus and b) LL-Triangle, with deionized water as the liquid phase. 45

Figure 3.5. Flow in LL-Triangle (left) demonstrating increased gas holdup in centre of mixer, a behaviour that is absent in the LL-Rhombus (right) for the same flow rates. Liquid velocity is 0.53 m/s, and gas velocity is 0.080 m/s in the LL-Triangle and 0.081 m/s in the LL-Rhombus. 46

Figure 3.6. Flow regime maps of a) LL-Rhombus and b) LL-Triangle, with 0.5 wt% aqueous ethanol solution as the liquid phase. 47

Figure 3.7. Flow in the LL-Triangle mixer demonstrating the effect of increased gas flow rate on flow morphology where surfactant is present. Gas velocities are a) 0.091 m/s and b) 0.65 m/s, and

the liquid velocity is 0.27 m/s. Note that a) demonstrates bubble flow, and b) demonstrates bubble flow with froth formation..... 48

Figure 3.8. Pressure drop over varying liquid and gas velocities in the LL-Rhombus (R) and LL-Triangle (T) reactors with a) water and b) 0.5 wt% aqueous ethanol as the liquid phase. 49

Figure 3.9. Parity plot of predicted vs measured pressure drop values. 52

Figure 3.10. Comparison of kla at varying gas and liquid flow rates in the LL-Rhombus (R) and LL-Triangle (T) with a) water and b) 0.5 wt% aqueous ethanol as the liquid phase..... 55

Figure 3.11. Comparison of extraction efficiency, E, at varying gas and liquid flow rates in the LL-Rhombus (R) and LL-Triangle (T) with a) water and b) 0.5 wt% aqueous ethanol as the liquid phase. 56

Figure 3.12. Parity plot of predicted vs measured kla values in the bubbly flow regime..... 58

Figure 4.1. Simplified process flow diagram for the lab-scale pressure drop measurements. 64

Figure 4.2. LL mixer geometry and orientation within the plate reactors. (a). Size 300 LL-Rhombus mixer. (b) A5 Size 300 Rhombus. (c) A5 Size 200 Rhombus. (d) A5 Size 100 and 100* Rhombus (e) A5 Size 100* Triangle. Note that the size 100 and 100* plates have the same mixer layout but differ in their channel depths. 66

Figure 4.3. CFD generated velocity profiles (a), streamline maps (b), and turbulent viscosity (vt) fields (c) at the midplane (δ = 0.625 mm) of the LL Rhombus mixer with water. For (a) and (b), u (m/s) varies from, depending on the flowrate, $umin$ (blue) = 0 m/s to $umax$ (red) = 0.45 (10 g/min), 0.91 (20 g/min), 1.28 (30 g/min), 2.21 m/s (50 g/min), 3.39 (70 g/min) and 5.37 (100 g/min). For (c), vt (m^2/s) varies from vt, min (blue) = 0 (blue) to vt, max (red) = (10 g/min), 6.7×10^{-6} (20 g/min), 2.2×10^{-5} (30 g/min), 4.1×10^{-5} (50 g/min), 5.0×10^{-5} (70 g/min), and 6.2×10^{-5} (100 g/min) [141]. 70

Figure 4.4. Pressure drops (a) and resulting mean energy dissipation rates (b,c) in the lab scale (size 300) and production scale (size 200 – 100*) microreactor plates with water. Dashed lines represent predicted mean energy dissipation rates, with both the Rhombus and Triangle size 100* mixers sharing the same black dashed line, when (b) a constant friction factor model is assumed across all scales, and (c) when the experimentally determined friction factor model is used for $f2$. 73

Figure 4.5. Friction factor analysis for the lab-scale (size 300) and production scale (sizes 200 – 100*) plates with water. (a) Overall friction factors from equations (4.4) and (4.8). (b) Relative contributions of chaotic flow as a function of Re. (c) Relative contributions of chaotic flow as a function of mean energy dissipation rate. 74

Figure 4.6. Pressure drops (a) and resulting mean energy dissipation rates (b,c) in the lab scale (size 300) and production scale (size 200 – 100*) microreactor plates with water. Dashed lines represent predicted mean energy dissipation rates, with both the Rhombus and Triangle size 100* mixers sharing the same black dashed line, when (b) a constant friction factor model is assumed during scale-up, and (c) when the experimentally determined friction factor model is used for $f2$. Filled data points are extrapolated to ϵ = 91.8 W/kg. 76

Figure 4.7. Friction factor analysis for the lab-scale (size 300) and production scale (sizes 200 – 100*) plates with 96 wt% $H_2SO_{4\,(aq)}$. (a) Overall friction factors from equations (4.4) and (4.8). (b) Relative contributions of chaotic flow as a function of Re. (c) fc/f as a function of mean energy dissipation rate. Filled data points are extrapolated to ϵ = 91.8 W/kg..... 78

Figure 4.8. Orientation of the tubes for testing the shell and tube reactor (right) with static mixer inserts (left). 80

Figure 4.9 Pressure drops (a) and resulting mean energy dissipation rates (b) with water through the static mixer geometry shown in Figure 4.8, as compared with the size 300, 200, and 100* Rhombus LL-microreactor plates. 81

Figure 4.10. Pressure drops (a) and resulting mean energy dissipation rates (b) with 96 wt% $H_2SO_{4\,(aq)}$ through the static mixer geometry shown in Figure 4.8, as compared with the size 300, 200, and 100* Rhombus LL-microreactor plates. Filled data points are extrapolated to ϵ = 91.8 W/kg. 82

Figure 4.11. Friction factor analysis for the static mixer geometry with water as compared with the size 300, 200, and 100* Rhombus. (a) Overall friction factors from equations (4.4) and (4.8). (b) Relative contributions of chaotic flow as a function of Re. (c) Relative contributions of chaotic flow as a function of mean energy dissipation rate..... 83

Figure 4.12. Friction factor analysis for the static mixer geometry with 96 wt% $H_2SO_{4\,(aq)}$ as compared with the size 300, 200, and 100* Rhombus. (a) Overall friction factors from equations (4.12) and (4.13). (b) Relative contributions of chaotic flow as a function of Re. (c) Relative contributions of chaotic flow as a function of mean energy dissipation rate. Filled data points are extrapolated to ϵ = 91.8 W/kg. 84

Figure 5.1. Reaction apparatus for the two solid forming reactions. Pre-mixing and reactor heating are included for the reaction in Scheme 5.2 but are omitted for the reaction in Scheme 5.1. 93

Figure 5.2. EDDC solubility as a function of temperature. 100

Figure 5.3. *In-situ* H-NMR analysis of EDDC-forming reaction with 0.17 M glyoxal and 0.34 M CHA. 102

Figure 5.4. H-NMR analysis of EDDC-forming reaction showing side-product formation. 102

Figure 5.5. Clog formation without pulsation with 3.7 wt% solids. [Glyoxal] = 0.4 M; [CHA] = 0.8 M; space time = 30 min. 104

Figure 5.6. Stable operation for 5 hours with 5.8 wt% solids. [Glyoxal] = 0.6 M; [CHA] = 1.2 M; space time = 30 min. High intensity pulsation allows the system to operate in the turbulent flow regime, leading to higher pressure oscillations and continuous flow of solid suspensions. 105

Figure 5.7. Pressure profiles during the tests showing a decrease in amplitude (left) and frequency (right) with 7.9 wt% solids, leading to rapid clog formation when pulsation is stopped. [Glyoxal] = 0.8 M; [CHA] = 1.6 M; space time = 30 min. Left figure: amplitudes, a = 46.9 mm; b = 37.5 mm; c = 28.2 mm; d = 18.8 mm; e = 0 mm with clog formation. Right figure: frequencies, a = 3.68 Hz, b = 2.45 Hz, c = 1.64 Hz, d = 0.82 Hz, e = 0 Hz with clog formation. 107

Figure 5.8. Pressure profile for reaction 2 showing oscillation dampening due to gas formation and accumulation resulting in clogging at the reactor inlet. a = dampening of pulsation energy. b = onset of pressure increase due to CO formation. c = manual system venting 110

Figure 5.9. Residence Time Distribution 112

Figure 5.10. Particle Size Distribution for Scheme 5.1. [Glyoxal] = 0.2 M, [CHA] = 0.4 M. Space time = 30 min. 117

Figure 5.11. EDDC particle morphology after 30 minutes in batch or flow with varying pulsation frequency. Scale bar = 100 µm 117

Figure 6.1. a: Crystal structure of ZS-9. Blue: oxygen, green: silicon, red: zirconium [194]. b: Counter ion binding pore opening of ZS-9. 126

Figure 6.2. General and simplified process flow diagram for continuous ZS-9 suspension production. Region 1 (left) represents the mixing point and upstream components that were varied

during development. Region 2 (right) represents the region downstream of the mixing point that remained constant throughout development. 129

Figure 6.3. Examples of product analysis via XRD. a: amorphous solid indicated by a broadening of the baseline. b: Side product formation indicated by peaks that do not correspond to the reference sample. c: pure and crystalline ZS-9. 131

Figure 6.4. Progression of the mixing point and upstream components of the system for continuous ZS-9 suspension production. 135

Figure 6.5. Representative pressure profile for continuous ZS-9 suspension production with a 390 min run time. 136

Figure 6.6. Effect of crystallization coil space time on the product XRD profile in setup 3c. Note that the change in space time is accompanied by a change in Reo/Ren, having values of 88 for experiment 6718-34 and 263 for experiment 6718-37. All other reaction conditions are as listed in Table 6.1. 138

Figure 6.7. Effect of crystallization coil temperature on the product XRD profile. Reactions at 252°C were performed in setup 3b while the reaction at 245°C was performed in setup 3c Top row: Reo/Ren = 105. Bottom row: Reo/Ren = 175. All other reaction conditions are as listed in Table 6.1. 140

Figure 6.8. Effect of seeding temperature on the product XRD profile. Top row: Reo/Ren = 105 in setup 3a. Bottom row: Reo/Ren = 175 in setup 3b. All other reaction conditions are as listed in Table 6.1. 141

Figure 6.9. Effect of pulsation intensity (Reo/Ren) on the product XRD profile. All other reaction conditions are as outline in Table 6.1. 143

Figure 6.10. Analysis of the ZS-9 product at the final selected operating conditions. a: XRD profile showing pure ZS-9 with no amorphous content. b: scanning electron microscopy showing cubic ZS-9 crystals, scale bar = 25 µm. c: PSD reporting 9.81 vol% of product crystals below 3 µm diameter..... 144

Figure 6.11. ϵo and Reo/Ren as a function of increasing reactor diameter. Dashed black and blue lines correspond to ϵo = 27.8 W/kg (seeding coil) and Reo/Ren = 175, respectively. 151

Figure 7.1. Defining features of a mini-monoplant. 157

Figure 7.2. Three key advantages realized through the intensification of monoplants into mini-monoplants for pharmaceutical production 157

Figure 7.3. Flow regime maps in the LL-Rhombus (a) and the LL-Triangle (b) for both the water/$CO_{2\,(g)}$ (top) and 0.5 wt% EtOH $_{(aq)}$ (bottom) systems..... 159

Figure 7.4. Pressure drop modelling for all data (left) and kla modelling for the bubble flow data (right) for both the LL-Rhombus and LL-Triangle with and without surfactant..... 160

Figure 7.5. Measured and scale-up rule-predicted (dashed lines) energy dissipation rates with water (top) and 96 wt% $H_2SO_{4\,(aq)}$ (bottom) presented alongside relative contributions of turbulent flow as a function of energy dissipation rate (rate)..... 161

Figure 7.6. Continuous operation for 300 minutes with a constant pulsation energy input and a solid suspension of 5.8 wt%..... 162

Figure 7.7. Pulsation dampening and resulting blockage caused by the formation of gas in a closed pulsated system. 163

Figure 7.8. Final operating system configuration for the continuous production of a ZS-9 suspension under oscillatory flow..... 164

Figure 7.9. Lab-produced ZS-9 product profile showing pure and crystalline ZS-9 (a), cubic particles (b), and an average particle diameter of 5.37 μm with 9.81 vol% having a diameter below 3 μm. 165

List of Tables

Table 3.1. Correlated Blasius equation parameters for LL-Rhombus and LL-Triangle geometries for 214 < Re_l < 856. 50

Table 3.2. Correlation parameter values and 95% confidence intervals for tested geometries and continuous phases. For the CO_2-water and rhombus data, 214 < Re_l < 856 and 0.15 < u_g/u_l < 36.5. For all other data, 214 < Re_l < 428 and 0.14 < u_g/u_l < 18.0. 52

Table 3.3. kla model fits and 95% confidence intervals for LL-Rhombus and LL-Triangle with water and 0.5 wt% aqueous ethanol as the liquid phases over the ranges of 0.565 < ϵ < 6.91 W/kg and 0.14 < ug/ul < 0.56. 57

Table 4.1. Tested flowrate ranges and space times for each fluid and microreactor plate pairing. 65

Table 4.2. Scaled-up reactor geometries and dimensions. 67

Table 4.3. Dual-term friction factor correlation values for the large-scale plates with water. All correlations have an R^2 value greater than 0.999. 75

Table 4.4. Dual-term friction factor correlation values for the large-scale plates with 96 wt% H_2SO_4 $_{(aq)}$. All correlations have an R^2 value greater than 0.999. 79

Table 5.1. Identification and description of different components in the apparatuses for Scheme 5.1 and Scheme 5.2. 93

Table 5.2. Reaction conditions for Scheme 5.1 and Scheme 5.2. 97

Table 5.3. Residence time moments and dimensionless flow numbers at varying pulsation and flow rates 115

Table 6.1. Base reaction conditions for parametric analysis of the operating conditions. 137

Table 6.2. Friction factor correlations and conditions for helically coiled tubes. 148

Table 6.3. Correlations and resulting critical Reynolds numbers for flow through helical coils. 149

Table 6.4. Dimensions for the scaled-up oscillatory coil reactor and resulting oscillatory flow parameters where geometric similarity is maintained throughout the system. 152

1. Introduction

Pharmaceutical products have been historically produced through batch or semi-batch stirred tank reactors, where multipurpose manufacturing assets are periodically allocated to a single product through scheduled production campaigns. The scale of these production campaigns can range from several kilograms to 100 tonnes in a year, with a single campaign lasting as little as a few days or as long as a few months. The reactors used in this approach are necessarily flexible and able to accommodate the wide range of reaction kinetics, phases (including solids which are often involved in pharmaceutical production processes), and throughputs present in the pharmaceutical industry, and are amenable to cleaning and re-use for multiple production campaigns throughout the year [2,3]. This approach, however, often results in significant lead time before a product becomes commercially available and does not allow for a particularly rapid response to fluctuation in market demand. This method of production is in direct contrast to those used in the bulk chemical industry, where dedicated continuous processes are commonly employed to stably generate products long term, and where flexibility is generally not a requirement [4].

In recent years, there has been a growing interest in applying the principles of process intensification and continuous flow to pharmaceutical manufacturing. This, in part entails a reduction of process equipment volume in order to continuously run reactions at intensified conditions, allowing for similar productivities to those of batch campaigns to be achieved with a significantly reduced process footprint. A high degree of automation should also be included in these processes, as outlined by Industry 4.0 [5], with product quality monitoring and control via process analytical technology and real-time release testing. Doing so, however, will require a shift in reaction technologies to those that are amenable to intensified continuous processing, as the commonly used batch vessels lack the surface-to-volume ratio to effectively and safely control the

intensified reactions that tend to be more exothermic and susceptible to thermal runaway and explosions.

Micro- and milli-scale reactor technologies, classified by having characteristic lengths in the micrometer and millimeter range, respectively, are intensified reactor technologies that, when operated continuously, can achieve the production rates required for clinical and commercial pharmaceutical production. The increased surface-to-volume ratio of such reactors imparts improved heat and mass transfer, tighter process control, reduced solvent usage, more homogeneous reaction environments, and safer handling of hazardous materials when compared to larger-scale batch equipment [6,7]. The reduced dimensions of these reactors, however, makes running reactions containing a solid component more difficult due to the elevated risk of clogging [3]. Of particular interest to this thesis are plate-type microreactors and coiled tube reactors, where plate-type microreactors may be employed for fast reactions containing liquid and/or gas phases, and coiled tube reactors find application in longer reactions containing solids via imposing an oscillation on the reaction medium.

The objective of this thesis is thus to explore new and emerging trends in pharmaceutical production and to propose alternative methods to pharmaceutical production. Mini-monoplant production is presented, and key value-generating factors are identified from lab-scale development of best-in-class pharmaceutical processes, to factory-scale development for accelerated times to market, and finally mini-monoplant production at commercial scale. Within the scope of such a method of process development, intensified reaction technologies are developed and characterized for reaction systems with various phases including liquid, gas-liquid, liquid-solid, and liquid-liquid-solid.

1.1 Thesis Outline

Chapter 2 consists of a literature review of current methods of pharmaceutical production and process intensification, leading to the proposal of mini-monoplant technology for pharmaceutical production. In this chapter, pharmaceutical process development is described from lab-scale, where intensified and continuous reaction technologies are employed to develop best-in-class processes. This is followed by further process development at factory scale for a reduction in the time to market, and finally followed by a description of mini-monoplant technology and commercial scale and its associated logistics. This chapter explores the potential benefits of process intensification and dedication to larger scale pharmaceutical production. This work has been published under the title “Mini-monoplant technology for pharmaceutical production”.

Chapters 3, 4, 5, and 6 expand on the toolbox approach for reactor selection proposed by Plouffe et al [8] by developing and characterizing reactors for systems containing phases that were previously less explored in the present reactor geometries. These reactors represent additional tools that may be implemented into mini-monoplants under intensified conditions.

In chapter 3, gas-liquid flow and mass transfer are explored in LL-microreactors. This chapter explores the effect of geometry and surfactant on flow regimes and interphase mass transfer in a reactor geometry that was previously developed for liquid-liquid systems. This work has been published under the title “Gas-liquid flow and mass transfer in LL-microreactors”.

In chapter 4, micromixing performance is evaluated in various LL-microreactor plates within the scope of scaling-up a micromixing dependent viscous and exothermic nitration. Pressure drop data are analyzed in order to derive scale-rules for predicting the mean micromixing performance of the large-scale reactor plates with both water and 96 wt% $H_2SO_{4\,(aq)}$. This work will be published upon completion of production scale process development for the nitration.

Chapter 5 presents a baffleless oscillatory flow coil reactor for continuous handling of solid suspensions. The solid handling capabilities are explored through two test reactions; a precipitation reaction and a phase catalysis reaction. Finally, fluid flow patterns in the reactor are characterized by residence time distribution studies. This work has been published under the title “Handling of solids and flow characterization in a baffleless oscillatory flow coil reactor”.

In Chapter 6, a larger scale version of the baffleless oscillatory flow coil reactor is implemented for continuous production of an active pharmaceutical ingredient (API) suspension at elevated temperature and pressure. The effects of residence time, temperature, and oscillation intensity on the product quality are examined. Finally, mixing-based scale-up calculations are performed leading to the proposal of a larger reactor geometry for production of the API in the tonne scale. This work will be submitted for publication at a later date.

Finally, overall conclusions for the thesis and recommendations for future research are presented in Chapter 7.

2. Mini-Monoplant Technology for Pharmaceutical Manufacturing

Brendon J. Doyle[a], Petteri Elsner[b], Bernhard Gutmann[b], Olivier Hannaerts[b], Christof Aellig[b], Arturo Macchi[*,a], and Dominique M. Roberge[*,b].

[a]Centre for Catalysis Research and Innovation, Department of Chemical and Biological Engineering, University of Ottawa, K1N 6N5, Ottawa, Canada

[b]API Development Services, Lonza AG, CH-3930, Visp, Switzerland

This manuscript has been published: Brendon J. Doyle, Petteri Elsner, Bernhard Gutmann, Olivier Hannaerts, Christof Aellig, Arturo Macchi, and Dominique M. Roberge. Mini-Monoplant Technology for Pharmaceutical Manufacturing. Organic Process Research & Development 2020 24 (10), 2169-2182

Abstract

Pharmaceutical production has historically relied on multi-purpose batch vessels in order to produce material through scheduled production campaigns. Although this method is flexible, it is becoming less effective in addressing the changing landscape of pharmaceutical production where more complex and potent molecules are required to be produced more rapidly and can have fluctuations in their demand. In this article, a method for developing intensified and dedicated pharmaceutical processes, known as mini-monoplants, is described. Key value generating aspects are described at each stage of development, from lab-based development of best-in-class processes, to factory-based development for an accelerated time to market, and finally to mini-monoplant technology for production at commercial scale.

Keywords: Pharmaceutical manufacturing, Process intensification, Continuous flow design, Scale-up, FlowPlate.

2.1 Introduction

The class of bulk chemicals generally comprises two divisions of chemical production, namely the production of approximately 20 base chemicals and 300 intermediates. About 85% of all chemicals are produced through modifications of the base chemicals, with the first level of transformations leading to the intermediate chemicals. The value of these chemicals is relatively low compared to those that are more advanced and require more complex transformations, but their immense volume and necessity as a feed for other processes allows them to maintain a significant share of the chemical market, accounting for 60% of chemical sales in the EU in 2018 (excluding pharmaceuticals) [9]. The large production requirements of these chemicals lead to dedicated continuous processes that are run over long periods of time, a processing mode which is known to be more economical when flexibility in the reactions, capacity, and equipment is not required [4]. The cost efficiency of these plants is dependent on them being large and long-operating due to the economy of scale which tends to lead to larger and riskier investments [10,11].

Conversely, processes in the pharmaceutical and fine chemical industries typically require a high degree of flexibility due to their short lifetimes and a constantly changing product market. The scale of these processes is significantly smaller than in the bulk chemicals industry and is usually in the order of a few kilograms to 100 tonnes per year [12]. As a result, these chemicals are most often produced in modular and/or multi-purpose plants that utilize primarily batch or semi-batch stirred tank reactors. These reactors are often not optimized to any specific reaction, but rather are able to accommodate a wide range of phases and reaction rates relatively easily. This flexibility allows for production of different chemicals through a schedule of campaigns that can last as little as a few days or as long as a few months, making it possible to produce tens of different products annually in a single train [2,3]. This flexibility does not come without cost, however, as

batch vessels tend to have reduced performance as their scale increases. Most products in this industry are developed at lab-scale in the drug discovery stage and are primarily scaled up by increasing the vessel size while maintaining a similar geometry. However, the increase from a lab-scale flask to a production-scale vessel imparts a drastic reduction of the reactor surface-to-volume ratio and a significant resulting decrease in the heat transfer performance of the system. In the interest of safety, these reactions are then usually run diluted or semi-batch wise. Reactions run under such conditions are slower and inherit poor mass transport due to the reduced concentrations and small interfacial areas in large multiphase systems. Furthermore, this dilution requires an excessive amount of solvent - a situation which should be avoided due to the amount of waste and the environmental impact of its disposal. As a result, production scale pharmaceutical processes are often run (semi)batch-wise at sub optimal efficiency with large E-factors (defined as mass of waste per unit mass of product) [13] and relatively low space-time yields, both of which afford opportunities for process intensification [8,14–16].

In this article, a model for pharmaceutical process design is proposed based on principles already in use in the bulk chemical industry. While it is generally accepted that both industries possess the potential to benefit from process intensification, there exist specific barriers and challenges for each that need to be addressed and evaluated on a case-specific basis. Specifically, in the pharmaceutical industry, the batch campaign approach to production represents a key area where value may be generated through a shift to alternative methods of processing. For those campaigns that are longer with production quantities approaching the range of bulk chemical production, dedicated processes that more closely resemble those found in the bulk chemistry industry should be considered [17]. The goal of this article is thus to provide a pragmatic perspective on pharmaceutical process design that utilizes a set of established technologies to

select the most optimal design when given a particular reaction environment. Challenges and developments pertaining to process intensification within the pharmaceutical industry are presented, leading to a model for development of dedicated, intensified pharmaceutical processes from early lab-scale to commercial production via mini-monoplant technology.

2.2 **Process Intensification**

Process intensification is a well-established concept for improving the efficiency and economics of chemical production while reducing its environmental impact [18]. This has traditionally been proposed as a reduction in process equipment volume [19] in order to allow more intensified reaction temperatures and pressures, however it may also include methods of combining multiple unit operations into one device or module and bringing them physically closer to each other [11,20]. In both cases, limitations in mass and heat transfer are reduced as well as solvent holdup and distances between unit operations. The definition of process intensification has been extended by Stankiewicz and Moulijn to include "the development of novel apparatuses and techniques that, compared to those commonly used today, are expected to bring dramatic improvements in manufacturing and processing, substantially decreasing equipment-size/production-capacity ratio, energy consumption, or waste production, and ultimately resulting in cheaper, sustainable technologies" [21], with the fundamental principles of process intensification lying in the spatial, thermodynamic, functional, and temporal domains from the molecular to processing scales [22]. Accompanying this concept of process intensification is the Industry 4.0 standard for a high degree of automation and information processing in chemical production [5]. In this idea, processing equipment are able to communicate with each other and their operators digitally, leading to a high level of information transparency and availability as well as the ability of machines and artificial intelligence to help with decision making and performing

of physically difficult tasks. Product quality can be monitored and adjusted using process analytical technology (PAT) [23] and Real Time Release Testing (RTRT) [24]. A factory running autonomously in this manner is dubbed a 'smart factory' and is predicted to greatly improve product quality assurance and control [25]. Despite the known benefits of process intensification and automation, general barriers exist to its widespread implementation such as cost, complexity, and a general hesitation to break the status quo. As such there is a so-called 'rush to be second' where most managers want to wait for proven full-scale evidence of process intensification before committing [18]. The best opportunities for the implementation of new intensified technologies will therefore come from situations where new plants or processes are being developed [18]. The barriers described above are being addressed through the establishment of various institutes or consortiums, such as the pioneering IMM (Fraunhofer-Institut für Mikrotechnik und Mikrosysteme) [26], and followed in other countries by CMAC (Continuous Manufacturing and Crystallization) [27], RCPE (Research Center Pharmaceutical Engineering) [28], SSPC (Synthesis and Solid State Pharmaceutical Centre) [29], MEPI (Maison Européenne des Procédés Innovants) [30], and RAPID (Rapid Advancement in Process Intensification Deployment) [31,32], as well as efforts from various companies within the pharmaceutical industry [33].

2.2.1 Pharmaceutical Process Intensification

In the pharmaceutical industry, where short-lived production campaigns are primarily performed in (semi)batch reactors, the desire to miniaturize and intensify will generally require continuous processing. Continuous-flow at the micro or milli scale provides several advantages when compared to typical large-scale batch production processes, including improved heat and mass transfer, lower solvent requirements, better process control, enhanced reaction homogeneity, and safer handling of hazardous materials [6,7,34,35]. Productivities (defined as the amount of

product generated with a finite amount of resources, including labour) comparable to those in large-scale batch operation can be achieved when the system is run continuously in a smaller scale unit leading to a drastically smaller footprint. Several examples of continuous pharmaceutical production have been developed and published by researchers at Eli Lilly, including high temperature continuous crystallization [36] and continuous active pharmaceutical ingredient (API) production under cGMP conditions [37–40], as well as reports detailing collaborations and technology transfer between pharmaceutical companies and contract manufacturing organizations [39,41]. Of key importance to the intensification of pharmaceutical processes, and owing to the enhanced rates of heat and mass transfer, is the ability to perform reaction chemistries that would normally be considered 'forbidden' under standard batch operation [17,42]. Intensified reactions run under high temperature, pressure, and concentration result in faster reaction rates and larger productivities, especially with the implementation of automation and RTRT. In addition, higher energy reagents may be employed which can facilitate more direct synthesis routes with fewer steps and higher purity products [17,42]. For example, microreactors have previously shown success in the generation of explosive nitroglycerin [33] and can significantly broaden the safe operating window with explosive substances [43]. The selection of the appropriate continuous reactor technology depends on the reaction phases, kinetics, and reaction network, and these technologies may be broadly divided into three fundamental categories of plates, coils, and CSTRs [8]. Plate reactors are generally applicable to reactions containing liquid and/or gas phases, and when more plug flow is desired with rapid micromixing and/or heat transfer. Coil type reactors can be applied to plug flow reactions with slower kinetics that require longer residence times and less intensive heat transfer and can be extended to handle solids when oscillation is applied to reaction medium. For perfectly mixed reactions, one CSTR can be implemented for reactions with

specific network, or a cascade of CSTRs to handle a wide range of reactions, kinetics, and phases. Some specific continuous and intensified examples (shown in Figure 2.1) and applications of these (and related) reactor categories include plate microreactors [44–50], oscillatory flow reactors [51–59], coiled flow inverters [60–66], micro packed bed reactors [67,68], plug flow reactors with static mixer inserts [69–72], mixed-suspension-mixed-product-removal (MSMPR) [73,74], and miniaturized continuous stirred tank reactors (CSTRs) [75].

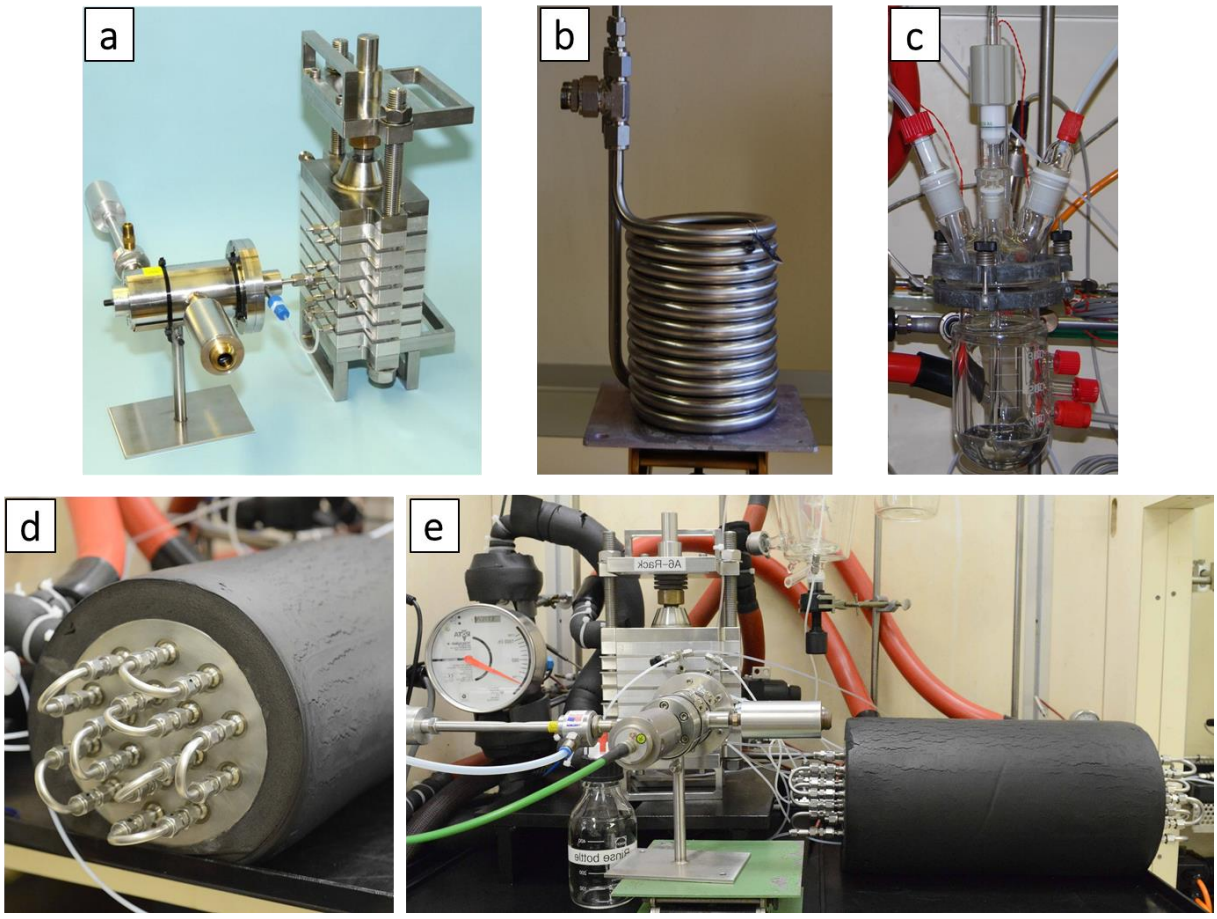

Figure 2.1. Examples of fundamental continuous reaction technologies. a = FlowPlate rack with ultrasound unit for deplugging. b = Coiled tubed reactor. c = CSTR. d = Tubular reactor with static mixer inserts. e = FlowPlate rack with ultrasound used in series with a tubular reactor with static mixer inserts.

Thus, pharmaceutical processes may be intensified through these three targets:

1) Intensification of the *synthesis route* via more direct and higher yield pathways
2) *Reactor technologies*, often miniaturized, with high surface area to volume ratios and reduced transport lengths that facilitate the use of the intensified reactions in target 1,
3) Increased *productivity* through continuous processing with a high degree of automation and RTRT

When all three targets are incorporated into the design of a pharmaceutical process, the result is a higher yield, higher productivity continuous process that can run relatively autonomously and with a smaller footprint than typical batch or semi batch processes. Specific benefits of optimizing these targets may be illustrated by comparing two cases: a non-GMP (early) intermediate and an API/late intermediate under GMP [76]. In the first case, production costs are driven primarily by throughput (defined as the mass of product per unit time) and productivity and would benefit from increasing the amount of automation in the process. In the second case, the production costs of the more complex API are governed by yield and selectivity, parameters which may be improved through using more intensified synthesis routes permitted by miniaturized reactor technologies. For example, Monteiro *et al*. have shown continuous synthesis (with 98% conversion and 85% selectivity) of a complex API via trifluoromethylation in a rack of FlowPlates followed by a CSTR for quenching [77]. However, the downside to continuous processing in this manner is the obvious and significant loss of flexibility that is usually desirable in these industries [12]. It can become difficult to handle the constant changing influx of reactions in less versatile continuous reactors, especially when there is a solid phase present in a miniaturized channel. Additionally, using a new or redesigned dedicated continuous process for each separate campaign can incur significantly higher development and implementation costs that may outweigh the value of the production campaign itself [78]. These costs will generally manifest where new technologies need to be

developed, especially in the cases of particularly slow reactions and work-up stages, where the choice to either invest in such technologies or simply use batch for these steps becomes a comparison of capital expenditure (CAPEX) and solvent usage depending on the stage of product development (i.e. in clinical phases or commercial production) and efficiency of technology.

2.2.2 Keeping pharmaceutical processing flexible through modularity

Ideally, pharmaceutical production technology should be intensified, continuous, and flexible enough to optimally produce a wide range of potential products; however, a perfect solution to obtain all three may not exist. Development of modular systems to achieve a balance between these three targets has been ongoing, with an early adopter of such a modular microreaction system developed by Ehrfeld Mikrotechnik and described in 2005 [79]. More recently and in the same vein, two modular platforms that aim to address these requirements have been developed at MIT. The first is a self-contained continuous manufacturing platform in a mobile cabinet that is capable of producing and purifying liquid API formulations [80,81]. The second is a reconfigurable universal bay for automatic chemical reaction optimization in which several different interchangeable reactors can be attached [82]. Utilizing one of these modules is likely less expensive than engineering and implementing a brand-new intensified process with specialized technology. This can be particularly beneficial to smaller firms where the required capital and infrastructure are not available for extensive process development, rapid switching between production campaigns is more desirable, and/or the amount of required product is smaller. Additionally, these flexible modules can allow production of specific therapeutic formulations that can accommodate the range of responses by patient populations. In cases where more capital is available for larger production campaigns, however, a more dedicated approach similar to that found in the bulk chemical industry may be more suitable.

2.3 **Mini-monoplant concept**

As mentioned, API production under GMP is generally driven by product yield [76] due to the complex reaction pathways required to transform intermediate chemicals into highly specialized products. However, it can often be difficult to move into continuous production when clinical development has been completed in batch due to GMP registration constraints [83]. Below, an approach is described for development of a continuous, intensified process at lab scale using a toolbox of established and developing reactor geometries that can be directly scaled up to production volume using established principles based on maintaining the relative transport and reaction rates upon geometrical scale-up [84,85].

In the early 2000s, a typical commercial scale batch production campaign at Lonza could last anywhere between 4 and 8 weeks, with an average yield and throughput around 77% and 1.5 tonnes/day, respectively [86], in the FCC (fine chemicals complex) facility with reactor size of 10’000 L (Figure 2.9, vide infra). The flexibility and versatility in batch processing equipment in a multi-purpose plant allowed for the equipment to be cleaned after completion of the campaign and reused in the subsequently scheduled production campaign. This business model relied on multi-purpose plants remaining well occupied and having numerous vessels or facility sizes to accommodate a wide range of customers and product demand. However, the system of scheduling processing equipment cannot effectively address the changing landscape of pharmaceutical processing where there is a focus on more complex, potent, lower demand, and specialized drugs that require an accelerated timeline to reach the market and have uncertainty in their demand. The latter two points may be addressed via dedicated manufacturing assets for a single product in a monoplant (i.e., a production plant dedicated to a single product, with the goal of rapid and

economical attainment of production capacity with the ability to adapt to market demand [87]) that can be designed (in batch or continuous-flow) and built within an existing facility.

This concept is illustrated in Figure 2.2. Whereas a multi-purpose plant will generally produce one large batch during a scheduled campaign, a monoplant can produce product batches year-round if required. This offers the capability to rapidly address any changes in product demand, while the multi-purpose plant may have to wait until the equipment is available for additional production which often results in overproduction during the launch phase of a new API. For complex molecules, it is also common to have lead times of several years for order to delivery since multiple campaigns are required for the different synthetic steps performed in a sequential manner. In addition, the cleaning and changeover steps required for multi-purpose plants are time and resource consuming, demanding full HAZOP analyses each time and requiring a level of cleanliness that is directly proportional to the potency of the API. Thus, the use of monoplants has a large potential to reduce the cost of goods when compared to initial batch campaigns and decrease the lead time from order to delivery from years down to potentially a few months, while also allowing for maintaining a buffer stock of key and stable intermediates that, in combination with the dedicated facilities, can facilitate rapid responses to fluctuations in customer demand.

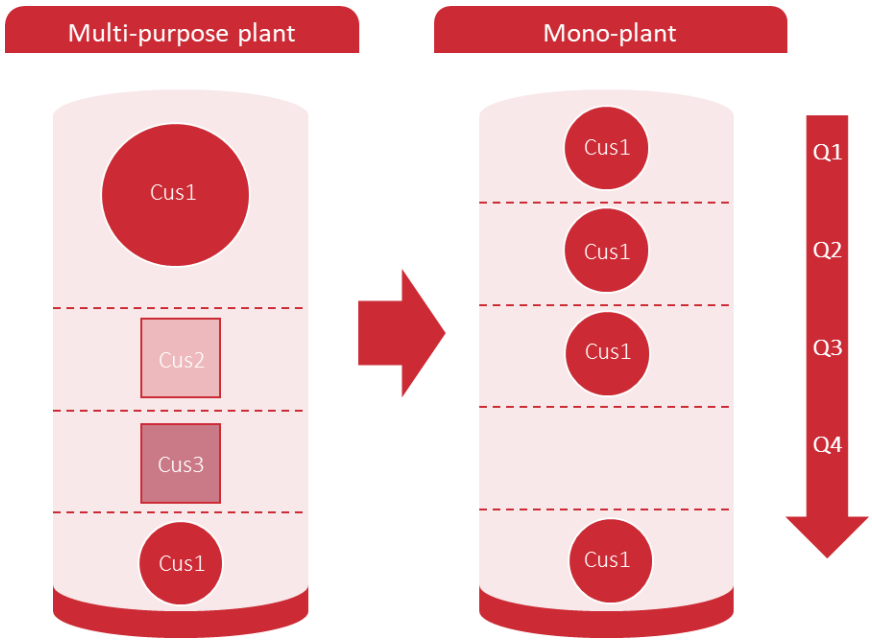

Figure 2.2. Schematic view of supply security comparison between a multi-purpose plant and a monoplant. CusX = Customer X.

When employing year-round monoplant batch production, automation and RTRT will be fundamental attributes to increase productivity. However, even further enhancements to productivity may be achieved by also addressing the first two intensification targets described in section 2.2.1. More desirable and novel reaction pathways are primarily enabled through continuous-flow processing in advanced, miniaturized reactor technologies, where dedication of such assets to production of a single product in a monoplant then results in a so-called 'mini-monoplant' (Figure 2.3).

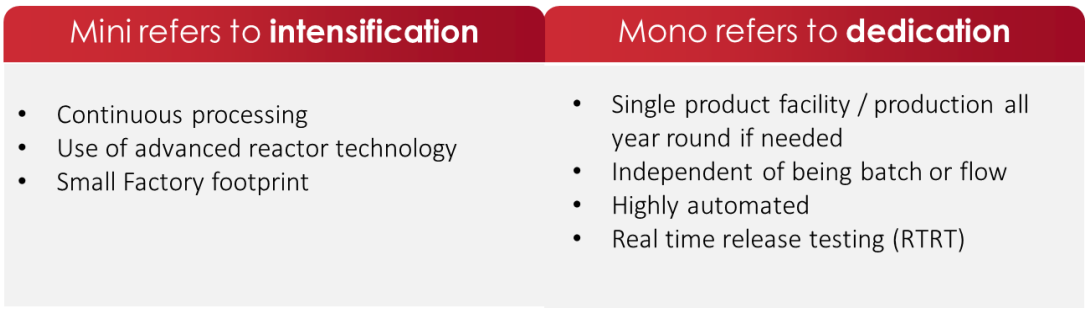

Figure 2.3. Defining factors in the design of a mini-monoplant.

The use of a mini-monoplant presents three key advantages in pharmaceutical production as shown in Figure 2.4. First, is the opportunity to develop best-in-class processes at lab scale where novel synthesis routes will improve safety, sustainability, and yield. Second, is accelerated development and time to market through a streamlined scale-up to factory-based production facilities. Here, the lab-scale process becomes the production setup which may be developed further and, when required, scaled-up using established geometrical scale-up methodologies [84,85], in an available production cabin within the factory [36]. And finally, is an overall reduction in capital and operating expenditures when the mini-monoplant is ultimately built and dedicated to continuously producing a single product, effectively increasing productivity while reducing the factory footprint and avoiding the time consuming and costly change-over steps required in typical multi-purpose plant production. In a situation when many multi-purpose plants are run at capacity, the mini-monoplant then becomes attractive for new investments and allows customers to maintain occupancy of their respective production facility.

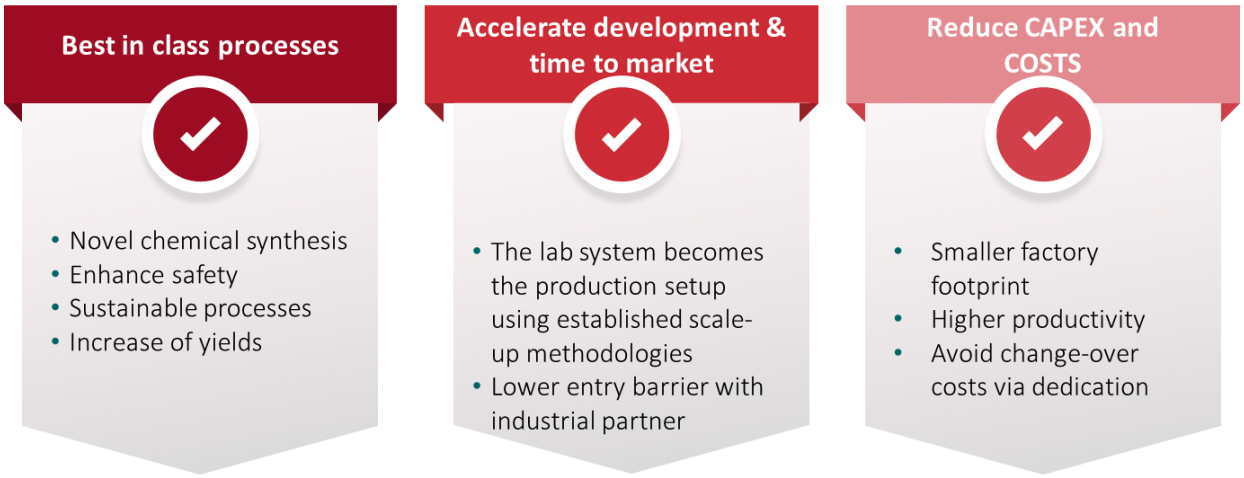

Figure 2.4. Three key advantages realized through the intensification of monoplants into mini-monoplants for pharmaceutical production.

2.3.1 Lab-based development of best-in-class pharmaceutical production processes

Development of a mini-monoplant can begin directly in the safety of a laboratory, where innovative and novel continuous processes can be performed with a small footprint. Lab-based process development allows engineers and chemists to focus on key value generating features for the finalized mini-monoplant, including process intensification, unit operations with advanced technologies and full automation over a range of throughputs that may typically span from 1 to 50 kg of product per day.

An example of such a process is shown in Figure 2.5 below, with a simplified process flow diagram shown in Figure 2.6. Here, lab-based development of a mini-monoplant was conducted within the space of three fume hoods. The system consisted of a rack of FlowPlate A6 microreactors (temperature maintained at 30°C) where a rapid type-A and highly exothermic nitration reaction was performed using a concentrated mixture of nitric acid and sulfuric acid. The excess acid was then quenched twice sequentially in two mixer settlers, in the first with water (to prevent excessive heat generation), and in the second with sodium bicarbonate (to quench any

remaining acid in the organic phase). A film evaporator was then used to remove the organic solvent so that the slightly soluble main intermediate could undergo a saponification reaction under bi-phasic conditions in a cascade of three CSTRs in series. The more water-soluble product was then back extracted into an organic solvent, a step which required an efficient multi-stage counter current liquid-liquid extractor.

The process pictured in Figure 2.5 had a throughput of 10 kg per day and had the capability to deliver material that was required for clinical trials. However, a bottleneck existed in this stage of development larger production amounts would require more than 100 L of organic solvent per day; an amount that was too large to be properly handled within a laboratory setting and necessitated larger and more capable infrastructure for further development.

Figure 2.5. Lab-based development of a continuous mini-monoplant contained within three fume hoods.

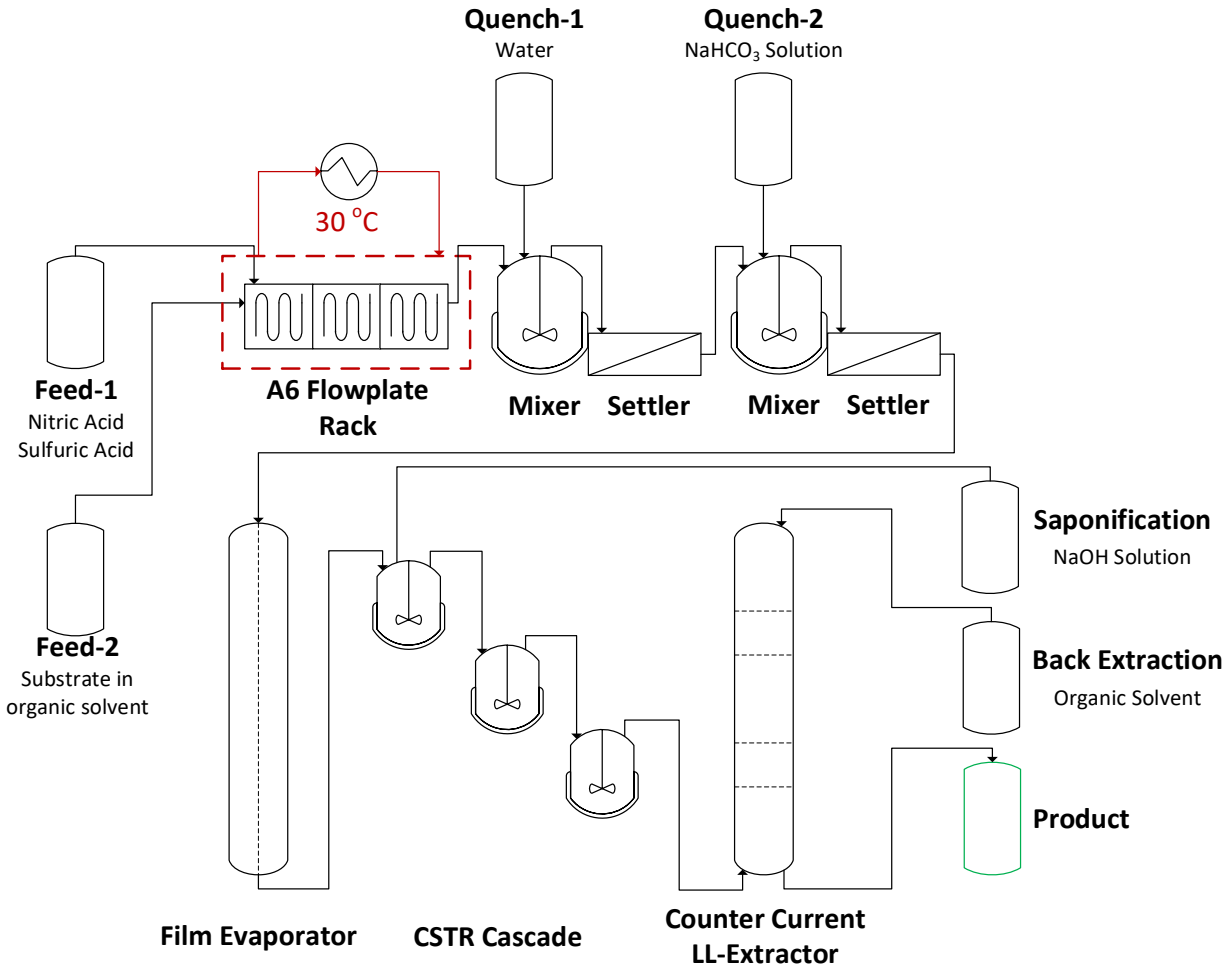

Figure 2.6. Simplified process flow diagram for the lab-based mini-monoplant development shown in Figure 2.5.

2.3.2 Factory-based development for accelerated development and time to market

Upon completion of lab-scale process development, further development of the process for larger production volumes can then be moved into an available cabin within an existing production infrastructure. As shown in Figure 2.7, the lab-scale process can be directly transferred to a cabin that allows for connection to all the factory infrastructure, including large volume storage tanks for the feeds and products. The cabin can be operated without explosion proof equipment as the processes are intensified and the reactive volume inside the cabin remains sufficiently small and

the cabin is well ventilated. The objectives here are to reach a similar flexibility as was available in a laboratory and to validate the scaling approach taken. During this stage of development, various unit operations within the process can be mounted onto mobile skids and used as flexible and multi-purpose modules. These may be base modules, such as dosing modules and reactor modules (Figure 2.8) [8,88], or more advanced modules, such as a specific reactor technology (e.g., photocatalytic [89] or electrochemical [90] reactors) or solid-liquid handling modules [59]. These modules allow for rapid process assembly during factory-based development and can provide significant time savings if they are pre-qualified for GMP production. Additionally, the modules may be cleaned and reused for additional processes upon completion of a production campaign. It is important to note, however, that these modules may be subject to usage in a campaign approach when multiple factory-based developments are occurring simultaneously.

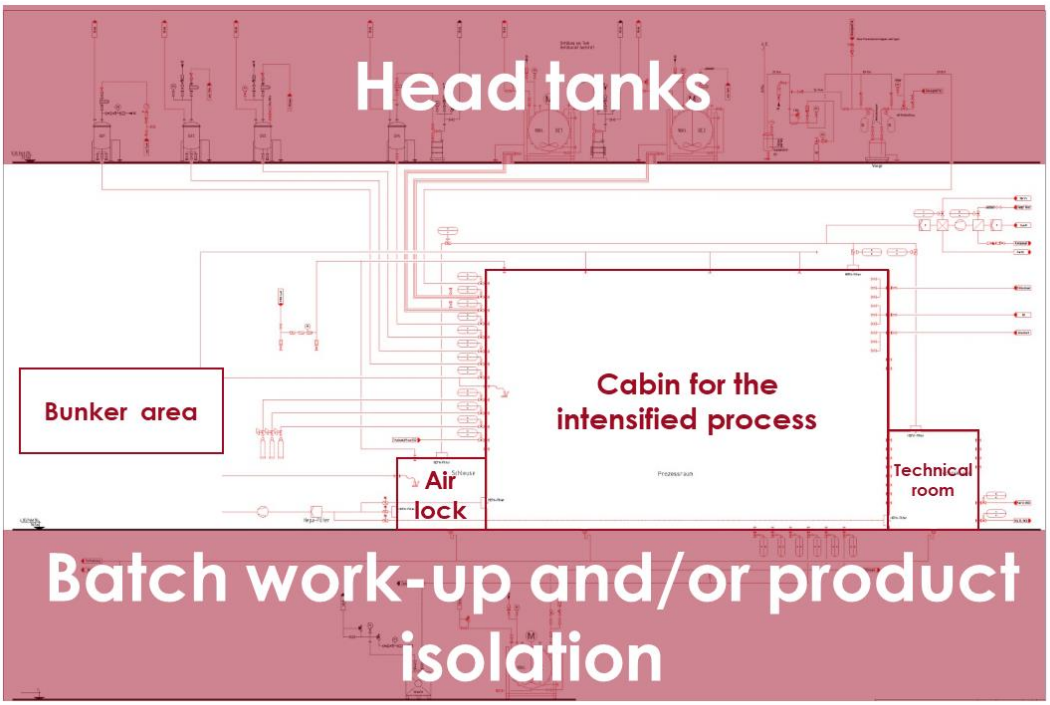

Figure 2.7. Factory-based process development. Use of an available cabin within the existing production infrastructure allows for a reduction in development time and time to market.

Figure 2.8. Reactor platform module. Reprinted with permission from reference [88]. Copyright 2015 Microinnova.

It is during the factory-based development that the first integrated process scale-up occurs. Here, flow rates can be increased when necessary to accommodate larger amounts of pharmaceutical demand which may occur during phases I to III of clinical development when the drug has not yet gone commercial. At this stage, the spatial advantages of operating a miniaturized continuous-flow process become clear, as illustrated in Figure 2.9. Often, when operated over time, a flow rate of 10 mL/min through a plate-type microreactor is sufficient for clinical development. The footprint of such a process is significantly smaller than the 250 L vessel that would be required for batch unit operations. It is of course assumed that a drastic intensification of reactive conditions has been achieved and the reaction has become mainly mass or heat transfer controlled. Under such circumstances, the volume of a plate type reactor is in the range of mL while the volume of a CSTR is in the range of 1–2 L. If the reaction is inherently slow and kinetically limited, larger

reactors (i.e., coiled tubes or stirred tanks) may be required. With respect to scaling, the flowrates and reactor sizes included in Figure 2.9 have scaling factors (i.e. multipliers of bulk flow rate or CSTR volume) ranging from 1 to 60, with the first approximately 5-fold scale increase often occurring during laboratory-based development, and the remaining occurring during factory-based development. With the use of modular equipment and GMP-ready modules (as is shown in Figure 2.8), two sets of equipment will be enough to cover the required scales during factory-based development, where one set is for low flow and the other is for high flow. In a dosing module, for example, a pump and flow controller can adequately span a 10-fold scale in flow rate, allowing a set of two dosing modules to readily handle the entire scaling range shown below. With respect to the reactor technology, a modular system with easily interchangeable reaction volumes is desirable (for example, FlowPlate technology with a range of swappable plate sizes, geometries, and volumes). Acquisition of an available pool of flexible process technologies will require a certain initial cost but will have long term benefits as additional and more effective options become readily available to engineers and chemists during process design and implementation.

With respect to scale-up methodologies, reactor dimensions are increased while maintaining geometric similarity and transport phenomena as is allowable within the specific micromixing requirements of a given reaction, permitting the use of a single, larger channel rather than multiple smaller channels in parallel. Moving to a factory-based setting is a pivotal stage of development, as it allows for long-term process stability testing to occur with solvent capacities that would otherwise be limited within a laboratory setting. During this stage of development, the process and factory must be designed with contingency methods of cleaning and de-plugging, which can include automated solvent switch and the use of ultrasounds.

	Continuous				Batch
	Flow rate Bulk	Flow rate Product	Plate Size mL-L scale	CSTR	Size
Minimum	10 mL/min	43 kg/month	FlowPlate® Lab	1 – 2 L	SSP (250 L)
Base	80 mL/min	346 kg/month	FlowPlate® A6	10 – 20 L	LP (600 L)
Maximum	300 to 600 mL/min	2592 kg/month	FlowPlate® AX	20 – 60 L	LP (2500 L)
Campaign	5 L/min	Ca. 22 tonnes/month	Static mixers / shell and tubes	200 – 600 L	FCC (10'000 L)

Figure 2.9. Comparison of required reactor sizes for various flow continuous-flow rates and for batch. The use of dedicated continuous technology drastically reduces the required footprint when compared to the batch and campaign approaches. Product flow rates assume a 10 wt% concentration of the bulk flow rate. AX = Size A5 or larger. SSP = Small Scale Plant, LP = Launch Plant, FCC = Fine Chemicals Complex.

In an example towards a factory-based development, 2-nitroethanol, which is an early intermediate required for an alternative synthesis of Aliskiren [91], was produced in a lab-based mini-plant via a Henry Reaction between formaldehyde and nitromethane (Scheme 2.1) [92]. The reaction is relatively fast, reaching around 50% conversion after 25 seconds. In this reaction, the molar ratio of nitromethane to formaldehyde has a significant impact on the selectivity of the reaction, as the product (**3**) can react further with formaldehyde to form **4** and **5** as by-products. The higher the relative amount of nitromethane, the higher of the selectivity of the reaction towards **3**, and subsequent recycling of the excess nitromethane after completion of the reaction is essential for safe operation to considerably reduce its hold-up and consequently its potential as an explosion hazard.

Scheme 2.1. Reaction between formaldehyde (**1**) and nitromethane (**2**) to form 2-nitroethanol (**3**) and by products **4** and **5**.

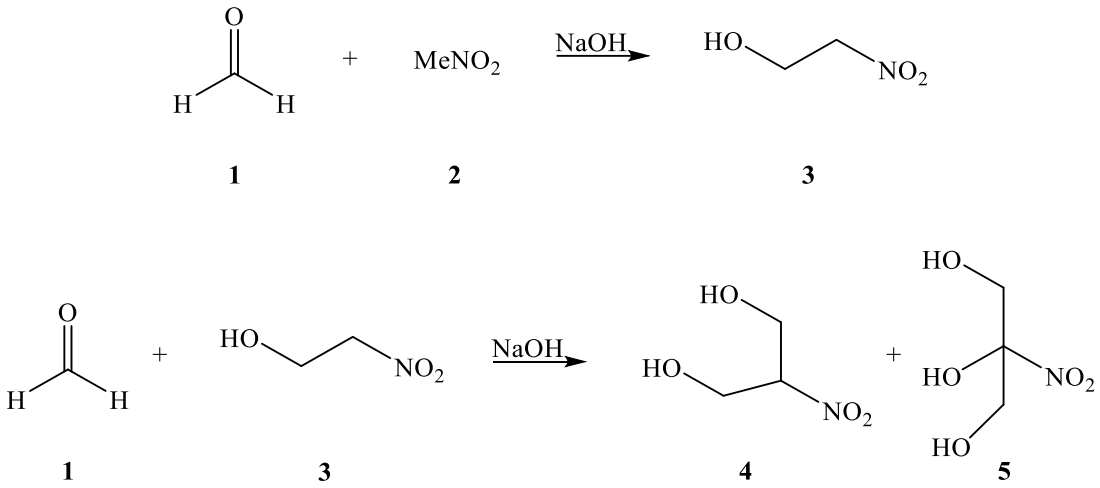

A simplified process-flow diagram of the mini-plant set up is shown in Figure 2.10. The formation of 2-nitroethanol took place in a series of A5 plate-type microreactors at 30°C, which included an initial SZ mixing plate followed by a series of residence time plates. The Henry reaction occurred under basic conditions and in a crucial safety step, the reaction mixture was then acidified in a CSTR as the removal of nitromethane from a basic mixture has the potential to become explosive. A filter was implemented downstream of the CSTR in order to handle the solids generated by the acid-base reaction (salt formation). The resulting mixture of 2-nitroethanol and nitromethane was separated by a wiped-film evaporator, generating crude **3** and allowing the excess nitromethane to be recycled, thereby reducing its hold-up in the laboratory and removing any feed impurities which would have otherwise led to the formation of precipitates and caused a pressure rise in the system. This represents a key advantage of developing a process from the beginning around continuous-flow in a mini-plant setup, as it closely mimics the processing environment that will occur in larger scale production units allowing for the identification and correction of any potential problems or instabilities early in development.

The scale-up of this process has been achieved in a nearly identical setup utilizing the same pumps, but by adjusting the number and volume of plates and using a larger wiped-film evaporator. The throughput was quadrupled to 1 kg/day of crude 2-nitroethanol and more than 5 kg were produced intermittently over 5 days. In fact, depending on the need, the flow rate could have been tuned from 1 up to 40 kg/day with a further increase in the capacity of the wiped-film evaporator – an investment that would be required upon a request for additional product. Although larger, this equipment would not have substantially increased the hold-up of crude 2-nitroethanol at 70°C, as its quantity would remain relatively small within the film. This system exemplifies the three targets of pharmaceutical intensification described above, where a novel synthesis route could be employed due to the intensified reactor and work-up unit operations, and a range of throughputs and productivities were possible by adjusting flow rates in the fully automated process.

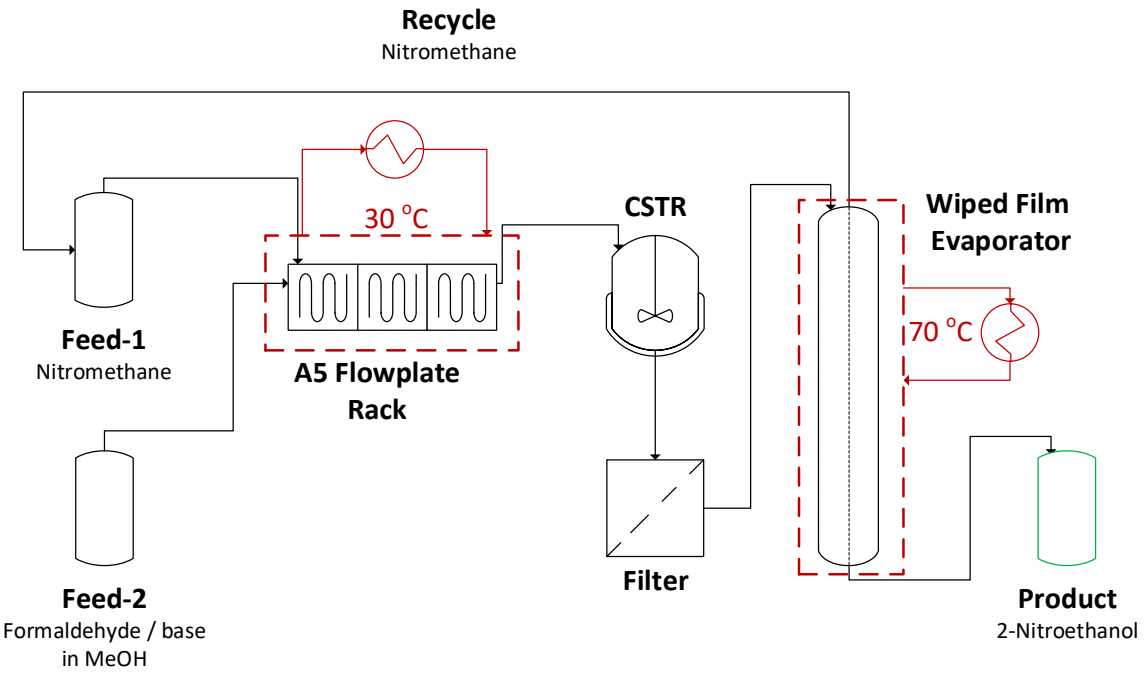

Figure 2.10. Production of 2-nitroethanol where unit operations are intensified via continuous operation.

In the example above, intensified work-up in the wiped film evaporator was essential for safe operation of the process. Oftentimes, however, intensified units for the work-up stages of a mini-plant may not yet be commercially available, as is especially the case when there is a solid phase present in the mixture. Other times, intensification of the work up stages may not be economical when the solvent is not inherently dangerous and is used in relatively small amounts (for example, when producing a product for clinical trials) when compared to the cost of developing miniaturized work-up units. In these cases, the work-up steps will generally default to non-intensified batch (exemplified in further detail in section 2.3.3 below). If there are no intensified modules available for the work-up steps during factory-based development, then these steps are performed in batch vessels. These larger batch vessels may also be used in cases where reactions are slow and kinetically limited. Importantly, the overall processes in both cases may be operated using the campaign approach, depending on the availability of modules, unit operations, and development space within the factory.

2.3.3 Mini-monoplant production technology at commercial scale

Once the factory-based development has been completed and the product has gone commercial, the process can then be installed in a dedicated production area within the plant. It is during this final stage of development that the temporal integrated process scale-up occurs, i.e., in the operational time of the process which may be run year-round where required. At this stage, complete automation is a prerequisite to increase productivity as the production is extending over time. It is also important to consider the cost and resulting value of developing and implementing RTRT in order to increase the overall productivity of the process. If the entire process including work-up is intensified and continuous (see Figure 2.10), then installation becomes a matter of simply transitioning the factory-based process into production via the acquisition of new, dedicated

production assets. If steps within the process, including reactions and/or work-up, were run in batch using the campaign approach during factory-based development, then the decision of whether to continue using batch at production scale or to transition into new continuous technologies should be evaluated on a case-specific basis through a comparison of the amount of solvent and/or CAPEX required for each.

In a process containing a solid product shown in Figure 2.11 below, the filtering, washing, and drying of the solid product are performed in a batch filter dryer vessel where two potential routes may be taken. In the first, two filter dryer vessels are operated intermittently, where one is performing the cake washing and drying of the solids while the other is filtering. In the second method, a surge tank is implemented upstream of a larger filter dryer vessel in order to buffer the feed and allow the filter dryer vessel to be periodically emptied [40]. In the first case, the cost of purchasing two filter dryer vessels is substantially larger than in the second case, where the purchase of a surge tank and a single larger volume filter dryer vessel will ultimately be lower, as volume gain is relatively inexpensive in vessels [3]. The size of this vessel should be big enough to enable a complete cycle of the filter-dryer while allowing for some additional buffer time. In this example the transition between continuous and batch operation is well defined, and such transitions are an important consideration during process design as they will increase the complexity of the process.

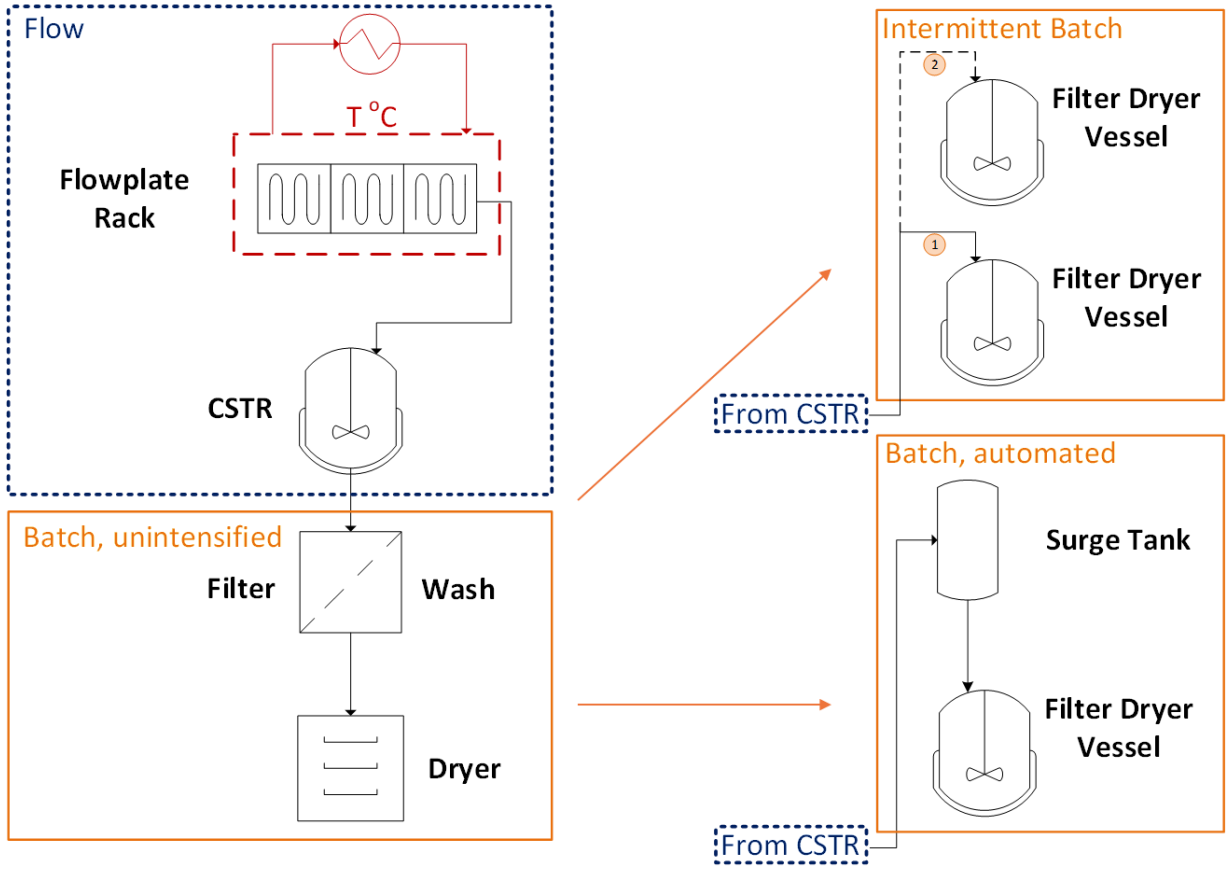

Figure 2.11. Potential routes for batch work-up downstream in a mini-monoplant.

The system with the surge tank and single filter dryer previously described is the planned approach for a mini-monoplant for commercial production of a tetraalkyl phosphonium salt (Scheme 2.2), to be implemented according to the overall process description below.

Scheme 2.2. Reaction between allyl-bromide (**6**) and trialkylphosphine (**7**) to form a tetraalkyl phosphonium salt (**7**)

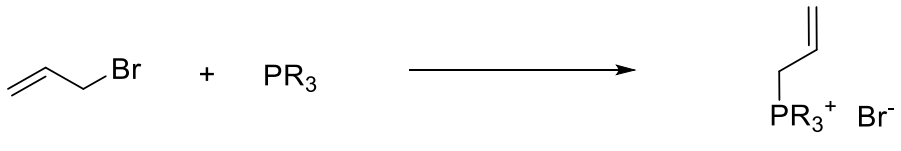

6 **7** **8**

Under the employed reactive conditions, the reaction has an adiabatic temperature rise of 118 °C with heat accumulation, with the first exotherm onset occurring at 100 °C. As such, the reaction requires very tight temperature control in order to prevent thermal runaway. In batch using a vessel size of 160 L, the temperature is controlled via dosage of **6** at 40 °C over the course of 30 minutes (for 5 kg of **8**). In the flow system shown below in Figure 2.12, the FlowPlate A6 allows for intensified reaction conditions and nearly full conversion to be reached after 2.5 minutes at 70 °C and 3 bar. Reactants **6** and **7** are first combined in an SZ-type mixing structure to allow for rapid mixing, followed by a series of residence time plates of which the quantity can be adjusted in order to accommodate the necessary residence time at a given flow rate. The two liquid feeds are not pre-heated due to thermal instability of the reactants. The resulting mixture is then co-fed with an anti-solvent into a stirred precipitation vessel run continuous with a jacket temperature of 10 °C. Once the precipitation vessel reaches a designated fill volume, the suspension is transferred to a surge or buffer tank via a suspension transfer module. The suspension from the surge tank is then transferred to a filter dryer where the solid product is separated from the mother liquor, washed, and dried. After discharge of the dried product, the filter dryer is then ready to receive new suspension from the surge tank which has been re-filled in the meantime. The reactor plates do not require intensive cleaning cycles as the quantity of formed phosphonium salt remains soluble in the reaction mixture at 70 °C, while those sections of the process containing a precipitated solid suspension can be rinsed with the process solvent. The primary heel of the filter dryer is removed periodically based on the stability data of the product.

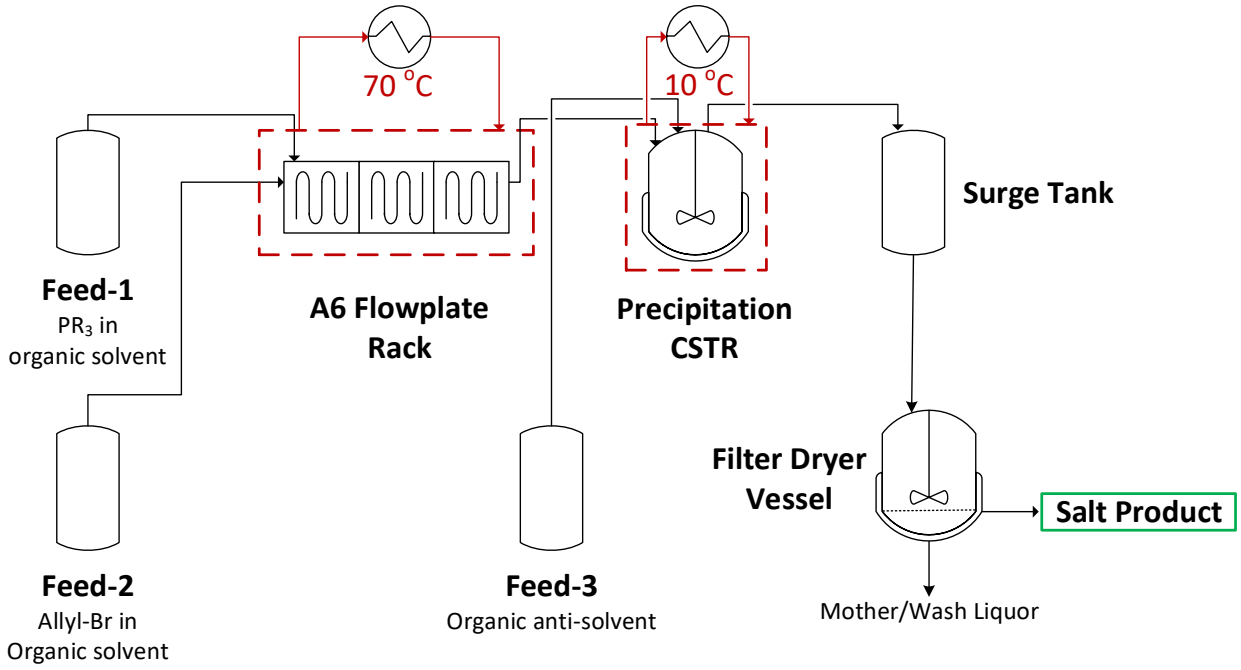

Figure 2.12. Intensified reaction with automated batch work-up. Here applied to the production of tetraalkyl phosphonium salt.

Logistically, installation of a mini-monoplant would occur in a complex within a plant containing 'mono-suites' for every new product. The complex would be designed with service infrastructure (i.e., solvent tank farm, cooling/heating systems, waste management, etc.) analogous to that which is normally available in a multi-purpose plant. Direct lines to solvent or water tanks/containers will be included, as well as lines to containers with standard concentrations of acids or bases when required. Such an approach is currently being taken at Lonza for biologics manufacturing, where significant investment has been initiated into a manufacturing complex called IBEX [93,94]. For small molecules, mono-suites can be retrofitted into existing multi-purpose facilities in order to limit investment.

The mono-suite itself would encompass cabins or rooms which include space for head tanks for solution preparation when required. At this stage, it is important to mention that these

tanks or containers are by no means the equivalent of a multi-purpose batch reactor in terms of both technological complexity and investment. Such tanks are significantly less expensive and can also consist of single use plastic containers. Some of them may require cooling or heating capacities depending on the contained solution's stability, viscosity, or liquefaction. It is also assumed that when the reactions are run under intensified conditions in miniaturized technologies, the solvent requirements (and their associated footprints) will be smaller when compared to an unintensified batch process with an equivalent production quantity. In addition, the mono-suite would require solid isolation capacity. The example given above (Figure 2.12) shows solid isolation via filter-dryer operation, but this could also be approached in a different manner.

The monoplant strategy is already in-use for batch technology [95]. The main driver behind widespread development of monoplants arises from the reduction of investment costs via the use of intensified continuous technologies. When batch technology is used in solid handling, for example, the investment costs and space requirements will be similar to those needed in a multi-purpose plant with comparable equipment size. The cost and space advantage will therefore manifest in the compact system design and year-round operation. Technological development in solid handling and crystallization is an important ongoing research topic, and will determine the extent to which this aspect of a process will be amenable to process intensification and continuous operation. For example, solid dosage and automatic feed preparation with solid substrates are now possible under continuous operation [96] - an approach that is also valid for work-up unit operations. Implementation of such technologies will occur when they bring sufficient advantages that supersede the investment needs.

2.4 **Conclusions**

Pharmaceutical production has historically relied on multi-purpose batch vessels utilized through a campaign approach. Although these vessels are flexible and can accommodate a wide range of reaction phases and kinetics, they are becoming less effective in their ability to address recent developments in pharmaceutical production where more complex, potent, and specialized drugs are becoming increasingly desirable with accelerated times to market and uncertainty in their demand. As is seen in the bulk chemical industry, rapid changes in product demand can be addressed through dedication of production assets to a single product in a monoplant. The more specialized products desired by the pharmaceutical and fine chemical industry can be produced though miniaturized and intensified production assets that allow for the use of previously 'forbidden' chemistries in a mini-plant. When applied in combination to the development of a pharmaceutical production process, the result is a mini-monoplant that is dedicated, highly intensified, and able to operate year-round to respond to fluctuations in product demand.

The road to development of a mini-monoplant for pharmaceutical production occurs through three main stages, namely, lab-based development, factory-based development, and mini-monoplant production at commercial scale. In lab-based development, mini-plant process development occurs within the safety of a laboratory, where chemists and engineers can focus on value generating features such as novel reaction pathways, intensified reactors, automation, and dedication. Here, novel and innovative continuous processes can be developed with a small footprint with throughputs that can span from 1 to 50 kg of product per day. Upon completion of the lab-scale development, the mini-plant can then be moved to an available cabin within the existing plant infrastructure, allowing for access to large volume feed and product storage tanks. This provides a similar flexibility as was available in the laboratory, and the usage of predesigned

(and potentially GMP-prequalified) multi-purpose unit operation modules can greatly reduce development time and time to market for introducing new technology into the pharmaceutical production process. The first stage of process scale-up occurs in factory-based development, where throughputs can be increased to meet the demands of clinical trials. Finally, when the product has gone commercial, dedicated production assets can be invested in and the process can be installed in a designated area within the plant. It is at this stage that the process can be considered a mini-mono plant, and the final temporal scale-up occurs with respect to the overall operating time of the process, of which dedication allows year-round operation if required in order to meet fluctuations and uncertainty in product demand. In-line with the ongoing paradigm shift towards continuous manufacturing in pharmaceuticals [97], process development via mini-monoplant technology is a pragmatic approach to pharmaceutical production using carefully selected processing units currently available to chemists and engineers. As this processing mode becomes more commonly adopted it is expected these technologies will develop and become more readily available, especially when/if regulatory and tax incentives that can help address the financial hesitation towards widespread adoption of novel technologies become available [98].

Abbreviations

API = Active pharmaceutical ingredient

PAT = Process analytical technology

RTRT = Real-time-release-testing

GMP = Good manufacturing practice

CAPEX = Capital expenditure

HAZOP = Hazard and operability

CSTR = Continuous stirred tank reactor

SSP = Small-scale plant

LP = Launch Plant

FCC = Fine chemicals complex

3. Gas-Liquid Flow and Interphase Mass Transfer in LL Microreactors

Brendon J. Doyle[1], Frederic Morin[1], Jan B. Haelssig[2], Dominique M. Roberge[3,*], and Arturo Macchi[1,*]

[1]Centre for Catalysis Research and Innovation, Department of Chemical and Biological Engineering, University of Ottawa, Ottawa, ON K1N 6N5, Canada.

[2]Department of Process Engineering and Applied Science, Dalhousie University, Halifax, NS B3H 4R2, Canada.

[3]API Development Services, Lonza AG, CH-3930 Visp, Switzerland.

This manuscript has been published: Doyle, B.J.; Morin, F.; Haelssig, J.B.; Roberge, D.M.; Macchi, A. Gas-Liquid Flow and Interphase Mass Transfer in LL Microreactors. Fluids 2020, 5, 223.

Abstract

This work investigates the impact of fluid ($CO_{2(g)}$, water) flow rates, channel geometry, and the presence of a surfactant (ethanol) on the resulting gas–liquid flow regime (bubble, slug, annular), pressure drop, and interphase mass transfer coefficient ($k_l a$) in the FlowPlate™ LL (liquid-liquid) microreactor, which was originally designed for immiscible liquid systems. The flow regime map generated by the complex mixer geometry is compared to that obtained in straight channels of a similar characteristic length, while the pressure drop is fitted to the separated flows model of Lockhart–Martinelli, and the $k_l a$ in the bubble flow regime is fitted to a power dissipation model based on isotropic turbulent bubble breakup. The LL-Rhombus configuration yielded higher $k_l a$ values for an equivalent pressure drop when compared to the LL-Triangle geometry. The Lockhart–Martinelli model provided good pressure drop predictions for the entire range of experimental data (AARE < 8.1%), but the fitting parameters are dependent on the mixing unit

geometry and fluid phase properties. The correlation of $k_l a$ with the energy dissipation rate provided a good fit for the experimental data in the bubble flow regime (AARE < 13.9%). The presented experimental data and correlations further characterize LL microreactors, which are part of a toolbox for fine chemical synthesis involving immiscible fluids for applications involving reactive gas–liquid flows.

Keywords: microreactor; gas–liquid flow; flow regime; pressure loss; interphase mass transfer; CO_2 absorption

3.1 **Introduction**

Process intensification, via miniaturization, is a method of rendering reactors more efficient, economical, environmentally friendly, and safer through a reduction of volume. The smaller length scales enhance heat and mass transfer rates by providing greater vessel specific area and reducing transport distances. These improvements in transport rates, as well as the smaller working volumes, allow for highly exothermic reactions to be run safely with less dilution and better yields [99]. In particular, continuously operated micro- and milli-scale reactors offer these advantages at production rates relevant to the pharmaceutical industry, which are typically less than 600 g/min [100]. In multiphase systems, small reactor dimensions have the added benefit of creating more consistent dispersions (e.g., segmented flow) and higher interfacial area, which yields higher and more predictable mass transfer rates [101]. However, continuous-flow microreactor technology is still a relatively young field. Therefore, further characterization must be performed for different types of reactors and fluids systems to enable process design and thereby drive more widespread use.

Several gas-liquid microreactor technologies (e.g., falling films, static mixers, tubular, membranes, packed beds) have been proposed for various applications and production rates [102,103]. In particular, the Corning™ Advanced-Flow™ reactor with heart-shaped mixing structures [46,47,104] and the FlowPlate™ reactor with LL (liquid-liquid) structures [8,105] can operate at relatively high throughputs and use Venturi-like contractions followed by chambers containing flow-impinging obstacles in order to change the magnitude and direction of the flow field. Specifically, the LL mixer focuses the immiscible fluids onto an obstacle that breaks the dispersed phase and desynchronizes the fragments. Variable volume chambers and non-symmetrical rhomboidal or triangular obstacles, with varying orientation at each consecutive

mixing unit, act together to reduce re-coalescence. The FlowPlate^{TM} reactor is offered in a variety of mixer and plate sizes rated for different flow rate ranges [44].

In gas-liquid reactions, the flow morphology has a determining impact on the specific area available for interphase mass transfer and on the pressure drop. Although many flow regimes have been identified, this work focuses on three main regimes: bubble flow, slug flow, and annular flow. Many methods of identifying these flow regimes have been used in the past, with the simplest being visual identification [106]. Additionally, several mechanisms have been proposed to predict the conditions under which flow regime transitions occur [13,14], but agreement over a large range of fluid physical properties and channel geometries has been poor [109]. For this reason, the comparison of empirically determined regime transitions from similar systems has been preferred by some authors [12-16] and will be used in this study.

Previous work has demonstrated the applicability of LL-Reactors for liquid-liquid systems with varying physical properties over a range of production rates relevant to the pharmaceutical industry [45,111]. It was shown that two-phase flow regime identification via visualization is crucial in understanding changes in interphase mass transfer rates with flow rate, allowing for the development of an effective scale-up methodology [45,105,111]. In particular, in liquid-liquid systems, the onset of the drop flow, which is analogous to bubble flow in gas-liquid systems, was identified as a key parameter in scale-up since interphase mass transfer rates depended on the energy dissipation rate resulting from chaotic advection, and not on reactor geometry, in this regime [45]. As such, the aim of this work is to investigate the applicability of LL-Reactors in gas-liquid systems by identifying key performance parameters in order to advance the toolbox approach developed by Plouffe et al. [8], as has been done for liquid-liquid reactions. First, the flow regimes are visually identified; next, the two-phase pressure drops over the length of the

reactor are measured and analyzed; and then, the mass transfer rates are measured using physical CO_2 absorption experiments, and the data are analyzed and correlated in terms of a volumetric mass transfer coefficient ($k_l a$). The analysis includes a range of gas and liquid flow rates, LL-Reactors using a rhombus or triangle as the obstacle, and a liquid phase with or without the addition of a surfactant.

3.2 **Materials and Methods**

A schematic of the experimental set-up is presented in Figure 3.1. The gas and liquid were fed continuously into the microreactor system via a Bronkhorst™ mini CORI-FLOW™ M12V10I mass flow controller (MFC), with an accuracy of ± 0.5% of flow rate, and a HiTec Zang SyrDos™ 2 syringe pump equipped with 25 mL DURAN™ borosilicate glass syringes, respectively. The microreactor system utilizes a FlowPlate™ Lab manufactured by Ehrfeld Mikrotechnik GmbH, which features a quartz viewing glass. Each reactor plate consists of a series of 21 micromixers machined into a size ISO 216 A7 (74 × 105 mm) Hastelloy™ C-22™ plate, with a total reaction zone volume of 0.95 mL. The characteristic lengths of the mixing units are taken at the contraction, where the width (w) is 0.5 mm and the depth (δ) is 1.25 mm, resulting in a hydraulic diameter (d_h) of 0.714 mm. The mixer arrangement and geometry are presented in Figure 3.2. Two mixer geometries were used—the LL-Rhombus and LL-Triangle—which differ only in the geometry of the obstacle. Both FlowPlates™ were operated horizontally and at ambient temperature (25 °C). The gas used is carbon dioxide (≥ 99.99 vol%, Linde AG), while the liquid was either deionized water or a 0.5 wt% ethanol in water solution to investigate the impact of surfactant on the flow morphology and resulting transport phenomena. The ethanol concentration is sufficient to inhibit bubble coalescence [112], but still low enough not to significantly change liquid equilibrium physical properties [113]. In practice, it may not be possible to know the type and amount of

surface-active species present in the liquid. Thus, this approach provides relative effects between two gas-liquid systems with different degrees of bubble coalescence inhibition in order to better anticipate the resulting trends in flow regime boundaries and associated pressure drop and interphase mass transfer.

Visualizations of the flow regimes were recorded with a camera through the viewing glass on the microreactor. Pressure measurements were taken and averaged over the course of 5 minutes at the gas inlet and reactor outlet using an Omega PX459 differential pressure transducer (15 ± 0.012 psi) and a HiTec Zang LabBox^{TM} 3 M data collection system in order to determine the pressure drop across the reactor. Interphase mass transfer rates were determined using physical CO_2 absorption experiments. The CO_2 concentrations in the liquid feed and outlet were measured via Warder titration [114] of 5 mL samples with phenolphthalein and methyl orange indicators after the system had reached steady state as observed by a constant pressure drop.

The liquid feed flow rate was varied from 5 to 40 mL/min and the gas feed flow rate was varied from 0.5 to 40 g/h for CO_2-deionized water flowing through the LL-Rhombus, whereas the impact of obstacle geometry and surfactant were conducted at liquid flow rates of 10 and 20 ml/min. Average gas velocities between the reactor inlet and outlet are reported throughout considering the consumption of CO_2 via absorption (up to 73% at lower gas flow rates) and gas expansion due to pressure losses (up to 0.44 bar). The superficial velocities are based on the mixer contraction cross-sectional area, which is where kinetic energy is greatest.

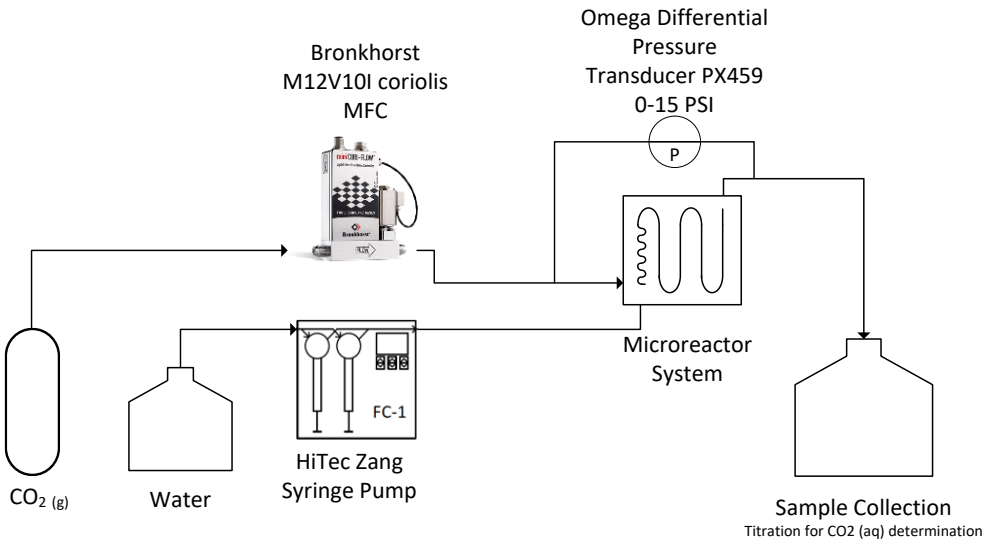

Figure 3.1. Set-up for flow visualization, pressure drop and interphase mass transfer experiments

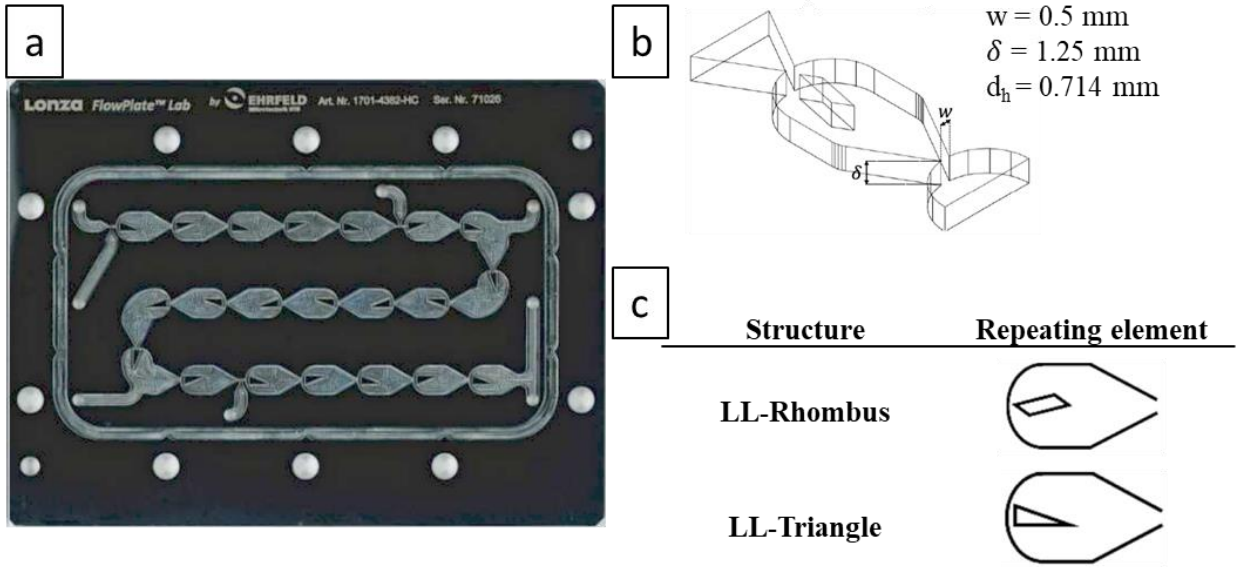

Figure 3.2. Geometry of FlowPlate™ and mixing elements: a) LL (liquid-liquid)-Reactor (triangle) size A7 plate arrangement [111] (licensed under https://creativecommons.org/licenses/by/4.0/); b) Three-dimensional visualization and characteristic dimensions of the (rhombus) mixing element; and c) Repeating mixing elements in the LL-Rhombus and LL-Triangle [111] (licensed under https://creativecommons.org/licenses/by/4.0/).

3.3 **Results and Discussion**

3.3.1 Flow Regimes

In the flow regime identification, the first few mixers were ignored since flow typically does not develop fully until the end of the first row of mixers. Regimes are shown in Figure 3.3 and were identified as one of the following based on distinct criteria: bubble flow, where gas bubbles are nearly spherical with a diameter less than half the mixer's largest width; slug flow, where the gas bubbles are nearly the mixer's width and elongated; and annular flow, where an uninterrupted gas core surrounded by a liquid film spans the length of the reactor (after flow is established following the first row of mixers). The bubble flow regime thus includes dispersed bubble flow and bubbly flow, while the annular flow regime comprises the slug-annular and churn flow regimes used by Triplett et al. [115] since differentiating between different annular sub-regimes is difficult for the scales and geometries of the mixers. Flow may also exhibit characteristics of two or more flow regimes, whether in one region over a span of time or in many regions at a given time, especially near transition boundaries, so "mixed" regimes are therefore identified where necessary.

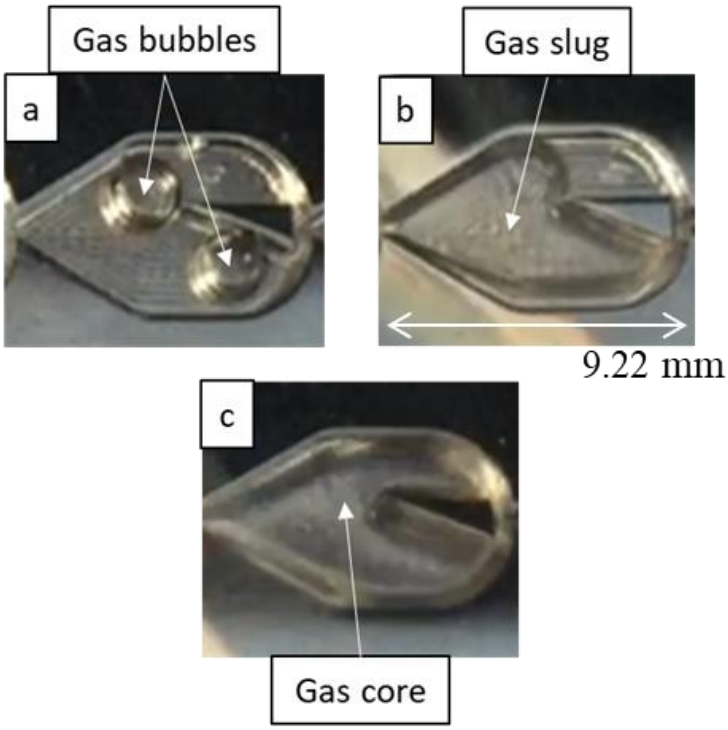

Figure 3.3. Flow regimes identified in this work: a) bubble flow, b) slug flow, and c) annular flow.

In larger-scale channel flows, gravitational effects have a significant impact on two-phase flow. However, in microchannels, interfacial tension and wetting properties are dominant compared to gravitational forces, and the flow may be treated as if it were under microgravity conditions. This means that the flow is independent of channel orientation and that flow regimes caused by gravity-induced phase separation will not occur. Ullmann and Brauner [107] propose that $Eo \lesssim 1.6$ as the requisite condition for using microchannel models. From equation (3.1), the *Eötvös* number at the widest part of the LL mixers used in this work is ~ 0.85 (width and depth of 5 and 1.25 mm, respectively), satisfying the condition for pseudo-microgravity flow and indicating that flow regime transitions should be treated as such.

$$Eo = \frac{\Delta\rho g \delta w}{\sigma} \qquad \textbf{(3.1)}$$

3.3.1.1 Effect of gas and liquid flow rates

Figure 3.4 presents flow regime maps prepared for the LL-Rhombus and LL-Triangle geometries using coordinates of gas and liquid superficial velocities, with the transition lines of Triplett et al. [115] for air-water flow in a 1.097 mm diameter circular microchannel ($Eo \approx 0.16$) superimposed as reference. The flow regime map of Triplett et al. [115] has served as a basis of comparison for many authors, including Yue et al. [110], who used a rectangular microchannel with a hydraulic diameter of 0.667 mm with a CO_2-water fluid system ($Eo \approx 0.067$). Notable deviations from the transition boundaries of Triplett et al. [115] include an onset of bubble flow from slug flow at lower liquid velocities in the LL-Reactors, and the presence of the annular flow regime at lower gas flow rates in the LL-Rhombus than in the LL-Triangle.

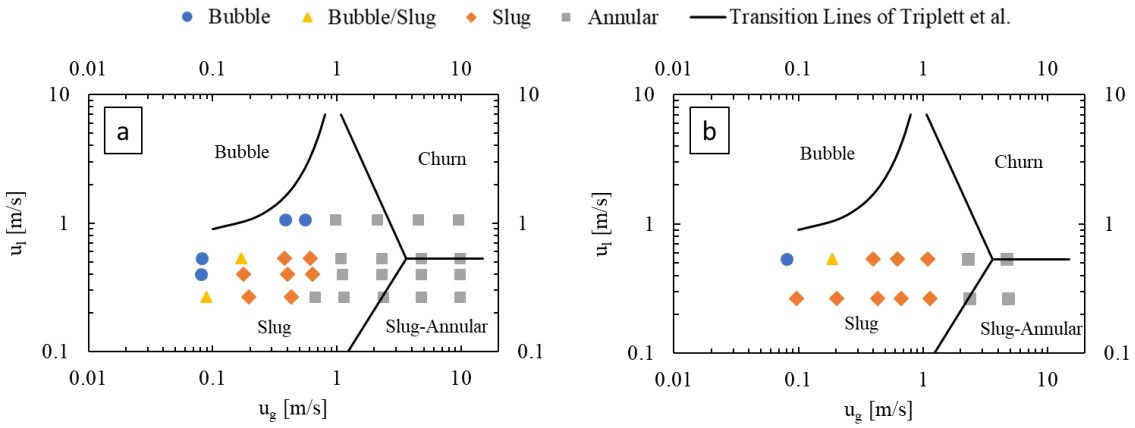

Figure 3.4. Flow regime maps of a) LL-Rhombus and b) LL-Triangle, with deionized water as the liquid phase.

Bubble flow can also be less predominant in the LL-Triangle than in the LL-Rhombus since the flat wall of the triangular obstacle impinges on incoming flow and abruptly redirects it toward the curved sides of the mixer [111]. Centrifugal forces then push the denser liquid phase toward the walls of the mixer, creating a greater gas holdup in the centre of the mixer. Furthermore, the

shape of the triangle will create a larger fluid recirculation zone beside the hypotenuse of the right triangle obstacle than is generated along the long leeward side of the rhombus. The combination of the sharper redirection of the flow and the larger recirculation zone on the leeward side of the obstacle promotes bubble coalescence, as shown in Figure 3.5. Note that the gas bubble attached to the triangle obstacle remains fixed over time, suggesting that parallelization of gas and liquid flows is present. In contrast, the narrow point of the rhombus obstacle causes a more gradual flow redirection, and less opportunity for re-coalescence.

Furthermore, the annular flow regime occurs at greater gas velocities in the LL-Triangle than in the LL-Rhombus due to the aforementioned impingement caused by the flat face of the triangle. Annular flow occurs when the inertia of the gas core is strong enough to overcome interfacial tension forces, among other factors [107]. When the fluids collide with the triangular obstacle, energy from the flow is dissipated into chaotic eddies that deform the gas-liquid interface. The resulting disruption of the gas core causes the slug-to-annular transition to shift to higher gas velocities in the LL-Triangle than in the LL-Rhombus, where the sharp and relatively narrow point of the rhombus causes less disruption in flow.

Figure 3.5. Flow in LL-Triangle (left) demonstrating increased gas holdup in centre of mixer, a behaviour that is absent in the LL-Rhombus (right) for the same flow rates. Liquid velocity is 0.53 m/s, and gas velocity is 0.080 m/s in the LL-Triangle and 0.081 m/s in the LL-Rhombus.

3.3.1.2 Effect of Surfactant

When the aqueous 0.5 wt% ethanol solution was used as the liquid phase, bubble flow was the dominant two-phase flow regime, being present at all the tested flow rate pairings, as shown in Figure 3.6. This is due to the surfactant decreasing surface forces, which promotes bubble breakage, as wells as forming a film at the gas-liquid interface that inhibits bubble coalescence (Gibbs-Marangoni effect), thereby allowing bubble flow to persist at lower liquid velocities (i.e., lower energy input). At the greater gas velocities, the encountered bubble flow resembled a froth that appears to move as a single fluid, as shown for the LL-Triangle geometry in Figure 3.7.

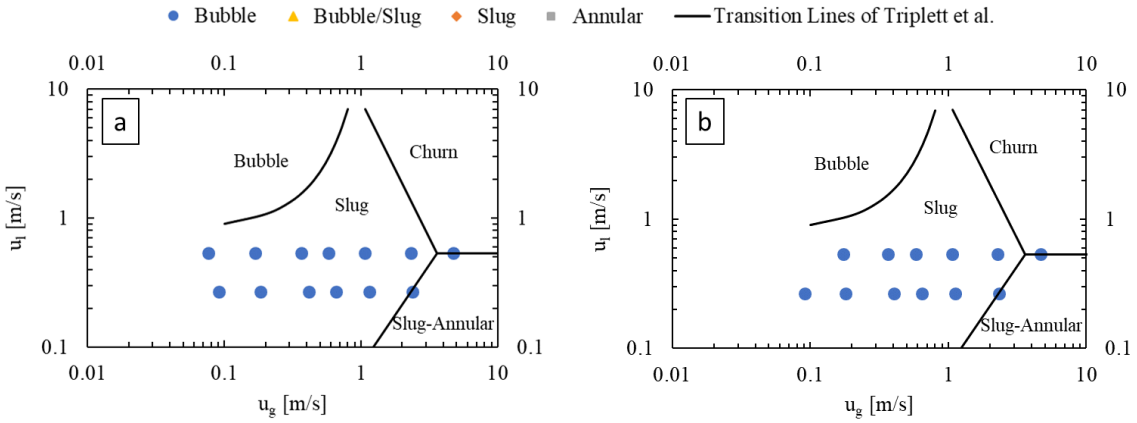

Figure 3.6. Flow regime maps of a) LL-Rhombus and b) LL-Triangle, with 0.5 wt% aqueous ethanol solution as the liquid phase.

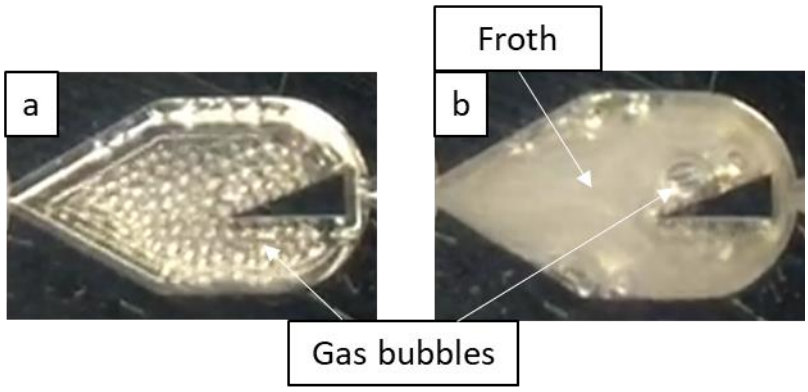

Figure 3.7. Flow in the LL-Triangle mixer demonstrating the effect of increased gas flow rate on flow morphology where surfactant is present. Gas velocities are a) 0.091 m/s and b) 0.65 m/s, and the liquid velocity is 0.27 m/s. Note that a) demonstrates bubble flow, and b) demonstrates bubble flow with froth formation.

3.3.2 Pressure Drop

3.3.2.1 Impact of Operating Conditions

For deionized water as the liquid phase, as shown in Figure 3.8a, the pressure drop was found to increase with liquid and gas velocities although the liquid flow has a more prominent effect. Furthermore, the two-phase pressure drops remain greater for the LL-Triangle compared to the LL-Rhombus due to the impingement of flow against the flat face of the triangular obstacle and because the triangle forms a longer narrow flow channel with the outer wall of the mixing unit. In both LL-plates, the increase in pressure drop with increasing gas flow rate is initially more rapid followed by a decrease in slope that generally coincides with the transitions to slug or annular flow, as seen in Figure 3.4.

An increase in gas or liquid velocities also raises the pressure drop when using the aqueous ethanol solution, as shown in Figure 3.8b, but the impact of liquid velocity is lower. Furthermore, the effect of obstacle geometry is rendered marginal, and the abrupt slope decrease with increasing

gas velocity is generally not observed due to the employed range of gas and liquid velocity combinations resulting only in bubble flow (Figure 3.6). The pressure drop was also generally greater when the surfactant was present, especially at higher gas velocities, since many small bubbles results in a frothy mixture, which would increase the effective drag force between the gas and liquid phases and therefore lead to a higher local liquid velocity.

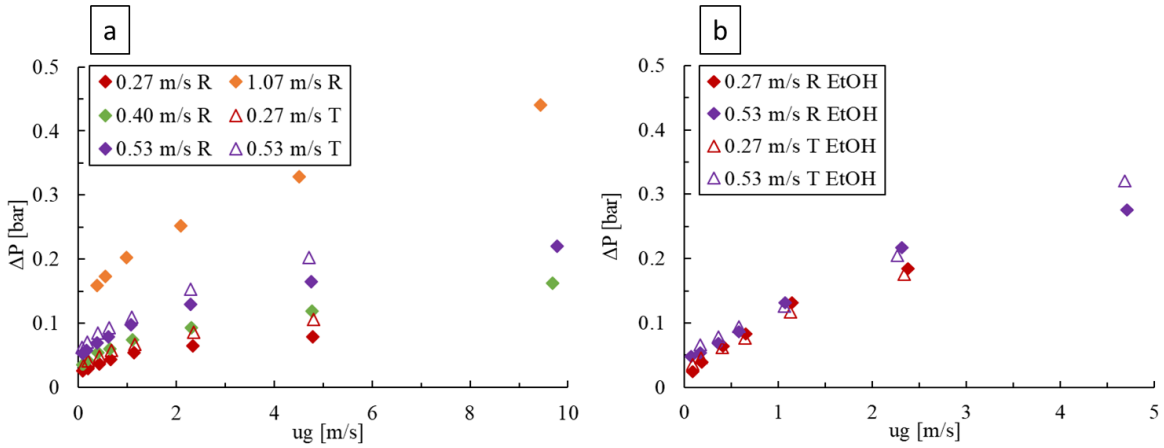

Figure 3.8. Pressure drop over varying liquid and gas velocities in the LL-Rhombus (R) and LL-Triangle (T) reactors with a) water and b) 0.5 wt% aqueous ethanol as the liquid phase.

3.3.2.2 Model

The data from both the water and aqueous ethanol solution were fitted to the two-phase flow model of Lockhart-Martinelli [116], which adds a two-phase friction multiplier, ϕ^2, to the pressure drop gradient of a single phase, as seen in equation (3.2). The two-phase friction multiplier is a function of the Martinelli parameter, χ, and of the Chisholm parameter, Ch (equations (3.3) and (3.4)). Since liquid is the wetting phase of the reactor and has the greater pressure-drop gradient, this phase and its associated friction multiplier ϕ_l^2 were chosen for the model.

$$\left(\frac{\Delta P}{\Delta L}\right)_{TPF} = \phi_l^2 \left(\frac{\Delta P}{\Delta L}\right)_l = \phi_g^2 \left(\frac{\Delta P}{\Delta L}\right)_g \quad \textbf{(3.2)}$$

$$\phi_l^2 = 1 + \frac{Ch}{\chi} + \frac{1}{\chi^2} \tag{3.3}$$

$$\chi = \frac{m_l}{m_g}\sqrt{\frac{\rho_g}{\rho_l}} = \frac{u_l}{u_g}\sqrt{\frac{\rho_l}{\rho_g}} \tag{3.4}$$

First, the liquid-only friction factors were calculated using the Darcy-Weisbach equation, with the number of mixers, *N*, replacing the traditional L/d_h term (equations (3.5) and (3.6)). The calculated friction factors were then correlated with the Blasius equation (equation (3.6)), where y values of 1 and 0 correspond to fully laminar and turbulent flow, respectively. Table 3.1 lists the resulting fit for each LL-plate, showing greater values of c for the LL-Triangle due to the blunt obstacle but significant and similar levels of turbulence in the liquid phase for both geometries.

$$\Delta P_l = f_l N_{mixer}\left(\frac{\rho_l u_l^2}{2}\right) \tag{3.5}$$

$$f_l = \frac{\Delta P}{N_{mixer}}\frac{2}{\rho u_l^2} = \frac{c}{Re_l^y} \tag{3.6}$$

Table 3.1. Correlated Blasius equation parameters for LL-Rhombus and LL-Triangle geometries for 214 < Re_l < 856.

Geometry	c	y
LL-Rhombus	3.68 ± 0.76	0.17 ± 0.035
LL-Triangle	5.01 ± 0.23	0.18 ± 0.008

Alternatively, and analogous to flow in a packed bed, the liquid-only pressure loss can be modeled with a friction factor ($f_l = f_{lam}/Re + f_{turb}$) having contributions from both laminar (f_{lam}) and turbulent (f_{turb}) flow terms to represent a gradual transitional regime [105]. Despite Re_l being 213–856 at the contraction, the laminar contribution to the pressure drop ranges from 8

to 29% for both the LL-Rhombus and LL-Triangle, which is relevant to the bubble breakdown mechanism with increasing power dissipation within the bubble flow regime.

Although *Ch* typically ranges from 5 to 20 depending on the flow regimes of the gas and liquid phases, many attempts have been made to correlate *Ch* to reactor geometry and flow parameters [110,116,117]. Yue et al. [110] suggest that the effects of gas and liquid mass flux on *Ch* are significant in microchannels and used gas-only and liquid-only *Reynolds* numbers in their model. A similar approach was used in this work (equation (3.7)), though the superficial velocity ratio was used in place of the gas *Reynolds* number since gas viscosity was not thought to significantly impact the two-phase pressure drop.

$$Ch = \beta_0 Re_l^{-\beta_1} \left(\frac{u_g}{u_l}\right)^{-\beta_2} \tag{3.7}$$

The pressure drop data were fit with the Talwar robust regression model, and the results for each geometry and liquid phase used are shown in Table 3.2. The impact of geometry on the two-phase friction multiplier for the CO_2-liquid water system was insignificant, whereas it is marginal for the CO_2-aqueous ethanol system where the pressure loss gap observed in single phase flow is diminished in two-phase flow.

Table 3.2. Correlation parameter values and 95% confidence intervals for tested geometries and continuous phases. For the CO_2-water and rhombus data, $214 < Re_l < 856$ and $0.15 < u_g/u_l < 36.5$. For all other data, $214 < Re_l < 428$ and $0.14 < u_g/u_l < 18.0$.

Continuous Phase	Geometry	β_0	β_1	β_2
Water	Rhombus & Triangle	10497 ± 4758	1.02 ± 0.070	0.58 ± 0.033
0.5 wt% aqueous ethanol	Rhombus	68721 ± 42191	1.28 ± 0.10	0.16 ± 0.06
	Triangle	51761 ± 27724	1.29 ± 0.091	0.20 ±- 0.052

The forecasted values show good agreement with experimental results as seen in Figure 3.9. For all fitted models, the average absolute relative error (AARE) is less than 8.1% and the maximum error is less than 37%, while the bias factor F_m is between 0.96 and 1.04.

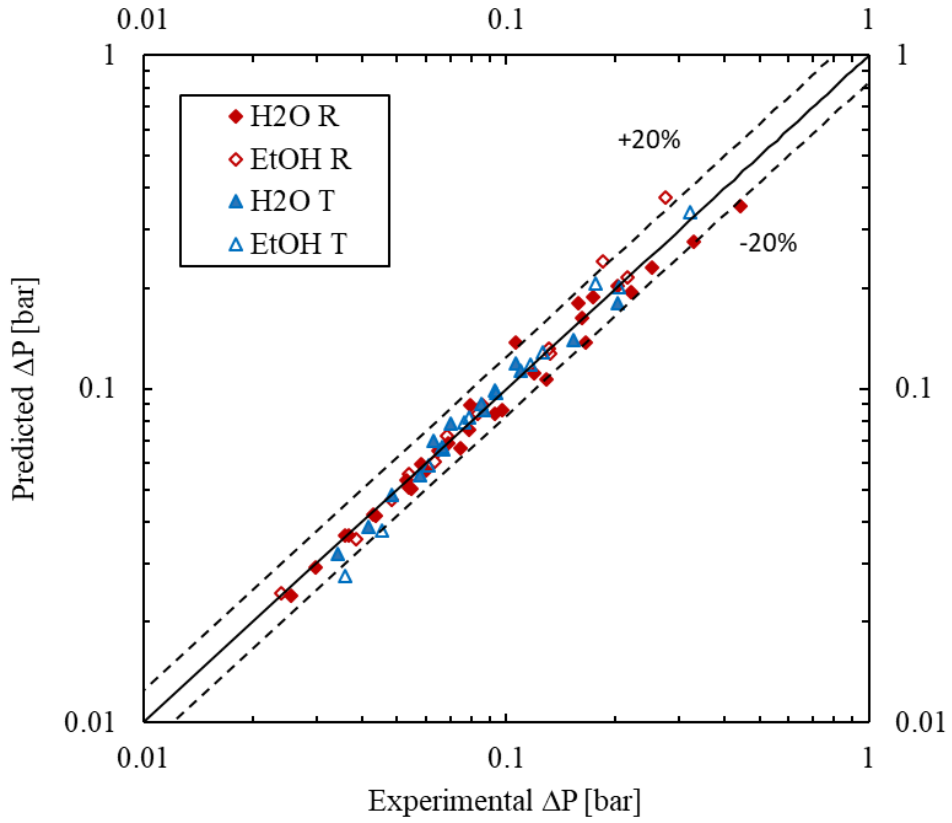

Figure 3.9. Parity plot of predicted vs measured pressure drop values.

3.3.3 Volumetric liquid-side mass transfer coefficient ($k_l a$)

The interphase mass transfer coefficient for a gas-liquid system is determined through a plug flow material balance over the volume of the reactor. Since nearly pure CO_2 was used as the gas phase, all resistance to mass transfer must exist in the liquid phase. Therefore, the volumetric liquid-side mass transfer coefficient, $k_l a$, is calculated via a mass balance on the dissolved gas in the liquid phase. If the phase holdups are unknown, then the specific surface area, a, is taken per unit volume of reactor according to equation (3.8).

$$k_l a(C^* - C) = Q_l \left(\frac{dC}{dV_R}\right) \tag{3.8}$$

Here, C is the dissolved CO_2 concentration in the bulk liquid phase and C^* is the liquid-side interfacial CO_2 concentration, which is equal to the equilibrium concentration as determined by Henry's law in equation (3.9). At 25 °C, the value of He_g for CO_2 in water was taken as 0.034 mol/kg·bar, and measured dissolved CO_2 concentrations in the liquid phase at the outlet were below 95% of saturation for the range of operating conditions.

$$C^* = P_g He_g \tag{3.9}$$

Integration of equation (3.8) over the reactor volume allows for average $k_l a$ determination by measuring the inlet and outlet concentrations of the dissolved CO_2 concentration according to equation (3.10):

$$k_l a = \frac{Q_l}{V_R} \ln\left(\frac{C^* - C_{in}}{C^* - C_{out}}\right) \tag{3.10}$$

where C^* is calculated using the average pressure between the inlet and outlet of the reactor, and C_{in} and C_{out} are the dissolved CO_2 concentrations in the feed (taken as 0 after measuring via titration) and at the outlet of the reactor, respectively.

3.3.3.1 Impact of Operating Conditions

For deionized water as the liquid phase, as shown in Figure 3.10a, $k_l a$ is greater at higher liquid velocities and increases monotonically with gas velocity before plateauing. Greater liquid velocities enhance bubble breakage and surface renewal via chaotic advection. Similarly, the initial rapid increase in $k_l a$ with gas velocity is caused by the corresponding fast increase in power dissipation (i.e., pressure drop) and gas holdup in bubble flow. The later slower increase in $k_l a$ with u_g appears to be due to a rise in length of gas bubbles in slug flow whereas the plateau is brought on by the onset of annular flow (as seen on flow regime maps of Figure 3.4), which are both changes in flow regime that decrease bubble specific area. The LL-Rhombus also produces higher $k_l a$ values than the LL-Triangle for fixed flow conditions. As discussed in section 3.3.1, the triangle obstacle is more prone to bubble coalescence due to redirection and recirculation of flow around the obstacle, which causes the onset of slug flow to occur at lower liquid velocities and would thereby decrease the interfacial area available for mass transfer.

Figure 3.10b, when ethanol is present, shows a similar impact of liquid and gas velocities where $k_l a$ values eventually reach a plateau at the greater gas velocities for a given liquid velocity. As with the pressure drop data, the impact of obstacle geometry is again marginal. For given fluid velocities and geometry, $k_l a$ values were generally higher with ethanol present due to the greater resulting specific interfacial area. Here, the plateau in $k_l a$ occurred when the flow resembled a froth where the chaotic eddies in the liquid phase were likely dampened or too small such that their effective contribution towards surface renewal and interfacial breakdown is decreased [107,118].

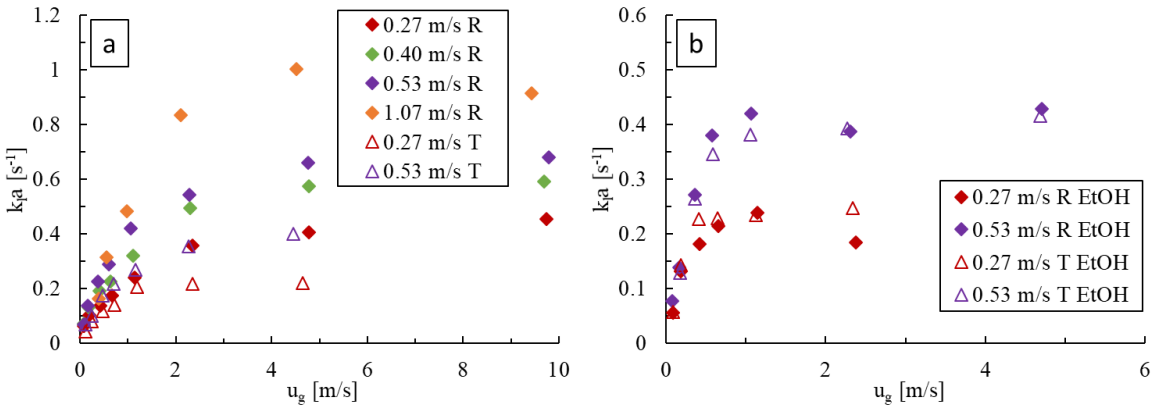

Figure 3.10. Comparison of $k_l a$ at varying gas and liquid flow rates in the LL-Rhombus (R) and LL-Triangle (T) with a) water and b) 0.5 wt% aqueous ethanol as the liquid phase.

The extraction efficiency, E, can also be used to examine the relative effects of increasing the gas and liquid velocities on CO_2 absorption, and it is calculated according to equation (3.11), where C^* is calculated at the outlet pressure.

$$E = 1 - \frac{C^* - C_{out}}{C^* - C_{in}} = \frac{C_{out}}{C^*} \tag{3.11}$$

With deionized water (Figure 3.11a), increasing the liquid velocity results in a decrease in the extraction efficiency, indicating that the loss in residence time has a greater impact than the increase in $k_l a$. Conversely, increasing the gas velocity results in higher extraction efficiencies that reach plateaus coinciding with the flow regime changes seen in Figure 3.4. These effects are observed in both obstacle geometries, with the LL-Rhombus producing overall higher extraction efficiencies than the LL-Triangle.

Similar trends are observed when 0.5 wt% aqueous ethanol is used (Figure 3.11b). Increasing the liquid velocity again results in a decrease in E due to the loss in residence time, while increasing the gas velocity generates higher E values until the plateau is reached corresponding to the formation of a froth. With surfactant, however, the effect of geometry is less

pronounced than when water alone is used, and both reactors produce similar extraction efficiencies over the range of flow rates tested.

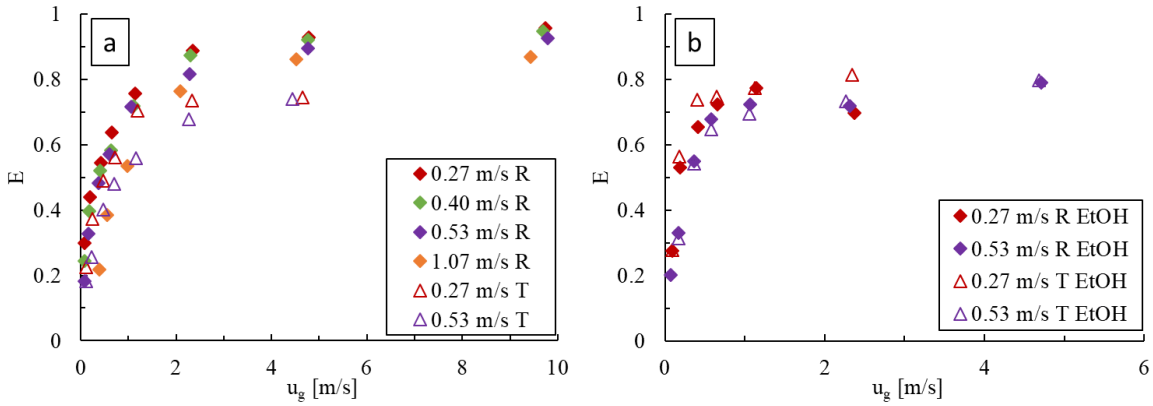

Figure 3.11. Comparison of extraction efficiency, ***E***, at varying gas and liquid flow rates in the LL-Rhombus (R) and LL-Triangle (T) with a) water and b) 0.5 wt% aqueous ethanol as the liquid phase.

3.3.3.2 Model

The $k_l a$ can be modelled as a function of power dissipation, ϵ, and the superficial velocity ratio, using equation (3.12) [46].

$$k_l a = \beta_3 \epsilon^{\beta_4} \left(\frac{u_g}{u_l}\right)^{\beta_5} \tag{3.12}$$

The parameter β_3 correlates positively with conditions favouring interfacial area creation, such as low interfacial tension. For dense bubbly flow dispersed by isotropic turbulent flow, the value of a/ε_g is proportional to $\epsilon^{0.4}\left(\frac{u_g}{u_l}\right)^{-0.6}$ [107]. Furthermore, k_l has been found proportional to $\epsilon^{\sim 0.25}$ for bubble columns and aerated stirred vessels [119], and the gas holdup, ε_g, has been found proportional to $\left(\frac{u_g}{u_l}\right)^{\sim 1.2}$ for the Corning™ Advanced-Flow™ reactor for $0.3 < \frac{u_g}{u_l} < 6.7$ [46]. The combined effect on a and k_l would then yield $\beta_4 \approx 0.65$ and $\beta_5 \approx 0.6$.

The power dissipation is calculated from the pressure drop using the following equation assuming no-slip between the phases.

$$\epsilon = \frac{\Delta P_{TPF} Q_t}{\rho_l V_R} \tag{3.13}$$

The parameters of the $k_l a$ model described by equation (3.12) were fitted to the bubble flow regime data where the $k_l a$ had not yet plateaued. Considering the confidence intervals on the model parameters, the data of all four combinations of liquid phases and reactor geometries were ultimately pooled, suggesting that obstacle shape and presence of ethanol have statistically marginal effects on the values of $k_l a$ for a given flow superficial velocity ratio and power dissipation. The resulting parameter values are given in Table 3.3, along with the upper and lower 95% confidence intervals. The associated parity plot is presented in Figure 3.12, where the AARE is 13.9% and bias factor F_m is 1.05. Furthermore, the value of β_4 is 0.55, close to the expected value of 0.65 discussed earlier, indicating that the power dissipation model approach is appropriate.

Table 3.3. $k_l a$ model fits and 95% confidence intervals for LL-Rhombus and LL-Triangle with water and 0.5 wt% aqueous ethanol as the liquid phases over the ranges of 0.565 < $\boldsymbol{\epsilon}$ < 6.91 W/kg and 0.14 < $\boldsymbol{u_g/u_l}$ < 0.56.

Parameter	$\boldsymbol{\beta_3}$	$\boldsymbol{\beta_4}$	$\boldsymbol{\beta_5}$
Value	0.124 ± 0.022	0.55 ± 0.12	0.41 ± 0.11

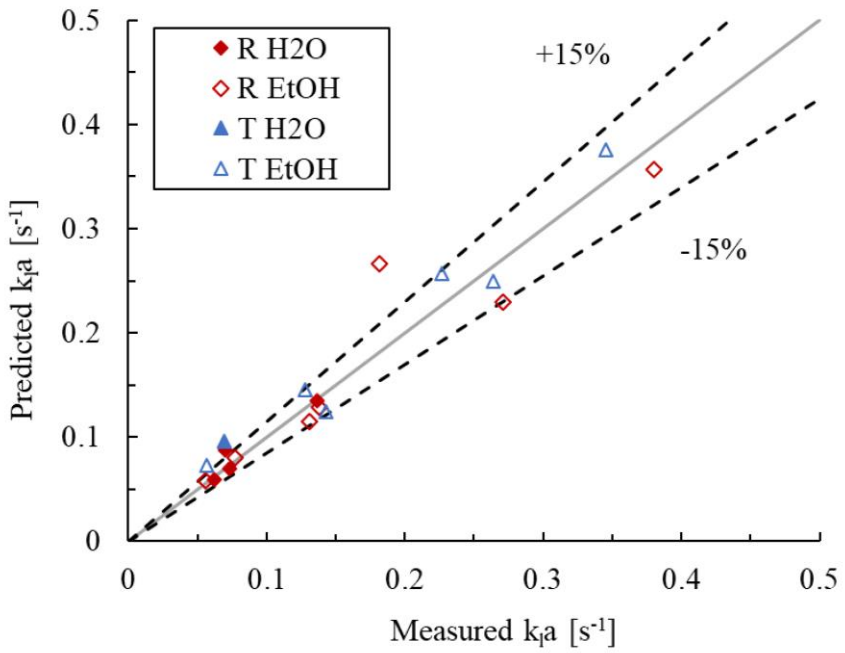

Figure 3.12. Parity plot of predicted vs measured $k_l a$ values in the bubbly flow regime.

3.4 **Conclusions**

With a flowing CO_2-water mixture, the LL-Rhombus and LL-Triangle produce flow regime maps comparable to those of microchannels with a hydraulic diameter of a similar size to the contraction of the LL-Reactors. However, the unique geometry decreases the range of slug flow in favour of bubble flow for low gas velocities and in favour of annular flow for high gas velocities. The LL-Rhombus is favourable to the LL-Triangle from a flow morphology perspective since the more gradual deviation of flow around the obstacle lowers opportunity for bubble re-coalescence. Furthermore, the LL-Rhombus is generally able to achieve higher $k_l a$ values at lower pressure drops for a given flow rate than the LL-Triangle. Finally, the addition of ethanol surfactant to the liquid water caused bubble flow to be present at every operating condition tested.

The Lockhart-Martinelli two-phase pressure drop model is accurate for each data set studied (AARE < 8.1 %), including for the frothy flow resulting from the aqueous ethanol, but it is limited to the fitted parameters which are specific to the combination of phases and geometries. A power

dissipation-based $k_l a$ model was shown to be accurate in predicting interphase mass transfer rates within the bubble flow regime for all flow systems (AARE < 13.9%), with the exponential fit of the power dissipation term similar to the expected value based on isotropic turbulent bubble breakage.

List of Nomenclature and Indices

Nomenclature [units]

a – Bubble interfacial area per unit reactor volume [m^2/m^3]

AARE – Average absolute relative error $\left(\frac{1}{n}\sum_{i=1}^{n}\frac{|Pred_i - Exp_i|}{Exp_i} \times 100\%\right)$ [%]

c – Parameter in equation (6)

C – Concentration [mol/m^3]

C^* – Equilibrium concentration [mol/m^3]

Ch – Chisholm parameter [-]

d_h – Hydraulic diameter of channel [m]

E – Extraction efficiency [-]

Eo – Eötvös number [-]

f_l – Liquid phase friction factor [-]

f_{lam} – Laminar friction factor contribution [-]

f_{turb} – Turbulent friction factor contribution [-]

F_m – Bias factor $\left(\exp\left[\frac{1}{n}\sum_{i=1}^{n} ln\left(\frac{Pred_i}{Exp_i}\right)\right]\right)$ [-]

g – Gravitational constant [m/s^2]

He – Henry's constant [mol/kg·Pa]

$k_l a$ – Volumetric liquid-side mass transfer coefficient [s^{-1}]

(Δ)L – Length of channel [m]

m – Mass flow rate [kg/s]

AARE – Average absolute relative error $\left(\frac{1}{n}\sum_{i=1}^{n}\frac{|P_i - E_i|}{E_i} \times 100\%\right)$ [%]

N_{mixer} – Number of mixers [-]

P – Pressure [Pa]

ΔP – Pressure drop [Pa]

Q – Volumetric flowrate [m^3/s]

Re – Reynolds number [-]

u – Superficial velocity [m/s]

V_R – Reactor volume [m^3]

w – Width of channel [m]

y – Parameter in equation (6)

Greek Symbols [units]

β – Fitting parameter [-]

δ – Channel height [m]

ϵ – Energy dissipation rate [W/kg]

ε_g – Gas holdup [-]

ρ – Density [kg/m^3]

$\Delta\rho$ – Difference in density between liquid and gas [kg/m^3]

σ – Surface tension [N/m]

ϕ^2 – Two-phase friction multiplier [-]

χ – Martinelli parameter [-]

Indices

g – Gas phase

l – Liquid phase

t – Total

TPF – Two-phase flow

4. Micromixing Study for the Scale-up of a Continuous Flow Viscous Nitration

Abstract

Micromixing performance is evaluated in various LL-microreactor plates within the context of scaling a viscous and exothermic nitration from lab scale at 75 mL/min to a production scale flowrate in the range of 327 mL/min. Lab-scale pressure drop data were analyzed for mean energy dissipation rates and relative contributions of chaotic and laminar flow patterns, leading to scale-up rules for predicting the flowrates required to maintain micromixing in larger scale microreactor plates. The scale-up rules were derived and tested for two different fluids: water and a 96 wt% $H_2SO_{4\ (aq)}$ solution. Measured energy dissipation rates in all scaled-up plates with both fluids exceeded those predicted by the scale-up rules. At equivalent energy dissipation rates, the relative contributions of chaotic flow patterns increased upon scale-up due to an accompanying increase in Re, although this effect was more pronounced with 96 wt% $H_2SO_{4\ (aq)}$ due to operation in a transitional regime, whereas the water data was generally chaotic flow dominated. Mean measures of micromixing performance were therefore conserved or improved upon scale-up.

4.1 **Introduction**

Microreactors are a promising reactor technology that allow for more intensified reaction conditions to be performed than those achievable in batch with comparable production rates when operated continuously [120,121]. Such reactors are classified by characteristic lengths in the micrometer scale, which affords them with large surface-to-volume ratios and enhanced rates of heat and mass transfer [122,123]. One particular resulting benefit of process intensification via microreactor technology is the ability to employ reaction pathways that would otherwise be unfeasible in batch due to safety concerns [17,42,124]. Because of the increased rates of heat and mass transfer, rapid and highly exothermic reactions can be more safely performed with greater temperature control. Nitrations are one such group of reactions that have several industrial applications, but are difficult to control and susceptible to side product formation, thermal runaway, and explosions [125], rendering them one of the most hazardous groups of reactions in the chemical industry [126]. When run in batch, these reactions are therefore typically run with intentionally lowered reaction rates and in dilute solutions with dropwise addition of the nitrating agent at low temperature for an extended period of time [127]. Under continuous flow, however, more rapid nitrations with improved yields and selectivities have seen successful and safe implementation in various micro-scale reactor technologies such as static mixers [127], packed beds [125], capillary microreactors [128,129], and plate-type microreactors [92,100,130–132].

Although microreactors are now seeing more widespread applications in laboratories, their use in larger-scale production processes is less common due to an inherently non-trivial scale-up. Microreactor production rates are generally increased from lab-scale by either increasing the channel diameter (scaling-up) or by operating several identical reactors in parallel (scaling-out or numbering up). Scaling-out allows the system to retain the intensification obtained at lab-scale,

but attention must be given to creating an even flow distribution and reagent dosage across the reactors, especially in the case of multiphase reactions [133,134]. On the other hand, scaling-up avoids any potential problems with flow distribution, but requires a pragmatic approach to reactor design in order to achieve intensification similar to that obtained at smaller-scales [84,85,135].

The objective of this chapter is to expand on and validate an existing turbulent scale-up methodology [84], commonly referred to as the $3/7^{th}$ rule, into transitional flow and larger scales of LL microreactor plates, within the scope of obtaining a larger production rate for a viscous exothermic nitration. The reaction has been successfully performed at lab-scale at a flowrate of 76 mL/min (140 g/min) but has a desired production capacity in the range of 327 mL/min (600 g/min). Scale-up calculations and extensions of the $3/7^{th}$ rule are presented for chaotic flow dominated and transitional flow regimes with the goal of maintaining mean micromixing performance in the mixing-dependent reaction at larger scale. An analysis of mean power dissipation and chaotic mixing is performed in order to test the validity of the scale-up methodology with two fluids having different physical properties; namely, a 96 wt% solution of H_2SO_4 in water comparable to the reaction medium, and water.

4.2 Materials and Methods

The overall flow system for measurement of the pressure drop data relevant to scale-up is shown in Figure 4.1. The scale-up methodology was tested with two solutions having two different densities and viscosities, namely, a 96 wt% solution of $H_2SO_{4\,(aq)}$ (μ = 0.020 Pa·s, ρ = 1.84 g/mL [135]), and water (μ = 8.90x10^{-4} Pa·s, ρ = 1.00 g/mL). The feed solution was pumped via a Fuji Super Metering Pump controlled by an Endress & Hauser Proline Promass 80A Coriolis flow meter. Flowrates were varied depending on the mixer and fluid being used and the ranges are presented in Table 4.1. The fluid then passed through an A5 LL microreactor plate, where pressure

measurements were taken at the inlet and outlet of the microreactor plate using WIKA M-11 0-100 barg pressure sensors and recorded via a Hitec Zang data acquisition board. The solution was then recycled back to the feed jar in order to reduce solution (96 wt% $H_2SO_{4\,(aq)}$) quantity in the lab. Experiments were performed at ambient temperature (21 °C), and did not rise significantly throughout the course of the experiments (less than 1 °C)

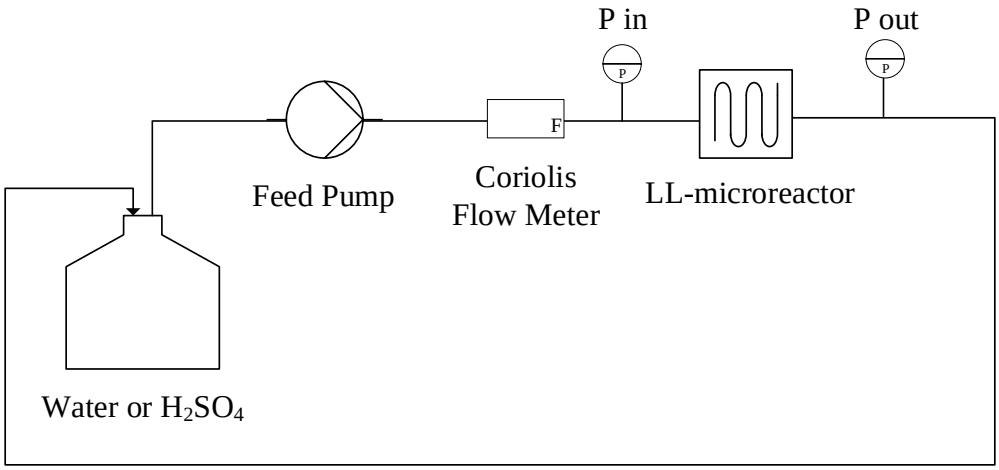

Figure 4.1. Simplified process flow diagram for the lab-scale pressure drop measurements.

Table 4.1. Tested flowrate ranges and space times for each fluid and microreactor plate pairing.

Mixer	Fluid	Tested Flowrates [mL/min]	Space Time [s]
Size 300 LL-Rhombus	96 wt% H2SO4	55.3-108.6	11.0-6.1
Size 200 LL-Rhombus		27.2-163.4	34.2-5.7
Size 100 LL-Rhombus		54.5 - 190.6	23.1-6.6
Size 100* LL-Rhombus		54.5 - 217.9	23.4-5.8
Size 100* LL-Triangle		54.5 - 217.9	21.0-5.2
Size 300 LL-Rhombus	Water	10-75	65.7-8.8
Size 200 LL-Rhombus		20-160	46.7-5.8
Size 100 LL-Rhombus		40-250	31.5-5.0
Size 100* LL-Rhombus		40-250	31.9-5.1
Size 100* LL-Triangle		40-250	28.7-4.6

More detail on the mixing structures and plates is provided in Figure 4.2 and Table 4.2. The microreactor plates consist of N equally spaced mixing structures (Figure 4.2b-e). The mixing structures themselves consist of a contraction following by an expansion into a mixing chamber containing either a rhombus (Figure 4.2a) or triangle shaped obstacle in order to induce chaotic secondary flow patterns. For momentum analysis, the mixer dimensions are commonly taken at the contraction where the flow velocity and resulting turbulence is at its highest (Table 4.2).

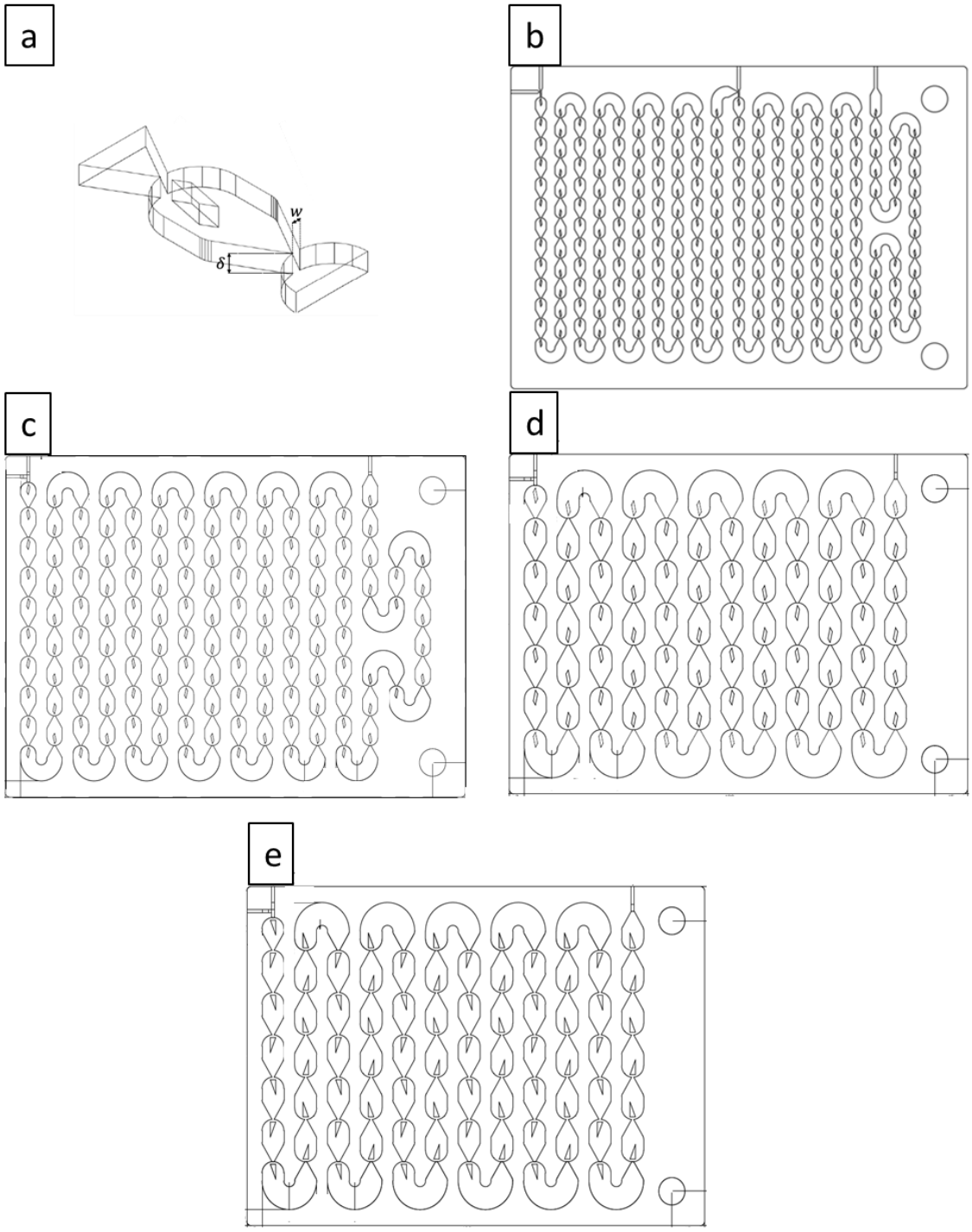

Figure 4.2. LL mixer geometry and orientation within the plate reactors. (a). Size 300 LL-Rhombus mixer. (b) A5 Size 300 Rhombus. (c) A5 Size 200 Rhombus. (d) A5 Size 100 and 100* Rhombus (e) A5 Size 100* Triangle. Note that the size 100 and 100* plates have the same mixer layout but differ in their channel depths.

Table 4.2. Scaled-up reactor geometries and dimensions.

Mixer Type [--]	Mixer Size [--]	Depth [mm]	Width [mm]	d_h [mm]	N [--]	V_R [mL]
Rhombus	300	1.25	0.5	0.714	234	11.03
Rhombus	200	1.75	0.7	1	133	15.53
Rhombus	100	2.2	1	1.375	73	20.95
Rhombus	100*	2.5	1	1.429	73	21.20
Triangle	100*	2.5	1	1.429	73	19.04

4.3 Scale-up methodology

Scale-up calculations in microreactors can be performed using an analysis of the flow regimes via the measured pressure drops and the resulting mean energy dissipation rates and friction factors [84]. It is assumed that the micromixing efficiency of a reactor will be maintained during scale-up if the mean energy dissipation rate is constant [137] and the relative contributions of chaotic/secondary and laminar flow patterns are maintained. The aforementioned nitration reaction is micromixing dependent, where slow micromixing times can result in the formation of a undesired side products. Micromixing rates are limited primarily via either engulfment in turbulent flow or diffusion in laminar flow, where the time constant for each can be calculated with the kinematic viscosity (ν), the mean energy dissipation rate (ϵ), and the diffusivity ($\mathcal{D}$) with equations (4.1) and (4.2) [137].

$$t_E = 17\left(\frac{\nu}{\epsilon}\right)^{0.5} \quad \textbf{(4.1)}$$

$$t_D = 2\left(\frac{\nu}{\epsilon}\right)^{0.5} \operatorname{arcsinh}\left(0.05\nu/\mathcal{D}\right) \quad \textbf{(4.2)}$$

The mean energy dissipation rate can be calculated using the pressure drop (ΔP), flowrate (Q), and volume of the reactor (V_R) according to equation (4.3). Substitution of equation (4.3) into the pressure drop model in equation (4.4), where N is the number of repeating mixing units, leads to equation (4.5) which is independent of flow regime, and where v is the volume of a single repeating mixing unit.

$$\epsilon = \frac{\Delta P Q}{\rho V_R} \quad \textbf{(4.3)}$$

$$\Delta P = fN\left(\frac{\rho u^2}{2}\right) \quad \textbf{(4.4)}$$

$$\epsilon = \frac{fQ^3}{2A_c v} \quad \textbf{(4.5)}$$

The flowrate required to maintain a constant energy dissipation rate when scaling up from reactor 1 to reactor 2 can then be calculated by setting $\epsilon_1 = \epsilon_2$, which gives the following relations:

$$\frac{f_1 Q_1^3}{A_{c,1}^2 v_1} = \frac{f_2 Q_2^3}{A_{c,2}^2 v_2} \quad \textbf{(4.6)}$$

$$Q_2 = Q_1\left(\frac{f_1}{f_2}\right)^{\frac{1}{3}}\left(\frac{A_{c,2}}{A_{c,1}}\right)^{\frac{2}{3}}\left(\frac{v_2}{v_1}\right)^{\frac{1}{3}} \quad \textbf{(4.7)}$$

When friction factor models are not available for the scaled-up plates, i.e. for f_2 before the plate has been acquired, they may be assumed to be equivalent to the model for f_1 (described below) when the plates are geometrically similar; an assumption which can later be corrected upon acquisition and testing of the larger scale plates.

In turbulent flow, micromixing via engulfment precedes diffusion and will ultimately determine the micromixing time [137]. A decrease in micromixing time may therefore be realized

via reduction in the size of convective fluid elements towards the length scale of diffusion, by increasing the relative proportion of chaotic energy dissipation of the total mean energy dissipation rate [138]. It is therefore necessary to also consider the relative contributions of laminar and chaotic flow to micromixing.

In complex structured microchannels, due to flow channeling, recirculation, and varying intensities of local energy dissipation rates throughout the mixing structures, friction factors often proceed from laminar to turbulent flow via a smooth transitional region similar to that seen in packed beds. The smooth transition is a result of localized zones of laminar and chaotic flow patterns dispersed throughout each repeating mixing unit, where within each there exist local distributions of energy dissipation rates. The result is a potentially broad range of local energy dissipation rates throughout a mixing structure that can result in local variations of micromixing times. In practice, however, it may be sufficient to consider only the mean energy dissipation rate throughout the reactor in predicting the ultimate micromixing times [139], as it has been previously postulated that, in laminar flow, as little as 3% of the total energy dissipated throughout a reactor may be attributed to the generation of mixing [140]. Such phenomena in the present size 300 mixer geometry are visualized clearly in the internally generated computational fluid dynamics (CFD) images in Figure 4.3 [141], showing flow channeling around the obstacle (Figure 4.3a) and fluid recirculation outside of these channeled streams (Figure 4.3b), leading to non-uniform distributions of turbulent viscosity throughout the mixers (Figure 4.3c).

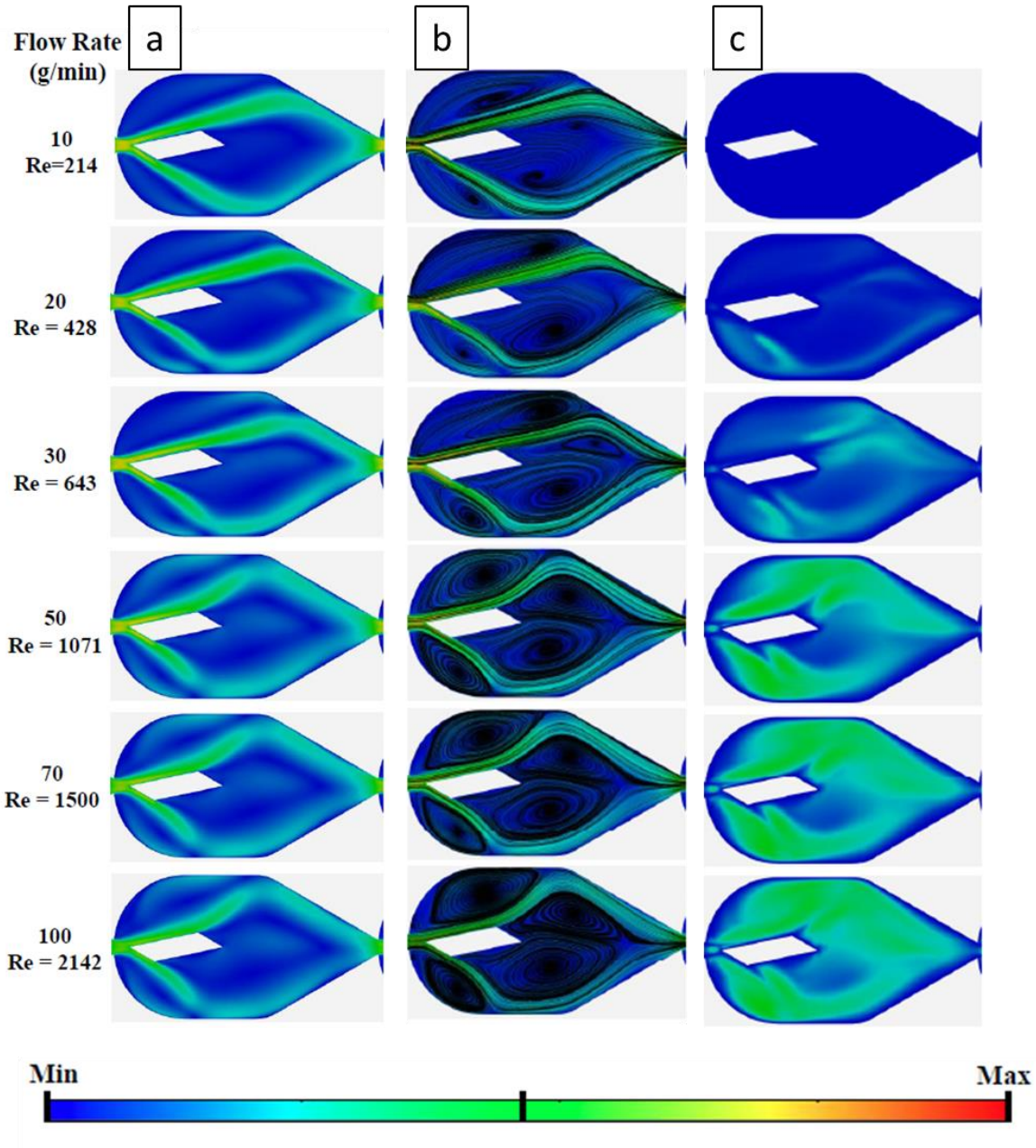

Figure 4.3. CFD generated velocity profiles (a), streamline maps (b), and turbulent viscosity ($\boldsymbol{\nu_t}$) fields (c) at the midplane (δ = 0.625 mm) of the LL Rhombus mixer with water. For (a) and (b), $\boldsymbol{u}$ (m/s) varies from, depending on the flowrate, $\boldsymbol{u_{min}}$ (blue) = 0 m/s to $\boldsymbol{u_{max}}$ (red) = 0.45 (10 g/min), 0.91 (20 g/min), 1.28 (30 g/min), 2.21 m/s (50 g/min), 3.39 (70 g/min) and 5.37 (100 g/min). For (c), $\boldsymbol{\nu_t}$ (m^2/s) varies from $\boldsymbol{\nu_{t,min}}$ (blue) = 0 (blue) to $\boldsymbol{\nu_{t,max}}$ (red) = (10 g/min), 6.7×10^{-6} (20 g/min), 2.2×10^{-5} (30 g/min), 4.1×10^{-5} (50 g/min), 5.0×10^{-5} (70 g/min), and 6.2×10^{-5} (100 g/min) [141].

In this transitional region, the resulting overall friction factor is the sum of the laminar (f_L) and turbulent chaotic components (f_C), as shown in equation (4.8) below.

$$f = \frac{f_L}{Re} + f_C \quad \textbf{(4.8)}$$

Substitution of equation (4.8) into equation (4.4) results in the following model for the pressure drop that accounts for both turbulent and laminar contributions, where f_L and f_C can be determined directly from the coefficients of the u^2 and u terms (C_1 and C_2) as shown below.

$$\Delta P = \frac{f_c N \rho}{2} u^2 + \frac{\mu N f_L}{2 d_h} u \quad \textbf{(4.9)}$$

$$\Delta P = C_1 u^2 + C_2 u \quad \textbf{(4.10)}$$

$$f_C = C_1 \left(\frac{2}{N\rho}\right) \quad \textbf{(4.11)}$$

$$f_L = C_2 \left(\frac{2 d_h}{N\mu}\right) \quad \textbf{(4.12)}$$

Thus, the relative contributions of laminar and chaotic secondary flows to the mean micromixing time can be approximated from f_L/f and f_C/f, respectively, and should ideally be matched upon scale-up at a given mean energy dissipation rate.

4.4 **Scale-up validation with water**

Pressure drops and the resulting mean energy dissipation rates with water for the lab-scale and production scale microreactors plates are presented in Figure 4.4. The predicted flowrates and mean energy dissipation rates for each scaled-up microreactor geometry are presented in Figure 4.4b and c as dashed lines for the range of tested lab-scale flowrates. When the friction factor model for the size 300 Rhombus plate is used throughout the scale-up calculations, the predicted energy dissipation rates are below those measured in the lab by an average of about 37%. However, this error is considered acceptable for the purposes of selecting a reactor size from the presented

geometries before the real pressure data has been acquired, as the energy dissipation rates are sufficiently spaced between the size 300, 200, and 100(*) scales. When the experimentally obtained models for f_2 are employed, the scale-up rules are significantly more accurate with an average error of about 4%. The mean energy dissipation rates with water upon scale-up may therefore be accurately predicted when the plate has been characterized with pressure drop data. As mentioned previously, however, this result alone does not confirm equivalent or lower micromixing times upon scale-up, and the relative amounts of laminar and chaotic flow patterns in each reactor geometry must also be considered.

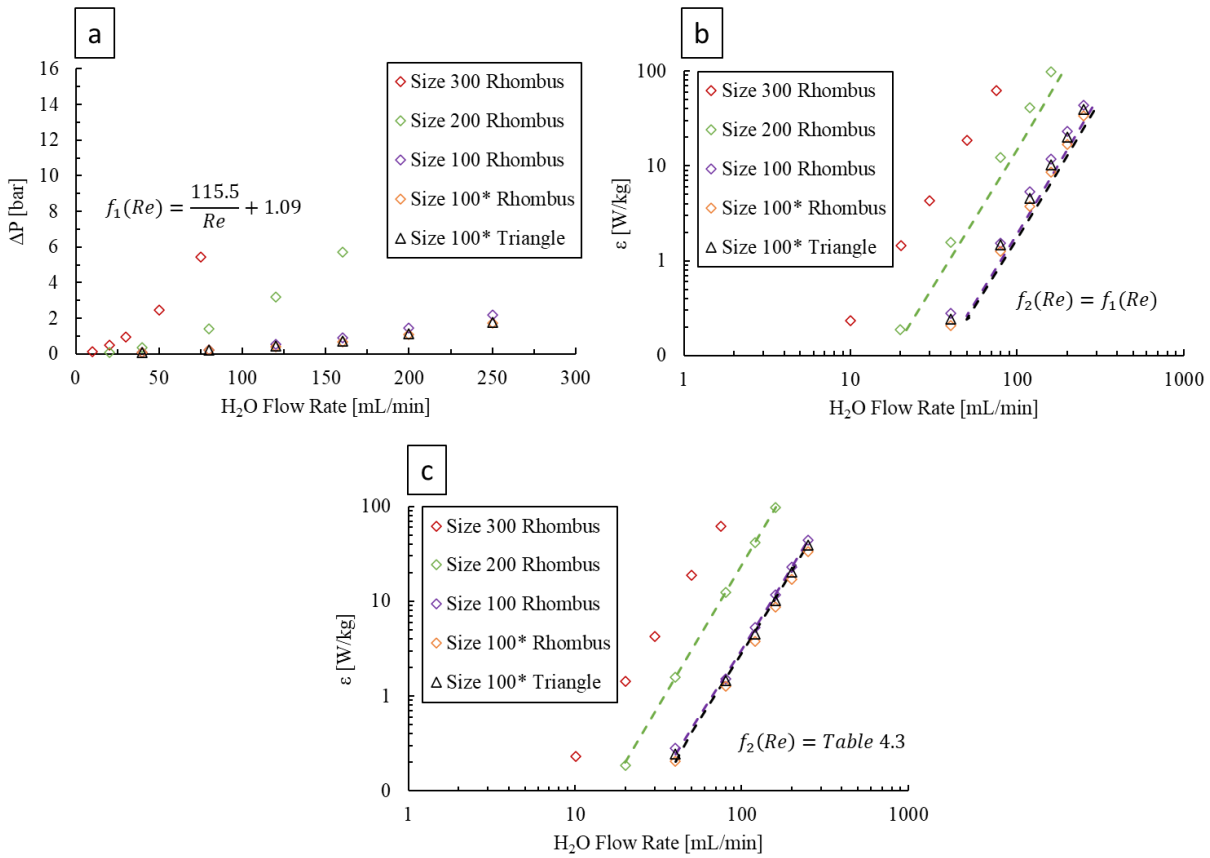

Figure 4.4. Pressure drops (a) and resulting mean energy dissipation rates (b,c) in the lab scale (size 300) and production scale (size 200 – 100*) microreactor plates with water. Dashed lines represent predicted mean energy dissipation rates, with both the Rhombus and Triangle size 100* mixers sharing the same black dashed line, when (b) a constant friction factor model is assumed across all scales, and (c) when the experimentally determined friction factor model is used for $\boldsymbol{f_2}$.

Analyses of the friction factors for water in each plate are presented in Figure 4.5 with the pressure drop correlations used for determining the resulting values of f_C and f_L shown in Table 4.3. The overall friction factors as a function of Re are shown in Figure 4.5a, and generally tend approach the value of f_C at the highest tested values of Re indicating significant contributions of chaotic advection to the overall flow patterns. This is further confirmed in Figure 4.5b, where the values of f_C/f begin to plateau above values of ~0.8 when Re is greater than ~1000, indicating

that micromixing is largely dominated by chaotic advection at Re above 1000 in all plates. When compared on a mean energy dissipation rate basis in Figure 4.5c, the amounts of turbulence are generally greater in the larger scale plates until they plateau, which is a direct result of the higher Re required to reach the same mean energy dissipation rate when the plates are larger. Thus, with water as the working fluid, the applied scale-up methodology should achieve similar or lower mean micromixing times at equal mean energy dissipation rates in the larger plates due to the accompanying increase in Re.

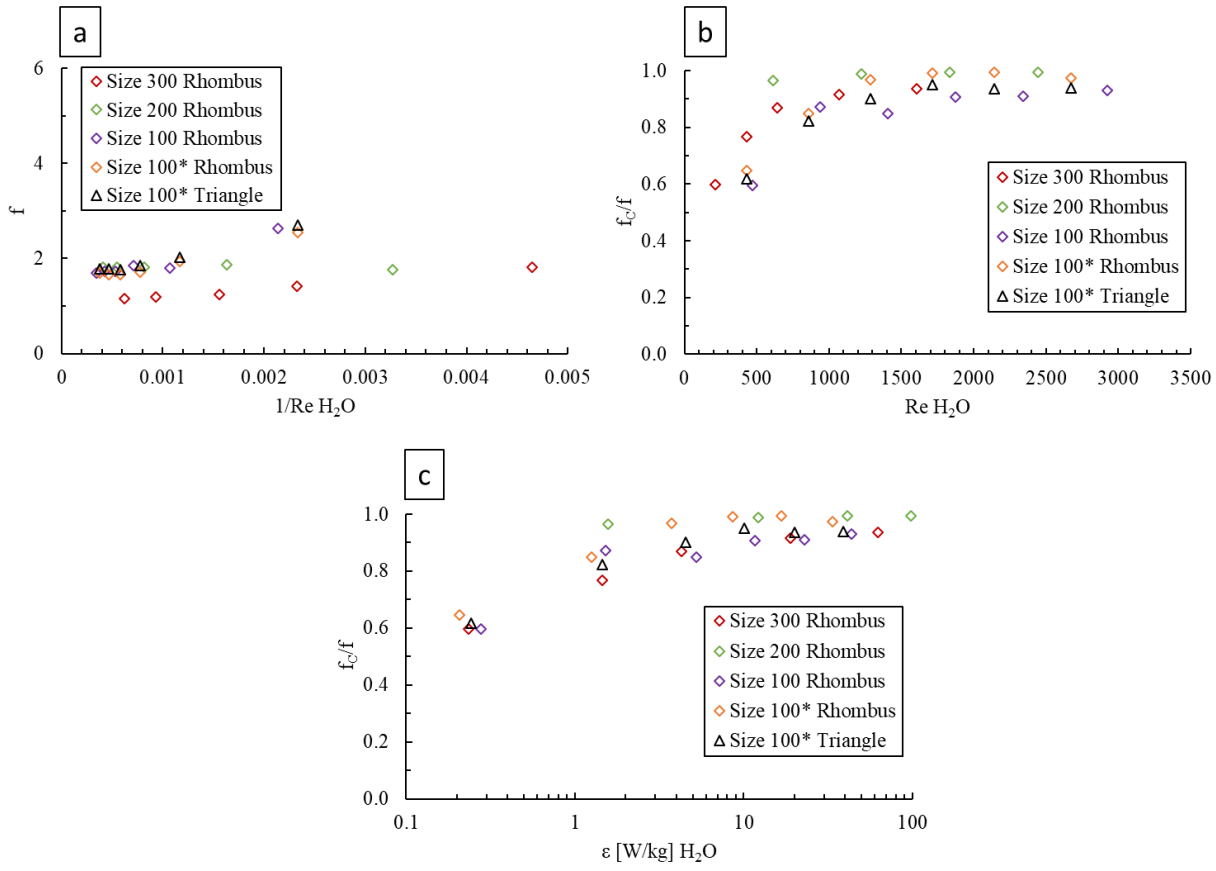

Figure 4.5. Friction factor analysis for the lab-scale (size 300) and production scale (sizes 200 – 100*) plates with water. (a) Overall friction factors from equations (4.4) and (4.8). (b) Relative contributions of chaotic flow as a function of $\boldsymbol{Re}$. (c) Relative contributions of chaotic flow as a function of mean energy dissipation rate.

Table 4.3. Dual-term friction factor correlation values for the large-scale plates with water. All correlations have an R^2 value greater than 0.999.

Plate	Fluid	$\Delta P = C_1 u^2 + C_2 u$		$f = f_L/Re + f_C$	
		C_1 [Pa·s^2·m^{-2}]	C_2 [Pa·s·m^{-1}]	f_L	f_C
Size 300 Rhombus	Water	127025	16836	115.5	1.09
Size 200 Rhombus		120864	701	23.1	1.81
Size 100 Rhombus		57735	7758	343.4	1.57
Size 100* Rhombus		60403	1891	83.1	1.65
Size 100* Triangle		61167	5488	241.3	1.67

4.5 Scale-up validation with 96 wt% $H_2SO_{4\,(aq)}$

Pressure drops and the resulting mean energy dissipation rates with 96 wt% $H_2SO_{4\,(aq)}$ for the lab-scale and production scale microreactors plates are presented in Figure 4.6. Flowrates of 96 wt% $H_2SO_{4\,(aq)}$ were limited to prevent larger pressure drops in the lab, such that testing of the scale-up methodology was performed stepwise from size 300 to size 200, followed by from size 200 to 100 and 100*. The predicted flowrates and mean energy dissipation rates for each scaled-up microreactor geometry are presented in Figure 4.6 b and c. Similarly to water, when the friction factor model is constant across scales the average error is about 36%, and when the experimentally obtained friction factor models are use the average error decreases significantly to about 1.7%. Using the experimental friction factor models allows for prediction of flowrates that will generate mean energy dissipation rates of 91.8 W/kg at each scale, resulting in values of 142.4 mL/min, 294.7 mL/min, 326.3 mL/min, and 306 mL/min for the size 200 Rhombus, size 100 Rhombus, size

100* Rhombus, and size 100* Triangle, respectively (represented by filled markers on Figure 4.6 and Figure 4.7). Thus, all plates should provide a sufficient mean energy dissipation rate at the target production flowrate, but relative contributions of secondary flows must also be examined.

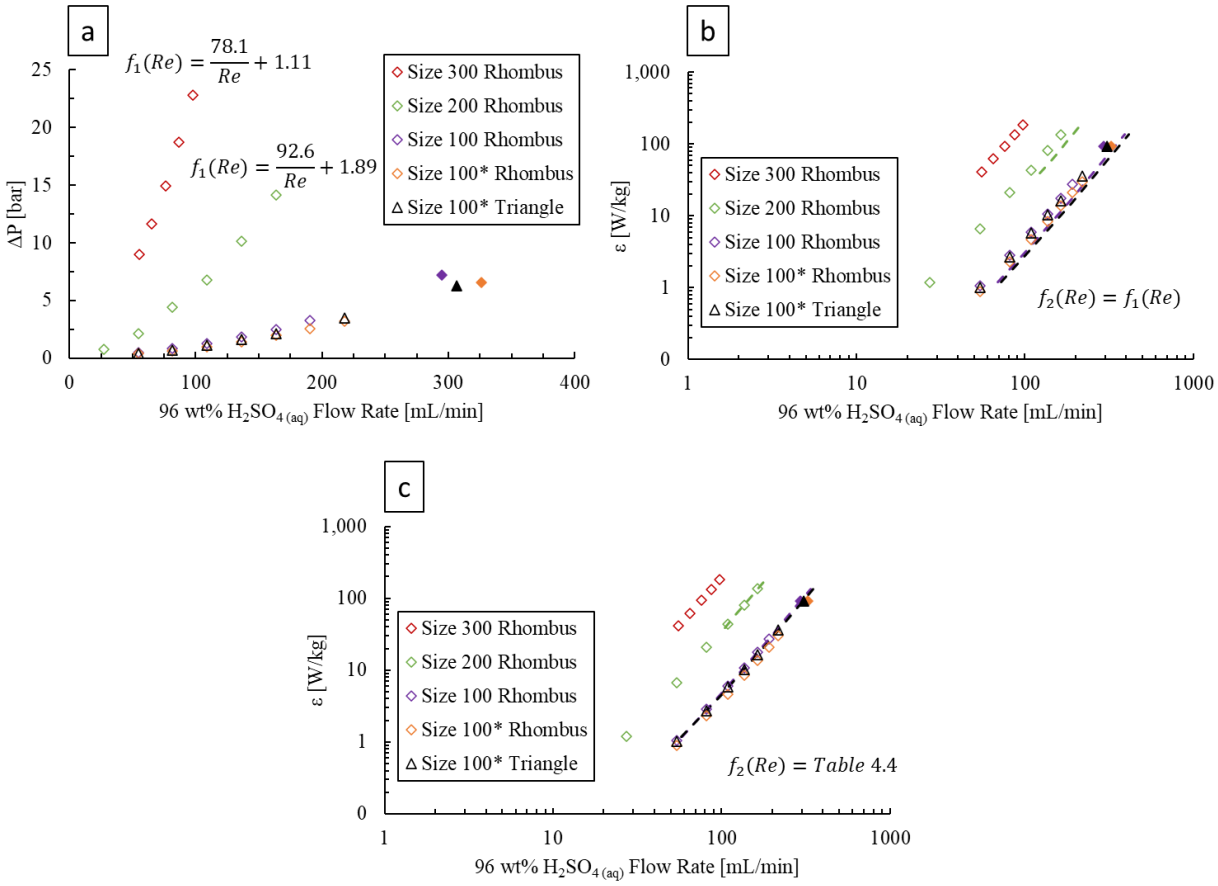

Figure 4.6. Pressure drops (a) and resulting mean energy dissipation rates (b,c) in the lab scale (size 300) and production scale (size 200 – 100*) microreactor plates with water. Dashed lines represent predicted mean energy dissipation rates, with both the Rhombus and Triangle size 100* mixers sharing the same black dashed line, when (b) a constant friction factor model is assumed during scale-up, and (c) when the experimentally determined friction factor model is used for $\boldsymbol{f_2}$. Filled data points are extrapolated to $\boldsymbol{\epsilon}$ = 91.8 W/kg.

Analyses of the friction factors for 96 wt% $H_2SO_{4\,(aq)}$ in each plate are presented in Figure 4.7 with the pressure drop correlations used for determining the resulting values of f_C and f_L shown in Table 4.4. Note that in this case, f_c may not represent chaotic flow patterns due to the low range

of tested Reynold's numbers ranging from 34-204 (owing to the high viscosity of 96 wt% $H_2SO_{4\,(aq)}$), and more likely represents secondary flows contributing to blending. The overall friction factors as a function of $1/Re$ are shown in Figure 4.7a, with the relative secondary flow contributions for each plate as a function of Re, ranging from about 0.4 to 0.8, shown in Figure 4.7b. When compared on a mean energy dissipation rate basis (Figure 4.7c), the relative secondary flow contributions are significantly larger in the scaled-up plates due to the higher required Re to reach an equivalent mean energy dissipation rate. This effect is similar to but more pronounced than that observed with water, as the data with 96 wt% $H_2SO_{4\,(aq)}$ covers the transitional flow regime between laminar and turbulent, whereas the water data showed a plateau-like profile in a more turbulent dominated regime. At the extrapolated production flowrates indicated above, the data suggest higher contributions of secondary flows than observed at lab-scale, suggesting that mean micromixing or blending times will be conserved or lowered in the larger-scale plates.

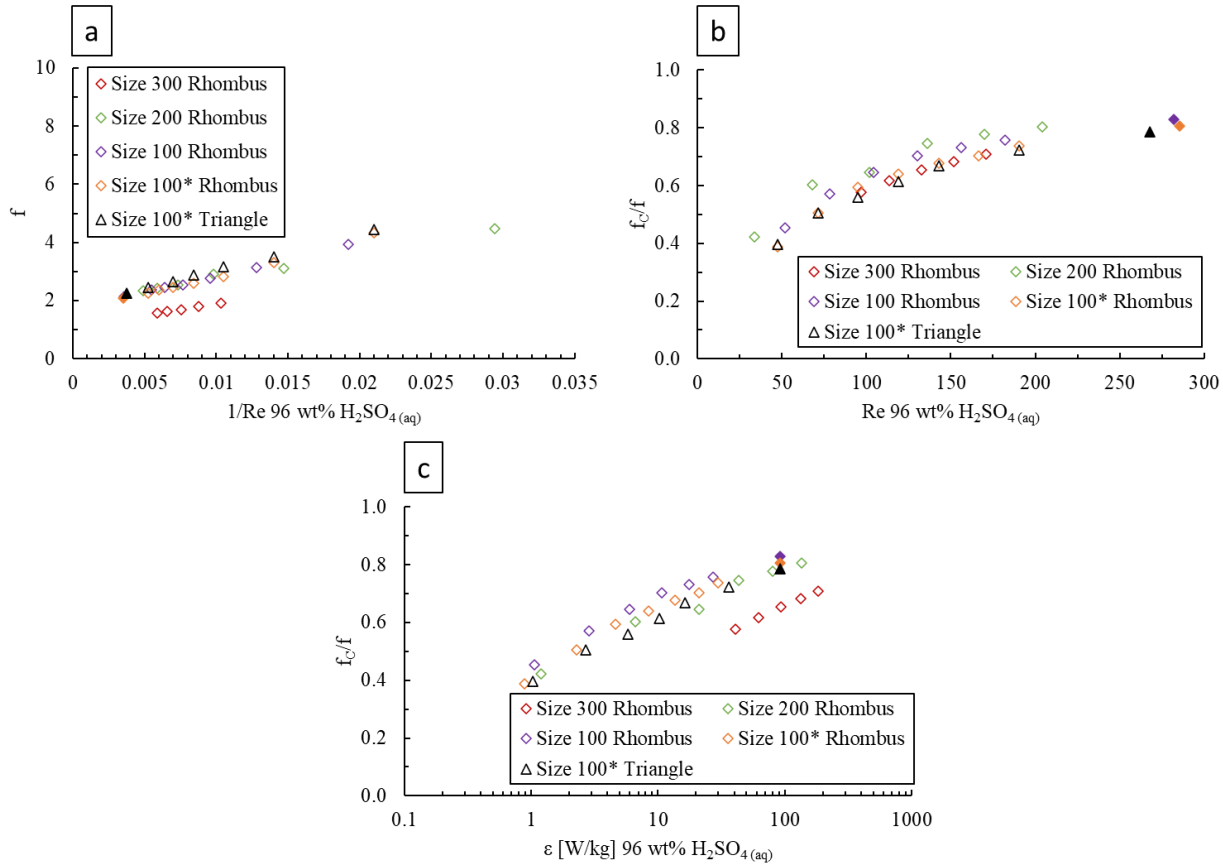

Figure 4.7. Friction factor analysis for the lab-scale (size 300) and production scale (sizes 200 – 100*) plates with 96 wt% $H_2SO_{4\,(aq)}$. (a) Overall friction factors from equations (4.4) and (4.8). (b) Relative contributions of chaotic flow as a function of $\boldsymbol{Re}$. (c) $\boldsymbol{f_c/f}$ as a function of mean energy dissipation rate. Filled data points are extrapolated to $\boldsymbol{\epsilon}$ = 91.8 W/kg.

Table 4.4. Dual-term friction factor correlation values for the large-scale plates with 96 wt% $H_2SO_{4\,(aq)}$. All correlations have an R^2 value greater than 0.999.

Plate	Fluid	$\Delta P = C_1 u^2 + C_2 u$		$f = f_L/Re + f_C$	
		C_1 [Pa·s^2·m^{-2}]	C_2 [Pa·s·m^{-1}]	f_L	f_C
Size 300 Rhombus	96 wt% $H_2SO_{4\,(aq)}$	238540	256017	78.1	1.11
Size 200 Rhombus		230198	123220	92.6	1.89
Size 100 Rhombus		119730	54625	102.9	1.79
Size 100* Rhombus		112071	58286	114.1	1.67
Size 100* Triangle		118734	65719	128.6	1.77

Thus, the present data suggests that global micromixing measures will be conserved or improved upon reactor scale-up in both fluid systems. However, additional work is necessary in order to obtain a more in-depth understanding of local energy dissipation rates via CFD modelling in the larger-scale reactors, as zones of low local energy dissipation rate and reduced micromixing may still lead to the formation of undesired side products. Additionally, micromixing alone does not characterize completely the performance of a reactor with a given reaction system, and macromixing studies should be performed via analysis of residence time distributions. Such studies allow for characterization of the degree of back mixing and recirculation within the mixers, leading to assessment of the degree of plug flow obtained at each reactor scale which will have a direct impact on product yield. Thus, in order to achieve complete scale-up of a reactor system, the mean and local micromixing performance should be maintained while also achieving the same level of plug flow in the larger scale reaction systems. More specifically, this should then include the distributions of both mixing times and residence times throughout each mixing unit and the reactor

volume. Ultimately, however, characterization of the reaction performance at large scale will have to occur within the safety of a dedicated, factory-based production facility [100].

4.6 **Comparison with Static Mixer**

As an alternative and cheaper reactor technology, a shell and tube reactor with Kenics^{TM} type static mixer inserts was also tested for operation at the production scale. In this case the reaction system was consistent with that presented in Figure 4.1, but with the LL-microreactor replaced with two 480 mm length stainless steel tubes (3.05 mm internal diameter) containing 4 Hastelloy Kenics^{TM} static mixing elements. The static mixer inserts had a 2.9 mm diameter and consisted of 24 geometrically alternating helical mixing elements 5 mm in length (120 mm total length per insert) (Figure 4.8). The void fraction of the tubes containing static mixing elements was 0.94, resulting in a reaction volume of 3.32 mL for each mixing section. The bend did not contain any static mixing elements and had a total volume of 0.77 mL. The total combined volume of both static mixer tubes and bend was therefore 7.41 mL. The bend was incorporated into the pressure drop measurements as it represents the repeating unit of a shell and tube reactor containing such mixing structures.

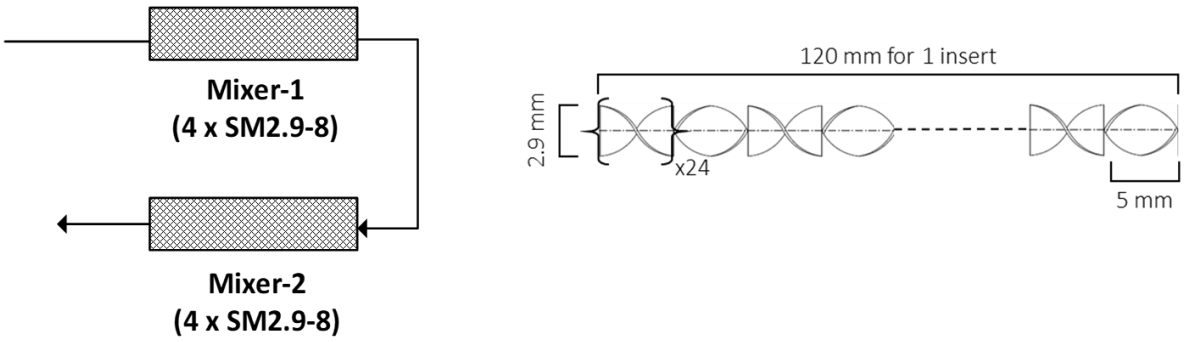

Figure 4.8. Orientation of the tubes for testing the shell and tube reactor (right) with static mixer inserts (left).

Pressure drops and the resulting energy dissipation rates for the static mixer with water and 96 wt% $H_2SO_{4\,(aq)}$ are shown in Figure 4.9 and Figure 4.10 below. In this case, a scale-up methodology was not employed as the reactor volume can be easily modified by adding or removing repeating static mixer-bend-static mixer subunits. The size 300, 200, and 100* Rhombus reactor geometries are included on the figures to provide a basis of comparison across the range plate sizes tested. With both fluids, the energy dissipation rates fall in between those of the size 200 and size 100* Rhombus plates. Importantly, with 96 wt% $H_2SO_{4\,(aq)}$, the static mixer geometry reaches the target energy dissipation rate of 91.8 W/kg at a flowrate of 179 mL/min, and well exceeds it at the production flow rate of 327 mL/min with an energy dissipation rate of 384.4 W/kg. However, as was the case in with the plate scale up methodology, it is also necessary to examine the relative contributions of chaotic flow patterns to the overall flow regime.

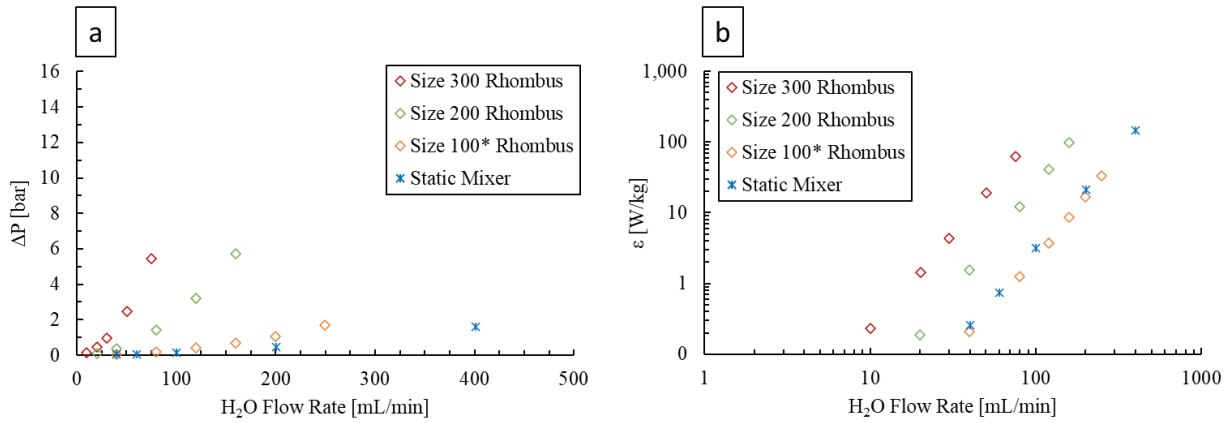

Figure 4.9 Pressure drops (a) and resulting mean energy dissipation rates (b) with water through the static mixer geometry shown in Figure 4.8, as compared with the size 300, 200, and 100* Rhombus LL-microreactor plates.

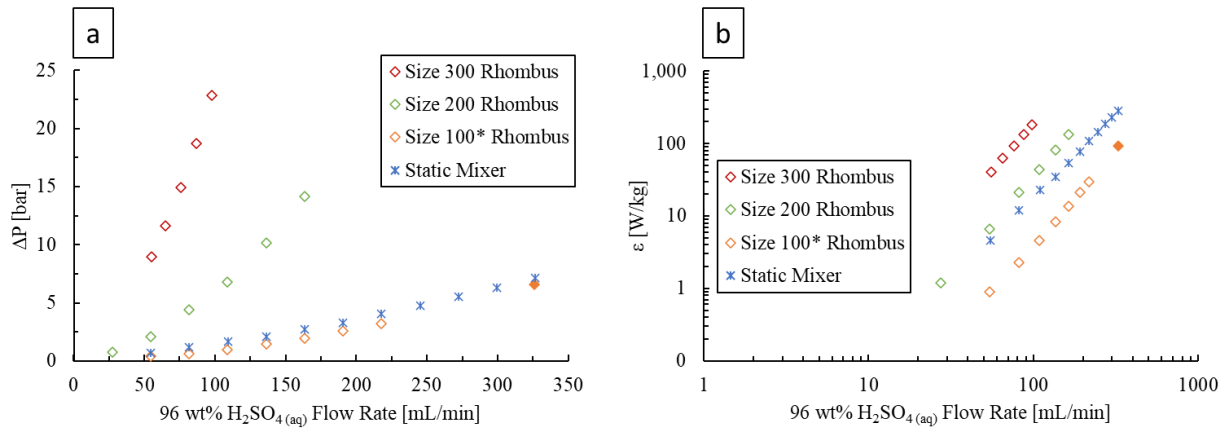

Figure 4.10. Pressure drops (a) and resulting mean energy dissipation rates (b) with 96 wt% $H_2SO_{4\,(aq)}$ through the static mixer geometry shown in Figure 4.8, as compared with the size 300, 200, and 100* Rhombus LL-microreactor plates. Filled data points are extrapolated to $\boldsymbol{\epsilon}$ = 91.8 W/kg.

Figure 4.11 and Figure 4.12 below show the friction factor analyses for both water and 96 wt% $H_2SO_{4\,(aq)}$, as compared again with the size 300, 200, and 100* Rhombus plates. With both fluids, there is a significant reduction in the contributions of secondary flow patterns when compared to the LL-microreactor plates. Similarly to the results presented in the scale-up above, this reduction is more substantial with 96 wt% $H_2SO_{4\,(aq)}$ as the working fluid where the data show more contributions from laminar flow, versus with water where the flow becomes more chaotic flow dominated and f_c/f begins to plateau. Because the nitration is mixing-dependent, the plate-type microreactors are considered in this case to be the better choice in reactor technology where their higher contributions to turbulent flow are expected to reduce micromixing times. Although the static mixers are a more cost-efficient technology, the presented geometry is ultimately oversized and likely does not generate enough secondary flow patterns to effectively maintain the micromixing time for the mixing-dependent reaction.

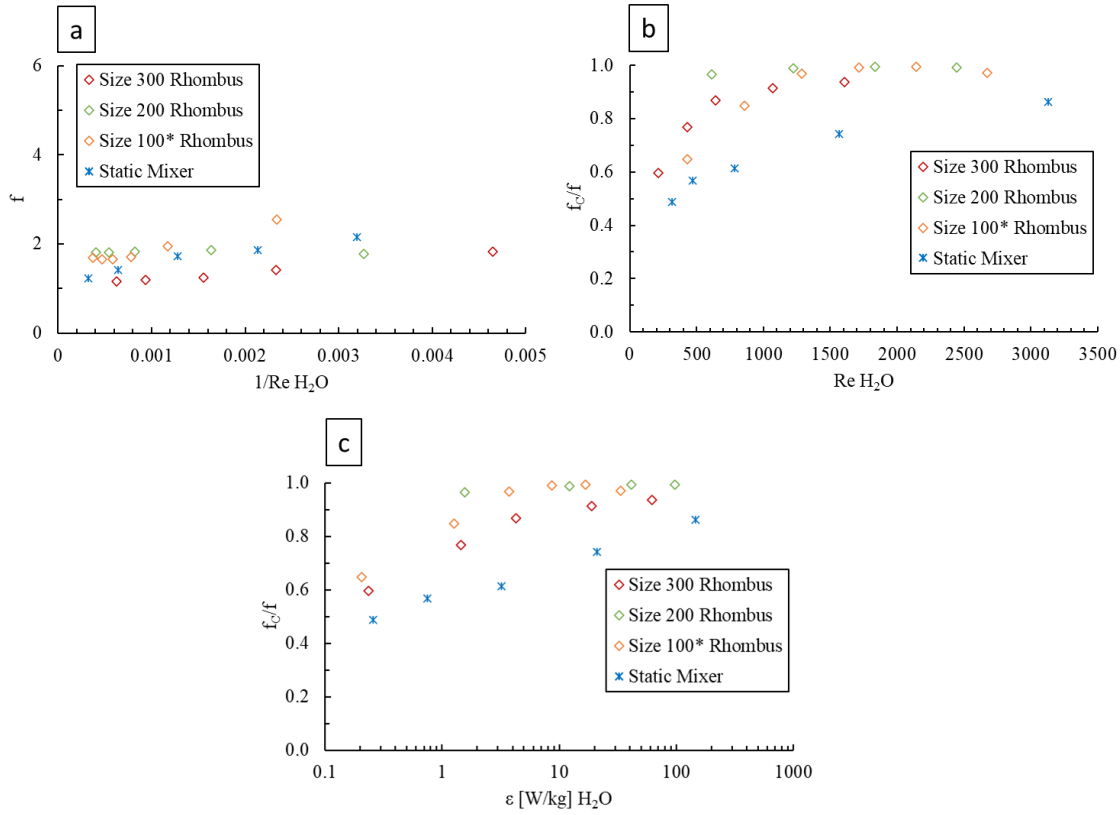

Figure 4.11. Friction factor analysis for the static mixer geometry with water as compared with the size 300, 200, and 100* Rhombus. (a) Overall friction factors from equations (4.4) and (4.8). (b) Relative contributions of chaotic flow as a function of $\boldsymbol{Re}$. (c) Relative contributions of chaotic flow as a function of mean energy dissipation rate.

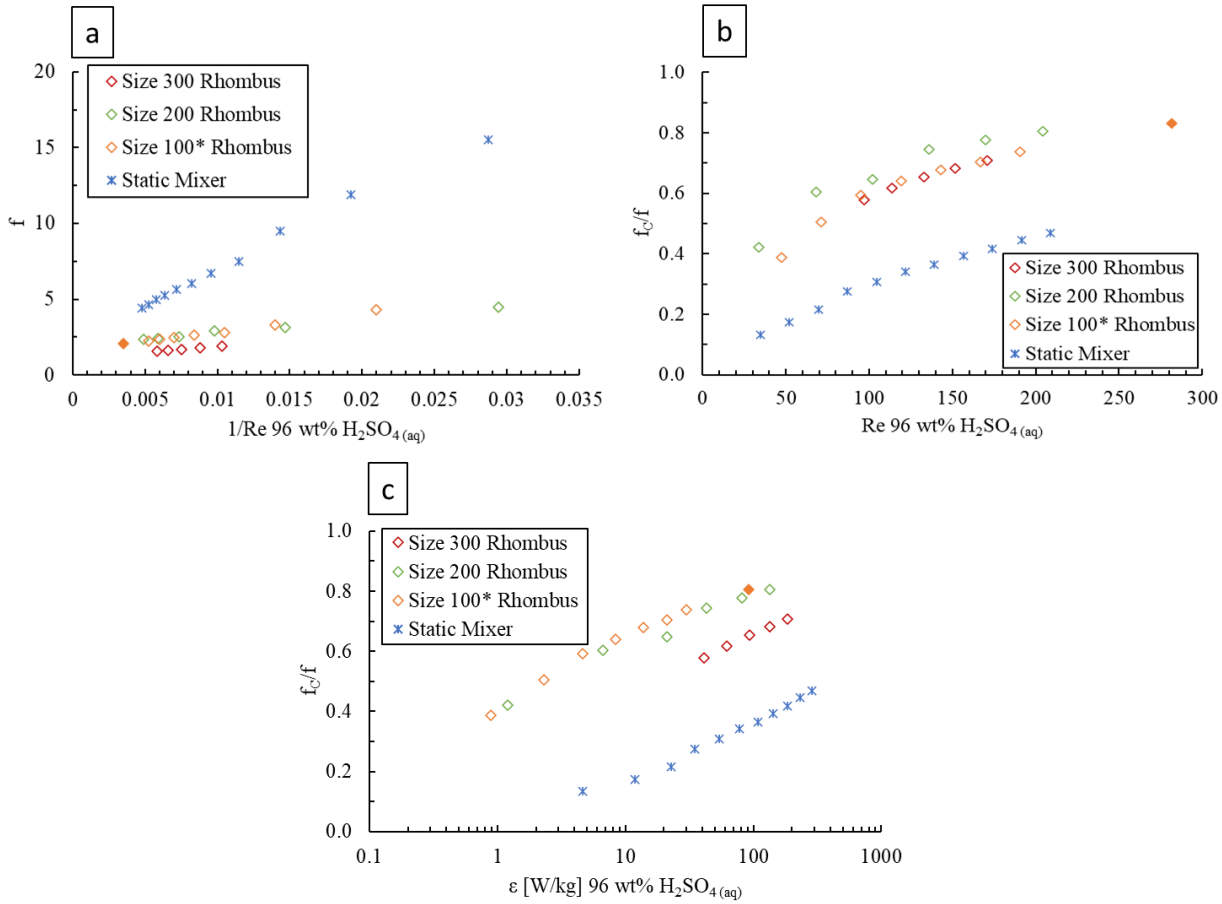

Figure 4.12. Friction factor analysis for the static mixer geometry with 96 wt% $H_2SO_{4\,(aq)}$ as compared with the size 300, 200, and 100* Rhombus. (a) Overall friction factors from equations (4.12) and (4.13). (b) Relative contributions of chaotic flow as a function of Re. (c) Relative contributions of chaotic flow as a function of mean energy dissipation rate. Filled data points are extrapolated to $\boldsymbol{\epsilon}$ = 91.8 W/kg.

4.7 **Conclusions**

In this chapter, the 3/7th rule commonly applied to fully turbulent flow was expanded into flow regimes that are largely (but not fully) turbulent or transitional. Scale-up rules were derived for two fluid systems, namely water and 97 wt% $H_2SO_{4\,(aq)}$, in order to determine the required flowrates to maintain mean energy dissipation rates in larger scale LL plate microreactors. In both systems, average energy dissipation rates were conserved or exceeded the values predicted by the

derived scale-up rules for all larger-scale plates. Analysis of friction factors was then performed in order to determine the relative contributions of chaotic advection to the overall flow patterns in each fluid/reactor pairing. Here, the relative levels of turbulence exceeded those achieved at equivalent mean energy dissipation rates at lab scale due to the increase of Re required to match mean energy dissipation rates in the larger diameter channels. This effect was more pronounced in the 96 wt% $H_2SO_{4\,(aq)}$ system as the present data was centered in transitional flow regime (f_C/f ranging from ~0.4 to 0.8), whereas much of the acquired data with water was largely dominated by chaotic flow patterns and plateaued at f_C/f values of about 0.8. With respect to the nitration reaction, extrapolated data points with 96 wt% $H_2SO_{4\,(aq)}$ suggest that all plates will achieve greater energy dissipation rates and contributions of chaotic advection than those obtained at 76 mL/min at lab-scale when subject to increased flowrates determined by the derived scale-up rules. A cheaper static mixer geometry was also tested but was found to not generate enough secondary flows at the production flowrate despite having a sufficient energy dissipation rate. Thus, global micromixing performance measures were conserved or improved upon scale-up with the use of the LL-microreactor plates, but further studies are required in order to achieve a full scale-up of the reaction system with respect to local energy dissipation rates and macromixing.

Nomenclature

Symbol	Meaning	Units
a	Fitting parameter for pressure drop modelling	--
C_1, C_2	Coefficients in pressure drop model	--
$\mathcal{D}$	Diffusivity	m^2/s
d_h	Hydraulic diameter	m^2
f	Overall friction factor	m
f_C	Chaotic friction factor	--
f_L	Laminar friction factor	--
L	Channel length	m
n	Fitting parameter for pressure drop modelling	--
N	Number of repeating mixing units	--
P	Pressure	Pa
Q	Volumetric flow rate	mL/min
Re	Reynolds number	--
t_D	Mixing time via diffusion	s
t_E	Mixing time via engulfment	s
u	Velocity	m/s
V_R	Reactor volume	m^3
w	Channel width	m

Greek Symbols

Symbol	Meaning	Units
δ	Channel depth	m
ϵ	Mean energy dissipation rate	W/kg
μ	Dynamic viscosity	Pa s
ν	Kinematic viscosity	m^2/s
ρ	Density	kg/m^3

5. Handling of Solids and Flow Characterization in a Baffle-Less Oscillatory Flow Coil Reactor

Brendon J. Doyle[a], Bernhard Gutmann[b], Michael Bittel[b], Thierry Hubler[b], Arturo Macchi[*,a], and Dominique M. Roberge[*,b].

[a]Centre for Catalysis Research and Innovation, Department of Chemical and Biological Engineering, University of Ottawa, K1N 6N5, Ottawa, Canada

[b]Chemical Manufacturing Technologies, Lonza AG, CH-3930, Visp, Switzerland

This manuscript has been published: Brendon J. Doyle, Bernhard Gutmann, Michael Bittel, Thierry Hubler, Arturo Macchi, and Dominique M. Roberge. Handling of Solids and Flow Characterization in a Baffle-Less Oscillatory Flow Coil Reactor. Industrial & Engineering Chemistry Research. 2020 *59* (9), 4007-4019.

Abstract

The solid handling ability and flow patterns of a baffle-less oscillatory flow coil reactor are investigated and characterized. Previous works in oscillatory flow have been generally conducted in straight channels with various baffled geometries. Solid handling capabilities of the reactor are examined through two reactions, namely a precipitation reaction and a phase transfer catalysis reaction. In the first reaction, the reactor geometry proved capable of continuously handling liquid-solid suspensions of 5.8 wt% for 5 hours and up to 7.9% for 2 hours. No signs of clogging were observed during these tests and the maximum run time of the reactor is currently unknown. However, when gas was formed in the second reaction, rapid system clogging is observed due to a ten-fold decrease in the energy dissipation rate as a result of the pulsation dampening effect by the gas. A broadening of residence time distributions with oscillation intensity is observed and,

accordingly, is accompanied by a broadening of solid product particle size distributions. Lower pulsation amplitude and frequencies were capable of keeping solids suspended in the precipitation reaction and may therefore be employed to achieve tighter residence time and particle size distributions.

5.1 **Introduction**

Pharmaceutical processes often involve a solid component as either a reagent, catalyst, or product. Continuous processing of these solid components presents a challenging obstacle as it renders systems vulnerable to fouling and clogging. As a result, unit operations that require the handling of solid components are often performed in sufficiently large batch vessels that are less likely to plug. However, from a process intensification standpoint, it is desirable to miniaturize and develop other processing techniques that can improve heat and mass transfer while maintaining or improving product quality and uniformity. In the pharmaceutical and fine chemical industries, intensification via miniaturization generally requires a shift from batch to continuous processing technology. Micro- and milli-scale reactors present a promising technology for continuous intensification at the lower production volumes required for pharmaceutical and fine chemical industries. Reducing the characteristic lengths of processing equipment into these smaller length scales provides significant improvements to heat and mass transfer through increasing the reactor surface area-to-volume ratio and reducing transport distances [111,142,143]. Selection of the optimal small-scale reactor technology in these applications, however, is non-trivial and requires a thorough understanding of the reaction kinetics, flow patterns, and phases. A toolbox approach was developed by Plouffe *et al.*[8] in order to facilitate reactor selection based on these parameters, but remains underdeveloped for micro and milli scale reactors where solids are present due to their inevitable amplification of the difficulties in solid handling. Furthermore, a review by Roberge *et al.* of 86 reactions carried out at Lonza reported that ca. 2/3 of the reactions studied involved a solid phase, effectively limiting the extended use of microreactors [3]. A miniaturized, intensified processing unit that can continuously handle solids without clogging or losing performance would be highly valuable to the pharmaceutical and fine chemical industries.

In order to prevent clogging of a channel by solid particles, it is generally required that a relatively high degree of mixing be implemented in the reaction system. Mixing can be achieved through active or passive methods; the active methods require an energy input from an external source, and passive methods take advantage of the energy from a pump by inducing mixing through changes in channel geometry [144]. Implementation of active mixing technologies leads to decoupling of the mixing energy from the flow rate, allowing for enhanced transport properties over a wide range of residence times. This is particularly beneficial when moving a batch reaction requiring longer residence times into continuous flow in which passive mixing alone would necessitate a high flow rate and/or large reactor length in order to achieve near plug flow that may inhibit its feasibility, e.g., elevated pressure loss [45]. One such active method for enhancing mixing is through imposing an oscillation on the reaction medium. This is usually implemented by pulsing the reaction medium itself or by oscillating baffles within the flow channel [145]. In general, these oscillatory flow reactors often utilize mixing elements such central baffles [146], single orifice baffles [52], multi-orifice plate baffles [52], helical baffles [147,148], and smooth periodic constrictions [52,57,58,149–151]. These geometries can provide near plug flow under net laminar flow conditions [152], with ratios of oscillatory to net flow Reynolds numbers (Re_o/Re_n) as high as 250 depending on the intensity of mixing induced by each geometry [51]. These reactors have also proven capable of handling solid suspensions, especially in crystallization applications [53,54,153,154]. Other intensified technologies that been developed for continuous solid handling include miniaturized CSTR cascades [75,155], an agitated cell reactor [156], plug flow reactors with static mixer inserts [157], an autoclave reactor with intermittent sampling [36], multiphase segmented flow [158–161], mixed-suspension-mixed-product-removal (MSMPR) [74,162], and a coiled flow inverter for crystallization [61,163,164].

In this experimental program, a metallic coil that is often used as a cost-effective continuous reactor at high pressure and temperature to gain residence time [8,165] is used in oscillatory-flow to run solid-liquid reactions. As such, active mixing is used in combination with passive mixing resulting from Dean secondary flows in a coiled baffle-less channel in order to lower the risk of dead zones and clogging. We considered an inner diameter of 4.6 mm (milli-reactor) as acceptable to manage solids leading to a geometry that still enables an order of magnitude increase in heat transfer rate when compared to batch. A lack of product preferentially cumulating in the dead zones of a reactor allows for uniform cleaning, which is essential for GMP applications. The oscillatory flow applied in this system often results in Reynolds numbers corresponding to turbulent mixing when compounded with the coiled geometry [56]. The higher intensity of oscillatory energy input, along with the use of elevated pressure, render this system more applicable to intensification of reactions and maintaining flow of solid suspensions under turbulent flow oscillatory conditions. The solid handling ability of the baffle-less coil geometry is tested with two reactions: the first is a room temperature precipitation reaction run at moderate pressure, and the second is an intensified liquid-liquid-solid phase transfer catalysis reaction run at elevated temperature and pressure. Finally, the effect of pulsation on macromixing within the reactor is characterized.

5.2 **Materials and Methods**

5.2.1 Reaction Apparatus

The schematic for the feed side of the flow reaction system pertaining to both reactions (Scheme 5.1 and Scheme 5.2, detailed below) is shown in Figure 5.1. Key components and differences in the apparatus for each reaction are identified and tabulated in Table 5.1. In both reactions, feeds 1 and 2 were pumped through Coriolis flow meters (Endress and Hauser Proline

Promass 80A) followed by one-way valves implemented to prevent back flow of feeds and solid particles. For the reaction in Scheme 5.2, an A7 size 600 LL-Triangle plate-type microreactor [111] was included downstream of the one-way valves in order to pre-mix the immiscible liquid feeds. For the reaction in Scheme 5.1, the miscible liquid feeds were mixed in a T-junction directly upstream of the pulsator. Pulsation was provided to the system by a LEWA LDB1 pulsator pump. The pulsator has a 14 mm head diameter and a maximum pressure tolerance of 80 barg. The amplitude and frequency of the pulsating flow in the coil can be adjusted manually from 0-70.4 mm and 0-4.09 Hz, respectively. The reactor itself is a coiled tube constructed by winding Hastelloy tubing around a hard cylinder, with a large enough radius of curvature to avoid indentation. It has a 6 m length, a 4.57 mm internal diameter, a 35 mm radius of curvature, and a pitch close to 0 mm. The reaction in Scheme 5.1 was run at ambient temperature (22.4°C) and showed slight temperature increases, up to a maximum 25 °C at the outlet. For Scheme 5.2, the coil reactor was heated by circulating silicon oil at 80°C through the coil jacket. Downstream of the reactor, 2 barg of back pressure was applied to the system via a N_2 line to prevent cavitation during flow reversal. The suspension was sent to a cascade of sampling containers that allows intermittent pressure decrease for the flow outlet at elevated pressure followed by depressurization in a cyclone. This sampling system was adapted from the work of White *et al*. at Eli Lilly (see Figure 1 in [36]). The pressure was monitored at various points throughout the system with WIKA-M11 pressure sensors in order to detect clogging as observed by a rapid increase in pressure caused by a restriction in flow.

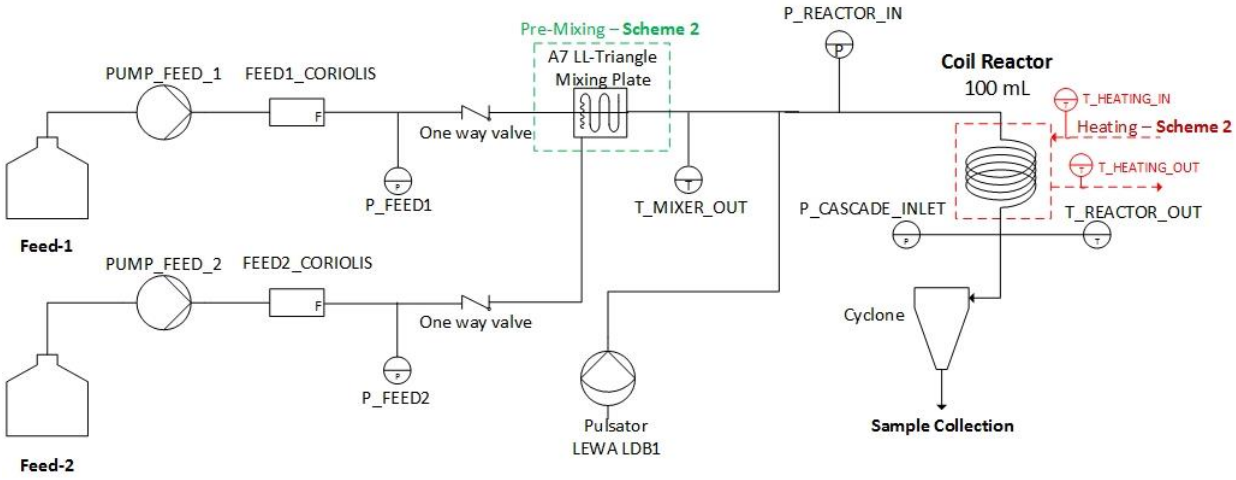

Figure 5.1. Reaction apparatus for the two solid forming reactions. Pre-mixing and reactor heating are included for the reaction in Scheme 5.2 but are omitted for the reaction in Scheme 5.1.

Table 5.1. Identification and description of different components in the apparatuses for Scheme 5.1 and Scheme 5.2.

Reaction	Component ID	Description
Scheme 5.1	Feed-1	Glyoxal in EtOH
	Feed-2	Cyclohexane in EtOH
	PUMP_FEED_1	Hitec Zang Syrdos
	PUMP_FEED_2	Hitec Zang Syrdos
	Pre-Mixing	T-Junction
	External Heating	None
Scheme 5.2	Feed-1	$NaOH_{(aq)}$
	Feed-2	Cyclohexene and Et_2MeN in $CHCl_3$
	PUMP_FEED_1	HNP mzr-7255 micro annular gear pump
	PUMP_FEED_2	Hitec Zang Syrdos
	Pre-Mixing	FlowPlate® A7 LL Triangle Plate Microreactor
	External Heating	80°C Silicon Oil

5.2.2 Solid Handling Characterization

In the first reaction, two moles of cyclohexylamine (CHA) are reacted in ethanol with one mole of glyoxal to form N,N'-(1E,2E)-Ethane-1,2-diylidenedicyclohexanamine (EDDC) and water (Scheme 5.1). This reaction has been employed previously as a model for investigating solid handling of continuous reactors [75,166]. EDDC forms rod-like particles [75] and is only slightly soluble in ethanol.

Scheme 5.1. EDDC Forming Reaction.

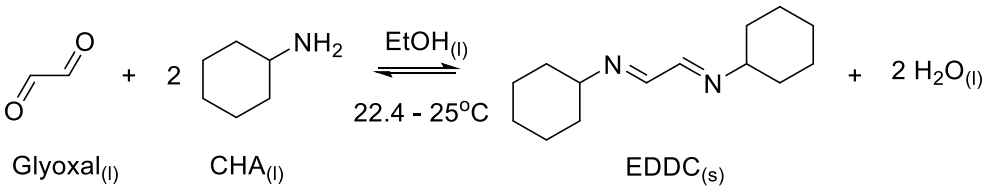

The reaction was first characterized in batch through product solubility testing and *in-situ* reaction H-NMR analysis. Batch products were collected by filtration and dried overnight under vacuum. EDDC solubility in ethanol was determined from 20°C to 35°C by creating a saturated solution with the dried solids and determining the mass dissolved in the liquid phase by filtration under vacuum and evaporation in a rotary evaporator. For the H-NMR, 800 µL each of 0.34M glyoxal and 0.68M CHA in deuterated ethanol (Ethanol-D6) were mixed in an NMR tube and CHA concentration was measured over the course of 100 minutes of reaction time with a Bruker Topspin 400 MHz NMR spectrometer.

For the flow reactions, the concentrations of feeds 1 and 2 were varied between 0.4 – 1.6 M glyoxal and 0.8 – 3.2 M CHA, respectively (1:2 molar ratio), and fed at 2 mL/min each (4 mL/min net flow, or Q_{net}) in order to investigate the reactors propensity for blockage. The amplitude and frequency of the pulsating flow in the coil were set each to either 0 or 46.9 mm and 3.68 Hz for

characterizing the solid handling capabilities of the reactor. Additional tests were performed in which either the amplitude or frequency were decreased step wise down to zero from 46.9 mm to 37.5, 28.2, and 18.8 mm for the amplitude and 3.68 Hz to 2.45, 1.64, and 0.84 Hz for the frequency. The maximum oscillatory velocity was 0.4 – 1.09 m/s, which is 61 to 266 times greater than the net flow velocity, leading to an asymmetrical oscillatory type pulsatile-flow in which the flow velocity vector becomes negative periodically during an oscillation cycle [56,167]. Reaction yields were measured by collecting and drying the solids overnight under vacuum and accounting for the weight % in solution. The reaction conditions for Scheme 5.1 in flow are summarized in Table 5.2.

5.2.3 Mixing Dependent Phast Transfer Catalytic Reaction

In the second studied reaction, dichlorocarbene (DCC) is produced from chloroform followed by its reaction with cyclohexene (CHE) (Scheme 5.2). DCC is a reactive intermediate in organic synthesis that can be used to generate a wide range of substrates and can be generated via deprotonation of chloroform with a concentrated $NaOH_{(aq)}$ solution [168]. Deprotonation of $CHCl_3$ occurs in the interfacial region of the reaction mixture, and the subsequent reaction of the produced DCC with CHE requires migration of DCC back into the bulk organic phase. Phase transfer catalysis (PTC) is a method often employed in organic synthesis for reactions involving reagents separated in immiscible phases, whereby a phase transfer agent is employed to transfer a reagent from one phase to the other (in this case to transfer DCC back into the organic phase) in order to react with another reagent [169,170]. Both the formation of DCC and its subsequent reaction with CHE are therefore dependent on the rates of interphase mass transfer out of and back into the bulk organic phase. The biphasic reaction system consists of a 35 wt% (12.51 M) NaOH aqueous phase fed at 7 mL/min and an organic chloroform phase fed at 14 mL/min containing 0.50 M CHE and 1.17 M diethylmethylamine (Et_2MeN) as a phase transfer agent (mole ratio 1:20.1:2.4:12.5

CHE:$CHCl_3$:Et_2MeN:NaOH). Chloroform acts as both a solvent and reagent, and deprotonation of chloroform by NaOH at the interface produces DCC, NaCl, and H_2O. The DCC can then form a complex with the Et_2MeN that migrates into the organic phase, where it is released and reacts with the cyclohexene ring to produce 7-7,dichlorobicyclo[4.1.0]heptane [168].

Scheme 5.2. DCC intermediate-forming reaction and subsequent addition to CHE.

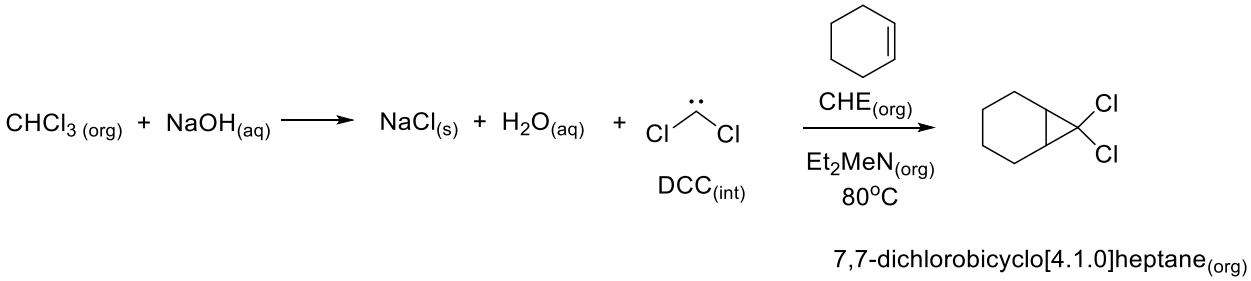

This reaction has been performed successfully with 97% CHE conversion and 99% selectivity using 35 wt% NaOH in a miniaturized packed bed reactor containing Teflon beads, but was subject to clogging when (1) the NaOH concentration was increased to 40 wt%, (2) other packing material was used, or (3) the temperature was increased to 90°C [68]. The coil reactor was therefore employed in this reaction under similar conditions in order to increase throughput and achieve greater rates of heat exchange. Ultimately, with the goal being to subsequently intensify the reaction by widening the operating conditions window and potentially increasing the NaOH concentration in a geometry that is less prone to clogging at higher $NaCl_{(s)}$ concentrations. This reaction provides a complementary study to previous work on interphase mass transfer in a larger oscillated baffle-less coil [56] with the addition of phase transfer catalysis and the requirement that the reactor be able to handle a solid-liquid-liquid mixture without clogging. Reaction conditions in flow for Scheme 5.2 are shown in Table 5.2. The pulsation amplitude and frequency were set to 70.4 mm and 3.68 Hz. The reaction was run at 80°C wth a 4.5 minute space time.

Table 5.2. Reaction conditions for Scheme 5.1 and Scheme 5.2.

Reaction	Operating Parameter	Value	Units
EDDC	$C_{CHA\ (reaction)}$	0.4 - 1.6	mol/L
	$C_{Glyoxal\ (reaction)}$	0.2 - 0.8	mol/L
	f	0, 0.82, 1.64, 2.45, 3.68	Hz
	x_{coil}	0, 18.8, 28.2, 37.5, 46.9	mm
	Q_{net}	4	mL/min
	t_R	30	min
	T (inlet - outlet)	22.4 - 25	°C
DCC	$C_{NaOH,\ (feed-1)}$	12.51	mol/L
	$C_{CHE,\ (feed-2)}$	0.50	mol//L
	$C_{Et2MeN,\ (feed-2)}$	1.17	mol/L
	f	3.68	Hz
	x_{coil}	70.4	mm
	Q_{feed-1}	7	mL/min
	Q_{feed-2}	14	mL/min
	t_R	4.5	min
	T	80	°C

5.2.4 Flow Characterization

Residence time distributions were measured at various pulsation frequencies via step change tracer experiments in order to characterize the effect of pulsation frequency on the flow patterns in the reactor. The reactor system in Figure 5.1 for Scheme 5.1 was filled with pure ethanol at a flow rate of 4 mL/min followed by a feed change to the tracer solution composed of 0.8M CHA in ethanol. The tested pulsation frequencies were 0 Hz, 0.82 Hz, 1.84 Hz, and 3.68 Hz with a constant amplitude of 46.9 mm. All non-zero pulsation frequencies again produced significantly large maximum oscillation velocities that resulted in asymmetrical pulsatile flow. Samples were taken at the outlet every 2.5 minutes over a period of 2.5 space times and analyzed for CHA concentration via gas chromatography (Agilent 6850) with anisole as an internal standard. An additional experiment at 40 mL/min was performed with 3.68 Hz pulsation and 0.5 min sampling time. After fitting the data to a dimensionless time (θ) exit-age distribution curve, ($E(\theta)$), or E-curve, the first and second moments of the residence time distribution, which represent the mean residence time (θ_m) and the variance (σ_θ^2), were then calculated according to equations (5.1) and (5.2).

$$\theta_m = \int_0^\infty \theta E(\theta) d\theta \quad \textbf{(5.1)}$$

$$\sigma_\theta^2 = \int_0^\infty (\theta - \theta_m)^2 E(\theta) d\theta \quad \textbf{(5.2)}$$

The flow in an oscillatory system can also be characterized with the net Reynolds number (Re_n) and oscillatory Reynolds number (Re_o) [171] according to equations (5.3) and (5.4), respectively, where ρ is the fluid density, u_n is the net fluid velocity, u_o is the oscillatory velocity, d_{tube} is the inner tube diameter, and μ is the fluid dynamic viscosity.

$$Re_n = \frac{\rho u_n d_{tube}}{\mu} \quad \textbf{(5.3)}$$

$$Re_o = \frac{\rho u_o d_{tube}}{\mu} \quad \textbf{(5.4)}$$

The oscillatory velocity, u_o, is calculated from the centre-to-peak pulsation amplitude in the coil, x_{coil}, and the angular frequency, ω, the time in the pulsation period, t, and the frequency, f, of pulsation using equations (5.5) and (5.6).

$$u_o = x_{coil}\omega \sin(\omega t) \quad \textbf{(5.5)}$$

$$\omega = 2\pi f \quad \textbf{(5.6)}$$

Because the oscillatory velocity varies constantly throughout the period of oscillation, a single value is taken when the sinusoidal component is equal to one and the oscillatory velocity is at its maximum [172]:

$$u_{o,max} = x_{coil}\omega \quad \textbf{(5.7)}$$

The relative contributions to the flow pattern of the net and oscillatory flows can then be compared using the magnitudes of their respective Reynolds numbers.

5.2.5 Particle Size Distribution and Morphology

Particle size distributions and particle morphologies of the EDDC forming reaction were measured as a function of pulsation frequency. 0.4 M glyoxal and 0.8 M CHA were fed to the reactor set up shown in Figure 5.1 at 4 mL/min. The reaction proceeded for 3 space times at each pulsation frequency before solids were collected for analysis by laser diffraction in a Malvern Mastersizer 2000 particle size analyzer and an Olympus BX53M optical microscope. During the residence time experiments, it was found that a period of 3 residence times was sufficient for the tracer concentration to stabilize, and the particle size samples were therefore taken when the reactor had reached steady state. For the microscopic imaging, the particles were re-suspended in ethanol to minimize changes to their morphology. Pulsation frequency was tested at 0.82, 1.84,

and 3.68 Hz. Results were compared to those obtained from a batch reaction having the same residence time and reagent concentrations carried out in a 100 mL flask with 600 rpm magnetic stirring.

5.3 Results and Discussion

5.3.1 EDDC Reaction Characterization

The solubility of EDDC was measured in ethanol and found to be strongly dependent on the system temperature (Figure 5.2). The solubility of EDDC is about 0.01g/gEtOH at 20°C. Greater temperatures result in greater solubility with a rapid increase in solubility occurring above 30°C. The operating temperature of the system ranged from about 22.4°C at the inlet to 25°C at the outlet due to the heat of reaction, and the product solubility was therefore taken to be about 0.011 g/gEtOH, or 1.1 wt%.

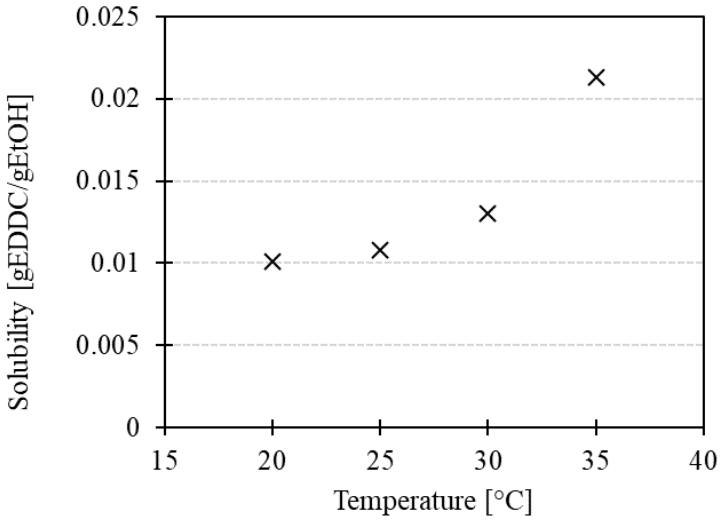

Figure 5.2. EDDC solubility as a function of temperature.

In-situ H-NMR analysis was performed in order to elucidate the rates of reagent conversion and product generation in a pre-mixed batch system. After mixing, CHA showed an immediate and rapid decrease, whereas EDDC appeared more gradually (Figure 5.3). This suggests that the

reaction proceeds through at least one intermediate before forming the final product. The concentration of EDDC in the undisturbed NMR vial exceeds the solubility into supersaturation. The asymptotic rate of CHA conversion corresponds to a 2nd order reaction with respect to the CHA concentration, where longer residence times are required to reach high conversion. A 44% yield of EDDC is seen after an equivalent coil space time of 30 minutes. The overall yield ($\tilde{Y}$) is defined on a basis of 100% CHA conversion according to equation (5.8) below, where the moles of EDDC (N) are adjusted to account for the reaction stoichiometry.

$$\tilde{Y} = \frac{2N_{EDDC}}{N_{CHA,0}}(100\%) \quad \textbf{(5.8)}$$

After 100 minutes, the EDDC yield had plateaued at about 55%, and 94% of the CHA had been consumed. This indicates side-product formation during the reaction which is confirmed by examining the H-NMR spectra at the beginning and end of the reaction shown in Figure 5.4. After 100 minutes, several peaks are observed that cannot be attributed to either CHA or EDDC. Glyoxal is not detected by H-NMR. Based on the results outlined in this section, a 30-minute residence time in flow was selected and quantitative solid yields were not expected due to the solubility of the product and lower than expected selectivity of the reaction under supersaturated batch conditions.

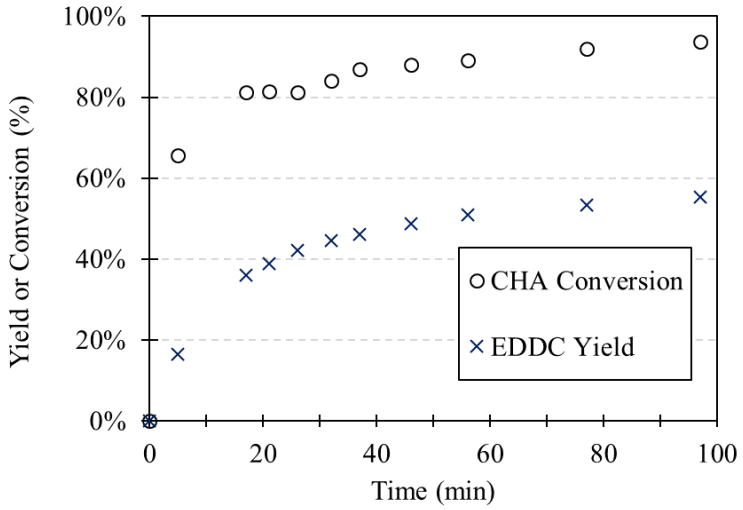

Figure 5.3. *In-situ* H-NMR analysis of EDDC-forming reaction with 0.17 M glyoxal and 0.34 M CHA.

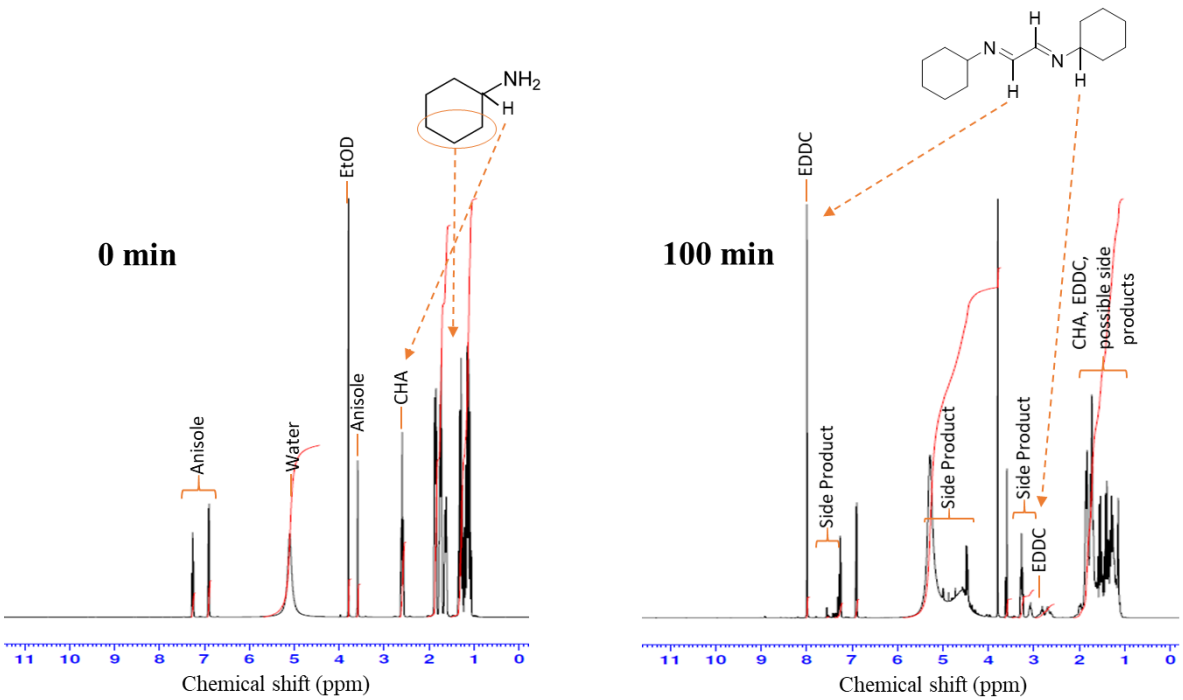

Figure 5.4. H-NMR analysis of EDDC-forming reaction showing side-product formation.

5.3.2 Effect of Pulsation on Solid Handling

In order to determine the effect of pulsation on solid handling in the coil, the EDDC forming reaction was first run without pulsation in order to investigate the reactor's propensity for blockage. After 55 minutes of reaction time (1.83 nominal space times) with a glyoxal concentration at 0.4 M (or ca. 3.7 wt% EDDC solids), the system showed rapid increases in the feed 2 pressure indicating that clogs were forming and dislodging. Instantaneous addition of a 46.9 mm, 3.68 Hz pulse in the coil at t=65 min resulted in immediate declogging and a return back to normal operating pressure (Figure 5.5). Subsequent instantaneous removal of the pulsation at t=85 min resulted in the formation of another clog starting at 100 minutes. Attempts to remove this clog at t=120 minutes with a gradual increase in pulsation frequency were unsuccessful, and it was found that a step change with sufficient force is required in order to dissociate blockages. After determining the reactor would clog on its own without pulsation, the reaction was then run with continuous 46.9 mm, 3.68 Hz pulsation for 120 minutes with glyoxal concentrations (and their corresponding stoichiometric CHA concentrations) of 0.2, 0.4, and 0.8 M. These runs resulted in experimental mean solid concentrations (taken in triplicate with one standard deviation reported) of 1.3 ± 0.1 wt%, 3.0 ± 0.2 wt%, and 7.9 ± 0.4 wt%, corresponding to isolated yields of 39 ± 3.9%, 39 ± 0.4%, and 48 ± 5.5%, respectively (solubility of EDDC in ethanol at 25°C is 1.1 wt%). In each case the reactor operated stably with no pressure spikes at any point in the system. It is therefore likely that this reactor geometry is capable of handling higher concentration solid suspensions without plugging, and it may also be possible to further intensify the geometry by decreasing the diameter and operating with the solid concentrations reported above.

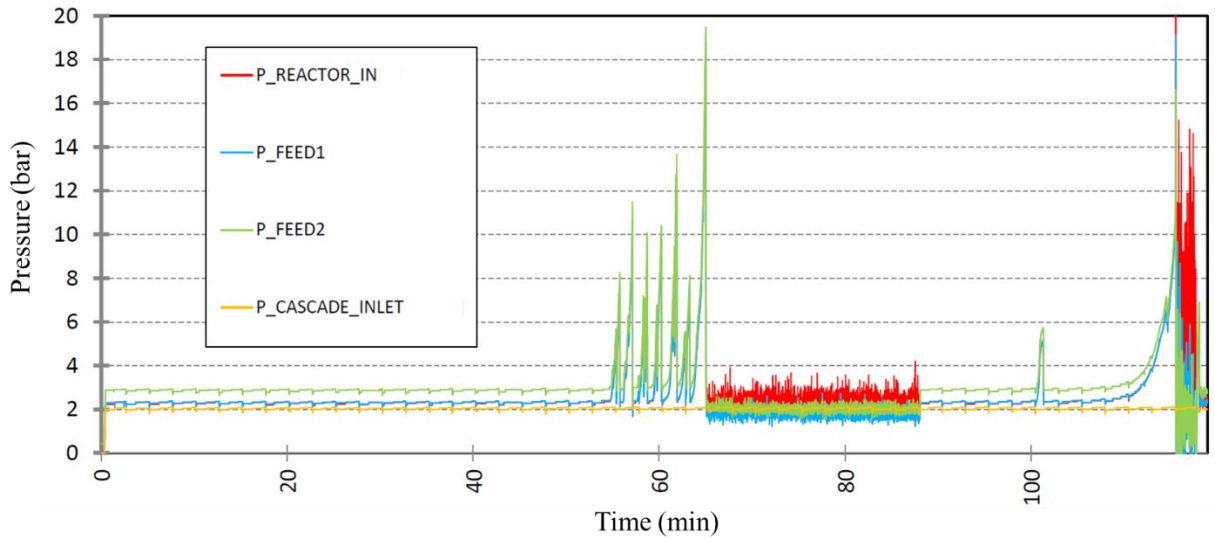

Figure 5.5. Clog formation without pulsation with 3.7 wt% solids. [Glyoxal] = 0.4 M; [CHA] = 0.8 M; space time = 30 min.

A long run with 3.68 Hz and 46.9 mm oscillation was then tested with 0.6 M glyoxal and 1.2 M CHA resulting in a solid concentration of 5.8 wt%. In this case, the system was capable of stable operation for 5 hours without any observable signs of blockage, at which point the experiment was then stopped deliberately (Figure 5.6). The maximum runtime of the reactor is therefore currently unknown. While the reactor inlet is the location where the pulsation energy is introduced, pressure oscillations are also observed in the feed lines downstream of the one-way check valves as a result of transmitted pressure waves. This is further observed by a lowering of the feed inlet pressures compared to the reactor inlet due to the aspiration of the pulsator pump. At the outlet of the reactor, represented by the cascade inlet pressure, the pressure oscillations are absent due to a dampening effect of gas present in the outlet of the system.

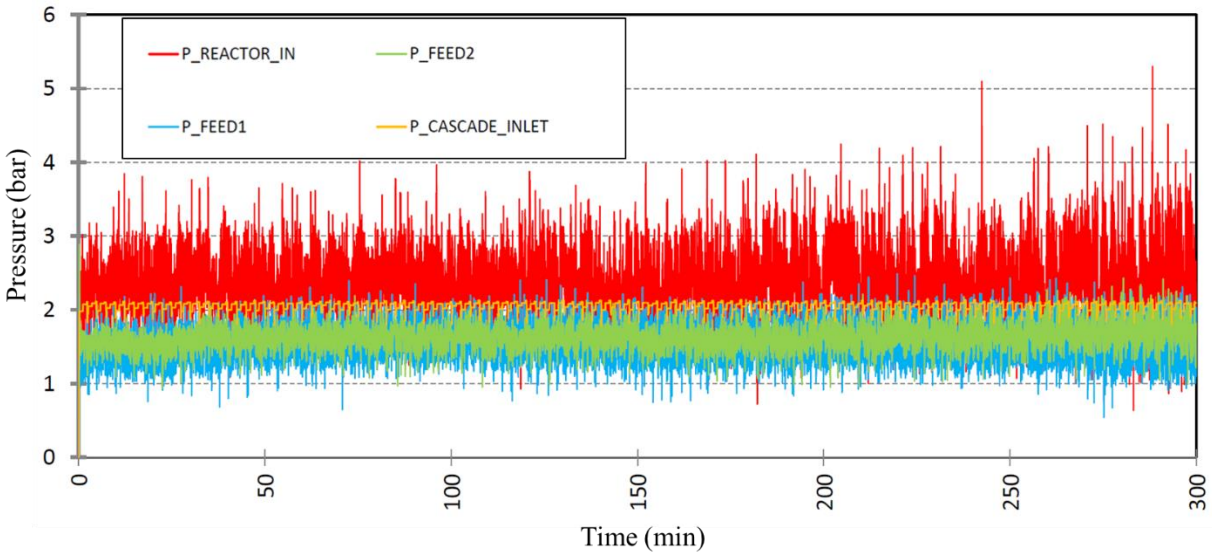

Figure 5.6. Stable operation for 5 hours with 5.8 wt% solids. [Glyoxal] = 0.6 M; [CHA] = 1.2 M; space time = 30 min. High intensity pulsation allows the system to operate in the turbulent flow regime, leading to higher pressure oscillations and continuous flow of solid suspensions.

In an oscillatory flow system, the average energy dissipation rate ($\bar{\epsilon}$) can be calculated from the net flow and oscillatory flow components ($\bar{\epsilon}_{net}$ and $\bar{\epsilon}_o$) according to equations (5.9) and (5.10), where the velocity and pressure were assumed to be in phase with a phase angle, δ, of 0 [173]. Here, V_R is the reactor volume, ΔP_{net} is the pressure drop due to the net flow, ΔP_o is the magnitude of the pressure oscillations, ρ_c is the density of the continuous phase, and Z is the length of the reactor.

$$\bar{\epsilon} = \bar{\epsilon}_{net} + \bar{\epsilon}_o \quad \textbf{(5.9)}$$

$$\bar{\epsilon} = \frac{\Delta P_{net} Q_{net}}{\rho_c V_R} + \frac{1}{2}\frac{\Delta P_o cos(\delta) x_{coil} \omega}{Z \rho_c} \quad \textbf{(5.10)}$$

Pressure fluctuations of about +/- 1.2 bar at the reactor inlet, corresponding to ΔP_o in equation (5.10), are observed as a result of the oscillations in flow velocity. Estimation of the energy dissipation rate using the reactor inlet pressure (P_REACTOR_IN) oscillations gives a

value of 13 W/kg. This is an order of magnitude higher than a previous work in continuous crystallization utilizing an oscillatory baffled reactor [174] which suggests that lower oscillatory frequencies and amplitudes may be sufficient for keeping solids suspended.

The effect of decreasing the amplitude and frequency on the reactor operation was thus tested with 7.9 wt% solids produced from reacting 0.8 M glyoxal and 1.6 M CHA (Figure 5.7). In these tests, the oscillation was initially set to 3.68 Hz and 46.9 mm for 70 minutes followed by step changes down to no pulsation in the either the amplitude (Figure 5.7, left) or frequency (Figure 5.7, right). The amplitude was decreased from 46.9 mm to 37.5 mm, 26.2 mm, 18.8 mm, and 0 mm from t=70min to t=125 min. The frequencies were decreased from 3.68 Hz to 2.45 Hz, 1.64 Hz, 0.82 Hz, and 0 Hz from t=70 min to t=110 min. In both cases, no clogging was observed until the oscillation was completely removed, at which point the system blocked rapidly at t=125 min for the amplitude decrease and t=110 min for the frequency decrease. Note that the impact of the pulsating pump aspiration is well observed in Figure 5.7 where lower pulsation power leads to greater pressure of feed lines 1 and 2.

This result suggests that the system may be capable of suspending solids over a wide range of oscillation intensities. In such single-phase reactions where the homogenous feeds require shorter mixing times followed by longer residence times to accommodate the reaction kinetics, this reactor geometry may be best applied as a “mix then reside” reactor where the oscillation intensity can potentially be lowered as it is only required for the purpose of keeping the solids suspended in solution. However, further characterization of the effects of pulsation intensity and solid concentration on the maximum run time of the reactor remains to be determined.

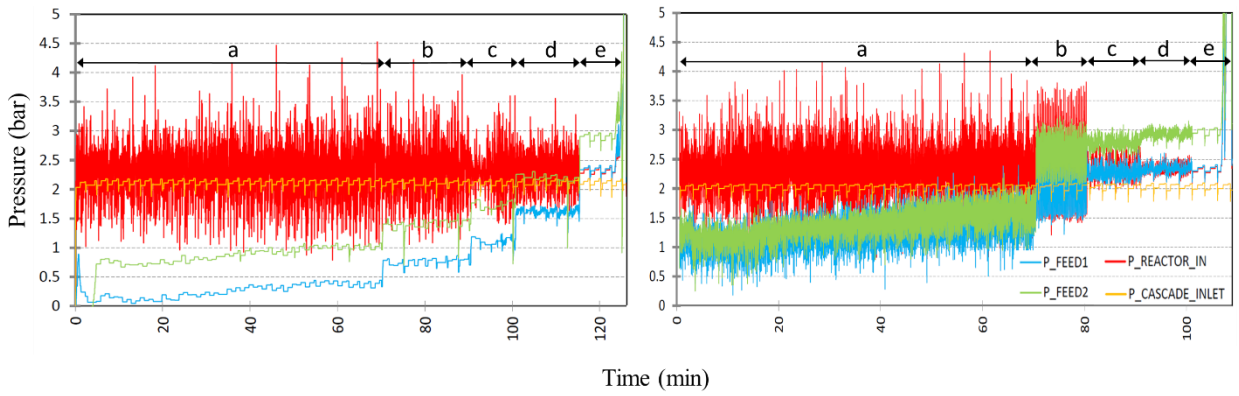

Figure 5.7. Pressure profiles during the tests showing a decrease in amplitude (left) and frequency (right) with 7.9 wt% solids, leading to rapid clog formation when pulsation is stopped. [Glyoxal] = 0.8 M; [CHA] = 1.6 M; space time = 30 min. Left figure: amplitudes, a = 46.9 mm; b = 37.5 mm; c = 28.2 mm; d = 18.8 mm; e = 0 mm with clog formation. Right figure: frequencies, a = 3.68 Hz, b = 2.45 Hz, c = 1.64 Hz, d = 0.82 Hz, e = 0 Hz with clog formation.

5.3.3 Effect of Gas Formation on Pulsation

As the reactor proved successful in continuously handling solid suspensions, a second reaction was then tested consisting of a liquid-liquid-solid system at intensified temperature and pressure. However, the reaction in Scheme 5.2 could not be run for longer than 20 minutes without signs of clogging (Figure 5.8) at the maximum energy dissipation rate. The reaction is highly dependent on the effectiveness of the interphase mass transfer and requires a constant power input throughout the reactive volume, i.e. as a "mix and reside" type system. Previous work has shown that the oscillatory flow coil reactor has similar liquid-liquid interphase mass transfer performance to a plate-type microreactor when the energy dissipation rate is around 20 W/kg [56] and the flow is in the drop flow regime [45]. It was therefore desirable to reach a similar or greater energy dissipation rate in this system in order to disperse the organic phase and enhance the rates of DCC formation and PTC. However, over the course of the reaction it was observed that the oscillations in the reactor pressure were dampened and eventually disappeared. Once DCC is formed, it can

undergo one of three reactions: 1) the PTC reaction shown in Scheme 5.2 to produce the desired product, 2) reaction with additional NaOH to form $CO_{(g)}$, $NaCl_{(s)}$, and $H_2O_{(aq)}$ (Scheme 5.3), and 3) reaction with itself to form an insoluble dark-coloured CCl_2 polymer chain (Scheme 5.4). Scheme 5.3 and 5.4 occur when DCC accumulates at the interface, and it is important to note that this can result from a reduced rate of DCC sequestration via PTC or from an excess of chloroform, as is the case here where it acts as both a solvent and reagent. This becomes increasingly likely as CHE is consumed and there is less reagent available to quench the DCC intermediate and produce the desired product.

Scheme 5.3. Mechanism of gas formation due to insufficient interphase mixing or excess $CHCl_3$ for Scheme 5.2.

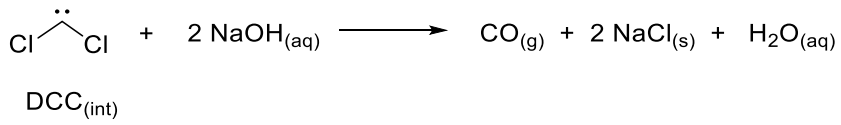

Scheme 5.4. Polymerization of excess DCC

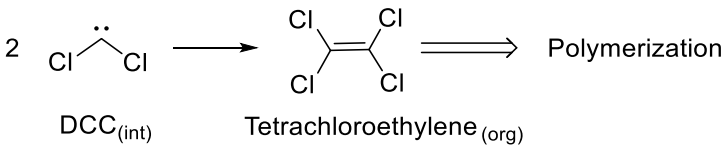

DCC polymerization did occur as seen by a darkening of the outlet solution, indicating a build up of DCC at the interface. When considering a reduction in mixing and PTC efficiency, it is believed that the CO gas formation that results from the DCC accumulation is responsible for the oscillation dampening. In a closed system, the compressibility of the gas acts as a dampener and lowers the energy input from pulsation. This is observed via the amplitude reduction of the oscillation in the reactor pressure at t=5 min that is normally present due to pulsation and a steady increase in the system pressure due to gas formation beginning at t=7 min (Figure 5.8). Periodic increases and decreases in all of the pressure signals are seen as a result of the product sampling

cycle, as well as two large decreases at t=15 min and t=21 min as a result of manual venting of the system. The feed pressures are higher than the reactor pressure due to the mixing plate upstream of the coil. When the oscillation is dampened, the energy dissipation rate in the coil is reduced from about 10 W/kg (t=3 min) to 0.8 W/kg (t=10 minutes). This reduced rate is significantly lower than the previously reported energy dissipation rate required for drop flow, and as a result, the pulsation energy is not dissipated effectively into eddy formation in the continuous aqueous phase for turbulent breakup of the dispersed organic phase. This is accompanied by a reduction in the interphase mass transfer rate, confirmed by the low conversion of CHE that reached a maximum of only 14% as measured by gas chromatography. There is no clear zone in the reaction system where gas formation would have initiated due solely to a reduction in mixing efficiency resulting in accumulation of DCC. It is therefore likely initiated by the excess $CHCl_3$ in the solvent leading to the reaction in Scheme 5.3. Gas formation presents a unique problem to a closed pulsated system where the energy input requires incompressibility of the reaction medium, which may be an inherent limitation of running such a reaction unless an effective method of isolating and purging, e.g. via a membrane, the gas while maintaining system pressure is devised. Operating at higher pressure may also work to inhibit gas formation by promoting its dissolution in the liquid phase.

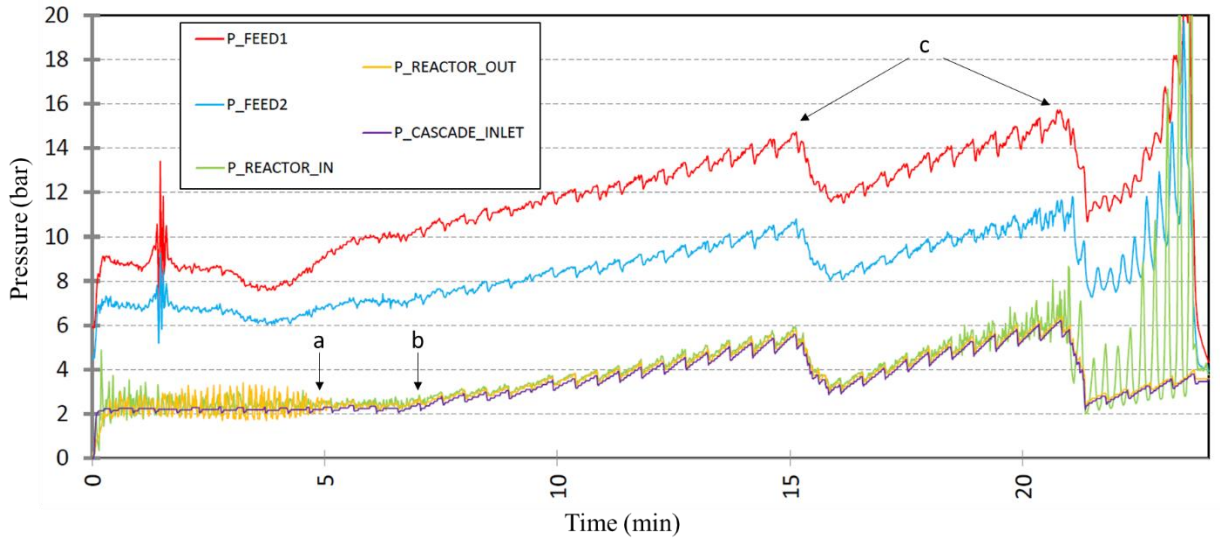

Figure 5.8. Pressure profile for reaction 2 showing oscillation dampening due to gas formation and accumulation resulting in clogging at the reactor inlet. a = dampening of pulsation energy. b = onset of pressure increase due to CO formation. c = manual system venting

5.3.4 Flow Characterization

Figure 5.9 shows residence time distributions as a function of pulsation frequency as investigated via step change experiments. The curves for 0 Hz and 3.68 Hz pulsation with 4 mL/min net flow represent the average of triplicate experiments. The resulting asymmetry is beyond the fit of a dispersion model, so the model proposed by Ham and Platzer [175] was employed in order to account for the tailing. An F-curve was fit to the step change raw data using equation (5.11).

$$F(\theta) = \left[1 - \left(\frac{\theta_k^M}{\theta^M}\right)\left(1 - \frac{\theta}{\theta_{max}}\right)^M\right]^8, for\ \theta_{\min} < \theta < \theta_{\max} \quad \textbf{(5.11)}$$

Here, θ is a dimensionless time, calculated by taking the ratio of the time and the reactor space time as calculated by equation (5.12). θ_k is a relationship between θ_{min} and θ_{max} (equation (5.13)), which are the theoretical times for the tracer to appear and to reach the feed concentration, respectively, according to the fitted model. M is the fitting parameter for the model.

$$\theta = \frac{t}{t_R} \quad \textbf{(5.12)}$$

$$\theta_k = \frac{\theta_{\min}\theta_{\max}}{\theta_{\min} - \theta_{\max}} \quad \textbf{(5.13)}$$

Taking the derivative of equation (5.11) leads to the E-Curve shown in equation (5.14) and Figure 5.9.

$$E(\theta) = \frac{8N\theta_K^M}{\theta^{M+1}}\left(1 - \frac{\theta}{\theta_{max}}\right)^{M-1}\left[1 - \left(\frac{\theta_k^M}{\theta^M}\right)\left(1 - \frac{\theta}{\theta_{max}}\right)^M\right]^7 \quad \textbf{(5.14)}$$

Significant tailing that increases with pulsation frequency is observed, indicating a large degree of axial dispersion due to the back mixing induced by pulsation. This is in agreement with previous works in oscillatory flow reactors [176] that indicate an optimal ratio of the oscillatory velocity to the net flow velocity in order to achieve a near plug flow RTD, with increases beyond this optimal ratio resulting in a more perfectly mixed RTD. Reported optima for this ratio range from 2-4 for conventional-scale oscillatory flow central orifice baffle reactors [177] and, at mesoscale (~5 mm in diameter [176]), from 4-8 for a central baffled oscillatory flow reactor [176], 5-10 for an integral baffled oscillatory flow reactor with smooth periodic constrictions [176], and up to 250 for a helical baffled reactor [51,147]. Examining the net and oscillatory Reynolds numbers presented in Table 5.3 shows that when the flow rate is kept constant at 4 mL/min, the ratio between the velocities is at least 59 and increases as high as 266. It remains unclear from the RTD curves where the optimal ratio of velocities lies for achieving a near plug flow RTD in this geometry. Increasing the flow rate tenfold with constant pulsation frequency results in a lower Reynolds number ratio of 27 and a narrower residence time distribution. In a longer coil with comparable space times to the 4 mL/min RTDs, the higher flow rate would have likely then produced a narrower and more plug flow RTD. It is also important to note that the presence of a solid phase may have an effect on the

presented liquid phase RTD, and the RTD of the solids themselves may differ due to the effects of gravity and any deposition that may occur [61,164]. It is expected, however, that the overall trend of RTD broadening with increasing frequency would remain the same at the present pulsation intensities.

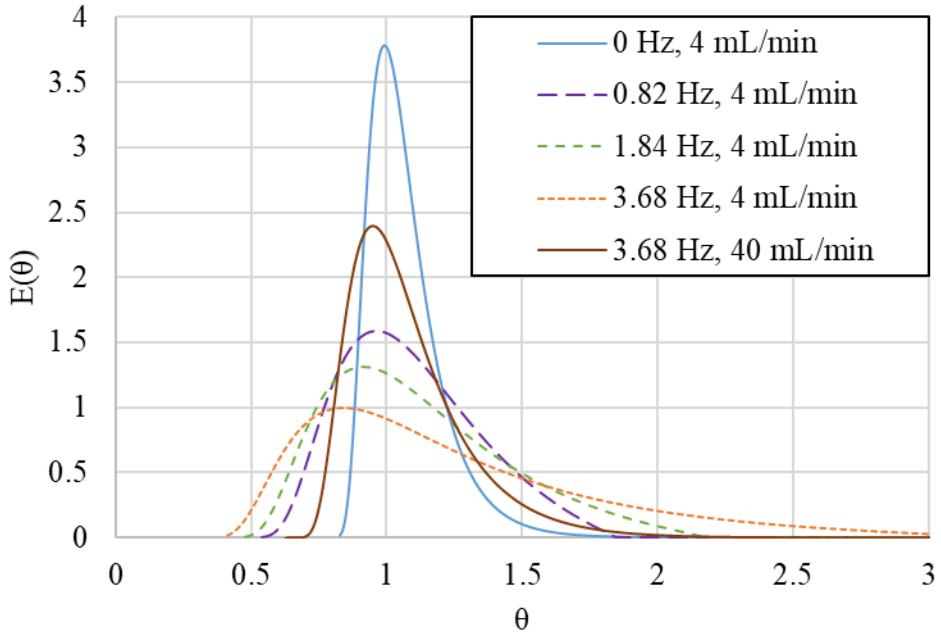

Figure 5.9. Residence Time Distribution

The first two moments of the residence time distributions were calculated and are tabulated as dimensionless values in Table 5.3. The experiments with no pulsation and 3.68 Hz pulsation were repeated in triplicate, and their mean values are reported in Table 5.3 along with their standard deviations. The mean dimensionless residence times are all above 1 and show an increase with increasing pulsation. Specifically, for these RTD experiments, the line for the pulsator did not have any net flow but was initially filled with ethanol before the step change to 0.8 M CHA in feed 1. This represents a region where the CHA tracer is able to diffuse into throughout the experiment, resulting in the observed mean residence time above 1. As pulsation is added and then increased, the increase in the mean residence time is a result of the larger degree of mixing with the pure

ethanol in this volume. This is also a contributor to the tailing observed in the RTD curves as the oscillation frequency is increased. The effect of this tailing cannot be decoupled from the measured RTD response at the reactor outlet, however further optimizations of this reactor geometry will aim to eliminate this dead zone. The pulsator feed volume is an integral part of the system that cannot be avoided in the case of RTD experiments and is important to consider in the case of operating with solid suspensions as this volume will contain solids under steady-state operation. The variance also shows an increase with pulsation frequency which is typical of oscillatory flow baffled reactors [176]. These trends indicate significant departure from plug flow and increased back mixing as pulsation increases. In certain cases with rapid mixing-limited reactions, however, the ability to separate mixing intensity from flow rate and have a continuous flow of solid/liquid suspensions at elevated pressure may be more important. As seen in section 5.3.2, high amplitudes and frequencies are not necessary to suspend solids in slower "mix then reside" type reactions, which will allow for a more plug flow RTD and product uniformity when the oscillatory flow component can be reduced.

Two relevant dimensionless groups for characterizing oscillatory flow in a coiled reactor are the Womersely number and the Dean number. The Womersley number (Wo) is calculated according to equation (5.15) and represents the ratio of the transient oscillatory inertial forces to the viscous forces [178]. The Dean number is used to characterize the generation of secondary flow, in the form of vortices, in a coiled tube and is calculated from the tube diameter and radius of curvature (r_{coil}) according to equation (5.16). In this case, the Dean number is calculated as an oscillatory Dean number (De_o), where the oscillatory Reynolds number is used in place of the net flow Reynolds number [179].

$$Wo = \frac{d_{tube}}{2}\sqrt{\frac{\omega\rho}{\mu}} \quad \textbf{(5.15)}$$

$$De_o = Re_o\sqrt{\frac{d_{tube}}{2r_{coil}}} \quad \textbf{(5.16)}$$

The secondary flow patterns generated in the coil depend on both the Womersley number and the oscillatory Dean number. For De_o above 200 and Wo less than 5.5 (i.e., for 0.82 Hz oscillation), the flow patterns have been shown to be dominated by the centrifugal effects, and the Dean vortices resemble those generated from steady forward flow without pulsation [179]. In oscillatory flow, these Dean vortices will oscillate back and forth along the flow path over the period of oscillation. When Wo is increased above 5.5, the increasing effect of the transient oscillatory inertial forces causes the secondary flow to be intensified and skewed towards the inner radius of the coil wall until Wo^2/De_o (i.e., the ratio of the inertia of the main flow to the secondary flow) reaches about 0.655, at which point the inertial forces become focused in the centre of the pipe and can result in stagnation of the secondary flows along the outer wall [179]. The oscillation intensities presented in Table 5.3 all have a Wo^2/De_o value of about 0.0955, while the highest obtained value of 0.24 occurred with low amplitude in section 5.3.2 (18.8 mm, Figure 5.7). This indicates that for all tested pulsation intensities, intense Dean secondary flows are generated throughout the pipe and the boundary layers along the walls, and hence any zones for stagnation and solid deposition resulting in clogging to occur, are minimized [180]. These secondary flows are essential in keeping solids suspended for continuous operation. In scaled-up applications of this reactor geometry, it is proposed that the transport properties of the reactor may be maintained through the manipulation of the oscillatory flow intensity. Macromixing performance may be maintained via similarity in the Re_o/Re_n ratios - as has been observed in baffled geometries [181,182], whereas the

micromixing performance may be maintained when the flow is sufficiently turbulent and there is similarity in the energy dissipation rates – as has been observed in comparisons between plate-type microreactors and a longer iteration of the current reactor geometry [56].

Table 5.3. Residence time moments and dimensionless flow numbers at varying pulsation and flow rates

Flow Rate	[mL/min]	4	4	4	4	40
Pulsation	[Hz]	0	0.82	1.84	3.68	3.68
$\boldsymbol{\theta_m}$**(M1) /** $\boldsymbol{t_R}$	[--]	1.04 +/- 0.046	1.09	1.12	1.20 +/- 0.055	1.07
$\boldsymbol{\sigma_\theta^2}$**(M2)**	[--]	0.018 +/- 0.0089	0.062	0.11	0.26 +/- 0.089	0.052
$\boldsymbol{Re}$	[--]	14	14	14	14	140
$\boldsymbol{Re_o}$	[--]	0	857	1901	3718	3718
$\boldsymbol{Re_o/Re_n}$	[--]	0	61	136	266	27
$\boldsymbol{Wo}$	[--]	0	4.6	6.8	9.5	9.5
$\boldsymbol{De_o}$	[--]	--	219	486	950	950

5.3.5 Particle Size Distribution and Morphology

Particle size distributions (PSD) and morphologies were examined in order to characterize the effects of pulsation on product uniformity. Figure 5.10 shows the particle size distributions from equal space time reactions in batch and in flow with varying pulsation. The results are quantified using the median volume equivalent diameter, or D_{v50}, and the span, which is calculated according to equation (5.17) where D_{v10} and D_{v90} are the volume equivalent diameters that will account for 10% and 90% of the distribution, respectively.

$$Span = \frac{D_{v90} - D_{v10}}{D_{v50}} \qquad \textbf{(5.17)}$$

The particles produced in batch have the smallest D_{v50} of 62.17 µm and the narrowest distribution with a span of 1.51. The particles sizes in batch were compared from 3 tests with 300 rpm, 600 rpm, and 900 rpm, and the effect of grinding by the stir bar was found to be marginal

(D_{v50} = 66.58, 62.17, and 57.32, respectively). The effect of stir speed on the solid yield was similarly marginal (5.04 wt%, 4.6 wt%, and 4.8 wt% for 340 rpm, 490 rpm, and 600 rpm, respectively), indicating that the mixing speed was sufficient to render the reaction kinetically limited. The smaller D_{v50} in batch is a result of the uniformity of mixing within the flask resulting in more frequent nucleation and smaller final products, whereas the smaller span is due to the particles all residing for an equal length of time in the flask. When the reaction is run in flow with pulsation, the D_{v50} and span both increase when compared to their batch counterpart. This can be explained by considering the RTD data, where the relatively broad particle size distributions with larger mean sizes are a result of the axial dispersion and tailing as observed in the RTD experiments assuming reactants and products follow similar trends. Increasing the mixing intensity in flow decreases the D_{v50} and broadens the span. The D_{v50} decrease is in agreement with previous works in oscillatory baffled crystallizers in batch [57,183,184] and occurs due to the effect of hydrodynamics on the nucleation rate [183] and the effect of mixing intensity nucleation uniformity [57]. The broadening of the span with increasing pulsation is in agreement with the broadening of the RTDs in flow with pulsation frequency. Thus, an intermediate pulsation frequency in this case may be best for producing more uniform particles that are relatively large and in the range of sizes (D_{v50} of 100 – 500 μm) usually desired for industrial crystallization [54].

Particle morphology as examined by light microscopy is shown in Figure 5.11. As expected from the PSDs, moving from batch to pulsated flow increases the mean particle size, and further increases in pulsation frequency result in smaller particles with less uniform sizes.

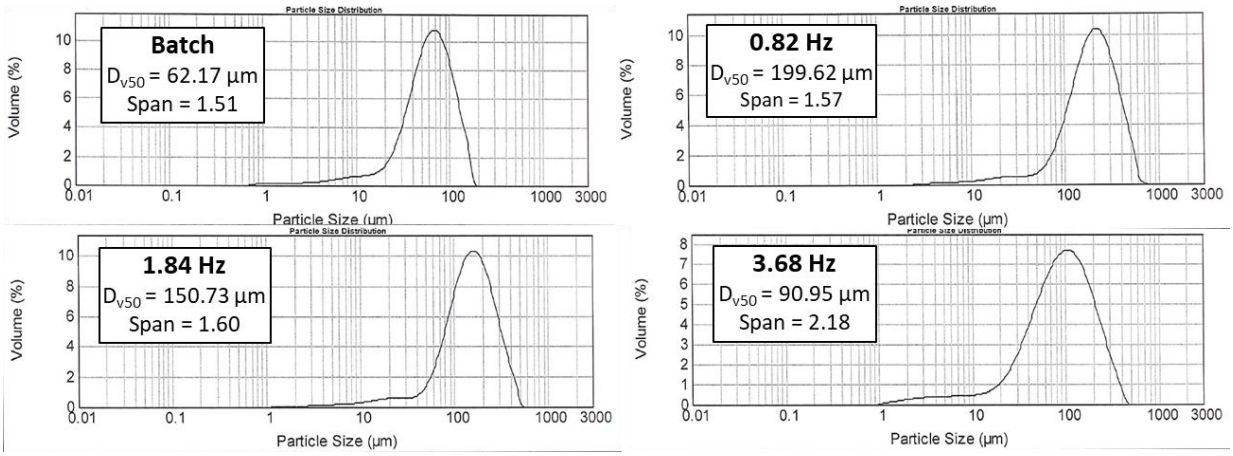

Figure 5.10. Particle Size Distribution for Scheme 5.1. [Glyoxal] = 0.2 M, [CHA] = 0.4 M. Space time = 30 min.

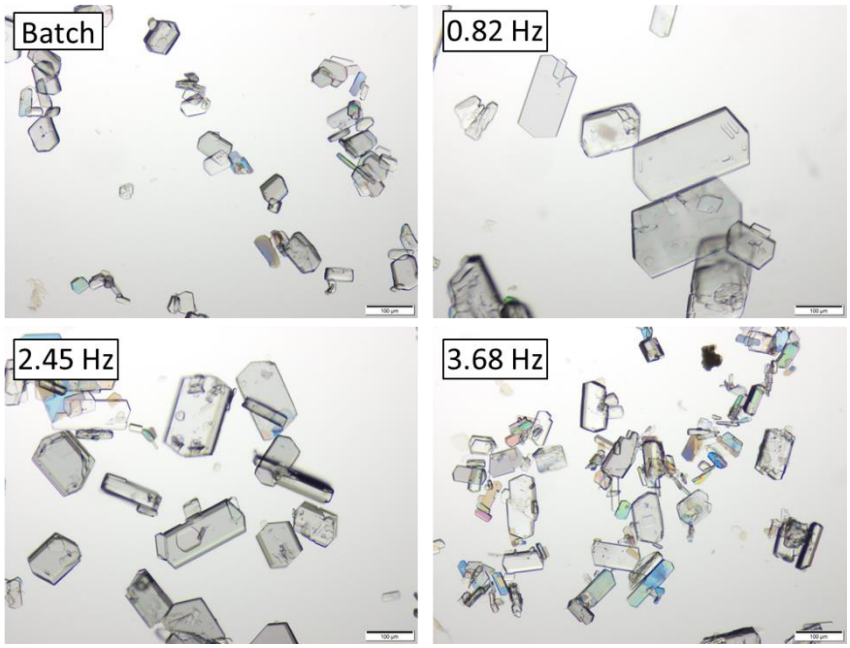

Figure 5.11. EDDC particle morphology after 30 minutes in batch or flow with varying pulsation frequency. Scale bar = 100 µm

5.4 **Conclusions**

In this report, the solid handling capabilities and flow patterns of a baffle-less oscillatory flow reactor are characterized. The reactor was tested with two reactions, namely a precipitation

reaction and a mass transfer limited phase transfer catalysis reaction. In the first reaction, the reactor geometry proved capable of continuously handling solid suspensions with stable operation for 120 minutes with solid concentrations as high as 7.9 wt% and for 5 hours with a solid concentration of 5.8 wt% at an energy dissipation rate of 13 W/kg. In all cases, no signs of clogging were observed and the maximum run time of the presented reactor geometry with constant pulsation remains unknown. Decreasing the amplitude and frequency did not result in clogging until the pulsation was turned off. Lower energy dissipation rates are therefore likely sufficient to suspend solids for "mix-then-reside" type reactions that are limited by the intrinsic reaction kinetics. However, the maximum run time with a given solid concentration and pulsation intensity remains to be determined.

In the second reaction, the formation of side-product gas resulted in a dampening of the pulsation energy as observed by an approximately 10-fold reduction from 10 W/kg to 0.8 W/kg in the oscillatory energy dissipation rate. In this case, clogging was observed as a result of the pulsation dampening and the operability for handling solid suspensions was reduced. Gas formation presents a unique problem in closed pulsated systems where the reaction medium must be incompressible in order for the pulsator to deliver sufficiently high power for keeping solids in suspension.

Although effective in preventing blockage, the relatively intense pulsation (Re_o/Re_n from 27 to 266) is also accompanied by a broadening of the residence time and particle size distributions. The results show that the oscillation is an effective method of separating mixing energy from flow in order to continuously flow an incompressible solid suspension, and further optimization of the relative net and oscillatory flow velocities is required to achieve a more plug flow residence time distribution. Alternatively, a 4.6 mm inner diameter coil has proven quite robust toward solid-

liquid handling and as such, the reactor size could potentially be further reduced in oscillatory-flow so that the net flow velocity is increased to decrease the Re_o/Re_n ratio. Further miniaturization would favor simpler process development at low flow rates.

Abbreviations

CHA = Cyclohexylamine

EDDC = N,N'-(1E,2E)-Ethane-1,2-diylidenedicyclohexanamine

DCC = Dichlorocarbene

CHE = Cyclohexene

PTC = Phase Transfer Catalysis

Nomenclature

Symbol	Meaning	Units
C	Concentration	mol/L
De_o	Oscillatory Dean number	--
D_{v10}	Volume equivalent diameter accounting for 10% of the particle size distribution	μm
D_{v50}	Mean volume equivalent diameter	μm
D_{v90}	Volume equivalent diameter accounting for 90% of the particle size distribution	μm
d_{tube}	Coil diameter	m
f	Oscillation frequency	--
M	Fitting Parameter for Eqs. 10 and 13	--
N	Number of moles	moles
P	Pressure	Pa
P_o	Oscillatory Pressure	Pa
Q_{net}	Net volumetric flow rate	mL/min

r_{coil}	Coil radius of curvature	m
Re_n	Net flow Reynolds Number	--
Re_o	Oscillatory Reynolds number	--
T	Temperature	°C
t	Time	s
t_R	Nominal space time (based on the reactor volume)	s
u_n	Net flow velocity	m/s
u_o	Oscillatory velocity	m/s
$u_{o,max}$	Maximum oscillatory velocity	m/s
V_R	Reactor volume	m^3
Wo	Womersley number	--
x_{coil}	Center to peak oscillation amplitude in the coil	m
$\check{Y}$	Overall yield on a basis of 100% conversion	%
Z	Coil length	m

Greek Symbols

Symbol	Meaning	Units
δ	Phase angle	rad
$\bar{\epsilon}$	Average energy dissipation rate	W/kg
$\bar{\epsilon}_{net}$	Net flow energy dissipation rate	W/kg
$\bar{\epsilon}_o$	Oscillatory energy dissipation rate	W/kg
θ	Dimensionless time	--
θ_k	Relationship between θ_{min} and θ_{max} in Eq. 12	--
θ_m	Mean dimensionless residence time	--
θ_{max}	Dimensionless time for tracer to reach feed concentration	--
θ_{min}	Dimensional time for tracer to appear	--
μ	Dynamic viscosity	Pa s
ρ	Density	kg/m^3
ρ_c	Continuous phase density	kg/m^3
σ_θ^2	Dimensionless variance	--

ω	Oscillation angular frequency	rad/s

6. Continuous and Intensified Production of an API Suspension Under Oscillatory Flow

Abstract

A baffleless oscillatory flow coil reactor is implemented for the continuous production of a sodium zirconium cyclosilicate (SZC) species (ZS-9) suspension at elevated temperature and pressure. Development of the process and the resulting effects on product quality are outlined, including both mechanical changes to the reaction system itself and parametric tests of the operating conditions. The reaction apparatus proceeded through several iterations, where physical changes upstream of the crystallization coil from a simple T-junction mixing point to the final system containing a pre-filled seeding loop led to significant improvements in product quality. The effects of system temperatures, fluid space times, and oscillation intensity are then outlined, leading to final operating conditions consisting of a 1-hour crystallization fluid space time at 245°C, a 173°C seeding temperature, and a velocity ratio (Re_o/Re_n) ratio of 175, and a ZS-9 production rate of 40 g/hr. Finally, a mixing-based scale-up methodology is proposed for the design of a production scale system for a ZS-9 production rate of 11.9 kg/hr.

6.1 **Introduction**

Solids are frequently encountered in the pharmaceutical industry at various stages of processing. This is particularly evident when considering the active pharmaceutical ingredient (API) itself, where, as of 2009, over 90% of APIs were crystalline forms of small organic molecules [185]. Continuous processing of these molecules at relatively low production rates is rather difficult due to problems associated with pipe fouling and clogging, resulting in the usage of primarily batch unit operations that are versatile and less likely to plug when solid handling is required. However, due to the heat transport limitations associated with larger-volume batch reactors and in the interest of process safety, reactions in such vessels are often performed diluted or semi-batchwise resulting in less efficient utilization or prevention of specific reaction pathways [42], and leading to significant solvent requirements and large E-factors (i.e., the mass of waste generated per mass of product) [13]. It is therefore desirable to intensify these processes in order to improve their overall performance and environmental sustainability [21]. The definitions of process intensification itself are broad, but most encompass a general requirement to miniaturize processing equipment [19], allowing for one to employ more intensified reaction pathways and conditions [143]. Continuous processing is generally required in order to achieve a meaningful production capacity in a miniaturized reaction system and leads to several advantages over large-scale batch processes including enhanced heat and mass transfer and reduced footprints of equipment, resulting in increased sustainability, better yields and/or conversions, and safer hazardous materials handling [54]. Miniaturized process can also generally obtain higher pressure ratings without incurring the large costs associated to the construction of larger high pressure vessels [186]. However, continuous processing of solid suspensions in miniaturized reaction systems is difficult due to the amplified risk of channel blockage.

Crystallization is an important unit operation in the purification and refining of pharmaceutical products [187,188] that is often performed in batch and is, as a result, frequently subject to inter-batch variability [189]. When operated continuously, a more uniform crystallization environment can be obtained that offers better control over the product crystal properties [190]. Examples of continuous and intensified crystallization systems include mixed-product mixed-suspension removal (MSMPR) crystallizers [73,74,162], oscillatory flow reactors [53,54,59,153,174,183,184,191], coiled tubular crystallizers [61,190], miniaturized continuous stirred tank reactors (CSTRs) [75,155], and a cascade of chambers having off-center inlets and outlets [192]. These reactors employ either active and/or passive mixing techniques in order to maintain flow of a solid suspension and to prevent clogging, where active mixing relies on an external energy input and passive mixing makes use of the pumping energy to generate mixing through variations in channel geometry [144]. The use of active mixing results in a decoupling of the flow rate and mixing energy, allowing for both properties to be tuned independently to the needs of a given reaction environment.

Sodium zirconium cyclosilicate (SZC) is an insoluble microporous inorganic compound that is used in the treatment of acute hyperkalemia (i.e., elevated serum potassium levels). The compound selectively exchanges sodium for potassium within the gastrointestinal tract, effectively lowering the potassium levels in the serum [193]. Several forms of SZC exist from ZS-1 to ZS-11, where ZS-9 is considered the most effective in absorption of potassium [194] and, in its orally administered form, should have a particle diameter greater than 3 μm in order to prevent absorption into the patient's bloodstream [195]. Previous methods of ZS-9 generation have been performed via batch operation, where the principle reaction occurs over the course of 72 hours at 200°C in an 18.9 L vessel with a proposed larger-scale production vessel of 200 litres or larger [195].

Given the potential for process intensification and increased productivities in miniaturized continuous reaction technologies, the objective of this work is to develop such a system for continuous crystallization of a ZS-9 suspension under oscillatory flow in a baffleless coiled tube. The employed reactor system has previously shown its capability in continuously handling solid suspensions composed of 7.9 wt% solids [59]. The Hastelloy and stainless-steel construction of the reaction system permits operation under high temperatures and pressures in an alkaline reaction environment. A combination of both active and passive mixing is used, via high intensity pulsations and the generation of Dean secondary flows through the coil curvature. The baffleless geometry of the coil lowers the risk of dead zones and clogging and allows for more effective cleaning for GMP applications. A description is provided outlining development of the reaction platform, where mechanical changes to the system itself resulted in longer run times without clogging and higher purity ZS-9. Parametric tests of the operating conditions including temperatures, fluid space times, and oscillation intensity are described leading to the selection of a final set of production operating conditions. Finally, a scale-up methodology is proposed for ZS-9 production at the tonne scale.

6.2 Materials and Methods

6.2.1 ZS-9 Crystallization Reaction

ZS-9 is a crystalline compound consisting of oxygen, silicon, and zirconium, the structure of which is shown in Figure 6.1a. The cubic crystal structure is composed of a microporous network of octahedral Zr and tetrahedral Si units covalently bound to shared oxygen atoms, giving the overall structure a negative charge that is balanced by positive counter ions within the pore openings (Figure 6.1b) [194]. Formation of the solid occurs through a high temperature hydrothermal crystallization using reactive sources of zirconium, silicon, and an alkali metal. In

the present iteration, these reagents were supplied to the reaction as zirconium acetate (ZrOAc), sodium silicate ($(NaOH)_x(Na_2SiO_3)_y$) solution, and sodium hydroxide (NaOH) in an aqueous environment. The overall balanced reaction is shown in equation (6.1).

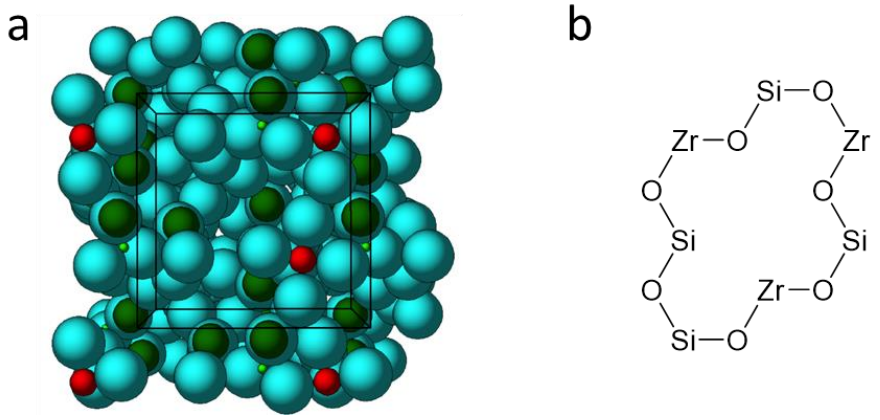

Figure 6.1. a: Crystal structure of ZS-9. Blue: oxygen, green: silicon, red: zirconium [194]. b: Counter ion binding pore opening of ZS-9.

$$3(Na_2O \cdot SiO_2)_{n\,(aq)} + [ZrO_3]^{2-} + 2.7H_2O + 4HOAc \rightarrow Na_2ZrSi_3O_9x2.7H_2O + 4NaOAc + 2OH^- + H_2O \quad \textbf{(6.1)}$$

6.2.2 Lab-Based Development of the Continuous Reaction System [100]

A general and simplified process flow diagram of the continuous flow reaction system is shown in Figure 6.2. The system can be divided into two regions, namely, region 1 which consists of the mixing point and all upstream components from the crystallization coil entrance, and region 2 which consists of all components downstream from and including the crystallization coil. During development of the continuous system, region 1 was varied in order to obtain higher purity ZS-9 and longer reaction run times without clogging (see section 6.3 for more detail), whereas region 2 remained constant throughout. The system was prefilled with water before the start of each experiment (unless indicated otherwise, see section 6.3). Feed 1 was a 100% ZrOAc solution

(American Elements, ZR-AC-03-SOL) and feed 2 consisted of a 7.5 wt% NaOH (from 25 wt% stock) and 31 wt% sodium silicate ($(NaOH)_x(Na_2SiO_3)_y$, 10.6 wt% Na_2O, 26.5 wt% SiO_2) solution (Sigma-Aldrich, 338443) in deionized water. Feed 1 was pumped by a 500 mL ISCO 500D syringe pump at 1.23 g/min while Feed 2 was pumped at 6.85 g/min by (depending on the setup configuration) either a flusys WADose HPLC pump or two intermittently operated ISCO 260D syringe pumps. Both solutions were fed via 1.75 mm ID stainless steel tubing and passed through one-way valves implemented to prevent any back flow that may occur due to oscillation of the fluid. Feed 1 was dosed as a pure ZrOAc solution at a lower flowrate in order to more closely resemble the dropwise addition of ZrOAc that has been employed during batch production[195]. The two feeds were mixed downstream of the one-way valves at the point where the oscillation was imposed on the fluid by the pulsator. All tubing after the one-way valves (where solids were present) had an internal diameter of 4.57 mm. The mixing point was a key area of variation during development of the system and more details are provided in section 6.3. The pulsator itself was a LEWA LDB1 reciprocating pump with a 14 mm diameter head, maximum operating pressure of 80 barg, and in-coil fluid amplitude and frequency ranges that can be adjusted from 0-70.4 mm and 0-4.09 Hz, respectively. Generally, the pulsator was operated at its maximum capacity (i.e., 70.4 mm amplitude and 4.09 Hz) unless indicated otherwise. The reaction mixture was then fed to the crystallization coil, which was a helical tubular reactor constructed from Hastelloy tubing. The crystallization coil had a volume of 400 mL, a length of 24000 mm, a coil radius of 151 mm, and a pitch of 10 mm. The crystallization coil was heated by a Huber T305 thermostat circulating DW-Therm HT heat transfer oil. The suspension containing the product was then fed to a 27.3 mL Hastelloy helical coil (1670 mm length, 120 mm coil diameter, 6 mm pitch) which was cooled to 12 °C by water from a service line. The cooled product suspension was then sent to a cascade of

sampling containers which allowed for intermittent sampling at high pressure followed by a cyclone for depressurization. The cascade sampling system used in this work was adapted from the work of White et al. [36] and was used in a previous and smaller iteration of the present oscillatory flow helical coil reactor [59]. 60 barg of back pressure was applied to the system at the inlet of the sampling cascade via a N_2 cylinder in order to maintain a liquid-phase reaction mixture and to prevent cavitation during oscillation. Pressure measurements were taken around the system with WIKA M-11 0-100 barg pressure sensors and temperatures were measured with PT100 temperature sensors. Data was recorded and pump control was performed via a Hitec Zang laboratory process control system.

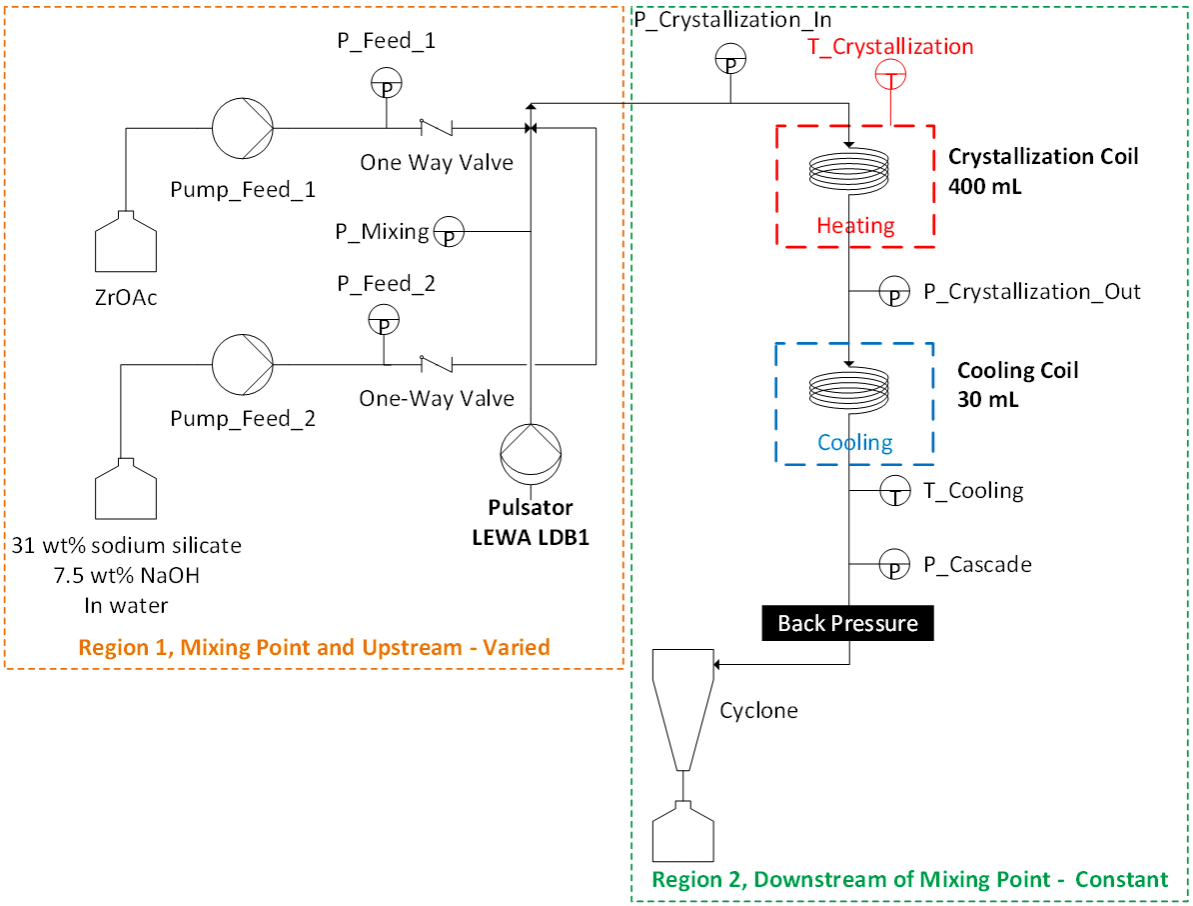

Figure 6.2. General and simplified process flow diagram for continuous ZS-9 suspension production. Region 1 (left) represents the mixing point and upstream components that were varied during development. Region 2 (right) represents the region downstream of the mixing point that remained constant throughout development.

6.2.3 Product Collection and Analysis

The product suspension was collected for 30 minutes, after operation for 2 fluid space times (fluid space time in the crystallization coil is in general 1 hour), from the sampling cascade and filtered through a filter funnel under vacuum with a pore size of either p40 (16 – 40 µm) or p16 (10 – 16 µm) depending on availability. The filter cake was then collected and washed with

deionized water for 30 minutes at 42 °C with magnetic stirring in order to remove any remaining mother liquor in the product. The product cake was then dried overnight under vacuum at 50 °C. The dried product was then ground lightly with a mortar and pestle to break up any large clumps and obtain a consistent and fine powder. Primary analysis of the product powder was performed via X-ray diffraction (XRD). Samples were compared to a standard spectrum obtained from pure ZS-9. Samples that did not contain pure ZS-9 were not analyzed further. For an example of the analysis via XRD, see Figure 6.3 showing an amorphous solid indicated by a broad baseline (a), a crystalline solid containing side species of SZC (b), and a pure and crystalline ZS-9 product (c). Those samples that were determined to be pure ZS-9 were further characterized by determining the amount (%) of amorphous content and by collecting particle size distributions (PSD) using a Malvern Laser Diffraction Mastersizer 2000.

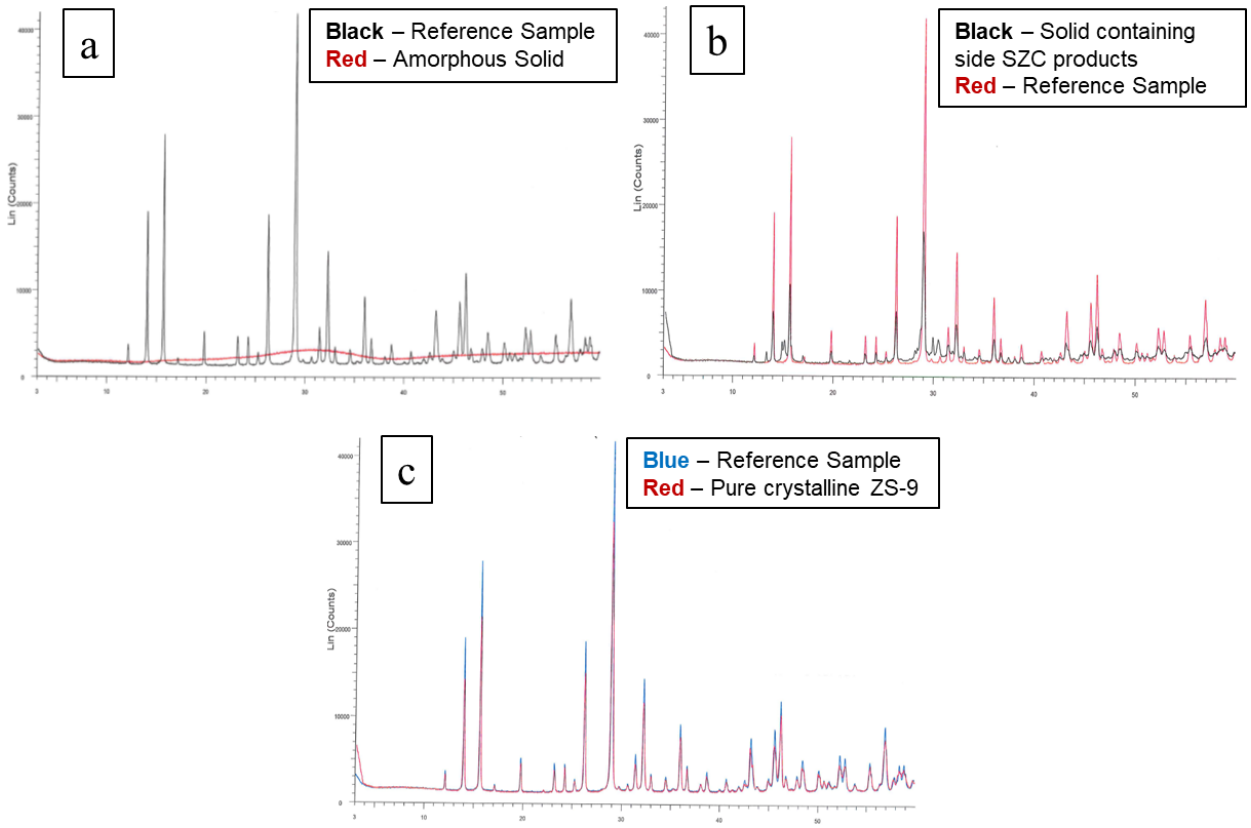

Figure 6.3. Examples of product analysis via XRD. a: amorphous solid indicated by a broadening of the baseline. b: Side product formation indicated by peaks that do not correspond to the reference sample. c: pure and crystalline ZS-9.

6.3 Development of the Continuous Reaction System

During development of continuous reaction system, region 1 (Figure 6.2) was identified as a key area where modifications to the system itself could provide improvements to product quality and longer run times without clogging. Only the mechanical changes to the system itself are described in this section, whereas details regarding parametric tests related to the operating conditions (i.e., temperatures, pulsation intensity, and fluid space time) are described in section 6.4. The progression from the first to final iterations of region 1, identified here as setups 1 through 3c, respectively, is shown in Figure 6.4. Initially in setup 1, pulsation was applied to feed 1 and

the reagent feeds were mixed at a simple T-junction before being feed to the crystallization coil. The resulting product was a mixture of ZS-9 and ZS-7, where the concentration of ZS-7 was much greater than that of ZS-9. In order to increase the amount of ZS-9 produced in the reactor, a seeding container with 10 wt% ZS-9 seeds ($D_V(10)$ = 8 µm, $D_V(50)$ = 14 µm, $D_V(90)$ = 25 µm, 0% below 3 µm) in water was then added in setup 2 to the feed 1 line. After opening the seeding container, seeds were fed to the system by gravity and through mixing generated by the pressure oscillations. Samples collected from setup 2 still showed a mixture of ZS-7 and ZS-9, but in this case the purity had improved, and the relative concentration of ZS-9 was higher than that of ZS-7. In both setups, amorphous solids were present in the product.

Setup 3a saw significant and essential changes made to region 1 of the continuous reaction system. First, a seeding loop with a heated seeding coil was installed that allowed for a 1 wt% solution of ZS-9 seeds in water to be pre-loaded into the mixing point and seeding coil. In order to do so, the seeding solution was fed at atmospheric pressure via an Ismatec MCP Standard pump with a PTFE tubing pump head, where it passed through the mixing point and seeding coil and subsequently returned to the feed jar. At the outlet of the seeding coil, a 3-way valve with ball valves at either outlet was installed to allow the seeding solution to exit at atmospheric pressure while region 2 of the system was held at 60 bar. Continuous seeding throughout the course of the reaction was not possible in this case due to the high system pressure well exceeding the operating range of the peristaltic pump. Prior to initiation of the reaction, the seeding loop was closed and region 1 was pressurized. At the mixing point, injectors for each feed were installed by feeding 1/8” tubing through the 1/4” 4-way junction, such that the injectors were directly pointed at each other, in order to promote better reagent mixing by bringing the initial contact point between the two feeds closer together. Installation of the described components to region 1 resulted in a product

that contained pure ZS-9 but had a significant amount of amorphous content present. However, the 1/8” injector of feed 1 was prone to clogging and was only able to run for 240 minutes total over the course of two tests (150 min and 90 min each, washed with water in between) before blockage occurred. In addition, the check valves of the flusys WADose pump (feed 2) began to fail, likely due to the constant and intense pressure oscillations throughout the system.

In order to improve the run times from setup 3a, the 1/8” injectors were removed from the 1/4” 4-way junction. The feeds in setup 3b were thus mixed in the same orientation as setup 3a, but with all tubes that can contact a suspension now 1/4” in diameter. For the feed 2 dosage, the flusys WADose pump was replaced with two intermittently operated ISCO 260D syringe pumps. These pumps were more stable under the oscillating pressure of the system due to their reliance on only one large constantly pumping syringe versus the small alternating chambers and check-valve of the flusys WADose. In order to achieve a near-constant feed 2 dosage, the pumping modes of the two ISCO pumps were switched manually such that one pump was always refilling while the other was pumping. It is also possible to automate the switching process so that no manual input is required. The result of the described modifications was an extension of system run times before clogging, where 1415 minutes of intermittent running time over several experiments was possible before the first clog appeared at the feed 1 inlet to the mixing point (five experiments of 150 min, one experiment of 180 min, one experiment of 210 minutes, and one experiment of 275 min, with water washing in between each experiment). The maximum continuous run-time of this system is not known.

The final iteration of the continuous reaction system saw small changes implemented in order to further extend the system runtime before clogging and to more closely resemble the dropwise addition of ZrOAc in batch production. For the reduction of clogging frequency, the positioning

of the inlets for feed 1 and feed 2 were separated in such that they were 15 cm apart and were no longer pointed directly at one another. It was believed that the lower flowrate of feed 1 relative to feed 2 was resulting in a directional imbalance of the net flow that caused clogs to form at the feed 1 inlet when they were directly opposite to one another. Related to the dropwise addition of ZrOAc in batch, setup 3c saw the seeding loop prefilled with ZS-9 seeds in feed 2 rather than in water as was used previously. The system was therefore prefilled with seeds in feed 2 up to the exit of the seeding coil, with the rest of the system prefilled with water. Using this setup, continuous runtimes were extended with several long runs being completed having run times of 390 min, 405 min, 405 min, 300 min, and 300 minutes. A representative pressure profile for the system during extended runs in setup 3c, taken from the 390 min run, is shown in Figure 6.5. No sudden pressure spikes indicating clog formation were observed over the course of the long runs. Large oscillations in the system pressures are seen as a result of the pulsating flow that reach an average value of about +/- 18 bars at steady state. A broadening of the oscillations is observed, as well as a decrease in the feeds 1 and 2 pressures that results from increased pumping pressure from the pulsator after about 60 minutes when the system becomes filled with the solid suspension. Several periodic downward spikes in feed 2 are also observed as a result of the manual switching and filling of the ISCO pumps which could effectively be removed via automated pump switching. Importantly, using this new orientation of the feed inlets, the fittings at the feed 1 inlet became much more accessible and were therefore changed periodically to prevent any potential blockage from occurring. Total runtimes over several experiments in this setup can therefore not be directly compared to the other setups. Crystalline and pure ZS-9 was produced using this setup using operating conditions that were determined in the parametric studies described in the following section.

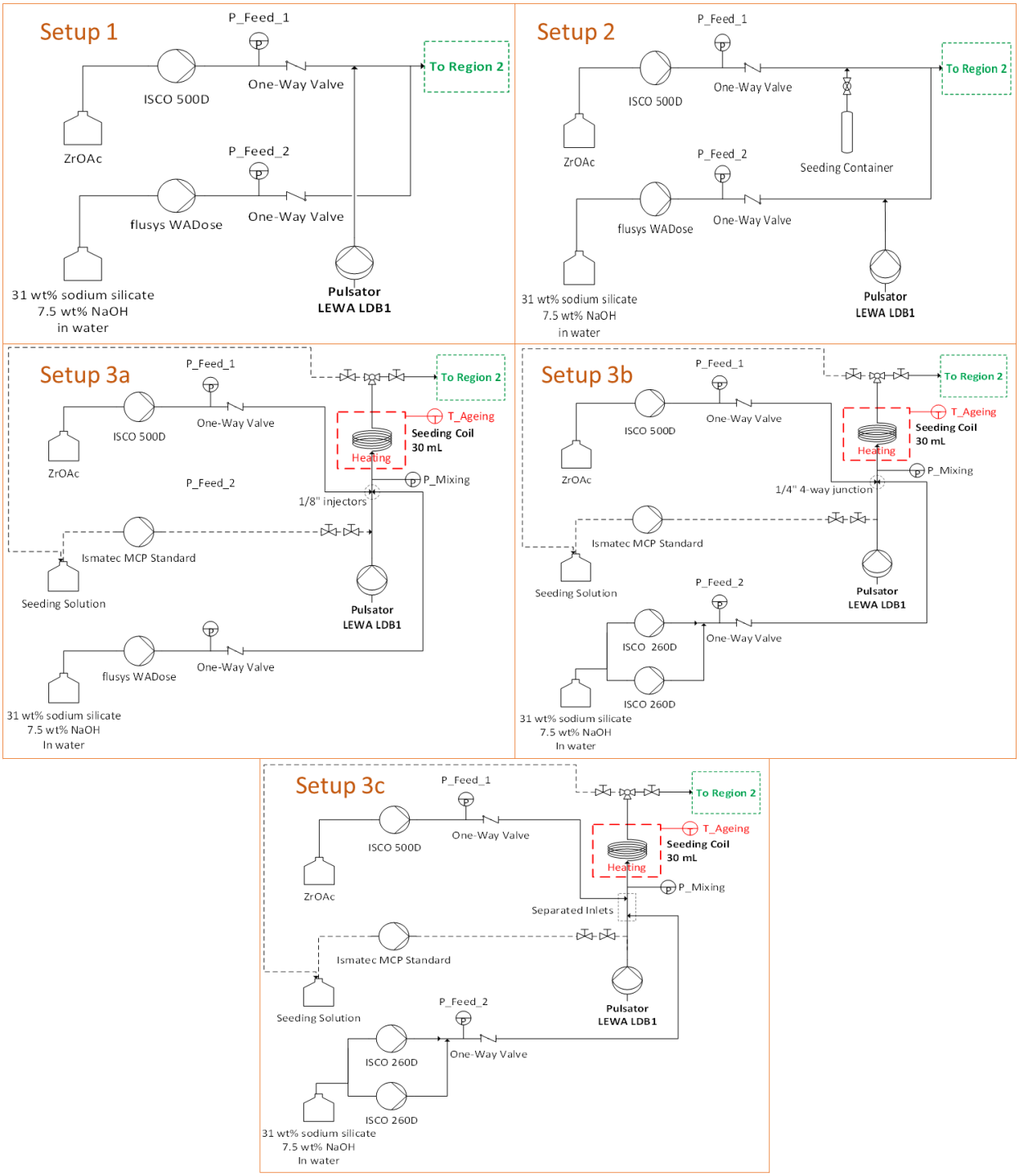

Figure 6.4. Progression of the mixing point and upstream components of the system for continuous ZS-9 suspension production.

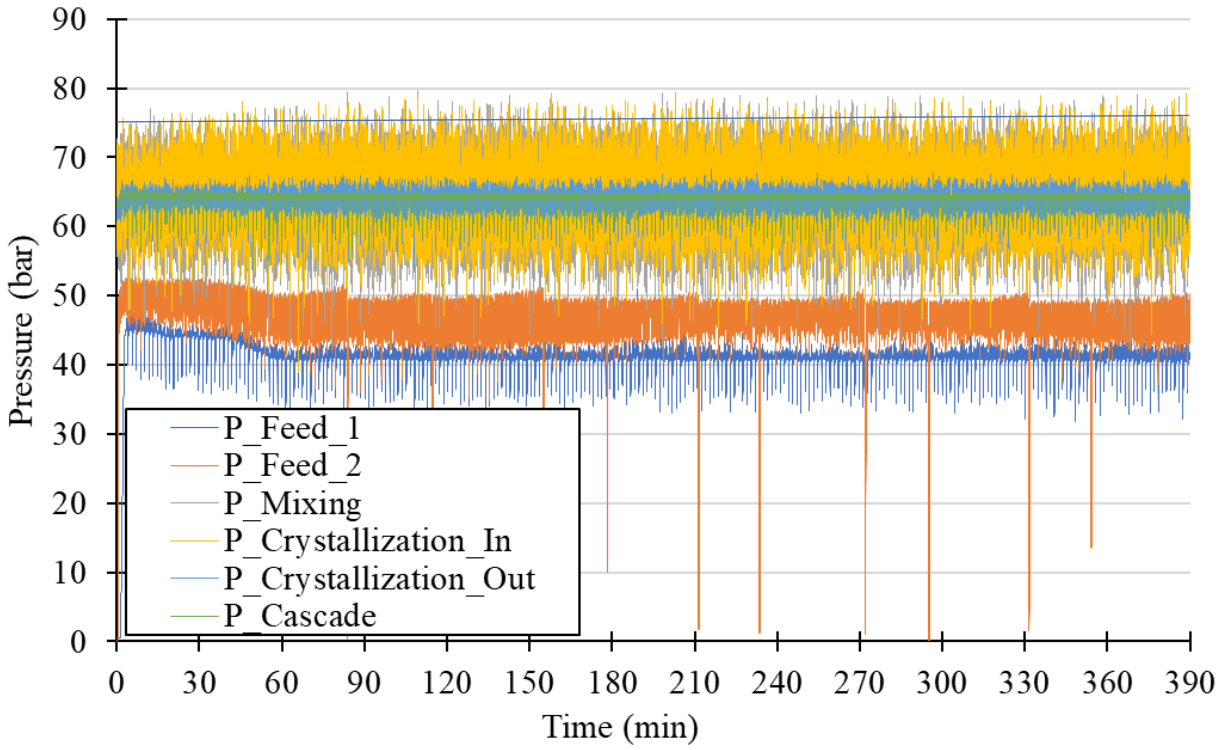

Figure 6.5. Representative pressure profile for continuous ZS-9 suspension production with a 390 min run time.

6.4 **Parametric Analysis of Reaction Conditions**

With longer run times possible in setup 3c, it was then necessary to bring the product quality within a certain set of specifications. Namely, the product needs to be pure and crystalline ZS-9 having a cubic shape, and where less than 3 vol% of said particles have a diameter (of a sphere with an equivalent volume) below 3 µm. Several operating conditions were varied in order to bring the product within the range of these specifications, including fluid space time, crystallization temperature, seeding temperature, and oscillation intensity. A summary of the base reaction conditions is shown in Table 6.1. Unless indicated otherwise, results were compared within the experiments performed in setup 3c.

Table 6.1. Base reaction conditions for parametric analysis of the operating conditions.

Parameter	Value	Unit
Crystallization Fluid Space Time	1	hr
Crystallization Temperature	252	℃
Seeding Temperature	173	℃
Re_o	62455	--
Re_n	356	--
Re_o/Re_n	175	--
Strouhal Number, St_r	0.0052	--

The effect of fluid space time is shown in Figure 6.6. When the space time is cut in half to 30 minutes in the crystallization coil, the result is pure ZS-9 with a large portion of amorphous content. At the base value of 1 hour, product quality is improved with pure ZS-9 having only 1.4% amorphous content. When the space time is extended further to 1.5 hours, the resulting product is primarily composed of ZS-7. These results indicate that formation of the product proceeds first through an amorphous solid that requires a certain time at elevated temperature to rearrange and become crystalline ZS-9, but when given too much time the solid transitions to ZS-7.

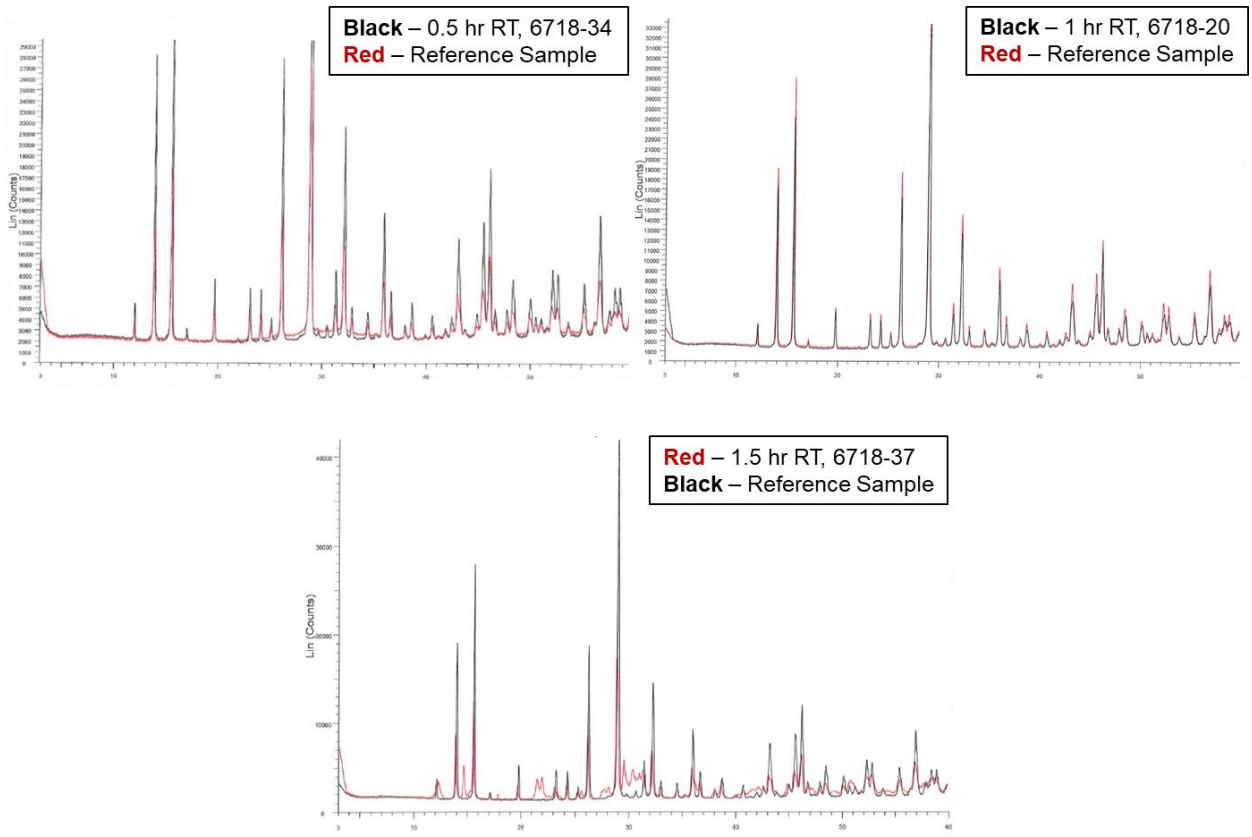

Figure 6.6. Effect of crystallization coil space time on the product XRD profile in setup 3c. Note that the change in space time is accompanied by a change in $\boldsymbol{Re_o/Re_n}$, having values of 88 for experiment 6718-34 and 263 for experiment 6718-37. All other reaction conditions are as listed in Table 6.1.

Given the transition of the product from an amorphous solid, to crystalline ZS-9, to crystalline ZS-7, there are presumably many potential combinations of crystallization temperature and space time that can be employed in order to arrive at the desired crystalline ZS-9 product. Accordingly, the effect of crystallization temperature on the product composition was then tested with a 1-hour crystallization time. The results of varying the crystallization temperature between 262°C and 245°C are shown in Figure 6.7. Note that in this figure, only the experiment at 245°C was performed in setup 3c, whereas the rest were performed in setup 3b. It is also important to note

that two different pulsation intensities are shown in this figure, with the first two tests at 262°C and 252°C having an Re_o/Re_n of 105, and the second two tests at 252°C and 245°C having an Re_o/Re_n value of 175. With Re_o/Re_n of 105 and at the highest tested crystallization temperature (262°C), the product is primarily ZS-7. Decreasing the crystallization temperature to 252°C resulted in more ZS-9 being produced, albeit still in a mixture with ZS-7 due to the lowered pulsation intensity. Attributing the resultant product mixture to the lower mixing intensity is clear when comparing the two products shown in Figure 6.7 from crystallizations at 252°C, where the higher intensity oscillation produced significantly more ZS-9 with only a small amount of ZS-7, the effect of which is discussed further below. With Re_o/Re_n of 175, decreasing the temperature further from 252°C to 245°C resulted in a better-quality product consisting of crystalline ZS-9 with no ZS-7 content. Importantly, the crystallization at 245°C also generated larger particles, with only 9.81 vol% having a diameter below 3 μm compared to 12 vol% at 252°C. However, because the reaction at 245°C was performed in setup 3c with a different injection approach to that employed in the reaction at 252°C, attributing the improvement in product quality to the temperature decrease alone is not possible, and it may be a result of both the temperature and injection approach.

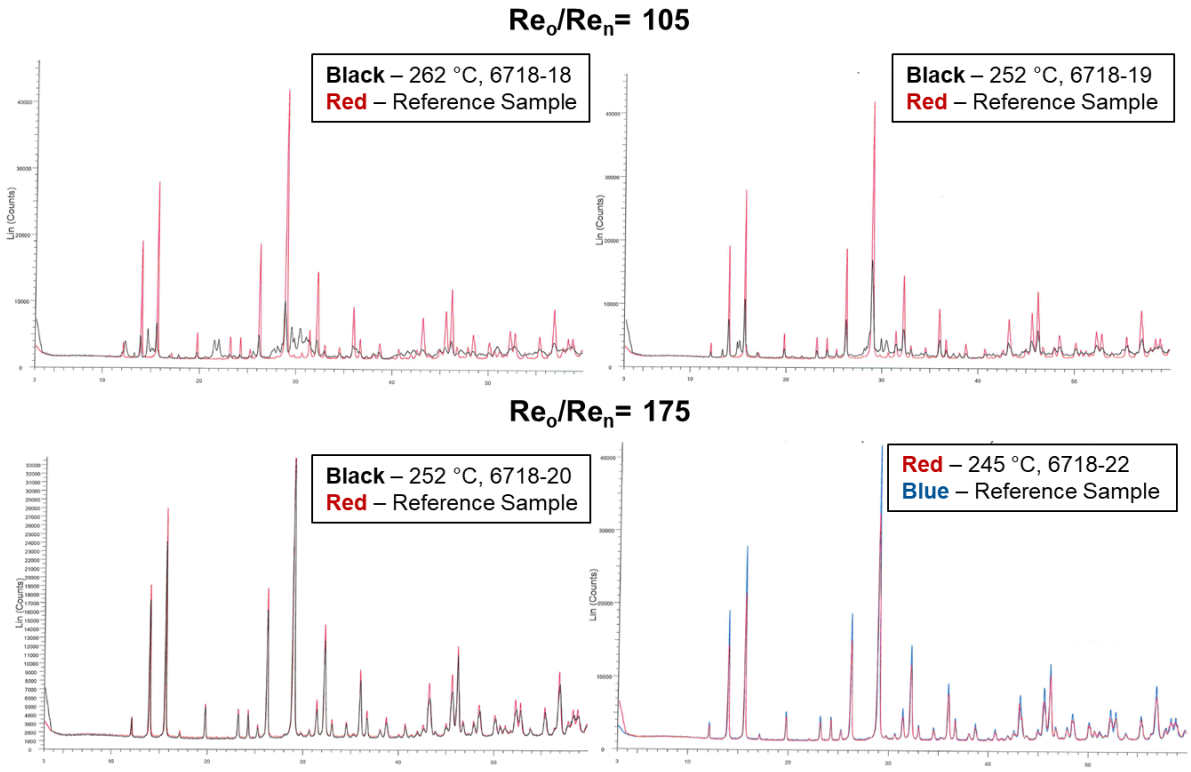

Figure 6.7. Effect of crystallization coil temperature on the product XRD profile. Reactions at 252°C were performed in setup 3b while the reaction at 245°C was performed in setup 3c Top row: $\boldsymbol{Re_o/Re_n}$ = 105. Bottom row: $\boldsymbol{Re_o/Re_n}$ = 175. All other reaction conditions are as listed in Table 6.1.

Next, the effect of the seeding temperature on the product quality was tested over a range of 70°C to 173°C, the results of which are shown in Figure 6.8. In all cases, the resulting product was pure ZS-9. Differences arose, however, in the amount of amorphous content present in each sample, where higher seeding temperatures resulted in lower percentages of amorphous content. The exact reason for this is unclear and may be a result of increased micromixing rates due to the lowered solution viscosity, and/or a result of a quickened transition through the amorphous phase at elevated temperature. It was essential to allow time for all the Zr starting material to convert to ZS-9 with the correct stoichiometry before forming the crystalline product, as failing to do so can

result in the formation of other SZC species. As mentioned previously with regards to crystallization space time and temperature, there are likely many possible combinations of seeding space times and temperatures that will help to produce pure and crystalline ZS-9. However, given that 1 hour of crystallization time was determined to be the most beneficial within the tested operating conditions (vide supra), the fluid space time within the 30 mL seeding coil was thus fixed at a corresponding time of 3.9 minutes. Higher seeding temperatures were not tested in the present reaction system but may result in more crystalline products.

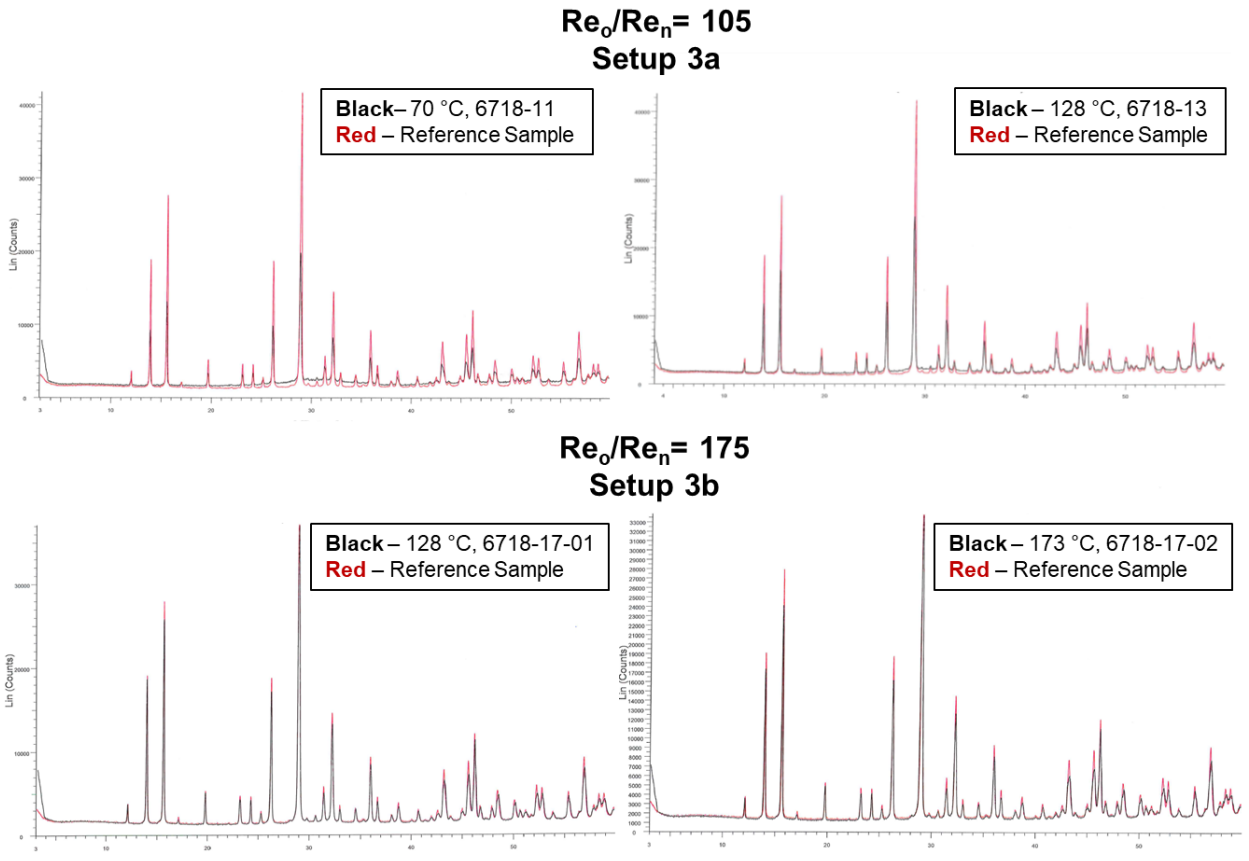

Figure 6.8. Effect of seeding temperature on the product XRD profile. Top row: $\boldsymbol{Re_o/Re_n}$ = 105 in setup 3a. Bottom row: $\boldsymbol{Re_o/Re_n}$ = 175 in setup 3b. All other reaction conditions are as listed in Table 6.1.

During the tests on the space times and operating temperatures, it was observed that the pulsation intensity, i.e. the Re_o value, had a significant impact on the product quality. The effect of the pulsation intensity was therefore tested between the range of Re_o/Re_n from 105 to 175 using the base conditions outlined in Table 6.1, and the results are shown in Figure 6.9. At the presented reaction conditions, only the reaction having the highest Re_o/Re_n value resulted in a pure ZS-9 product. When looking at Figure 6.8, however, it is clear that ZS-9 can also be produced with lower pulsation intensities (although with higher amorphous content) when the seeding temperature is also lower. In batch experiments, it was found that amorphous solid formation is instantaneous upon dropwise addition of ZrOAc to feed-2. It is therefore hypothesized that when the seeding temperature is high (i.e., 173°C), SZC formation becomes micromixing limited with lower pulsation intensities, and a lower micromixing time (via increased pulsation intensity) is likely required to quickly provide a more uniform reaction environment with respect to reagent concentrations in order to promote ZS-9 formation over other SZC species. Conversely, at lower seeding temperatures the SZC formation may be kinetically limited, with formation of ZS-9 occurring more rapidly than ZS-7.

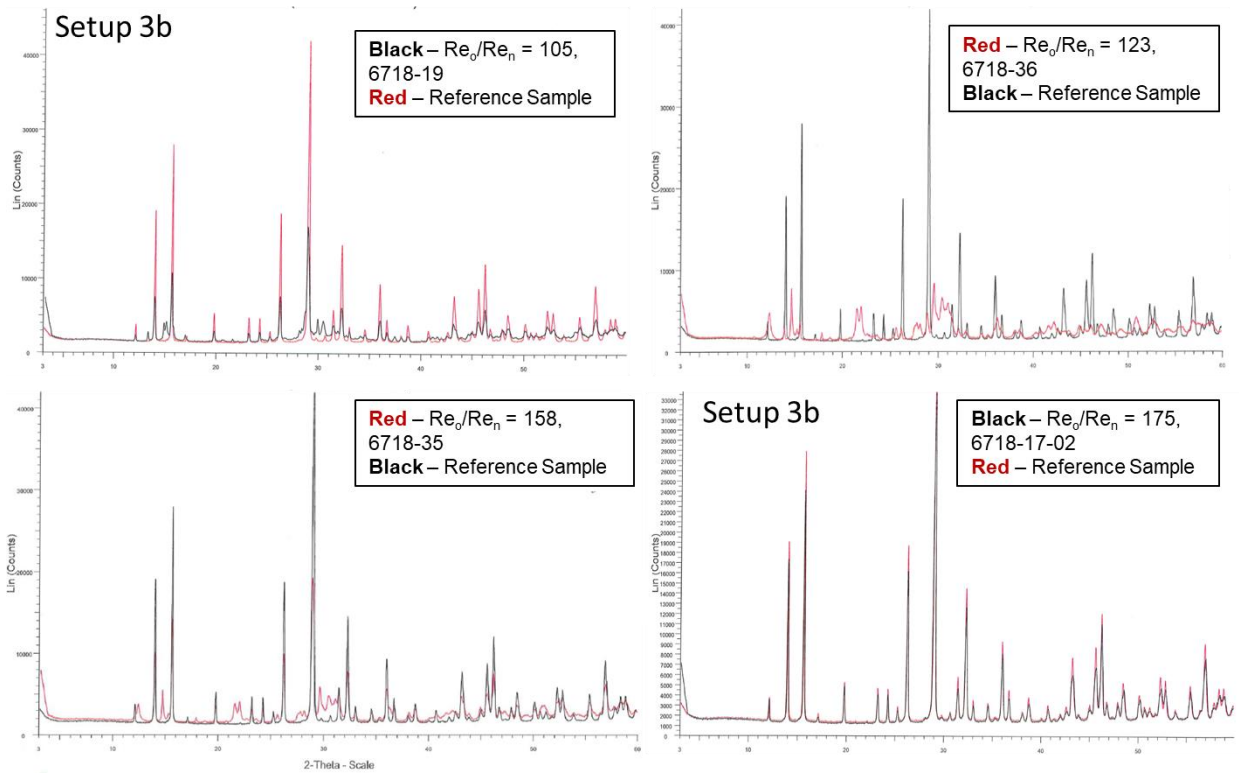

Figure 6.9. Effect of pulsation intensity ($\boldsymbol{Re_o/Re_n}$) on the product XRD profile. All other reaction conditions are as outline in Table 6.1.

Based on the results above, the final operating conditions for ZS-9 production were selected to have a 1 hour crystallization fluid space time at 245°C, a 173°C seeding temperature, and a Re_o/Re_n ratio of 175. Analyses of the product, including XRD, scanning electron microscopy (SEM), and PSD, are shown in Figure 6.10 below. With these reaction conditions, pure cubic ZS-9 crystals are generated with no amorphous content, and with 9.81 vol% of particles having a diameter less than 3 µm. Although the particles did not ultimately meet the goal of less than 3 vol% below 3 µm, the remaining ~7 vol% of small particles could be removed via filtration[195]. With these operating conditions, solid product was produced at a rate of 40 g/hour from an 8.5 wt% ZS-9 solution.

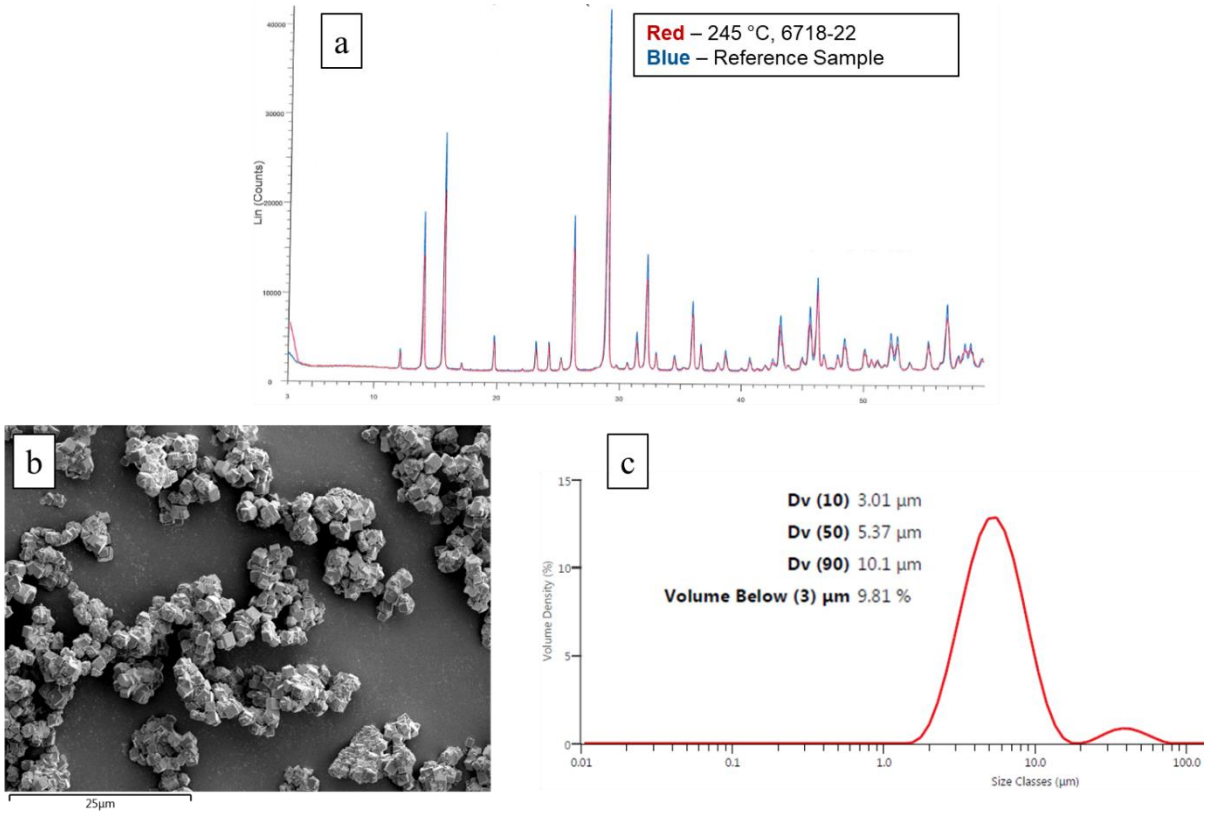

Figure 6.10. Analysis of the ZS-9 product at the final selected operating conditions. a: XRD profile showing pure ZS-9 with no amorphous content. b: scanning electron microscopy showing cubic ZS-9 crystals, scale bar = 25 µm. c: PSD reporting 9.81 vol% of product crystals below 3 µm diameter.

6.5 **Scale-Up to Production Scale**

The desired final amount of ZS-9 production lies in the tonne scale. Considering the rate of ZS-9 production achieved in the above experiments at lab scale, a substantially higher throughput and resulting reactor volume will be required in order to produce such a quantity of material in a reasonable time frame. For the purpose of the analysis and discussion below, the scaled-up product throughput is set at a rate of 1 tonne in 3.5 days, or 11.9 kg/hr of product, which is 288 times greater than that obtained at lab-scale. Using an 8.5 wt% solution (as obtained at lab-scale) results in a net throughput of roughly 140 kg/hr or 117 L/hr. The volumes of the larger coils should

therefore be 117 L for the crystallization coil (1-hour fluid space time) and 11.4 L for the seeding coil (3.9 min fluid space time).

In baffled oscillatory flow reactor geometries, scale-up has previously been performed by maintaining both geometric similarity in the baffle size and orientation, and dynamic similarity in the fluid mixing as governed by a set of dimensionless groups [196–198], i.e., the net flow Reynold's number (Re_n), the oscillatory Reynold's number (Re_o), the Strouhal number (St_r), shown in equations (3.2) to (6.4), and the resulting velocity ratio (Re_o/Re_n).

$$Re_n = \frac{\rho u_n D}{\mu} \tag{6.2}$$

$$Re_o = \frac{\rho u_o D}{\mu} \tag{6.3}$$

$$St_r = \frac{D}{4\pi x_o} \tag{6.4}$$

Here, ρ is the fluid density (taken to be 796 kg/m^3 for water at 245°C), u_n is the net fluid superficial velocity, u_o is the oscillatory superficial velocity, D is the tube inner diameter, μ is the fluid dynamic viscosity (0.11 mPa·s at 245°C), and x_o is the center-to-peak oscillation amplitude in the reactor. u_o is calculated via equations (6.5) and (6.6), where ω is the angular frequency, t is the time in the pulsation period, and f is the frequency of oscillation.

$$u_o = x_o \omega \sin(\omega t) \tag{6.5}$$

$$\omega = 2\pi f \tag{6.6}$$

Due to the constantly changing fluid velocity resulting from the pressure oscillations, a single oscillatory velocity is typically taken at the maximum, i.e., when the sinusoidal component is equal to 1:

$$u_o = x_o \omega \tag{6.7}$$

In a previous study performed by Ahmed *et al.* [198], geometrically similar scale-up by conserving the value of these dimensionless variables was quantified at the macromixing scale, and the number of CSTRs in series (N) was found to remain conserved between oscillatory helical baffled reactors (OHBRs) of 10 and 25 mm in diameter, leading to the scale-up correlation below that was further validated in a 50 mm diameter OHBR.

$$N = 10 Str_r^{-0.3} \left(\frac{Re_o}{Re_n}\right) e^{-0.1\left(\frac{Re_o}{Re_n}\right)} + 0.85 Re_n^{0.6} \tag{6.8}$$

Applications of similar scale-up methodologies are also presented in two case studies by Stonestreet and Harvey [197]. Thus, in oscillatory baffled reactors, macromixing may be controlled during scale-up via geometrical similarity and the dimensionless groups presented above.

Rapid mixing of the feeds in the seeding coil is also essential to favour production of the correct SZC crystal form (ZS-9). Micromixing times (treated herein as mean micromixing times when considering potential distributions of energy dissipation rates within the reactor) in the seeding coil should therefore be maintained upon scale-up, where engulfment has previously been shown to play a major role in oscillatory baffled reactor micromixing times [51], and the timescale for engulfment (t_E) is inversely proportional the energy dissipation rate (ϵ) according to equation (6.9) [137].

$$t_E = 17 \left(\frac{\nu}{\epsilon}\right)^{0.5} \tag{6.9}$$

The micromixing time may therefore be maintained upon scale-up by operating at an equivalent energy dissipation rate in the seeding coil.

In order to maintain macromixing via the Re_n, Re_o, and St_r, at the larger scale production rate indicated above, applying equations (3.2) to (6.7) leads to parallelization of reactors in order to achieve reasonable geometric dimensions (Z/D_c) and oscillation amplitudes and frequencies. However, equation (6.8) shows that if both St_r and Re_o/Re_n are maintained, increasing the flowrate (Re_n) will likely result in a higher value of N and an improvement in macromixing. A single large-scale reactor then become available if Re_n is allowed to increase. Thus, the following design methodology is proposed to determine reactor dimensions that conserve both St_r and Re_o/Re_n in the crystallization coil and ϵ_o in the seeding coil.

The total energy dissipation rate in an oscillatory system can be calculated according to equations (6.10) and (6.11) below as a summation of the net and oscillatory flow components.

$$\epsilon = \epsilon_{net} + \epsilon_o \tag{6.10}$$

$$\epsilon = \frac{\Delta P_{net} Q_{net}}{\rho V_R} + \frac{1}{2}\frac{\Delta P_o cos(\delta) x_{coil} \omega}{Z\rho} \tag{6.11}$$

Here, ΔP_{net} is the net flow pressure drop, Q_{net} is the net volumetric flow rate, V_R is the reactor volume, ΔP_o is the center-to-peak pressure oscillation amplitude, δ is the phase angle which in this case is assumed to be 0, and Z is the reactor length. In an oscillatory system, ΔP_o can be modelled according to equation (6.12) using the maximum oscillatory velocity and friction factor (λ).

$$\Delta P_o = \frac{\lambda Z \rho u_o^2}{2D} \tag{6.12}$$

Substitution of equation (6.12) into equation (6.11) leads to the following relation for the energy dissipation rate that is independent of the reactor length.

$$\epsilon_o = \frac{\lambda Z \rho u_o^3}{4D\rho Z} = \frac{\lambda u_o^3}{4D} \quad \textbf{(6.13)}$$

Several models for friction factors in helically coiled channels have been proposed [199], including those by Srinivasan [200] presented in Table 6.2 where Re_o and the oscillatory Dean number (De_o, equation (6.14)) have been used in place of the original Re and the Dean number (De).

$$De_o = Re_o \sqrt{\frac{D}{Dc}} \quad \textbf{(6.14)}$$

Table 6.2. Friction factor correlations and conditions for helically coiled tubes.

Correlation	Author	Conditions
$\lambda = 32/Re_o$	Srinivasan[200]	$0.0097 < D/D_c < 0.135$ $Re_o\sqrt{D/D_c} < 30$
$\lambda = 5.22\left(Re_o\sqrt{\frac{D_c}{D}}\right)^{-0.6}$	Srinivasan[200]	$30 < Re_o\sqrt{D/D_c} < 300$
$\lambda = 1.8\left(Re_o\sqrt{\frac{D_c}{D}}\right)^{-0.5}$	Srinivasan[200]	$300 < Re_o\sqrt{D/D_c} <$ $Re_{crit}\sqrt{D/D_c}$
$\lambda = 1.084\left(Re_o\sqrt{\frac{D_c}{D}}\right)^{-0.2}$	Srinivasan[200]	$Re_o > Re_{crit}$

In order to determine which of the above models is applicable, the critical Reynolds number in a helically coiled tube can be calculated according to correlations presented in the literature [201] and summarized in Table 6.3 below. At the final selected operating conditions, Re_o, having a value of 62455, is an order of magnitude greater than Re_c.

Table 6.3. Correlations and resulting critical Reynolds numbers for flow through helical coils.

Correlation	Reference	Calculated Re_c
$Re_{crit} = 2000\left(1 + 13.2\left(\frac{D}{D_c}\right)^{0.6}\right)$	[202]	5237
$Re_{crit} = 2100\left(1 + 12\left(\frac{D}{D_c}\right)^{0.5}\right)$	[203]	6484

The correlation of Srinivasan [200] for $Re_o > Re_{crit}$ is therefore employed for estimation of the friction factor and substituted into equation (6.13) as follows:

$$\epsilon_o = \frac{\left(1.084\left(Re_o\sqrt{\frac{D_c}{D}}\right)^{-0.2}\right)u_o^3}{4D} \quad \textbf{(6.15)}$$

At the lab scale operating conditions outlined previously, the resulting energy dissipation rate in the seeding coil is about 27.8 W/kg. The energy dissipation rate in the larger seeding coil should therefore be the same or higher, where higher energy dissipation rates will result in reduced micromixing times.

Because ϵ_o in the seeding coil and Re_o/Re_n in the crystallization coil are inherently linked by the oscillatory velocity generated by the pulsator, it is necessary to perform the calculations in tandem with the crystallization coil. The highest tested velocity ratio produced the best quality product as shown previously in Figure 6.9. It is therefore desirable to achieve an equal or similar velocity ratio in the larger scale crystallization coil while also maintaining the calculated St_r value (0.0052). Geometrical similarity in the helical reactor may be maintained though constant ratios of inner diameter to coil diameter ($D/D_c = 0.030$) and inner diameter to pitch ($D/P = 0.46$). Thus, in order to achieved the desired macromixing and micromixing in the scaled-up reactor, the

following conditions should be satisfied: 1) in the crystallization coil, Re_o/Re_n = 175, St_r = 0.0052, D/D_c = 0.030, D/P = 0.46, and 2) in the seeding coil, ϵ_o = 27.8 W/kg using the friction factor model of Srinivasan [200] and equation (6.15) above.

The required Re_o in the crystallization coil can thus be obtained from equation (6.16).

$$Re_o = 175 Re_n \tag{6.16}$$

Conversely, when the seeding coil $\epsilon_o$is fixed at 27.8 W/kg, u_o in the seeding coil can be calculated for a given diameter from equation (6.17) below.

$$u_o = \left(\frac{4\epsilon D}{1.084 \left(\frac{\rho D}{\mu} \sqrt{\frac{D_c}{D}} \right)^{-0.2}} \right)^{\frac{1}{2.8}} \tag{6.17}$$

In the most direct method of scale-up, geometrical similarity of the whole system is maintained and both seeding and crystallization coils will have the same diameter (as was the case in lab-scale development). The scale-up calculations can therefore be initiated from either equation (6.16) using the crystallization coil Re_o/Re_n, or from equation (6.17) using a value of ϵ_o = 27.8 W/kg in the seeding coil. The results from both methods of calculation as a function of reactor diameter are shown in Figure 6.11. The result is the same in either case, and when the diameter of both reactors is increased to 47.00 mm, both ϵ_o and Re_o/Re_n values are conserved upon scale-up. A summary of the dimensions and oscillatory conditions for the larger reactors is outlined in Table 6.4. Note that in the scaled-up reactor, the value of Re_n is significantly larger than in the lab-scale system, which is expected to improve macromixing with respect to the number of tanks in series as described above in equation (6.8). Additionally, although the solids themselves may be subject to a different RTD than that of the fluid phase [61,164], a similar improvement is expected with the

increase in Re_n. Importantly, if even lower micromixing times are desirable in the seeding coil, a smaller diameter coil may be implemented as the energy dissipation rate increases rapidly with a decrease in diameter. However, larger diameter coils will benefit from reduced clogging rates, longer continuous run times, and lower power requirements. The pulsator is also an important consideration during scale-up, as the model used during lab-based development is not capable of generating the oscillation amplitude and frequency shown in Table 6.4. A larger pulsator will therefore be required that can generate the desired oscillatory velocity as well as have a tolerance to accommodate the increased magnitude in pressure oscillation.

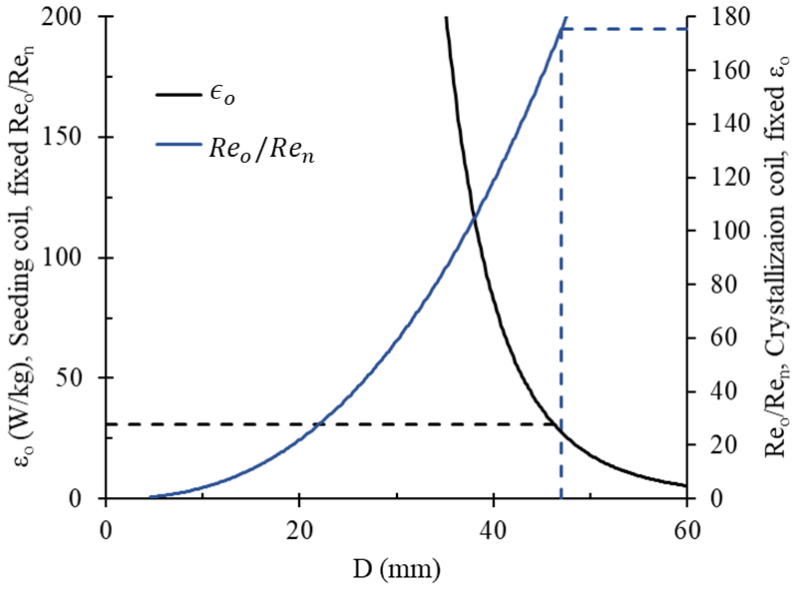

Figure 6.11. $\boldsymbol{\epsilon_o}$ and $\boldsymbol{Re_o/Re_n}$ as a function of increasing reactor diameter. Dashed black and blue lines correspond to $\boldsymbol{\epsilon_o}$ = 27.8 W/kg (seeding coil) and $\boldsymbol{Re_o/Re_n}$ = 175, respectively.

Table 6.4. Dimensions for the scaled-up oscillatory coil reactor and resulting oscillatory flow parameters where geometric similarity is maintained throughout the system.

		Lab-scale		**Production-scale**	
Coil	--	Seeding Coil	Crystallization Coil	Seeding Coil	Crystallization Coil
V_R	L	0.0273	0.400	11.4	117
D	mm	4.57		47.0	
D_c	mm	240	352	1234	1553
P	mm	6	10	15	102
Z	m	1670	24	6.6	100.8
Re_n	--	356		9952	
Re_o/Re_n	--	175		175	
Re_o	--	62455		1744500	
St_r	--	0.0052		0.0052	
x_o	mm	70.4		114.3	
f	Hz	4.09		6.8	
ϵ_o	W/kg	27.8	27.2	27.8	27.2

Using the above methodology, dimensions for a scaled-up reactor have been proposed with the objective of maintaining macromixing, micromixing, and heat removal. Operating conditions have been proposed that will serve as a basis for ZS-9 production at larger scale. However, further characterization and development of the larger scale reactor will ultimately have to occur in a factory based setting[100] in order to validate the scale-up methodology and the use of mean micromixing times in order to arrive at final operating conditions for commercial production.

6.6 **Conclusions**

In this chapter, development of an intensified continuous flow system for production of ZS-9 was outlined. The Hastelloy and stainless-steel construction of the reaction system allowed for system operation at temperatures of up to 262 °C and maximum oscillatory pressures up to 80 barg. The reaction system was divided into two regions, where region 1 was comprised of all

components up the crystallization coil inlet and was identified as the key region where physical system modifications would lead to longer run times and higher purity products. Development of this region progressed through several iterations from a simple T-junction mixing point leading into the crystallization coil, to the final iteration which included a seeding loop and preheated seeding coil. In this setup, several long run experiments were performed with run times of 390 min, 405 min, 405 min, 300 min, and 300 min, respectively. Through an investigation of operating conditions, this system was capable of continuously producing pure and crystalline ZS-9 with no pressure spikes indicating the formation of blockages.

Several operating conditions were tested in the various reaction setups in order to reach a set of product specifications that included pure ZS-9 with no amorphous content and cubic particles where less than 3 vol% had a size below 3 µm. During these tests, it was found that ZS-9 formation proceeds first through generation of and amorphous solid, followed by crystalline ZS-9, and followed thereafter by a transition to ZS-7. A 1-hour fluid space time in the crystallization coil at 245 °C was determined suitable for producing ZS-9 that is crystalline and had not yet transitioned to ZS-7. With the fluid space time thus fixed within the system, a higher seeding temperature of 173°C was also found to reduce the amount of amorphous content in the product. At these operating conditions, full intensity oscillation (i.e., Re_o/Re_n value of 175) was necessary to produce the correct ZS-9 product. The final product was produced at a rate of 40 g/h in an 8.5 wt% suspension with 9.81 vol% of particles having a size less than 3 µm; sieving will therefore be required to remove the small particles.

Scaled-up reactor dimensions were proposed in order to obtain a ZS-9 production rate of 1 tonne per 3.5 days. A larger volume and diameter reactor was required in order to achieve the desired production rate within a reasonable space-time. Macromixing scale-up was proposed

through maintaining geometrical similarity, the velocity ratio Re_o/Re_n, and Str. Micromixing scale-up calculations were performed using friction factor correlations for helical coils and the resulting energy dissipation rates. The relevant transport rates within the system were found to be maintained or enhanced when both reactors have an internal diameter of 47.00 mm. Using this diameter, the lengths of each proposed reactor are 6.6 m and 100.8 m for the seeding and crystallization coils respectively, and the oscillator should be operated with an in-coil amplitude and frequency of 114.3 mm and 6.8 Hz. These operating parameters will serve as a basis for further characterization and development of the continuous ZS-9 production system in a factory-based setting in order to determine the final operating conditions for production at commercial scale.

Nomenclature

Symbol	Meaning	Units
D	Tube inner diameter	m
D_c	Coil diameter	m
De_o	Oscillatory Dean number	--
D_{v10}	Volume equivalent diameter accounting for 10% of the particle size distribution	µm
D_{v50}	Mean volume equivalent diameter	µm
D_{v90}	Volume equivalent diameter accounting for 90% of the particle size distribution	µm
D	Coil diameter	m
f	Oscillation frequency	--
N	Number of tanks in series	--
P	Coil Pitch	m
P_{net}	Net flow pressure	Pa
P_o	Oscillatory pressure	Pa

Q_{net}	Net volumetric flow rate	mL/min
r_{coil}	Coil radius of curvature	m
Re_{crit}	Critical Reynolds number	--
Re_n	Net flow Reynolds number	--
Re_o	Oscillatory Reynolds number	--
St_r	Strouhal number	--
t_E	Mixing time via engulfment	s
u_n	Net flow velocity	m/s
u_o	Oscillatory velocity	m/s
$u_{o,max}$	Maximum oscillatory velocity	m/s
V_R	Reactor volume	m^3
x_{coil}	Center to peak oscillation amplitude in the coil	m
Z	Coil length	m

Greek Symbols

Symbol	Meaning	Units
δ	Phase angle	rad
ϵ	Average energy dissipation rate	W/kg
ϵ_{net}	Net flow energy dissipation rate	W/kg
ϵ_o	Oscillatory energy dissipation rate	W/kg
λ	Friction factor	--
μ	Dynamic viscosity	Pa s
ν	Kinematic viscosity	m^2/s
ρ	Density	kg/m^3
ω	Oscillation angular frequency	rad/s

7. Conclusions and Future Research

7.1 Conclusions

In this thesis, alternative and emerging technologies for pharmaceutical production were explored. Mini-monoplant technology was presented as an alternative means to pharmaceutical process development, where intensification, dedication, and continuous processing (when applicable) are key value-generating factors at all stages of process development. Mini-monoplant development occurs through three principal stages of lab-based development, factory-based development, and finally mini-monoplant technology at production scale. In lab-based development chemists and engineers work towards best-in-class processes through the use of novel reaction pathways, intensified reactors, automation, and dedication, with a small footprint in the safety of a laboratory. Then, in factory-based development, the miniplant developed in the lab can be moved to an available cabin within the existing plant infrastructure where access to large volume feed and product storage tanks allows for process scale-up with respect to throughput in order to meet the product demand for clinical trials. Here, a similar level of flexibility as was available in the laboratory is expected, and the use of predesigned and potentially GMP-prequalified modules can result in a significant reduction in development time and time to market. Following this stage of development, and when a pharmaceutical product has gone commercial, acquisition and installation of dedicated production assets in a dedicated area within the plant results in a so-called mini-monoplant. At this stage, the final scale-up with respect to overall process operation time occurs and where dedication facilitates year-round operation if required in order to rapidly respond to fluctuations in product demand.

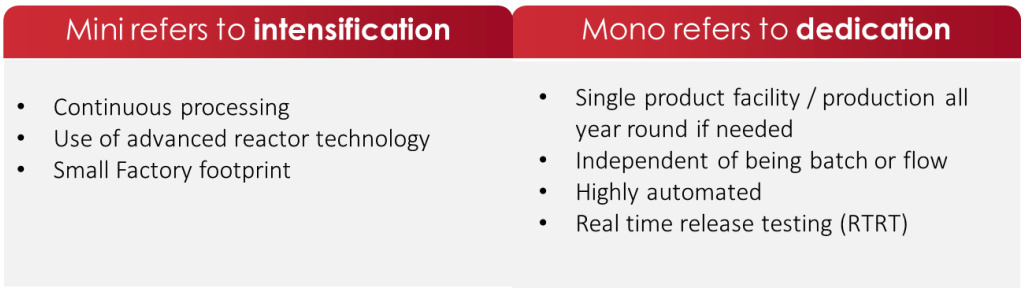

Figure 7.1. Defining features of a mini-monoplant.

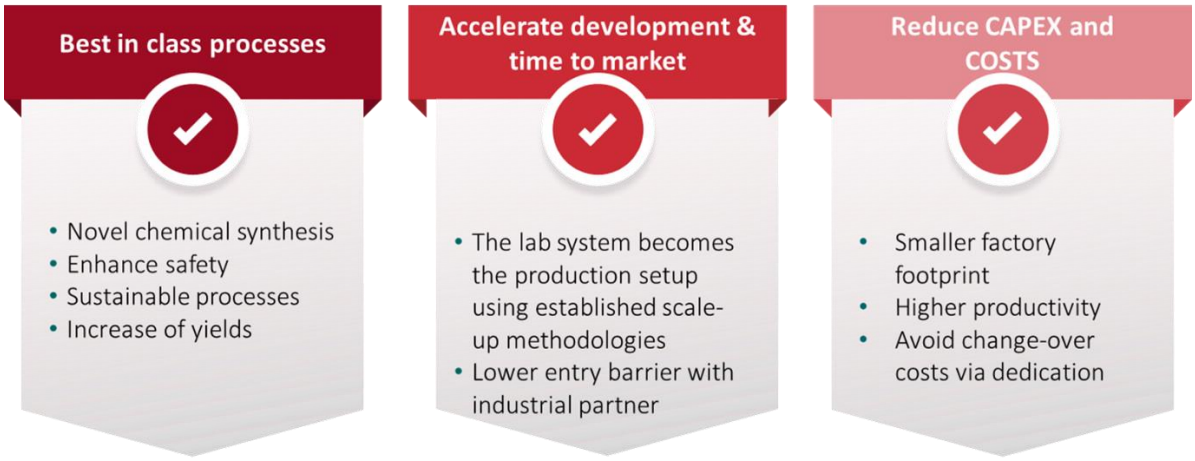

Figure 7.2. Three key advantages realized through the intensification of monoplants into mini-monoplants for pharmaceutical production

Within the context of mini-monoplant technology, several reactor geometries were then explored covering a range of scales, throughputs, phases, and reaction types. Plate-type microreactors were characterized for gas-liquid flow and interphase mass transfer, and for scale-up within the scope of performing a viscous and exothermic nitration reaction. Baffleless oscillatory flow coil reactors were then described and tested for their solid handling capabilities and macromixing, followed by continuous production of an API at high temperature and pressure in a larger baffleless oscillatory flow coil reactor.

In the gas-liquid study, the effects of geometry and surfactant on flow regimes and interphase mass transfer were studied in size 300 LL-Rhombus and LL-Triangle microreactor plates with

$CO_{2(g)}$ and either water, or water containing 0.5 wt% ethanol as a surfactant. Both geometries generated flow regimes comparable to other microchannels with similar hydraulic diameters, although with a tendency to favour bubble flow at low gas velocities and annular flow at high gas velocities. The LL-Rhombus was found to be more favourable to the LL-Triangle in generating higher $k_l a$ values at lower pressure drops. When ethanol was used as a surfactant, bubble flow was present at every tested operating condition. Finally, the pressure drops and $k_l a$ values were modelled using the Lockhart-Martinelli two-phase pressure drop model and a power-dissipation based model, respectively, with each having an average absolute relative error less than 8.1% and 13.9%.

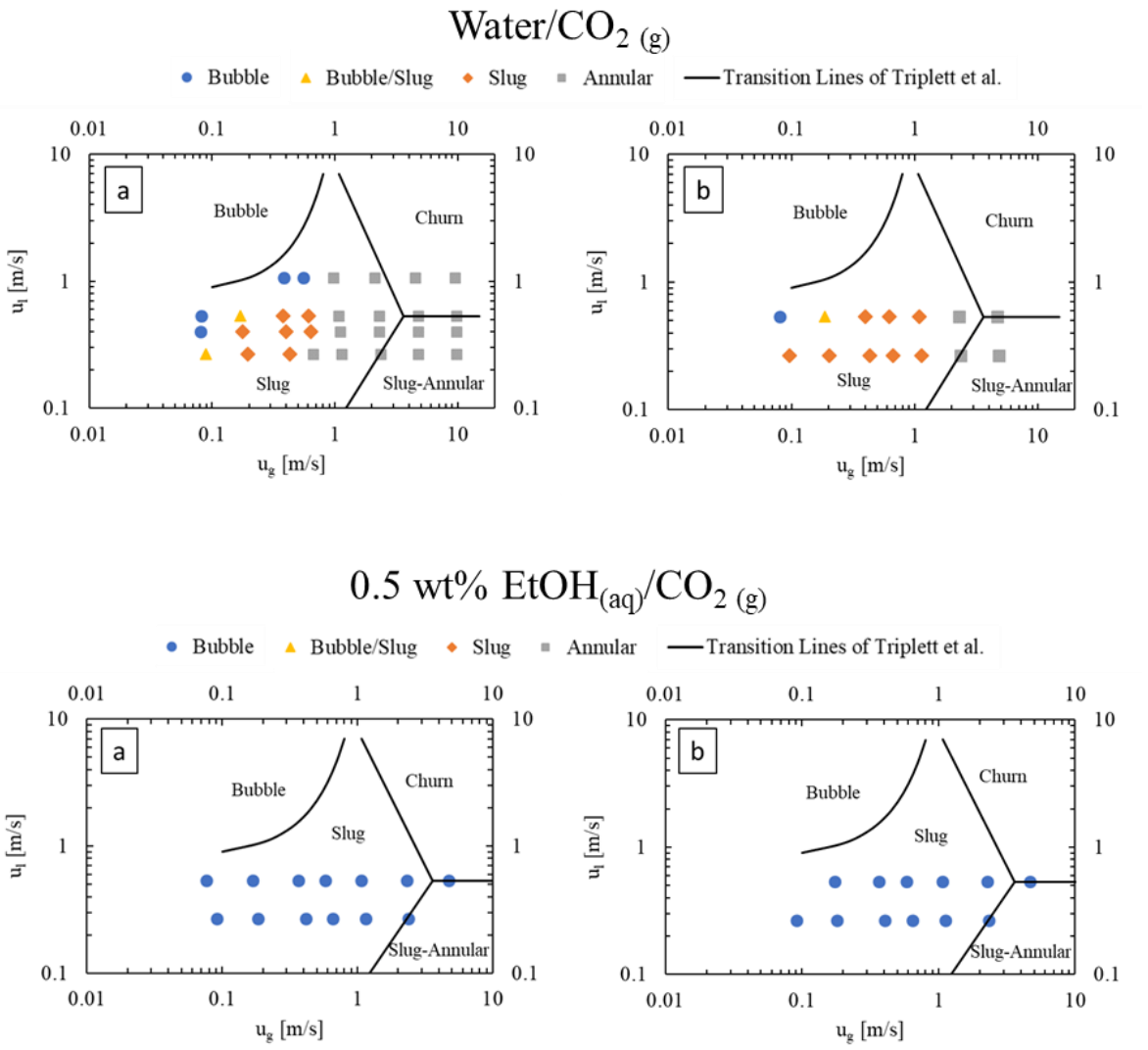

Figure 7.3. Flow regime maps in the LL-Rhombus (a) and the LL-Triangle (b) for both the water/$CO_{2\ (g)}$ (top) and 0.5 wt% $EtOH_{\ (aq)}$ (bottom) systems.

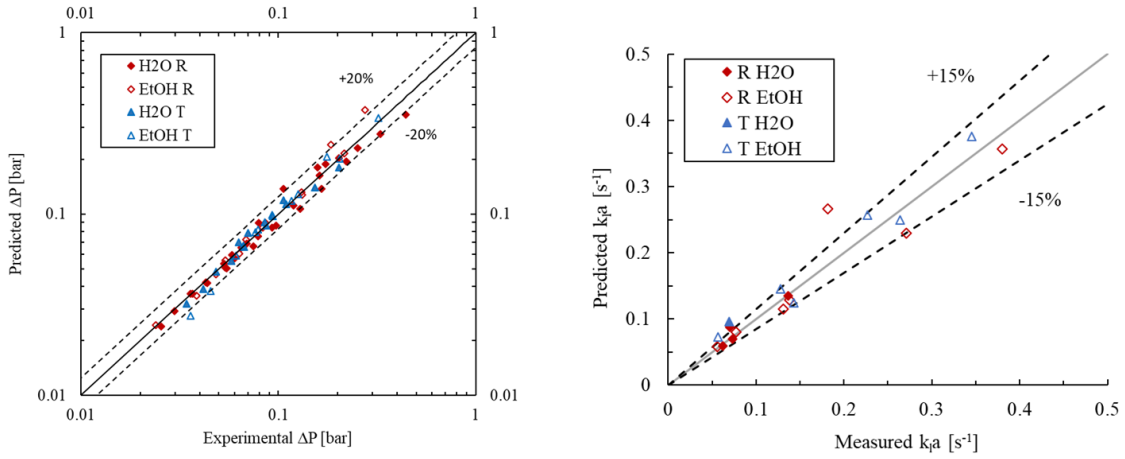

Figure 7.4. Pressure drop modelling for all data (left) and $\boldsymbol{k_l a}$ modelling for the bubble flow data (right) for both the LL-Rhombus and LL-Triangle with and without surfactant.

Mean micromixing performance was then evaluated in various LL-microreactor plates in order to facilitate the scale-up of a viscous nitration from 75 mL/min to flowrates in the range of 350 mL/min at production scale. The 3/7th rule for scale-up in fully turbulent flow was extended into flow regimes that were either transitional or contained significant contributions from turbulent flow patterns. Scale-up rules were derived for both water and 96 wt% $H_2SO_{4\,(aq)}$ in order to predict larger-scale flowrates where mean energy dissipation rates would be conserved. In both systems, the experimentally obtained mean energy dissipations exceeded the values predicted by the derived scale-up rules. Friction factors were then analyzed to determine the relative contributions of turbulent flow patterns in each operating condition and were found to increase with channel diameter at equivalent energy dissipation rates due to an increase in Re. This effect was more apparent with 96 wt% $H_2SO_{4\,(aq)}$ due to operation in the transitional flow regime, whereas the water data was largely turbulent. A static mixer geometry was also tested, but resulted in a significant decrease in the relative contributions of turbulent flow and was thus deemed oversized for the mizing limited nitration. Mean micromixing performance measures were therefore conserved or improved upon scale-up with the use of LL-microreactor plates, but further characterization of the

reaction itself at large scale is still required in order to determine the ultimate effect on product yield.

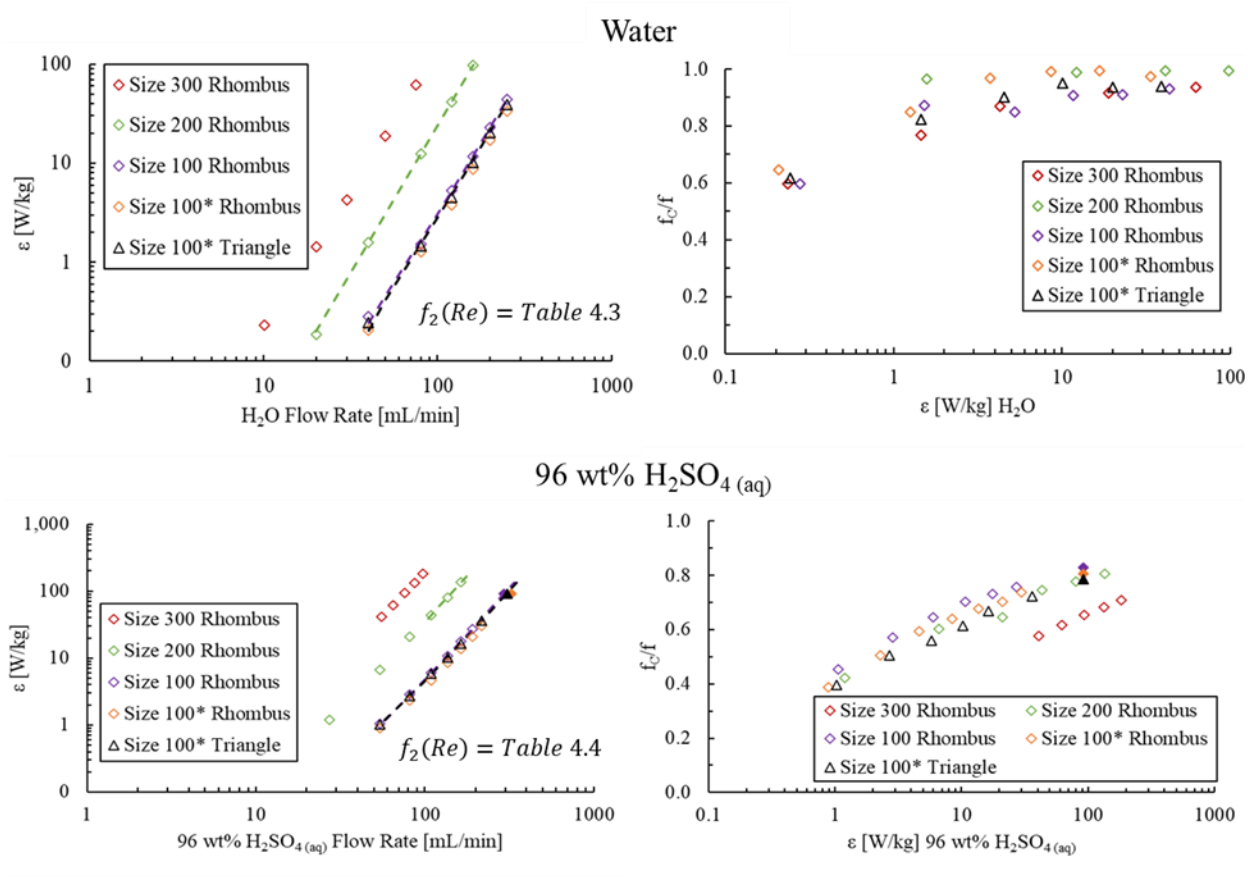

Figure 7.5. Measured and scale-up rule-predicted (dashed lines) energy dissipation rates with water (top) and 96 wt% $H_2SO_{4\ (aq)}$ (bottom) presented alongside relative contributions of turbulent flow as a function of energy dissipation rate (rate)

Next, the solid handling capabilities and flow patterns of the baffleless oscillatory flow coil were characterized through two solid forming reactions: a precipitation reaction and a mass transfer limited phase transfer catalysis reaction. In the first reaction, a continuous oscillatory energy dissipation rate of 13 W/kg allowed for continuous operation with a solid concentration of 5.8 wt% for 5 hours, or with solid concentrations up to 7.9 wt% for 120 minutes with no observed pressure spikes indicating clog formation. Importantly, lower oscillation power inputs were also

effective in preventing blockage and the maximum run time with a given solid suspension is currently unknown. In the second reaction, formation of $CO_{(g)}$ as a side product resulted in a tenfold dampening of the pulsation energy dissipation rate from 10 W/kg to 0.8 W/kg and subsequent clogging, suggesting that gas formation in a closed pulsated system is a unique problem and the reaction medium must be incompressible. Finally, macromixing was characterized through RTD studies and showed that the relatively intense pulsation energy input resulting in broadening of residence time and particle size distributions. However, as lower pulsation intensities proved capable of preventing clogging with incompressible flows in the presented reactor system, further optimization of the relative net and oscillatory flow velocities may allow for more plug flow residence time distributions.

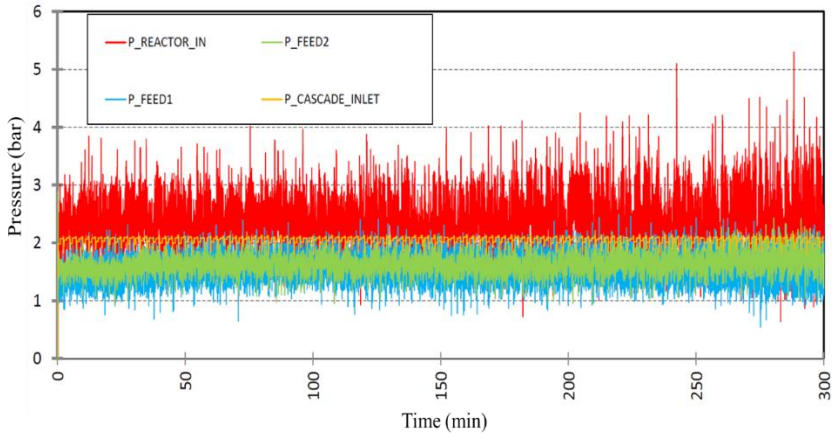

Figure 7.6. Continuous operation for 300 minutes with a constant pulsation energy input and a solid suspension of 5.8 wt%.

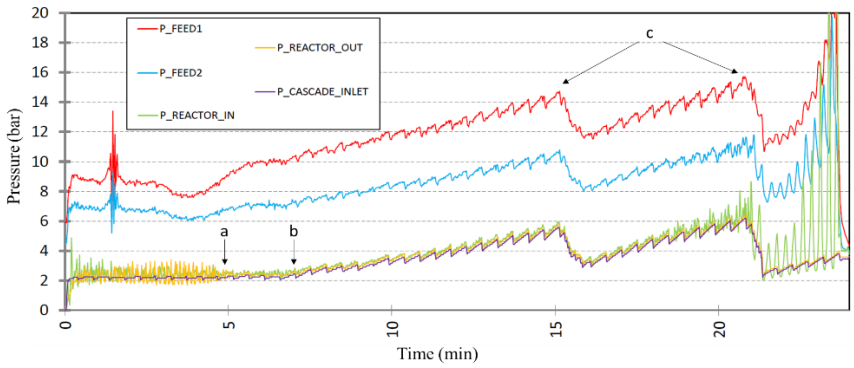

Figure 7.7. Pulsation dampening and resulting blockage caused by the formation of gas in a closed pulsated system.

Finally, a larger volume baffleless oscillatory flow reactor was implemented in the continuous production of a ZS-9 suspension at high temperature and pressure. Development of the reaction system itself was outlined, particularly with respect to the region upstream of the crystallization coil entrance, where physical changes made to the system led to longer continuous run times and higher purity ZS-9 product. This region proceeded through several iterations which began initially as a simple T-junction mixing point and ended with a seeding loop and preheated seeding coil. Next, parametric studies of the operating conditions for the reaction were performed in order to generate pure and crystalline ZS-9 as cubic particles with less than 3 vol% having a diameter below 3 µm. Through these results, it was proposed that ZS-9 formation proceeds first through the generation of an amorphous solid, followed by crystalline ZS-9, and then through a transition to crystalline ZS-7. Accordingly, the final operating conditions were proposed as follows and generated an 8.5 wt% solution of ZS-9 at 40 g/h: 1 hour residence time at 245 °C in the crystallization coil, a seeding temperature of 173 °C, and full intensity oscillation input (with Re_o/Re_n = 175). The ZS-9 particles produced under these conditions were ultimately larger than desired (9.81 vol% > 3 µm) and will require sieving. Finally, scaled-up reactor dimensions were proposed for producing ZS-9 at a rate of 1 tonne per 3.5 days, with the goal of maintaining both

macromixing through geometric similarity, velocity ratio, and Strouhal number, and micromixing through friction factor correlations for helical coils and the resulting energy dissipation rates. Overall performance at both mixing scales is suggested to be conserved when geometric similarity is maintained throughout the entire system, and both the seeding and crystallization coils have internal diameters of 47.00 mm. The corresponding lengths of each proposed reactor are 6.6 m and 100.8 m for the seeding and crystallization coils, respectively, and the required pulsation amplitude and frequency are 114.3 mm and 6.8 Hz. Ultimately, however, these operating conditions will serve as a basis for further characterization and development of the production scale system in factory-based development.

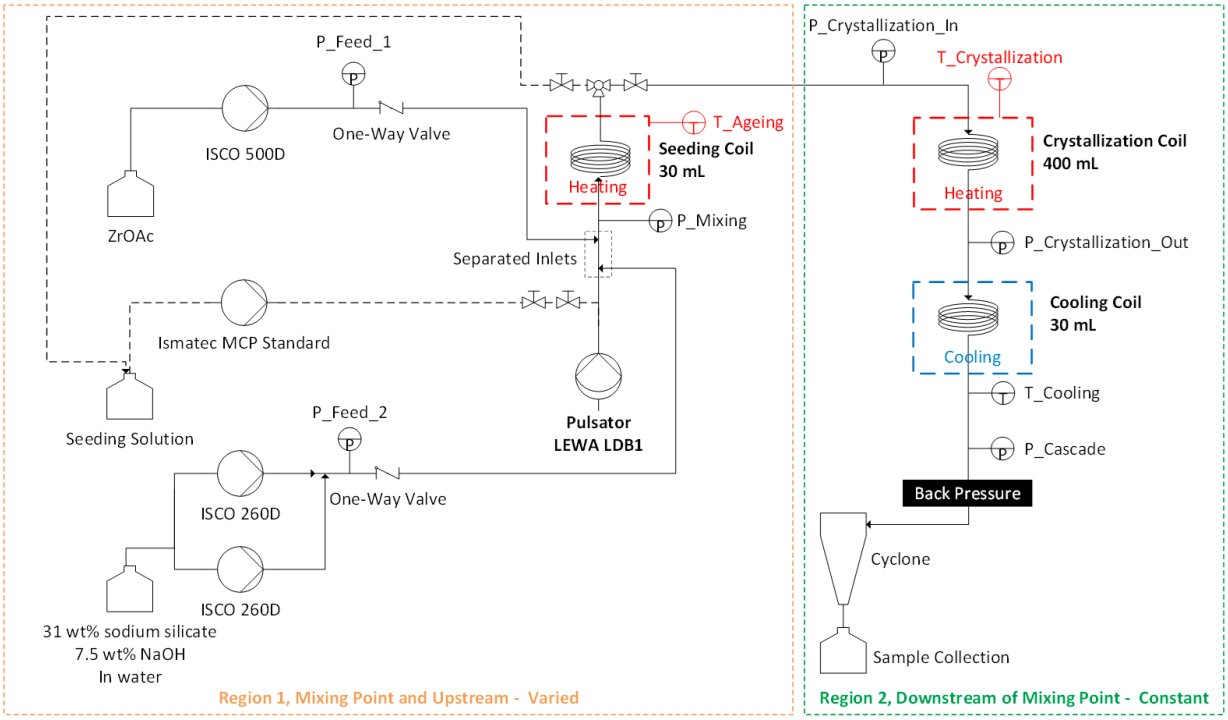

Figure 7.8. Final operating system configuration for the continuous production of a ZS-9 suspension under oscillatory flow.

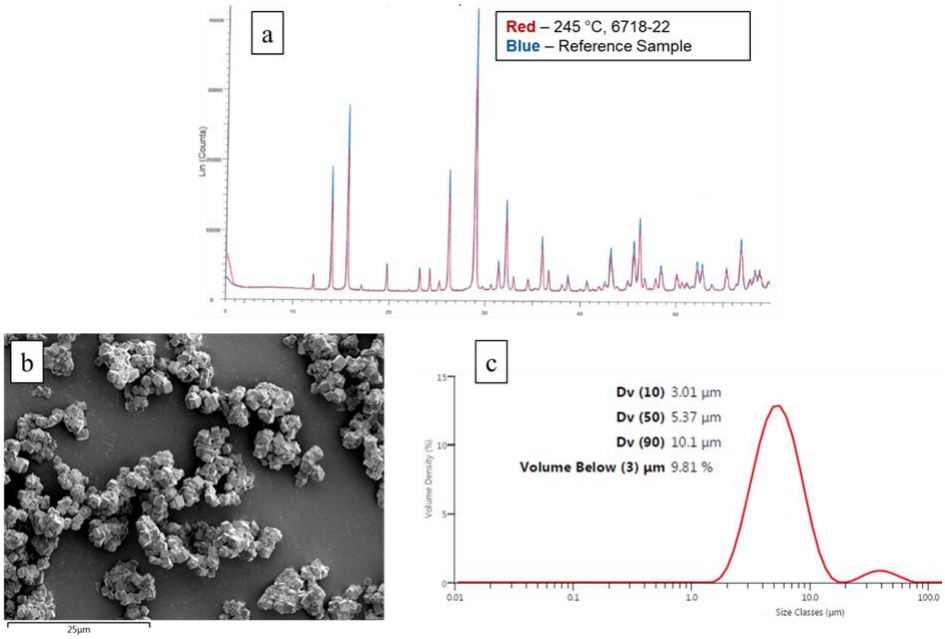

Figure 7.9. Lab-produced ZS-9 product profile showing pure and crystalline ZS-9 (a), cubic particles (b), and an average particle diameter of 5.37 µm with 9.81 vol% having a diameter below 3 µm.

7.2 **Recommendations for future research**

Based on the results obtained and presented in this thesis, the following recommendations are proposed for future research in order to obtain a more in-depth understanding of the present reactor systems:

- CFD modelling of the presented reaction systems, including gas-liquid flow in the size 300 plate microreactors, single phase flow in the size 200 and larger plate microreactors, and single-phase oscillatory flow in the baffeless coil reactors. Such work will deepen the understanding of the underlying fluid mechanics in each of the reaction systems, including variations in local energy dissipation rates and mixing patterns.
- Performance of the large-scale nitration reaction in a factory-based setting in order to validate the scale-up methodology. This work will provide reaction yields at large scale

in order to complete the nitration scale up work, which will thus include lab-scale reaction data, the scale-up methodology included in Chapter 4, and finally production scale reaction data.

- Longer, continuous operation of the baffleless oscillatory flow coil reactors in a factory-based setting in order to determine typical maximum operation times. Presently, it is not known for how long the baffleless oscillatory flow coil reactor can operate continuously with solid suspensions. Factory-based development will allow for the larger reagent volumes required to perform such work.
- Development and characterization of the production scale oscillatory flow coil reactor for ZS-9 production in a factory-based setting in order to validate the scale-up methodology. Similarly to the nitration scale-up, real reaction data are required to evaluate the proposed scale-up methodology in Chapter 6, where the reactor and reagent volumes required will necessitate a factory-based setting.

8. References

1. Plouffe, P.; Macchi, A.; Roberge, D.M. From Batch to Continuous Chemical Synthesis-A Toolbox Approach. *Org. Process Res. Dev.* **2014**, *18*, 1286–1294, doi:10.1021/op5001918.
2. Moulijn, J.A.; Makkee, M.; Van Diepen, A.E. *Chemical Process Technology*; 2nd ed.; John Wiley & Sons, 2013; ISBN 978-1-444-32025-1.
3. Roberge, D.M.; Ducry, L.; Bieler, N.; Cretton, P.; Zimmermann, B. Microreactor technology: A revolution for the fine chemical and pharmaceutical industries? *Chem. Eng. Technol.* **2005**, *28*, 318–323, doi:10.1002/ceat.200407128.
4. Bieringer, T.; Buchholz, S.; Kockmann, N. Future Production Concepts in the Chemical Industry: Modular – Small-Scale – Continuous. *Chem. Eng. Technol.* **2013**, *36*, 900–910, doi:10.1002/ceat.201200631.
5. Lasi, H.; Fettke, P.; Kemper, H.-G.; Feld, T.; Hoffmann, M. Industry 4.0. *Bus. Inf. Syst. Eng.* **2014**, *6*, 239–242, doi:10.1007/s12599-014-0334-4.
6. Baumann, M.; Moody, T.S.; Smyth, M.; Wharry, S. A Perspective on Continuous Flow Chemistry in the Pharmaceutical Industry. *Org. Process Res. Dev.* **2020**, doi:10.1021/acs.oprd.9b00524.
7. Bogdan, A.R.; Dombrowski, A.W. Emerging Trends in Flow Chemistry and Applications to the Pharmaceutical Industry. *J. Med. Chem.* **2019**, *62*, 6422–6468.
8. Plouffe, P.; Macchi, A.; Roberge, D.M. From Batch to Continuous Chemical Synthesis–A Toolbox Approach. *Org. Process Res. Dev.* **2014**, *18*, 1286–1294, doi:10.1021/op5001918.
9. Cefic 2020 Facts & Figures of the European Chemical Industry 2020, 78.
10. Venvik, H.J.; Yang, J. Catalysis in microstructured reactors: Short review on small-scale syngas production and further conversion into methanol, DME and Fischer-Tropsch

products. *Catal. Today* **2017**, *285*, 135–146, doi:https://doi.org/10.1016/j.cattod.2017.02.014.

11. Baldea, M.; Edgar, T.F.; Stanley, B.L.; Kiss, A.A. Modular manufacturing processes: Status, challenges, and opportunities. *AIChE J.* **2017**, *63*, 4262–4272, doi:10.1002/aic.15872.
12. Pashkova, A.; Greiner, L. Towards Small-Scale Continuous Chemical Production: Technology Gaps and Challenges. *Chemie Ing. Tech.* **2011**, *83*, 1337–1342, doi:10.1002/cite.201100037.
13. Sheldon, R.A. E factors, green chemistry and catalysis: an odyssey. *Chem. Commun.* **2008**, 3352–3365, doi:10.1039/B803584A.
14. Illg, T.; Löb, P.; Hessel, V. Flow chemistry using milli- and microstructured reactors—From conventional to novel process windows. *Bioorg. Med. Chem.* **2010**, *18*, 3707–3719, doi:https://doi.org/10.1016/j.bmc.2010.03.073.
15. May, S.A. Flow Chemistry, Continuous Processing, and Continuous Manufacturing: A Pharmaceutical Perspective. *J. Flow Chem.* **2017**, *7*, 137–145, doi:10.1556/1846.2017.00029.
16. Kockmann, N.; Gottsponer, M.; Zimmermann, B.; Roberge, D.M. Enabling Continuous-Flow Chemistry in Microstructured Devices for Pharmaceutical and Fine-Chemical Production. *Chem. – A Eur. J.* **2008**, *14*, 7470–7477, doi:10.1002/chem.200800707.
17. Hessel, V.; Vural Gürsel, I.; Wang, Q.; Noël, T.; Lang, J. Potential Analysis of Smart Flow Processing and Micro Process Technology for Fastening Process Development: Use of Chemistry and Process Design as Intensification Fields. *Chem. Eng. Technol.* **2012**, *35*, 1184,1204.

18. Reay, D.A.; Ramshaw, C.; Harvey, A.P. *Process Intensification : Engineering for Efficiency, Sustainability and Flexibility*; 2nd ed.; Butterworth-Heinemann: Oxford, 2013; ISBN 0-08-098304-9.

19. Ramshaw, C. The incentive for process intensification. In Proceedings of the BHR Group Conference Series Publication; Mechanical Engineering Publications Limited, 1995; Vol. 18, pp. 1–4.

20. Roy, S. Consider modular plant design. *Chem. Eng. Prog.* **2017**, *113*, 28–31.

21. Stankiewicz, A.I.; Moulijn, J.A. Process intensification: Transforming chemical engineering. *Chem. Eng. Prog.* **2000**, *96*, 22–34.

22. Van Gerven, T.; Stankiewicz, A. Structure, Energy, Synergy, Time□The Fundamentals of Process Intensification. *Ind. Eng. Chem. Res.* **2009**, *48*, 2465–2474, doi:10.1021/ie801501y.

23. Burcham, C.L.; Florence, A.J.; Johnson, M.D. Continuous Manufacturing in Pharmaceutical Process Development and Manufacturing. *Annu. Rev. Chem. Biomol. Eng.* **2018**, *9*, 253–281, doi:10.1146/annurev-chembioeng-060817-084355.

24. Devi, N.R.G.; Chandramouli, R. Real Time Release Testing-A Review. *J. Pharm. Res.* **2018**, *16*, 314–318.

25. Burke, R.; Mussomeli, A.; Laaper, S.; Hartigan, M.; Sniderman, B. The smart factory: Responsive, adaptive, connected manufacturing. *Deloitte Insights* **2017**, *31*, 1–10.

26. Fraunhofer IMM Available online: https://www.imm.fraunhofer.de/ (accessed on Apr 2, 2020).

27. CMAC Future Manufacturing Research Hub Available online: https://www.cmac.ac.uk/ (accessed on Apr 1, 2020).

28. RCPE Available online: https://www.rcpe.at (accessed on Apr 1, 2020).

29. SSPC Available online: https://sspc.ie/ (accessed on Apr 1, 2020).

30. MEPI Available online: https://www.mepi.fr/ (accessed on Apr 1, 2020).

31. AIChE About RAPID: Institute Roadmap Available online: https://www.aiche.org/rapid/about.

32. Bielenberg, J.; Palou-Rivera, I. The RAPID Manufacturing Institute – Reenergizing US efforts in process intensification and modular chemical processing. *Chem. Eng. Process. - Process Intensif.* **2019**, *138*, 49–54, doi:https://doi.org/10.1016/j.cep.2019.02.008.

33. Dencic, I.; Hessel, V. Industrial Microreactor Process Development up to Production. In *Microreactors in Organic Chemistry and Catalysis*; Wirth, T., Ed.; Wiley Online Books; Wiley-VCH Verlag GmbH & Co. KGaA: Weinheim, Germany, 2013; pp. 373–446 ISBN 9783527659722.

34. Britton, J.; Jamison, T.F. The assembly and use of continuous flow systems for chemical synthesis. *Nat. Protoc.* **2017**, *12*, 2423.

35. Bloemendal, V.R.L.J.; Janssen, M.A.C.H.; van Hest, J.C.M.; Rutjes, F.P.J.T. Continuous one-flow multi-step synthesis of active pharmaceutical ingredients. *React. Chem. Eng.* **2020**, *5*, 1186–1197, doi:10.1039/D0RE00087F.

36. White, T.D.; Alt, C.A.; Cole, K.P.; Groh, J.M.; Johnson, M.D.; Miller, R.D. How to Convert a Walk-in Hood into a Manufacturing Facility: Demonstration of a Continuous, High-Temperature Cyclization to Process Solids in Flow. *Org. Process Res. Dev.* **2014**, *18*, 1482–1491, doi:10.1021/op500239f.

37. Brewer, A.C.; Hoffman, P.C.; White, T.D.; Lu, Y.; McKee, L.; Boukerche, M.; Kobierski, M.E.; Mullane, N.; Pietz, M.; Alt, C.A.; et al. Design, Development, and Execution of a Continuous-flow-Enabled API Manufacturing Route. In *Organometallic Chemistry in*

Industry: A Practical Approach; Colacot, T.J., Johansson Seechurn, C.C.C., Eds.; Wiley-VCH Verlag GmbH & Co. KGaA: Weinheim, Germany, 2020; pp. 23–60 ISBN 9783527345175.

38. Cole, K.P.; Reizman, B.J.; Hess, M.; Groh, J.M.; Laurila, M.E.; Cope, R.F.; Campbell, B.M.; Forst, M.B.; Burt, J.L.; Maloney, T.D.; et al. Small-Volume Continuous Manufacturing of Merestinib. Part 1. Process Development and Demonstration. *Org. Process Res. Dev.* **2019**, *23*, 858–869, doi:10.1021/acs.oprd.8b00441.

39. Reizman, B.J.; Cole, K.P.; Hess, M.; Burt, J.L.; Maloney, T.D.; Johnson, M.D.; Laurila, M.E.; Cope, R.F.; Luciani, C. V; Buser, J.Y.; et al. Small-Volume Continuous Manufacturing of Merestinib. Part 2. Technology Transfer and cGMP Manufacturing. *Org. Process Res. Dev.* **2019**, *23*, 870–881, doi:10.1021/acs.oprd.8b00442.

40. Cole, K.P.; Groh, J.M.; Johnson, M.D.; Burcham, C.L.; Campbell, B.M.; Diseroad, W.D.; Heller, M.R.; Howell, J.R.; Kallman, N.J.; Koenig, T.M.; et al. Kilogram-scale prexasertib monolactate monohydrate synthesis under continuous-flow CGMP conditions. *Science (80-.).* **2017**, *356*, 1144–1150, doi:10.1126/science.aan0745.

41. McWilliams, J.C.; Allian, A.D.; Opalka, S.M.; May, S.A.; Journet, M.; Braden, T.M. The Evolving State of Continuous Processing in Pharmaceutical API Manufacturing: A Survey of Pharmaceutical Companies and Contract Manufacturing Organizations. *Org. Process Res. Dev.* **2018**, *22*, 1143–1166, doi:10.1021/acs.oprd.8b00160.

42. Gutmann, B.; Kappe, C.O. Forbidden Chemistries — Paths to a Sustainable Future Engaging Continuous Processing. *J. Flow Chem.* **2017**, *7*, 65–71, doi:10.1556/1846.2017.00009.

43. Kockmann, N.; Thenée, P.; Fleischer-Trebes, C.; Laudadio, G.; Noël, T. Safety assessment

in development and operation of modular continuous-flow processes. *React. Chem. Eng.* **2017**, *2*, 258–280, doi:10.1039/C7RE00021A.

44. Macchi, A.; Plouffe, P.; Patience, G.S.; Roberge, D.M. Experimental Methods in Chemical Engineering: Micro-Reactors. *Can. J. Chem. Eng.* **2019**, *97*, 2578–2587, doi:10.1002/cjce.23525.

45. Mielke, E.; Plouffe, P.; Mongeon, S.S.; Aellig, C.; Filliger, S.; Macchi, A.; Roberge, D.M. Micro-reactor mixing unit interspacing for fast liquid-liquid reactions leading to a generalized scale-up methodology. *Chem. Eng. J.* **2018**, *352*, 682–694, doi:https://doi.org/10.1016/j.cej.2018.07.043.

46. Nieves-Remacha, M.J.; Kulkarni, A.A.; Jensen, K.F. Gas-Liquid Flow and Mass Transfer in an Advanced-Flow Reactor. *Ind. Eng. Chem. Res.* **2013**, *52*, 8996–9010, doi:10.1021/ie4011707.

47. Nieves-Remacha, M.J.; Jensen, K.F. Mass transfer characteristics of ozonolysis in microreactors and advanced-flow reactors. *J. Flow Chem.* **2015**, *5*, 160–165, doi:10.1556/1846.2015.00010.

48. Reichmann, F.; Tollkötter, A.; Körner, S.; Kockmann, N. Gas-liquid dispersion in micronozzles and microreactor design for high interfacial area. *Chem. Eng. Sci.* **2017**, *169*, 151–163, doi:http://dx.doi.org/10.1016/j.ces.2016.10.028.

49. Nieves-Remacha, M.J.; Kulkarni, A.A.; Jensen, K.F. Hydrodynamics of Liquid–Liquid Dispersion in an Advanced-Flow Reactor. *Ind. Eng. Chem. Res.* **2012**, *51*, 16251–16262, doi:10.1021/ie301821k.

50. Znidar, D.; O'Kearney-McMullan, A.; Munday, R.; Wiles, C.; Poechlauer, P.; Schmoelzer, C.; Dallinger, D.; Kappe, C.O. Scalable Wolff–Kishner Reductions in Extreme Process

Windows Using a Silicon Carbide Flow Reactor. *Org. Process Res. Dev.* **2019**, *23*, 2445–2455, doi:10.1021/acs.oprd.9b00336.

51. McDonough, J.R.; Oates, M.F.; Law, R.; Harvey, A.P. Micromixing in oscillatory baffled flows. *Chem. Eng. J.* **2019**, *361*, 508–518, doi:https://doi.org/10.1016/j.cej.2018.12.088.
52. Ahmed, S.M.R.; Phan, A.N.; Harvey, A.P. Mass transfer enhancement as a function of oscillatory baffled reactor design. *Chem. Eng. Process. - Process Intensif.* **2018**, *130*, 229–239, doi:https://doi.org/10.1016/j.cep.2018.06.016.
53. Jiang, M.; Ni, X.-W. Reactive Crystallization of Paracetamol in a Continuous Oscillatory Baffled Reactor. *Org. Process Res. Dev.* **2019**, *23*, 882–890, doi:10.1021/acs.oprd.8b00446.
54. McGlone, T.; Briggs, N.E.B.; Clark, C.A.; Brown, C.J.; Sefcik, J.; Florence, A.J. Oscillatory Flow Reactors (OFRs) for Continuous Manufacturing and Crystallization. *Org. Process Res. Dev.* **2015**, *19*, 1186–1202, doi:10.1021/acs.oprd.5b00225.
55. Ni, X. Continuous oscillatory baffled reactor technology. *Innov. Pharm. Technol.* **2006**, *20*, 90–96.
56. Mongeon, S.S.; Roberge, D.M.; Bittel, M.; Elsner, P.; Macchi, A. Liquid-Liquid Mass Transfer in an Oscillatory-Flow Mesoscale Coil Reactor without Baffles. *Org. Process Res. Dev.* **2016**, *20*, 733–741, doi:10.1021/acs.oprd.5b00356.
57. Cruz, P.; Rocha, F.; Ferreira, A. Effect of operating conditions on batch and continuous paracetamol crystallization in an oscillatory flow mesoreactor. *CrystEngComm* **2016**, doi:10.1039/C6CE01648K.
58. Reis, N.; Harvey, A.P.; Mackley, M.R.; Vicente, A.A.; Teixeira, J.A. Fluid Mechanics and Design Aspects of a Novel Oscillatory Flow Screening Mesoreactor. *Chem. Eng. Res. Des.* **2005**, *83*, 357–371, doi:https://doi.org/10.1205/cherd.03401.

59. Doyle, B.J.; Gutmann, B.; Bittel, M.; Hubler, T.; Macchi, A.; Roberge, D.M. Handling of Solids and Flow Characterization in a Baffleless Oscillatory Flow Coil Reactor. *Ind. Eng. Chem. Res.* **2020**, *59*, 4007–4019, doi:10.1021/acs.iecr.9b04496.

60. Sharma, L.; Nigam, K.D.P.; Roy, S. Single phase mixing in coiled tubes and coiled flow inverters in different flow regimes. *Chem. Eng. Sci.* **2017**, *160*, 227–235, doi:https://doi.org/10.1016/j.ces.2016.11.034.

61. Hohmann, L.; Gorny, R.; Klaas, O.; Ahlert, J.; Wohlgemuth, K.; Kockmann, N. Design of a Continuous Tubular Cooling Crystallizer for Process Development on Lab-Scale. *Chem. Eng. Technol.* **2016**, *39*, 1268–1280, doi:10.1002/ceat.201600072.

62. Saxena, A.K.; Nigam, K.D.P. Coiled configuration for flow inversion and its effect on residence time distribution. *AIChE J.* **2018**, *30*, 363–368, doi:10.1002/aic.690300303.

63. Klutz, S.; Kurt, S.K.; Lobedann, M.; Kockmann, N. Narrow residence time distribution in tubular reactor concept for Reynolds number range of 10–100. *Chem. Eng. Res. Des.* **2015**, *95*, 22–33, doi:https://doi.org/10.1016/j.cherd.2015.01.003.

64. Kurt, S.K.; Gelhausen, M.G.; Kockmann, N. Axial Dispersion and Heat Transfer in a Milli/Microstructured Coiled Flow Inverter for Narrow Residence Time Distribution at Laminar Flow. *Chem. Eng. Technol.* **2015**, *38*, 1122–1130, doi:10.1002/ceat.201400515.

65. López-Guajardo, E.; Ortiz-Nadal, E.; Montesinos-Castellanos, A.; Nigam, K.D.P. Coiled flow inverter as a novel alternative for the intensification of a liquid-liquid reaction. *Chem. Eng. Sci.* **2017**, *169*, 179–185, doi:https://doi.org/10.1016/j.ces.2017.01.016.

66. Kurt, S.K.; Warnebold, F.; Nigam, K.D.P.; Kockmann, N. Gas-liquid reaction and mass transfer in microstructured coiled flow inverter. *Chem. Eng. Sci.* **2017**, *169*, 164–178, doi:https://doi.org/10.1016/j.ces.2017.01.017.

67. Zhang, J.; Teixeira, A.R.; Jensen, K.F. Automated measurements of gas-liquid mass transfer in micropacked bed reactors. *AIChE J.* **2018**, *64*, 564–570, doi:10.1002/aic.15941.

68. von Keutz, T.; Cantillo, D.; Kappe, C.O. Enhanced mixing of biphasic liquid-liquid systems for the synthesis of gem-dihalocyclopropanes using packed bed reactors. *J. Flow Chem.* **2019**, *9*, 27–34, doi:10.1007/s41981-018-0026-1.

69. Chevrel, M.; Hoppe, S.; Meimaroglou, D.; Falk, L.; Durand, A. Continuous Pilot-Scale Tubular Reactor for Acrylic Acid Polymerization in Solution Designed Using Lab-Scale Rheo-Raman data. *Macromol. React. Eng.* **2016**, *10*, 354–363, doi:10.1002/mren.201500058.

70. Myers, K.; Janz, E.; Cathie, N.; Jones, M. Employ Static Mixers for Process Intensification. *Chem. Eng. Prog.* **2018**, *114*, 55–63.

71. Kumar, V.; Shirke, V.; Nigam, K.D.P. Performance of Kenics static mixer over a wide range of Reynolds number. *Chem. Eng. J.* **2008**, *139*, 284–295, doi:https://doi.org/10.1016/j.cej.2007.07.101.

72. Biard, P.-F.; Dang, T.T.; Bocanegra, J.; Couvert, A. Intensification of the O3/H2O2 advanced oxidation process using a continuous tubular reactor filled with static mixers: Proof of concept. *Chem. Eng. J.* **2018**, *344*, 574–582, doi:https://doi.org/10.1016/j.cej.2018.03.112.

73. Power, G.; Hou, G.; Kamaraju, V.K.; Morris, G.; Zhao, Y.; Glennon, B. Design and optimization of a multistage continuous cooling mixed suspension, mixed product removal crystallizer. *Chem. Eng. Sci.* **2015**, *133*, 125–139, doi:https://doi.org/10.1016/j.ces.2015.02.014.

74. Acevedo, D.; Jarmer, D.J.; Burcham, C.L.; Polster, C.S.; Nagy, Z.K. A continuous multi-

stage mixed-suspension mixed-product-removal crystallization system with fines dissolution. *Chem. Eng. Res. Des.* **2018**, *135*, 112–120.

75. Mo, Y.; Jensen, K.F. A miniature CSTR cascade for continuous flow of reactions containing solids. *React. Chem. Eng.* **2016**, *1*, 501–507, doi:10.1039/C6RE00132G.

76. Roberge, D.M.; Zimmermann, B.; Rainone, F.; Gottsponer, M.; Eyholzer, M.; Kockmann, N. Microreactor Technology and Continuous Processes in the Fine Chemical and Pharmaceutical Industry: Is the Revolution Underway? *Org. Process Res. Dev.* **2008**, *12*, 905–910, doi:10.1021/op8001273.

77. Monteiro, J.L.; Carneiro, P.F.; Elsner, P.; Roberge, D.M.; Wuts, P.G.M.; Kurjan, K.C.; Gutmann, B.; Kappe, C.O. Continuous Flow Homolytic Aromatic Substitution with Electrophilic Radicals: A Fast and Scalable Protocol for Trifluoromethylation. *Chem. – A Eur. J.* **2017**, *23*, 176–186, doi:10.1002/chem.201604579.

78. Mullin, R. Off the drawing board. *Chem. Eng. News* **2019**, *97*, 28–33.

79. Snyder, D.A.; Noti, C.; Seeberger, P.H.; Schael, F.; Bieber, T.; Rimmel, G.; Ehrfeld, W. Modular Microreaction Systems for Homogeneously and Heterogeneously Catalyzed Chemical Synthesis. *Helv. Chim. Acta* **2005**, *88*, 1–9, doi:10.1002/hlca.200490304.

80. Zhang, P.; Weeranoppanant, N.; Thomas, D.A.; Tahara, K.; Stelzer, T.; Russell, M.G.; O'Mahony, M.; Myerson, A.S.; Lin, H.; Kelly, L.P.; et al. Advanced Continuous Flow Platform for On-Demand Pharmaceutical Manufacturing. *Chem. – A Eur. J.* **2018**, *24*, 2776–2784, doi:10.1002/chem.201706004.

81. Adamo, A.; Beingessner, R.L.; Behnam, M.; Chen, J.; Jamison, T.F.; Jensen, K.F.; Monbaliu, J.-C.M.; Myerson, A.S.; Revalor, E.M.; Snead, D.R.; et al. On-demand continuous-flow production of pharmaceuticals in a compact, reconfigurable system.

Science (80-.). **2016**, *352*, 61–67, doi:10.1126/science.aaf1337.

82. Bédard, A.-C.; Adamo, A.; Aroh, K.C.; Russell, M.G.; Bedermann, A.A.; Torosian, J.; Yue, B.; Jensen, K.F.; Jamison, T.F. Reconfigurable system for automated optimization of diverse chemical reactions. *Science (80-.).* **2018**, *361*, 1220–1225, doi:10.1126/science.aat0650.

83. M. Roberge, D. The complexity of technology, implementation: Flow versus batch processing. *Chim. Oggi* **2012**, *30*, 4–4.

84. Plouffe, P.; Bittel, M.; Sieber, J.; Roberge, D.M.; Macchi, A. On the scale-up of micro-reactors for liquid–liquid reactions. *Chem. Eng. Sci.* **2016**, *143*, 216–225, doi:https://doi.org/10.1016/j.ces.2015.12.009.

85. Kockmann, N.; Gottsponer, M.; Roberge, D.M. Scale-up concept of single-channel microreactors from process development to industrial production. *Chem. Eng. J.* **2011**, *167*, 718–726, doi:10.1016/j.cej.2010.08.089.

86. Roberge, D.M. An Integrated Approach Combining Reaction Engineering and Design of Experiments for Optimizing Reactions. *Org. Process Res. Dev.* **2004**, *8*, 1049–1053, doi:10.1021/op0400160.

87. Behme, S. Facility Design. In *Manufacturing of Pharmaceutical Proteins*; John Wiley & Sons, Ltd, 2015; pp. 253–300 ISBN 9783527683109.

88. Microinnova Continuous Modular Chemistry Plants Available online: https://www.microinnova.com/index.php/en/technology/continuous-modular-chemistry-plants (accessed on Mar 30, 2020).

89. Sundar, K.P.; Kanmani, S. Progression of Photocatalytic reactors and it's comparison: A Review. *Chem. Eng. Res. Des.* **2020**, *154*, 135–150,

doi:https://doi.org/10.1016/j.cherd.2019.11.035.

90. Walsh, F.C.; Ponce de León, C. Progress in electrochemical flow reactors for laboratory and pilot scale processing. *Electrochim. Acta* **2018**, *280*, 121–148, doi:https://doi.org/10.1016/j.electacta.2018.05.027.

91. Sedelmeier, G. New Methods 2008.

92. Roberge, D.M.; Noti, C.; Irle, E.; Eyholzer, M.; Rittiner, B.; Penn, G.; Sedelmeier, G.; Schenkel, B. Control of Hazardous Processes in Flow: Synthesis of 2-Nitroethanol. *J. Flow Chem.* **2014**, *4*, 26–34, doi:10.1556/JFC-D-13-00016.

93. Lonza's Ibex Biomanufacturing Complex in Visp, Switzerland Available online: https://www.pharmaceutical-technology.com/projects/lonza-ibex-biomanufacturing-complex-visp/ (accessed on Jun 23, 2020).

94. Lonza Ibex™ Solutions Available online: https://pharma.lonza.com/offerings/specialized-capabilities/ibex (accessed on Jun 23, 2020).

95. McCoy, M.; Thayer, A.M.; Mullin, R. Building pharmaceutical outsourcing partnerships. *C&EN Glob. Enterp.* **2017**, *95*, 36–45, doi:10.1021/cen-09511-cover.

96. Blackshields, C.A.; Crean, A.M. Continuous powder feeding for pharmaceutical solid dosage form manufacture: a short review. *Pharm. Dev. Technol.* **2018**, *23*, 554–560, doi:10.1080/10837450.2017.1339197.

97. Kleinebudde, P.; Khinast, J.; Rantanen, J. *Continuous Manufacturing of Pharmaceuticals*; John Wiley & Sons, Ltd: Chichester, UK, 2017; ISBN 9781119001324.

98. Badman, C.; Cooney, C.L.; Florence, A.; Konstantinov, K.; Krumme, M.; Mascia, S.; Nasr, M.; Trout, B.L. Why We Need Continuous Pharmaceutical Manufacturing and How to Make It Happen. *J. Pharm. Sci.* **2019**, *108*, 3521–3523, doi:10.1016/j.xphs.2019.07.016.

99. Gutmann, B.; Cantillo, D.; Kappe, C.O. Continuous-Flow Technology—A Tool for the Safe Manufacturing of Active Pharmaceutical Ingredients. *Angew. Chemie Int. Ed.* **2015**, *54*, 6688–6728, doi:10.1002/anie.201409318.

100. Doyle, B.J.; Elsner, P.; Gutmann, B.; Hannaerts, O.; Aellig, C.; Macchi, A.; Roberge, D.M. Mini-Monoplant Technology for Pharmaceutical Manufacturing. *Org. Process Res. Dev.* **2020**, *24*, 2169–2182, doi:10.1021/acs.oprd.0c00207.

101. Hessel, V.; Angeli, P.; Gavriilidis, A.; Löwe, H. Gas−Liquid and Gas−Liquid−Solid Microstructured Reactors: Contacting Principles and Applications. *Ind. Eng. Chem. Res.* **2005**, *44*, 9750–9769, doi:10.1021/ie0503139.

102. Dencic, I.; Hessel, V. Gas–Liquid Reactions. In *Microreactors in Organic Chemistry and Catalysis*; Wirth, T., Ed.; Wiley-VCH Verlag GmbH & Co. KGaA, 2013; pp. 221–288 ISBN 9783527659722.

103. Kashid, M.N.; Renken, A.; Kiwi-Minsker, L. Gas–liquid and liquid–liquid mass transfer in microstructured reactors. *Chem. Eng. Sci.* **2011**, *66*, 3876–3897, doi:10.1016/j.ces.2011.05.015.

104. Wu, K.-J.; Nappo, V.; Kuhn, S. Hydrodynamic Study of Single- and Two-Phase Flow in an Advanced-Flow Reactor. *Ind. Eng. Chem. Res.* **2015**, *54*, 7554–7564, doi:10.1021/acs.iecr.5b01444.

105. Plouffe, P.; Bittel, M.; Sieber, J.; Roberge, D.M.; Macchi, A. On the scale-up of micro-reactors for liquid – liquid reactions. *Chem. Eng. Sci.* **2016**, *143*, 216–225, doi:10.1016/j.ces.2015.12.009.

106. Wu, B.; Firouzi, M.; Mitchell, T.; Rufford, T.E.; Leonardi, C.; Towler, B. A critical review of flow maps for gas-liquid flows in vertical pipes and annuli. *Chem. Eng. J.* **2017**, *326*,

350–377, doi:https://doi.org/10.1016/j.cej.2017.05.135.

107. Ullmann, A.; Brauner, N. The prediction of flow pattern maps in minichannels. *Multiph. Sci. Technol.* **2007**, *19*, 49–73, doi:10.1615/MultScienTechn.v19.i1.20.

108. Akbar, M.; Plummer, D.; Ghiaasiaan, S. On gas-liquid two-phase flow regimes in microchannels. *Int. J. Multiph. Flow* **2003**, *29*, 855–865.

109. Chinnov, E.; Ron'shin, F.; Kabov, O. Regimes of two-phase flow in micro- and minichannels (review). *Thermophys. Aeromechanics* **2015**, *22*, 265–284.

110. Yue, J.; Chen, G.; Yuan, Q.; Luo, L.; Gonthier, Y. Hydrodynamics and mass transfer characteristics in gas–liquid flow through a rectangular microchannel. *Chem. Eng. Sci.* **2007**, *62*, 2096–2108.

111. Mielke, E.; Roberge, D.M.; Macchi, A. Microreactor Mixing-Unit Design for Fast Liquid-Liquid Reactions. *J. Flow Chem.* **2016**, *6*, 279–287, doi:10.1556/1846.2016.00026.

112. Dargar, P.; Macchi, A. Effect of surface-active agents on the phase holdups of three-phase fluidized beds. *Chem. Eng. Process. Process Intensif.* **2006**, *45*, 764–772, doi:https://doi.org/10.1016/j.cep.2006.03.004.

113. Song, S.; Peng, C. Viscosities of Binary and Ternary Mixtures of Water, Alcohol, Acetone, and Hexane. *J. Dispers. Sci. Technol.* **2008**, *29*, 1367–1372.

114. Benedetti-Pichler, A.A.; Cefola, M.; Waldman, B. Warder's method for the titration of carbonates. *Ind. Eng. Chem. Ed.* **1939**, *11*, 327–332, doi:10.1021/ac50134a012.

115. Triplett, K.A.; Ghiaasiaan, S.M.; Abdel-Khalik, S.I.; Sadowski, D.L. Gas-liquid two-phase flow in microchannels - Part I: two-phase flow patterns. *Int. J. Multiph. Flow* **1999**, *25*, 377–394, doi:10.1016/S0301-9322(98)00054-8.

116. Balasubramaniam, R.; Ramé, E.; Kizito, J.; Kassemi, M. *Two Phase Flow Modeling:*

Summary of Flow Regimes and Pressure Drop Correlations in Reduced and Partial Gravity; National Aeronautics and Space Administration: Cleveland, Ohio, 2006;

117. Ju Lee, H.; Yong Lee, S. Pressure drop correlations for two-phase flow within horizontal rectangular channels with small heights. *Int. J. Multiph. Flow* **2001**, *27*, 783–796, doi:https://doi.org/10.1016/S0301-9322(00)00050-1.
118. Hebrard, G.; Zeng, J.; Loubiere, K. Effect of surfactants on liquid side mass transfer coefficients: A new insight. *Chem. Eng. J.* **2009**, *148*, 132–138, doi:https://doi.org/10.1016/j.cej.2008.08.027.
119. Kawase, Y.; Moo-Young, M. Mathematical models for design of bioreactors: Applications of: Kolmogoroff's theory of isotropic turbulence. *Chem. Eng. J.* **1990**, *43*, B19–B41, doi:https://doi.org/10.1016/0300-9467(90)80048-H.
120. Malet-Sanz, L.; Susanne, F. Continuous Flow Synthesis. A Pharma Perspective. *J. Med. Chem.* **2012**, *55*, 4062–4098, doi:10.1021/jm2006029.
121. Porta, R.; Benaglia, M.; Puglisi, A. Flow Chemistry: Recent Developments in the Synthesis of Pharmaceutical Products. *Org. Process Res. Dev.* **2016**, *20*, 2–25, doi:10.1021/acs.oprd.5b00325.
122. Barrow, D.; Taylor, S.; Morgan, A.; Giles, L. Properties and Use of Microreactors. *Microreactors Org. Chem. Catal.* 2013, 1–33.
123. Portha, J.-F.; Falk, L.; Commenge, J.-M. Local and global process intensification. *Chem. Eng. Process. Process Intensif.* **2014**, *84*, 1–13, doi:https://doi.org/10.1016/j.cep.2014.05.002.
124. Hessel, V.; Kralisch, D.; Kockmann, N.; Noël, T.; Wang, Q. Novel Process Windows for Enabling, Accelerating, and Uplifting Flow Chemistry. *ChemSusChem* **2013**, *6*, 746–789,

doi:https://doi.org/10.1002/cssc.201200766.

125. Halder, R.; Lawal, A.; Damavarapu, R. Nitration of toluene in a microreactor. *Catal. Today* **2007**, *125*, 74–80, doi:https://doi.org/10.1016/j.cattod.2007.04.002.

126. Barton, J.; Rogers, R. *Chemical reaction hazards*; 2nd ed.; Gulf Professional Publishing: Houston, Tex, 1997; ISBN 088415274X.

127. Russo, D.; Tomaiuolo, G.; Andreozzi, R.; Guido, S.; Lapkin, A.A.; Di Somma, I. Heterogeneous benzaldehyde nitration in batch and continuous flow microreactor. *Chem. Eng. J.* **2019**, *377*, 120346, doi:https://doi.org/10.1016/j.cej.2018.11.044.

128. Li, L.; Yao, C.; Jiao, F.; Han, M.; Chen, G. Experimental and kinetic study of the nitration of 2-ethylhexanol in capillary microreactors. *Chem. Eng. Process. Process Intensif.* **2017**, *117*, 179–185, doi:https://doi.org/10.1016/j.cep.2017.04.005.

129. Burns, J.R.; Ramshaw, C. A Microreactor for the Nitration of Benzene and Toluene. *Chem. Eng. Commun.* **2002**, *189*, 1611–1628, doi:10.1080/00986440214585.

130. Ducry, L.; Roberge, D.M. Controlled Autocatalytic Nitration of Phenol in a Microreactor. *Angew. Chemie Int. Ed.* **2005**, *44*, 7972–7975, doi:https://doi.org/10.1002/anie.200502387.

131. Antes, J.; Boskovic, D.; Krause, H.; Loebbecke, S.; Lutz, N.; Tuercke, T.; Schweikert, W. Analysis and Improvement of Strong Exothermic Nitrations in Microreactors. *Chem. Eng. Res. Des.* **2003**, *81*, 760–765, doi:https://doi.org/10.1205/026387603322302931.

132. Panke, G.; Schwalbe, T.; Stirner, W.; Taghavi-Moghadam, S.; Wille, G. A Practical Approach of Continuous Processing to High Energetic Nitration Reactions in Microreactors. *Synth.* **2003**, *2003*, 2827–2830, doi:10.1055/s-2003-42491.

133. Kashid, M.N.; Gupta, A.; Renken, A.; Kiwi-Minsker, L. Numbering-up and mass transfer studies of liquid–liquid two-phase microstructured reactors. *Chem. Eng. J.* **2010**, *158*, 233–

240, doi:https://doi.org/10.1016/j.cej.2010.01.020.

134. Amador, C.; Gavriilidis, A.; Angeli, P. Flow distribution in different microreactor scale-out geometries and the effect of manufacturing tolerances and channel blockage. *Chem. Eng. J.* **2004**, *101*, 379–390, doi:https://doi.org/10.1016/j.cej.2003.11.031.

135. Kockmann, N.; Roberge, D.M. Scale-up concept for modular microstructured reactors based on mixing, heat transfer, and reactor safety. *Chem. Eng. Process. Process Intensif.* **2011**, *50*, 1017–1026, doi:https://doi.org/10.1016/j.cep.2011.05.021.

136. Müller, H. *Sulfuric Acid and Sulfur Trioxide*; Major Reference Works; 6th ed.; Wiley-VCH Verlag GmbH & Co. KGaA, 2000; ISBN 9783527306732.

137. Bourne, J.R. Mixing and the Selectivity of Chemical Reactions. *Org. Process Res. Dev.* **2003**, *7*, 471–508, doi:10.1021/op020074q.

138. Ghanem, A.; Lemenand, T.; Della Valle, D.; Peerhossaini, H. Static mixers: Mechanisms, applications, and characterization methods – A review. *Chem. Eng. Res. Des.* **2014**, *92*, 205–228, doi:https://doi.org/10.1016/j.cherd.2013.07.013.

139. Holvey, C.P.; Roberge, D.M.; Gottsponer, M.; Kockmann, N.; Macchi, A. Pressure drop and mixing in single phase microreactors: Simplified designs of micromixers. *Chem. Eng. Process. Process Intensif.* **2011**, *50*, 1069–1075, doi:https://doi.org/10.1016/j.cep.2011.05.016.

140. Falk, L.; Commenge, J.-M. Performance comparison of micromixers. *Chem. Eng. Sci.* **2010**, *65*, 405–411, doi:https://doi.org/10.1016/j.ces.2009.05.045.

141. D'Orazio, A.; Haelssig, J.; Roberge, D.M.; Macchi, A. COMPARATIVE ANALYSIS OF MIXING IN LIQUID MICROREACTORS USING COMPUTATIONAL FLUID DYNAMICS. *MASc Thesis, Univ. Ottawa.* **2021**.

142. Kockmann, N. Pressure loss and transfer rates in microstructured devices with chemical reactions. *Chem. Eng. Technol.* **2008**, *31*, 1188–1195, doi:10.1002/ceat.200800065.

143. Wang, H.; Mustaffar, A.; Phan, A.N.; Zivkovic, V.; Reay, D.; Law, R.; Boodhoo, K. A review of process intensification applied to solids handling. *Chem. Eng. Process. Process Intensif.* 2017.

144. Hessel, V.; Lowe, H.; Schonfeld, F. Micromixers - a review on passive and active mixing principles. *Chem. Eng. Sci.* **2005**, *60*, 2479–2501, doi:10.1016/j.ces.2004.11.033.

145. Law, R.; Ramshaw, C.; Reay, D. Process intensification – Overcoming impediments to heat and mass transfer enhancement when solids are present, via the IbD project. *Therm. Sci. Eng. Prog.* **2017**, doi:10.1016/j.tsep.2017.02.004.

146. Rasdi, F.R.M.; Phan, A.N.; Harvey, A.P. Rapid determination of reaction order and rate constants of an imine synthesis reaction using a mesoscale oscillatory baffled reactor. *Chem. Eng. J.* **2013**, *222*.

147. Phan, A.N.; Harvey, A.P. Characterisation of mesoscale oscillatory helical baffled reactor—Experimental approach. *Chem. Eng. J.* **2012**, *180*, 229–236, doi:https://doi.org/10.1016/j.cej.2011.11.018.

148. Gron, H.; Schutte, R.; Drauz, K.; Stadtmuller, K.; Grayson, J.I. Oscillatory Flow Mixing Reactor 2008, 7.

149. Ferreira, A.; Adesite, P.O.; Teixeira, J.A.; Rocha, F. Effect of solids on O2 mass transfer in an oscillatory flow reactor provided with smooth periodic constrictions. *Chem. Eng. Sci.* **2017**, *170*, 400–409, doi:https://doi.org/10.1016/j.ces.2016.12.067.

150. Ferreira, A.; Teixeira, J.A.; Rocha, F. O2 mass transfer in an oscillatory flow reactor provided with smooth periodic constrictions. Individual characterization of kL and a. *Chem.*

Eng. J. **2015**, *262*, 499–508, doi:10.1016/J.CEJ.2014.09.125.

151. Reis, N.; Gonçalves, C.N.; Aguedo, M.; Gomes, N.; Teixeira, J.A.; Vicente, A.A. Application of a Novel Oscillatory Flow Micro-bioreactor to the Production of $γ$-decalactone in a Two Immiscible Liquid Phase Medium. *Biotechnol. Lett.* **2006**, *28*, 485–490, doi:10.1007/s10529-006-0003-x.

152. McDonough, J.R.; Phan, A.N.; Harvey, A.P. Rapid process development using oscillatory baffled mesoreactors – A state-of-the-art review. *Chem. Eng. J.* **2015**, *265*, 110–121, doi:https://doi.org/10.1016/j.cej.2014.10.113.

153. Lawton, S.; Steele, G.; Shering, P.; Zhao, L.; Laird, I.; Ni, X.-W. Continuous Crystallization of Pharmaceuticals Using a Continuous Oscillatory Baffled Crystallizer. *Org. Process Res. Dev.* **2009**, *13*, 1357–1363, doi:10.1021/op900237x.

154. McLachlan, H.; Ni, X.-W. An Investigation into Parameters Affecting Crystal Purity of Urea in a Stirred Tank and an Oscillatory Baffled Crystallizer. *Chem. Eng. Commun.* **2016**, *203*, 1189–1197, doi:10.1080/00986445.2016.1154851.

155. Chapman, M.R.; Kwan, M.H.T.; King, G.; Jolley, K.E.; Hussain, M.; Hussain, S.; Salama, I.E.; González Niño, C.; Thompson, L.A.; Bayana, M.E.; et al. Simple and Versatile Laboratory Scale CSTR for Multiphasic Continuous-Flow Chemistry and Long Residence Times. *Org. Process Res. Dev.* **2017**, *21*, 1294–1301, doi:10.1021/acs.oprd.7b00173.

156. Browne, D.L.; Deadman, B.J.; Ashe, R.; Baxendale, I.R.; Ley, S. V Continuous Flow Processing of Slurries: Evaluation of an Agitated Cell Reactor. *Org. Process Res. Dev.* **2011**, *15*, 693–697, doi:10.1021/op2000223.

157. Kreimer, M.; Zettl, M.; Aigner, I.; Mannschott, T.; van der Wel, P.; Khinast, J.G.; Krumme, M. Performance Characterization of Static Mixers in Precipitating Environments. *Org.*

Process Res. Dev. **2019**, *23*, 1308–1320, doi:10.1021/acs.oprd.8b00267.

158. Ufer, A.; Mendorf, M.; Ghaini, A.; Agar, D.W. Liquid/Liquid Slug Flow Capillary Microreactor. *Chem. Eng. Technol.* **2011**, *34*, 353–360, doi:10.1002/ceat.201000334.

159. Bannock, J.H.; Krishnadasan, S.H.; Nightingale, A.M.; Yau, C.P.; Khaw, K.; Burkitt, D.; Halls, J.J.M.; Heeney, M.; de Mello, J.C. Continuous Synthesis of Device-Grade Semiconducting Polymers in Droplet-Based Microreactors. *Adv. Funct. Mater.* **2013**, *23*, 2123–2129, doi:10.1002/adfm.201203014.

160. Liedtke, A.-K.; Bornette, F.; Philippe, R.; de Bellefon, C. Gas–liquid–solid "slurry Taylor" flow: Experimental evaluation through the catalytic hydrogenation of 3-methyl-1-pentyn-3-ol. *Chem. Eng. J.* **2013**, *227*, 174–181, doi:https://doi.org/10.1016/j.cej.2012.07.100.

161. Scott, C.D.; Labes, R.; Depardieu, M.; Battilocchio, C.; Davidson, M.G.; Ley, S. V; Wilson, C.C.; Robertson, K. Integrated plug flow synthesis and crystallisation of pyrazinamide. *React. Chem. Eng.* **2018**, *3*, 631–634, doi:10.1039/C8RE00087E.

162. Acevedo, D.; Peña, R.; Yang, Y.; Barton, A.; Firth, P.; Nagy, Z.K. Evaluation of mixed suspension mixed product removal crystallization processes coupled with a continuous filtration system. *Chem. Eng. Process. Process Intensif.* **2016**, *108*, 212–219, doi:https://doi.org/10.1016/j.cep.2016.08.006.

163. Hohmann, L.; Kurt, S.K.; Soboll, S.; Kockmann, N. Separation units and equipment for lab-scale process development. *J. Flow Chem.* **2016**, *6*, 181–190, doi:10.1556/1846.2016.00024.

164. Hohmann, L.; Schmalenberg, M.; Prasanna, M.; Matuschek, M.; Kockmann, N. Suspension flow behavior and particle residence time distribution in helical tube devices. *Chem. Eng. J.* **2019**, *360*, 1371–1389, doi:10.1016/j.cej.2018.10.166.

165. Johnson, M.D.; May, S.A.; Calvin, J.R.; Remacle, J.; Stout, J.R.; Diseroad, W.D.; Zaborenko, N.; Haeberle, B.D.; Sun, W.-M.; Miller, M.T.; et al. Development and Scale-Up of a Continuous, High-Pressure, Asymmetric Hydrogenation Reaction, Workup, and Isolation. *Org. Process Res. Dev.* **2012**, *16*, 1017–1038, doi:10.1021/op200362h.

166. Poe, S.L.; Cummings, M.A.; Haaf, M.P.; McQuade, D.T. Solving the clogging problem: Precipitate-forming reactions in flow. *Angew. Chemie - Int. Ed.* **2006**, *45*, 1544–1548, doi:10.1002/anie.200503925.

167. Nabavi, M.; Siddiqui, K. A critical review on advanced velocity measurement techniques in pulsating flows. *Meas. Sci. Technol.* **2010**, *21*, 42002, doi:10.1088/0957-0233/21/4/042002.

168. Makosza, M.; Fedorynski, M. Phase transfer catalysis in dichlorocarbene chemistry: basic principles and specific features. *Russ. Chem. Bull.* **2011**, *60*, 2141–2146, doi:10.1007/s11172-011-0332-3.

169. Starks, C.M.; Liotta, C.L.; Halpern, M.E. Basic Concepts in Phase-Transfer Catalysis. In *Phase-Transfer Catalysis: Fundamentals, Applications, and Industrial Perspectives*; Springer Netherlands: Dordrecht, 1994; pp. 1–22 ISBN 978-94-011-0687-0.

170. Wilson, B.; Sherrington, D.C.; Ni, X. Butylation of phenylacetonitrile in an oscillatory baffled reactor. *Ind. Eng. Chem. Res.* **2005**, *44*, 8663–8670, doi:10.1021/ie048855y.

171. Peacock, J.; Jones, T.; Tock, C.; Lutz, R. The onset of turbulence in physiological pulsatile flow in a straight tube. *Exp. Fluids* **1998**, *24*, 1–9, doi:10.1007/s003480050144.

172. Ni, X.; Gough, P. On the discussion of the dimensionless groups governing oscillatory flow in a baffled tube. *Chem. Eng. Sci.* **1997**, *52*, 3209–3212, doi:https://doi.org/10.1016/S0009-2509(97)00104-8.

173. Jimeno, G.; Lee, Y.C.; Ni, X.-W. On the evaluation of power density models for oscillatory baffled reactors using CFD. *Chem. Eng. Process. - Process Intensif.* **2018**, *134*, 153–162, doi:https://doi.org/10.1016/j.cep.2018.11.002.

174. Liu, Y.C.; Dunn, D.; Lipari, M.; Barton, A.; Firth, P.; Speed, J.; Wood, D.; Nagy, Z.K. A comparative study of continuous operation between a dynamic baffle crystallizer and a stirred tank crystallizer. *Chem. Eng. J.* **2019**, *367*, 278–294, doi:https://doi.org/10.1016/j.cej.2019.02.129.

175. Ham, J.-H.; Platzer, B. Semi-Empirical Equations for the Residence Time Distributions in Disperse Systems – Part 1: Continuous Phase. *Chem. Eng. Technol.* **2004**, *27*, 1172–1178, doi:10.1002/ceat.200407038.

176. Phan, A.N.; Harvey, A. Development and evaluation of novel designs of continuous mesoscale oscillatory baffled reactors. *Chem. Eng. J.* **2010**, *159*, 212–219, doi:https://doi.org/10.1016/j.cej.2010.02.059.

177. Stonestreet, P.; Veeken, P.M.J. Van Der The Effects of Oscillatory Flow and Bulk Flow Components on Residence Time Distribution in Baffled Tube Reactors. *Chem. Eng. Res. Des.* **1999**, *77*, 671–684, doi:https://doi.org/10.1205/026387699526809.

178. Womersley, J.R. Method for the calculation of velocity, rate of flow and viscous drag in arteries when the pressure gradient is known. *J. Physiol.* **1955**, *127*, 553–563, doi:10.1113/jphysiol.1955.sp005276.

179. Sudo, K.; Sumida, M.; Yamane, R. Secondary motion of fully developed oscillatory flow in a curved pipe. *J. Fluid Mech.* **1992**, *237*, 189–208, doi:DOI: 10.1017/S0022112092003380.

180. Siggers, J.H.; Waters, S.L. Unsteady flows in pipes with finite curvature. *J. Fluid Mech.*

2008, *600*, 133–165, doi:10.1017/S002211200800030X.

181. Smith, K.B.; Mackley, M.R. An Experimental Investigation into the Scale-up of Oscillatory Flow Mixing in Baffled Tubes. *Chem. Eng. Res. Des.* **2006**, *84*, 1001–1011.

182. Ni, X.; De Gélicourt, Y.S.; Baird, M.H.I.; Rao, N.V.R. Scale-up of single phase axial dispersion coefficients in batch and continuous oscillatory baffled tubes. *Can. J. Chem. Eng.* **2001**, *79*, 444–448, doi:10.1002/cjce.5450790318.

183. Brown, C.J.; Ni, X.-W. Determination of metastable zone width, mean particle size and detectable number density using video imaging in an oscillatory baffled crystallizer. *CRYSTENGCOMM* **2012**, *14*, 2944–2949, doi:10.1039/c2ce06628a.

184. Chew, C.M.; Ristic, R.I.; Dennehy, R.D.; De Yoreo, J.J. Crystallization of paracetamol under oscillatory flow mixing conditions. *Cryst. Growth Des.* **2004**, *4*, 1045–1052, doi:10.1021/cg0499131.

185. Alvarez, A.J.; Myerson, A.S. Continuous Plug Flow Crystallization of Pharmaceutical Compounds. *Cryst. Growth Des.* **2010**, *10*, 2219–2228, doi:10.1021/cg901496s.

186. Fryer, D.M. *High Pressure Vessels*; Harvey, J.F., Ed.; Springer US: Boston, MA, 1998; ISBN 9781461559894.

187. Gong, D.Z.S.X.S.D.J.W.J. Progress of Pharmaceutical Continuous Crystallization. *Eng. (Beijing, China)* **2017**, *3*, 354–364, doi:10.1016/j.eng.2017.03.023.

188. Blagden, N.; de Matas, M.; Gavan, P.T.; York, P. Crystal engineering of active pharmaceutical ingredients to improve solubility and dissolution rates. *Adv. Drug Deliv. Rev.* **2007**, *59*, 617–630, doi:https://doi.org/10.1016/j.addr.2007.05.011.

189. Chen, J.; Sarma, B.; Evans, J.M.B.; Myerson, A.S. Pharmaceutical Crystallization. *Cryst. Growth Des.* **2011**, *11*, 887–895, doi:10.1021/cg101556s.

190. Eder, R.J.P.; Radl, S.; Schmitt, E.; Innerhofer, S.; Maier, M.; Gruber-Woelfler, H.; Khinast, J.G. Continuously Seeded, Continuously Operated Tubular Crystallizer for the Production of Active Pharmaceutical Ingredients. *Cryst. Growth Des.* **2010**, *10*, 2247–2257, doi:10.1021/cg9015788.

191. Cruz, P.; Rocha, F.; Ferreira, A. Effect of operating conditions on batch and continuous paracetamol crystallization in an oscillatory flow mesoreactor. *CrystEngComm* **2016**, *18*, 9113–9121, doi:10.1039/C6CE01648K.

192. Sharma, M.K.; Suru, A.; Joshi, A.; Kulkarni, A.A. A Novel Flow Reactor for Handling Suspensions: Hydrodynamics and Performance Evaluation. *Ind. Eng. Chem. Res.* **2020**, *59*, 16462–16472, doi:10.1021/acs.iecr.9b06864.

193. Hoy, S.M. Sodium Zirconium Cyclosilicate: A Review in Hyperkalaemia. *Drugs* **2018**, *78*, 1605–1613, doi:10.1007/s40265-018-0991-6.

194. Stavros, F.; Yang, A.; Leon, A.; Nuttall, M.; Rasmussen, H.S. Characterization of structure and function of ZS-9, a K+ selective ion trap. *PLoS One* **2014**, *9*, e114686–e114686, doi:10.1371/journal.pone.0114686.

195. Keyser, D.J.; Guillem, A.F.; Gilmore, J. Microporous zirconium silicate for the treatment of hyperkalemia 2016, 103.

196. Ni, X.; Mackley, M.R.; Harvey, A.P.; Stonestreet, P.; Baird, M.H.I.; Rama Rao, N. V Mixing Through Oscillations and Pulsations—A Guide to Achieving Process Enhancements in the Chemical and Process Industries. *Chem. Eng. Res. Des.* **2003**, *81*, 373–383, doi:https://doi.org/10.1205/02638760360596928.

197. Stonestreet, P.; Harvey, A.P. A mixing-based design methodology for continuous oscillatory flow reactors. *Chem. Eng. Res. Des.* **2002**, *80*, 31–44,

doi:10.1205/026387602753393204.

198. Ahmed, S.M.R.; Phan, A.N.; Harvey, A.P. Scale-Up of Oscillatory Helical Baffled Reactors Based on Residence Time Distribution. *Chem. Eng. Technol.* **2017**, *40*, 907–914, doi:10.1002/ceat.201600480.

199. Ali, S. Pressure drop correlations for flow through regular helical coil tubes. *Fluid Dyn. Res.* **2001**, *28*, 295–310, doi:10.1016/S0169-5983(00)00034-4.

200. Srinivasan, P.S. Pressure drop and heat transfer in coils. *Chem. Eng.* **1968**, *218*, 113–119.

201. Di Piazza, I.; Ciofalo, M. Numerical prediction of turbulent flow and heat transfer in helically coiled pipes. *Int. J. Therm. Sci.* **2010**, *49*, 653–663, doi:10.1016/j.ijthermalsci.2009.10.001.

202. Itō, H. Friction Factors for Turbulent Flow in Curved Pipes. *J. Basic Eng.* **1959**, *81*, 123–132, doi:10.1115/1.4008390.

203. Srinivasan, P.S.; Nandapurkar, S.S.; Holland, F.A. Friction factors for coils. *Trans. Inst. Chem. Eng. Chem. Eng.* **1970**, *48*, 156–161.